The University Of Sheffield.

Organic Microcavities and OLEDs

by
Nikolaos Christogiannis

A thesis submitted for the degree of
Doctor of Philosophy
in Physics

Department of Physics and Astronomy
The University of Sheffield

July 2016

To my parents,
my sister, my good friends, and my love.

Abstract

The merging fields of photonics and organic electronics into organic optoelectronics has created a surge of enthusiasm over the possibility of developing low-cost and large-area advanced optoelectronic systems. These applications can combine the best functionalities of both fields, such as tailoring the organic semiconductors by chemical means, engineering the structure in which organic materials are embedded in, are to name a few. These advances have stimulated the excitement over the next generation of optoelectronic systems with enhanced capabilities and low-cost manufacturing processes compared to their inorganic counterparts. Such technology direction is mainly reflected by the high investments towards the aim of developing flexible, and roll-to-roll organic light-emitting diodes and organic solar cells.

Interestingly, more sophisticated applications require a deeper understanding of the underlying mechanisms at play that merge concepts from the fields of photonics and organic electronics. Particularly, organic light-emitting diodes (OLEDs) under certain constraints (such as cavity light confinement, strong exciton-photon interaction) exhibit modified spectral emission compared to OLED devices that are not bounded by the same conditions. The introduction of the polariton concept as a quasi-particle, which is part-light and part-matter, has emerged to describe such new physical phenomena caused by this photon-exciton intricate interaction. Polariton physics is well established in inorganic semiconductors were a plethora of physical phenomena have been demonstrated, such as the appearance of Bose-Einstein Condensation or low-threshold laser devices. The later is what has as yet to be demonstrated from the field of solid state physics utilising organic semiconductors.

This thesis is focused on the study of the physics and the engineering of organic light-emitting diodes that will aid in the realization of efficient organic polariton LEDs. The main body of work examines various organic semiconductor materials in their ability to reach the strong light and matter interaction regime and, subsequently, to be used in OLEDs as the emissive component. Furthermore, a degradation investigation highlights the issues that affect small-molecule based OLEDs, and finally, the possible pathways for achieving efficient polariton OLEDs are discussed.

Contents

Table of Figures

Chapter 1

Introduction

Chapter 1 is the introductory chapter of this thesis and is organized into three separate sections. A general historic overview is given in the first section where the concept of the organic polariton LED is introduced. The second section explains the motivation behind the experiments. Here, two main targets are explored. The first target focuses on the engineering of organic polariton devices and the second target focuses on the physics that govern their operation. The last section describes how this thesis is structured into chapters. The content of each chapter that follows is separately detailed.

1.1 General introduction

The field of organic electronics has made rapid progress over the past 50 years. Nowadays, organic materials can be engineered through a sequence of chemical synthetic steps that allows freedom of design depending on the desired property. For example, such property can be the emission wavelength or the addition of a functional unit that can enhance the material's solubility. This allows organic materials to be explored in a broad range of optoelectronic applications that in some instances may supersede the already established analogues of the inorganic semiconductor industry.

Historically, in the late 1960's light emission from an organic material following charge injection and recombination was reported for the first time from Williams and Schadt [1]. The electroluminescent medium was crystalline anthracene which was positioned between two structured electrodes. Under 100 V of applied bias electrons and holes were fused together and recombined to generate electroluminescence.

Thereafter, a major breakthrough in the field occurred in 1987 by the work of Tang and Van Slyke [2]. The authors demonstrated a high performance organic light-emitting diode (OLED) operating at a few volts by utilizing a double-layer heterostructure made from thin evaporated films of small molecule organic semiconductors. Since then, organic semiconductors have attracted considerable attention as the active materials for optoelectronic devices.

So far, the inorganic semiconductor industry has dominated the market with a wide range of commercial products including solar cells, LEDs, transistors, amplifiers, and lasers based on solid and more recently on flexible substrates [3-6]. However, there are issues associated with the fabrication of these devices. Examples include the high cost related to the complexity of the processing steps of inorganic materials and compounds such as Si, Ge, InGaN, GaAs, etc., the scarcity of available materials, and other environmental issues linked to the lack of available recycling units for these heavy element-based devices. For this reason, researchers have turned attention towards organic electronic materials and devices.

Since the Chemistry Nobel Prize award in 2000 to Heeger, MacDiarmid and Shirakawa for the demonstration of electrical conductive polymers, a range of applications have penetrated the market. One of the most significant applications is the organic light-emitting diode focusing on products such as lightning and displays. As an example, LG has already commercialised a 55" 4K curved OLED TV, which signifies the transition towards organic electronics for future applications.

Organic photovoltaic cells (OPVs) [7] and organic field-effect transistors (OFETs) [8] have also been investigated. Other applications describe the role of organic materials in connection to biological sciences for quick and inexpensive chemical and biological sensing [9, 10].

Despite all such previous research, there is still one missing demonstration from the field of solid state physics; an electrically pumped organic laser. There are three possible technical reasons to explain this: Firstly, the technology is not sufficiently mature yet to provide with high quality structure devices. Therefore, losses dominate the system and the population inversion threshold for lasing action cannot be reached. Secondly, interaction and loss processes inside the OLED device have not been fully understood. Thirdly, the very high

density of charge carriers that is required to reach population inversion is so large that the device is destroyed before electrically excited optical gain is realized.

Historically, there have been only a few reports on spectral narrowing from electrically excited OLEDs. However, all of them fail to provide with convincing evidence of lasing [11-14]. The most recent claim of lasing has been reported from an OLED device emitting at 610 nm employing a double microcavity Alq_3:DCM configuration [15]. A summary was published from Ifor Samuel et al. outlining a set of criteria that must be fulfilled to convincingly demonstrate lasing action [16].

Lasing can however be realised in an organic semiconductor by optical pumping. Examples include small molecule organic materials and conjugated polymers. An example of the former is the archetypal AlQ_3:DCM where light is absorbed by the higher gap host AlQ_3 molecules following an efficient non-radiative energy transfer in the lower gap of the guest DCM molecules [17, 18]. An example of the later are the poly(phenylene vinylene) (PPV) and polyfluorenes such as PFO and F8DP [19]. Based on the optical pumping concept a hybrid device has been fabricated by Y. Yang et al. [20] where an INGaN light-emitting diode is used to excite a periodically structured fluorine copolymer (DFB). It was explained that this is an effective way to use organic semiconductors as laser sources. Similarly, pumping the organic semiconductor with an OLED has been unsuccessful due to the low power density of the fabricated OLED [21].

Polariton physics has emerged as a potential candidate to achieve the organic laser diode. Most encouraging are the recent demonstrations of both room temperature electrically pumped inorganic polariton lasing [22, 23] and of the formation of organic polariton condensates in organic microcavity systems [24, 25]. From this point of view, coherent light emission is generated from the lowest energy state of the system in terms of a macroscopic thermodynamic phase transition. Because the mechanism of polariton lasing is stimulated scattering rather than stimulated emission of radiation, the energy required to reach threshold is less in a polariton laser [26, 27]; therefore, it has been suggested that the conditions to reach bosonic final state stimulation could occur at lower densities of carrier injection for an organic laser diode.

1.2 Motivation of present work

One of the missing demonstrations of organic semiconductor physics is the realisation of OLED-based lasers. So far, all efforts to fabricate high quality devices utilizing an organic semiconductor as the emissive layer and to subsequently achieve population inversion have been unsuccessful.

An alternative route that has been proposed to create coherent light emission by electrical means is by the use of quasiparticles, called polaritons, which are part light and part matter [28]. By taking advantage of their peculiar properties, it may be possible that OLED devices will reach the lasing threshold at low current densities before being damaged. Thus, the fabrication of organic light-emitting diodes that use organic materials where resonant energy is exchanged between photons and excitons and the study of their optoelectronic properties will assist in the creation of efficient organic polariton LEDs and in the development of an organic laser diode.

The objective of this research is two-fold and is based on the concept of resonant energy exchange between photons and excitons. The first objective investigates the fabrication aspects of the device which are the selection of the organic semiconductors in the OLED and how the device will be structured and engineered. The second objective of this thesis is to understand the physics that govern these devices. Therefore, this thesis brings together the concepts of the organic light-emitting diode and the strong exciton-photon coupling in organic microcavities.

This thesis describes the main contribution of the author to the ICARUS Marie Curie Initial Training Network (ITN) of the 7th Framework Program of the European Union Commission. The main focus of the network was the development of organic and hybrid organic-inorganic semiconductors that target novel optoelectronic applications.

1.3 Thesis Organization

This thesis is separated into eight chapters. The sequence of the chapters is organized in the following way:

Chapter 1 is an introduction of this thesis where an overview of the topic is given. The aims and the objectives of the project are also summarized.

Chapter 2 is an introduction to the basic theoretical concepts behind organic electronics. An introduction to organic semiconductors is given. It includes the origin of the HOMO and LUMO energy levels, the mechanisms of fluorescence and phosphorescence and the Förster and Dexter energy transfer mechanisms. Furthermore, charge injection and transport in organic semiconductors are discussed.

Chapter 3 gives an overview of the physics of the strong light and matter interaction in organic microcavities. It deals with light confinement in microcavity structures and explains the concepts of the strong and the weak coupling regimes being distinguished from each other.

In Chapter 4 the material requirements and the device structural characteristics of conventional OLEDs and polariton OLEDs are presented. The fabrication steps of organic light emitting diodes are also detailed. Then the various methods that were employed for both optical and electrical characterization are discussed.

Chapter 5 discusses the use of cyanine dye J-aggregates in polariton OLEDs. The impact of a bottom DBR mirror on the quality factor of the cavity and the performance of the device is analysed. Moreover, the experimental results are tested against theoretical predictions which are used to explain the population of the polariton states.

Chapter 6 discusses a series of materials that are used in polariton microcavities and OLEDs. The main obstacles for achieving efficient operation in such structures are explained.

Chapter 7 discusses the material and engineering challenges that govern organic polariton LEDs. The focus is based on small-molecules as the emissive materials in OLEDs and discusses the various degradation issues related to them.

Chapter 8 summarizes the thesis work. Specifically, some design rules are given in order to circumvent some of the problems that render solution-processed polariton OLEDs as inefficient. Possible architectures for achieving high polariton density are suggested. Finally, the future direction of the field and the research work that has to be carried out are discussed.

Chapter 2

Organic Microcavity LEDs: Fundamentals.

In this chapter the fundamental concepts of organic semiconductors are reviewed. The appearance of the HOMO and LUMO energy levels that are distinctive for each organic semiconductor is described and their physical properties are discussed. Optical mechanisms such as fluorescence and phosphorescence and electrical mechanisms such as charge injection and transport under electrical excitation are explained. This section is summarized with a general description of the operation of an OLED and the main losses that influence the performance of such devices.

2.1 Organic semiconductors

The current integrated circuit (IC) technology utilizes as main active components, materials with a variety of optoelectronic properties [5]. A common electrical property which is used to classify them is resistivity, ρ. This property is inversely proportional to the conductivity σ. Metal stripes that are used as connecting parts in integrated circuits, such as aluminium, have a room temperature resistivity of about 10^{-6} Ω·cm. Other parts of the integrated circuit use SiO_2 as an insulator or plastics for encapsulation with resistivity of about 10^{16} Ω·cm and 10^{18} Ω·cm, respectively. This physical property has a range of 24 orders of magnitude. Based on the resistivity classification, materials with less than 10^{-2} Ω·cm resistivity are called conductors. At the opposite side, materials with resistivity greater than about 10^{5} Ω·cm are called insulators. Materials in the middle are called semiconductors.

The term semiconductor was first used in connection to crystalline inorganic solids, but later the term was used to molecular systems as well. One of the differences between organic and inorganic materials is associated with the bonds they form. The bond in inorganic materials is mainly covalent. In this type of bonding, each atom shares its outer shell electrons with its neighbouring atoms. For example, in crystalline silicon each Si atom has four valence electrons which are shared with the four neighbour silicon atoms.

In organic solids covalent bonds exist only for the atoms within the molecule. The intermolecular interaction between different molecules is due to the weak Van der Waals interaction. Consequently, the molecular orbital overlap is small and therefore the molecules will remain unchanged. A common feature of all organic semiconductors is that they possess a low dielectric constant due to their small intermolecular overlap. As a result, the formation of excitons is associated with high binding energies of the order of hundred meVs.

There are various arrangements of the organic molecules in the solid state such as the crystalline, the amorphous, the glass, and the liquid crystal phases. Which phase dominates depends on the nature of the organic molecule and the deposition technique used, such as the solution-processed or the vacuum-sublimation techniques. A better understanding of the optoelectronic properties of organic solids can be gained through the chemistry that defines the bond formation of carbon atom. Promotion and hybridization are important concepts that will be described in the following section.

2.1.1 Promotion and hybridization in carbon atom

The carbon atom belongs to the group four and the second period (p-block) of the periodic table, thus it has six electrons in its ground state electronic configuration: $1s^2 2s^2 2p_x^1 2p_y^1 2p_z^0$. The $1s^2$ symbol refers to the atomic orbital with principle quantum number n=1, azimuthal quantum number l=0, and magnetic quantum number m=0. The superscript 2 is given because two electrons occupy the same s orbital with paired spins according to the Pauli Exclusion

Principle. Therefore, the 2s-orbital is occupied by two electrons and two out of three 2p-orbitals are occupied by one electron.

Before the molecular orbital is formed, the carbon atom passes through a step of promotion and hybridization. This is a concept that was introduced to explain the tetravalent bonding of molecules such as methane (CH_4), as the valence bond theory could not explain at the time these observations. One of the two electrons in the 2s-orbital is promoted to the remaining unoccupied $2p_z$-orbital; thus the system acquires an excited electronic configuration: $1s^2 2s^1 2p_x^1 2p_y^1 2p_z^1$. Next, hybridization proceeds by the remaining unpaired electron that reside in the 2s-orbital with a combination of the electrons each residing in the half-filled 2p-orbitals. These combinations are referred to as hybrid orbitals. The three schemes are explained in the following paragraphs and can be seen in Figure 2-1, denoted as sp, sp^2 and sp^3 hybrid orbitals.

sp^3 hybridization can be achieved by the combination of one 2s-orbital and the three 2p-orbitals forming four equivalent hybrids. The molecule acquires a tetrahedron structure with all hybrid orbitals pointing towards the corner of the tetrahedron with an angle of 109.5^0 by any two of them. Carbon can form totally four strong σ bonds with neighbour atoms. This is referred to as single bond (C-X).

In the sp^2 hybrid structure of carbon one 2s-orbital and two 2p-orbitals combine together to form three co-planar hybrid orbitals, with angle of 120^0 from each other. The remaining p_z orbital is perpendicular to the plane. The sp^2 hybrids are linked by strong σ-bonds connecting the hybrid orbitals with orbitals of other atoms, whereas the p_z orbital is responsible for the weaker, π-bonding. The bond is referred to as double-bond (C=X).

Finally, the sp hybridization is the combination of one 2s-orbital and one of the three 2p orbitals. This arrangement is co-linear with their segments pointing 180^0 in opposite directions. The other two 2p remaining orbitals are perpendicular to the axis of the hybrid structure and perpendicular to each other. Therefore, a triple bond is the result of one σ-bond of the hybrids and two π-bonds of the p-orbitals.

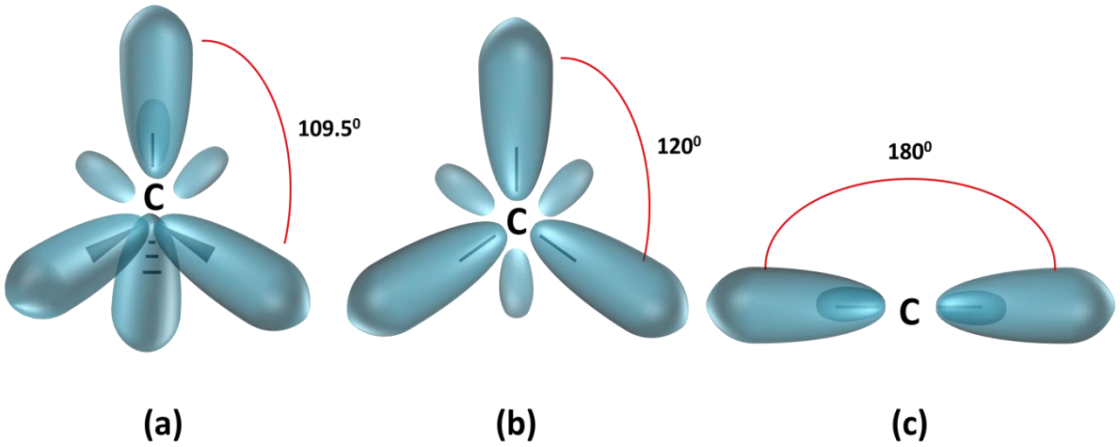

Figure 2-1– Schematic representation of the formed hybrid systems: (a) sp^3 hybridization, (b) sp^2 hybridization and (c) sp hybridization, redrawn based on ref. [29].

2.1.2 Molecular orbitals

As discussed in the last section, molecular orbitals result from the linear combination of atomic orbitals (LCAO). I now consider the electronic configuration and spatial distribution of electrons in such an organic molecule according to the molecular orbital picture.

As an example, the ethene molecule shown schematically in Figure 2-2 (a) will be considered. Figure 2-2 (b) illustrates the electron configuration of carbon atom in the sp^2 promoted excited state of ethene. There are three sp^2 hybrid orbitals and one half-filled occupied unhybridized p-orbital. When two adjacent sp^2 hybrid orbitals approach each other, their electronic wave functions will start to overlap to form molecular orbitals (Figure 2-2 (c)).

There are two scenarios according to the in- or out- of phase electronic wave function overlap. In the first case, when the wave functions are in-phase, a σ bonding orbital will be formed. These bonds show circular symmetry around the internuclear axis, have large interaction energy and high electron density between the two nuclei. In the second case, the wave functions are out-of-phase, a σ* anti-bonding molecular orbital is formed that is associated with a decreased energy density between the two nuclei.

Similarly, two cases result from the interaction of the remaining half-filled electron p orbitals. The wave functions interact constructively or destructively to give π bonding or π* anti-bonding orbitals; the two correspond to the HOMO and LUMO energy levels of the ethene molecule, respectively. The relative energy scheme for the formation of molecular orbitals is illustrated in Figure 2-2 (c).

In conjugated molecules electrons in π-orbitals are extensively delocalized. According to molecular orbital theory the incorporation of more molecules in the structure will shift the energy levels of the formed molecular orbitals due to the interaction with the additional electrons. Subsequently, the energy level splitting will result in the reduction of the π-π* energy bandgap. This bandgap energy is reduced further by the addition of new atoms to the molecular structure (e.g. to form polymer).

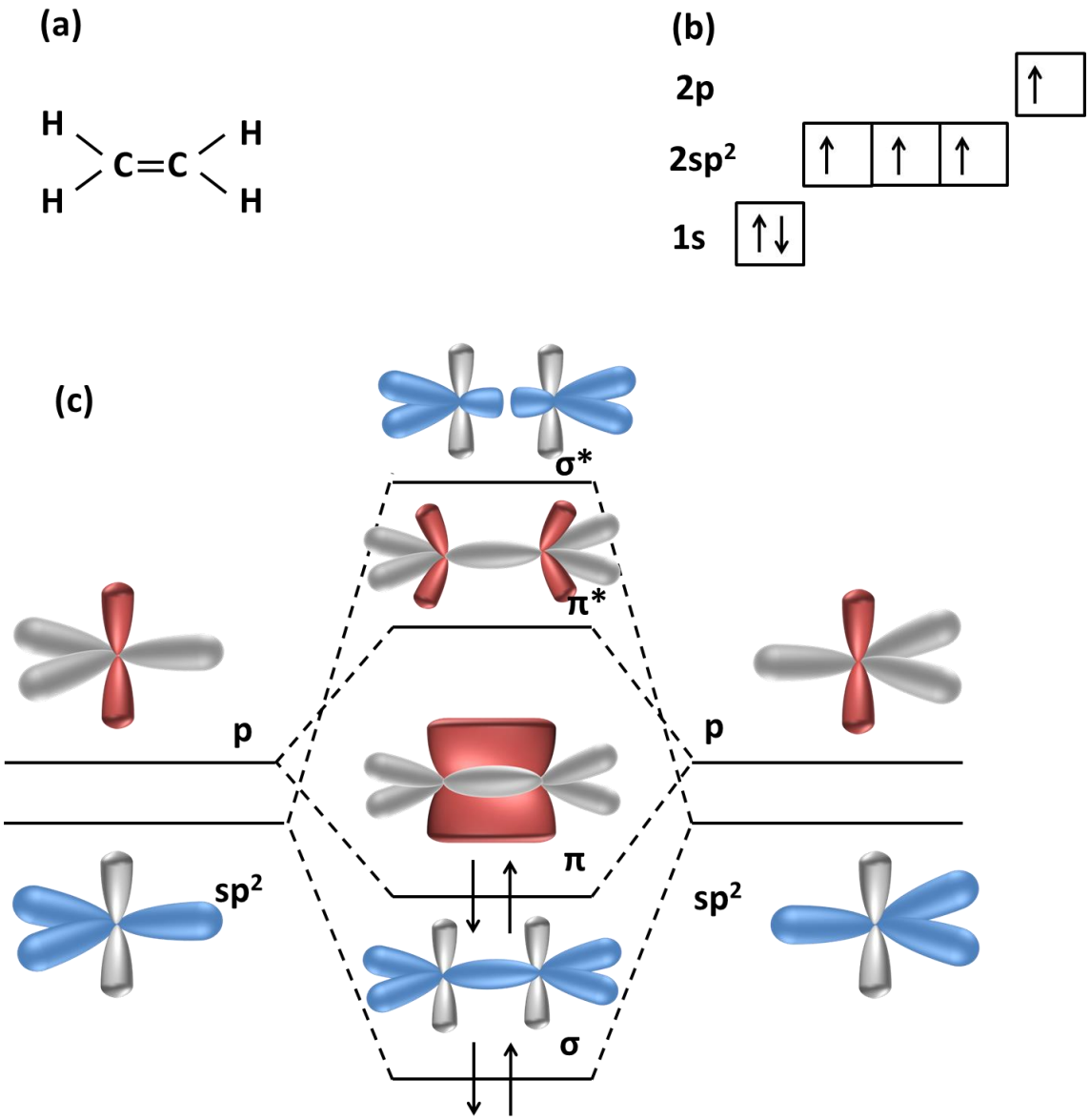

Figure 2-2 – (a) Schematic representation of the ethene molecule, (b) Electron configuration of carbon atom in its sp^2 hybrid state, (c) Molecular orbital formation. Redrawn based on ref. [30].

2.2 Optical properties

The energy bandgap of the π and π* transition is within the range 1.5-4 eV; this means that the absorption spectrum of the HOMO-LUMO bandgap is excited by visible and near-UV light. The π bonds can be excited easier than the σ bonds. Geometrically, the region which is responsible for light absorption is called chromophore. Alternatively, the region which is responsible for the molecule's emission is called fluorophore.

When light is absorbed by a molecule, an electron from the HOMO energy level is transferred to the LUMO energy level of the same molecule. This jump leaves behind a vacancy that is

termed as hole. This electron promotion from the HOMO to the LUMO energy level causes charge redistribution within the molecule. The generated electron and hole are attracted to each other by Coulomb forces. Thus, the electron-hole pair forms a charged quasi-particle that is neutral and is termed Frenkel exciton, localized to a single molecule. The coulomb energy of the bound pair is given by the equation:

$$E = \frac{q^2}{4\pi\varepsilon_0\varepsilon_r x} \tag{2.1}$$

Here, q is the elementary charge, ε_0 is the dielectric constant in vacuum, ε_r is the dielectric constant of the material and x the distance between the electron and the hole. One of the differences between the Coulomb interaction in organic and in inorganic semiconductors is based on the material's dielectric constant. For organic semiconductors ε_r is low (≈3.3 for Alq_3), whereas for inorganic semiconductors ε_r is high (≈ 11 for Si). This means that the separation distance in organic semiconductors is smaller and their binding energy higher. The binding energy in common organic materials is of the order of 1 eV and is larger than the thermal energy k_BT; therefore, Frenkel excitons are stable at room temperature.

One of the most important characteristics of Frenkel excitons is their spin states [31]. One way to classify those states is to consider the multiplicity (2S+1) which refers to the possible orientations of the spin angular momentum of electrons. Two electrons can combine together in the following ways based on their multiplicity:

When the molecule is in the ground state, the HOMO level is occupied by two electrons with antiparallel spin. This state is referred to as a singlet state as the addition of two electrons with antiparallel spins results in a net spin S=0 and subsequently, a multiplicity of 2S+1=1.

When the molecule is in the excited state, there are two possible orientations for the spin; namely spin up or spin down. The antiparallel, out-of-phase orientation results (as in the ground state case) in a singlet state with a total spin S=0. The in-phase, parallel orientation of the two spins creates a net spin state of S=1 and has multiplicity of 3. This state is termed triplet state.

Therefore, there is one possible combination for the singlet state and three possible combinations for the triplet state in the excited state of a molecule, as seen from equations (2.2-2.3):

$$\frac{1}{\sqrt{2}}(|\uparrow\downarrow\rangle - |\downarrow\uparrow\rangle) \quad \text{(Singlet state)} \tag{2.2}$$

$$\begin{cases} |\uparrow\uparrow\rangle \\ \frac{1}{\sqrt{2}}(|\uparrow\downarrow\rangle + |\downarrow\uparrow\rangle) \\ |\downarrow\downarrow\rangle \end{cases} \quad \text{(Triplet states)} \tag{2.3}$$

The absorption of a photon from the HOMO to the LUMO singlet state can be represented by $S_0 \rightarrow S_1$. Alternatively, the transition from the HOMO to the LUMO state in an organic semiconductor that is associated with a triplet state can be represented by $S_0 \rightarrow T_1$.

The triplet absorption transition cannot be directly generated, but indirectly created using the process of intersystem crossing (ISC). The various processes responsible for the absorption, emission or other energy state transitions of a molecule are described by the use of a Jablonski energy state diagram [31].

The Jablonski diagram is commonly used to describe electronic transitions of organic molecules and is shown in Figure 2-3. The vertical axis represents the potential energy of the system, whereas the horizontal axis has no physical meaning.

In the energy diagram, S_0, S_1, and S_2 refer to the singlet ground, 1st excited and 2nd excited energy states, respectively. The S_2 energy state reflects a higher energy transition from the ground state to a higher energy molecular state. For example in Figure 2-2 this energy could correspond to the $\pi \rightarrow \sigma^*$. Moreover, in the same diagram the exciton states are seen to split further into additional states. These are considered here as each molecule is associated with vibrations. These are called vibronic transitions and are denoted as 0,1,2,..

Similarly, the first triplet energy state is denoted as T_1 and is further split into sublevels due to the vibrational modes. There is no ground T_0 transition. Moreover, the T_1 triplet state is in principle lower in energy than the S_1 singlet state. The energy difference between the singlet and the triplet states has a quantum mechanical origin. It is associated with spatially asymmetric wavefunctions that result in reduced interactions between electrons.

The molecule can be optically excited or emitted through the singlet states. Therefore, the absorption transitions from $S_0 \rightarrow S_1, S_2, \ldots S_n$ are strong due to the high absorption coefficients $\varepsilon(S_0 \rightarrow S_n, n=1,2,..)$. Triplet absorption and emission transitions have low absorption coefficients due to the spin considerations. Only transitions related to the S_0 and S_1 levels will be considered here. Other higher energy transitions of singlet states are possible; however, they must be related to higher energy transitions in the deep UV spectral region.

When molecules undergo a transition from the S_0 state to a vibronic level of the S_1 state they will relax fast to the lowest vibronic level of the S_1 state. This process is called internal conversion (IC) and is associated with the release of heat through phonon emission. On the other hand, a singlet exciton may either decay back to the S_0 ground state by the release of a photon or relax non-radiatively by the release of many phonons (IC).

The radiative decay process is called fluorescence. Alternatively, through the process of intersystem crossing (ST) a singlet exciton can be converted to a triplet exciton by a spin-flip. This process has a very low probability and thus is unfavourable. The triplet exciton has two pathways for releasing its energy. It can either relax to the S_0 singlet state via the emission of a photon, a process which is termed as phosphorescence, or it can relax non-radiatively via phonon emission.

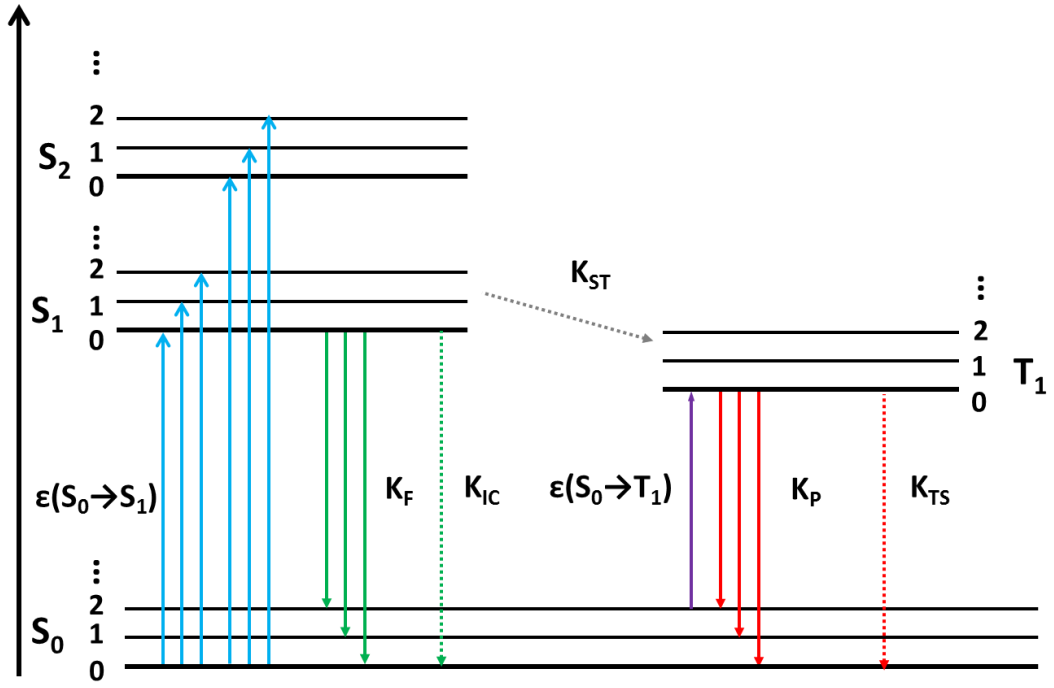

Figure 2-3: – Jablonski energy level diagram for an organic molecule. Singlet states: S_0, S_1, S_2. Triplet state: T_1. Absorption coefficients related to singlet-singlet and singlet-triplet transitions: $\varepsilon(S_0 \rightarrow S_1)$, $\varepsilon(S_0 \rightarrow T_1)$. Intersystem-crossing: K_{ST}, K_{TS}. Internal conversion: K_{IC}.

How fast or slow is each transition can be understood by considering the transition rates [31]. The fastest vibration rates are of the order of 10^{14} s^{-1}, the fastest fluorescent rates of the order of 10^{9} s^{-1} and the fastest phosphorescence rates of the order of 10^{3} s^{-1}. Alternatively, the spin interconversion rates have a wide range of rates, from 10^{-1} s^{-1} to 10^{12} s^{-1} and depend on the spin-orbit interaction overlap.

The possible radiative and the radiationaless processes are summarized as follows:

Processes that involve the absorption or emission of a photon [31]:

1) Singlet-singlet photon absorption, $S_0+hv \rightarrow S_1$; it is a spin allowed transition.
2) Singlet-triplet photon absorption $S_0+hv \rightarrow T_1$; it is a spin forbidden transition.
3) Singlet-singlet photon emission $S_1 \rightarrow S_0+hv$; it is a spin allowed transition, it is termed fluorescence and is characterized experimentally by the rate constant K_F.
4) Singlet-triplet photon emission $T_1 \rightarrow S_0+hv$; it is a spin forbidden transition, it is termed phosphorescence and is characterized experimentally by the rate constant K_P.

Processes that does not involve the absorption or emission of a photon:

1) Transition processes between same spin states $S_1 \rightarrow S_0+heat$, termed as internal conversion (IC) and are characterized by a rate constant K_{IC}.

2) Transition processes between different spin states $S_1 \rightarrow T_1$+heat, termed as intersystem crossing (ISC or ST) and are characterized by a rate constant K_{ST} or K_{ISC}.
3) Transition processes between the triplet and the ground excited states $T_1 \rightarrow S_0$+heat, termed intersystem crossing (ISC) and are characterized by a rate constant K_{TS} or K_{ISC}.

The Jablonski energy state diagram shows only electronic transitions where the nuclei of the atoms are thought of being fixed in a certain position. However, the real picture involves vibronic interactions as well.

When a molecule absorbs light on a timescale of 10^{-15} s the charge distribution in the molecule is rearranged. The nuclei will experience a different Coulomb force due to the shift of the electron cloud. The rearrangement of the nuclei will be much slower (10^{-12} s) as they are heavier. The Born-Oppenheimer approximation is based on this, that the motions of electrons in orbitals are much faster than the vibrational motions of nuclei. Thus, optical transitions occur vertically. The probability of coupling the optical transitions with vibrations can be described by the Frank-Condon factors.

To describe transitions that include vibrational interactions a Morse potential diagram is required, as seen characteristically from Figure 2-4 (a). In this diagram the ground (S_0) and the excited (S_1) state of a two-atom molecule as a function of the internuclear separation x are presented. Vertical lines represent absorption (blue curve) and emission (red curve) transitions. The horizontal lines represent the vibrational states that are bound by the Morse curves.

Absorption of a photon starts from the lowest v=0 vibrational level of the ground S_0 state since at room temperature this state is mostly populated. The most probable transition from v=0 of S_0 to the v' of S_1 will correspond to the vertical transition that has the maximum vibrational overlap. This corresponds to the v=0→ v'=3 vertical transition in the graph. Other transitions between v=0 and v' may occur but with lower probability.

The emission of photons follows the same principle. Now, the most populated level is the v'=0 of the excited S_1 state since all excited vibrations v' will relax to the v'=0 vibronic level before de-excitation. Emission is possible to all the v vibrational modes of the S_0 ground state.

Based on these the absorption and emission spectrum will be characterized by vibronic characteristics as seen from Figure 2-4 (b). The absorption and emission spectra exhibit mirror symmetry and are red-shifted. However, the experimentally obtained absorption and emission spectra show more broad characteristics. This is found more in conjugated polymers and can be both attributed to disorder. These are summarized in the following:

a) There is a high degree of disorder in organic materials that cause a high degree of energy distribution. During absorption measurements the energy peaks overlap; therefore the overall absorption band has broad characteristics.
b) The emission spectra of small molecules and polymers often show resolvable vibronic modes. In the emission measurement, as a consequence of energy transfer, a smaller amount of molecules is sampled. The formed exciton migrates before the emission of a photon. The emission spectrum represents only a fraction of the excited molecules.

c) When two molecules interact and are both in the ground state and of the same species it is possible to form an intermolecular energy state. This is termed aggregate. The aggregated state is characterized by a broad and red-shifted absorption and emission spectra relative to the individual transitions of the isolated molecules.
d) Excimer states result from the interaction between an excited molecule and a ground-state molecule of the same species. Excimers have a characteristic broad and featureless emission band which is red-shifted relative to the individual chromophore emission.
e) An exciplex is formed from the interaction between molecules of different species. One state remains in the ground state and the other in an excited state. An exciplex involves some degree of charge transfer; therefore, they act as donors and acceptors.

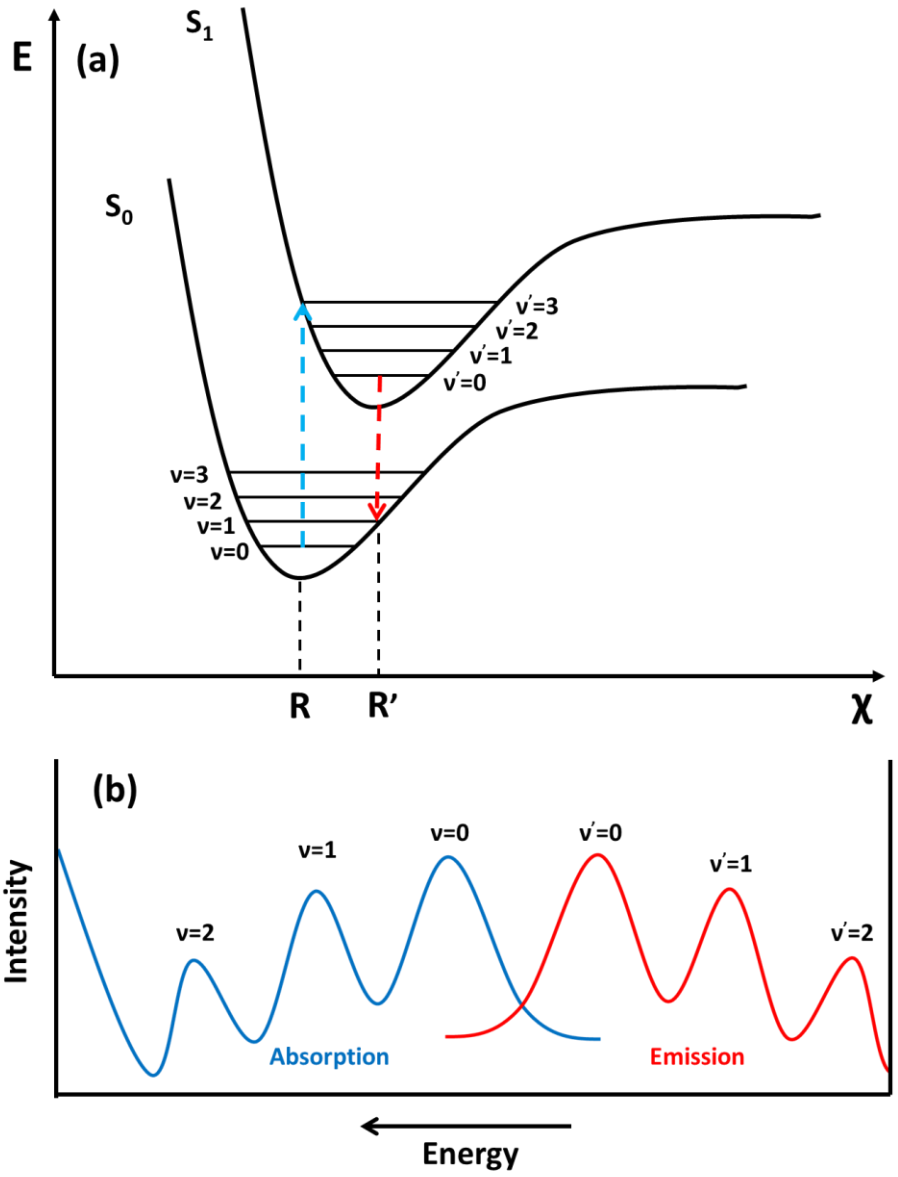

Figure 2-4 – (a) Morse potential energy diagram. The diagram illustrates the potential energy curves of the ground state and the excited state that correspond to a diatomic organic molecule. The vertical lines represent optical transitions and the horizontal lines represent vibrational states. (b) The expected absorption and emission spectra that correspond to the diatomic molecule of the Morse diagram.

2.3 J-aggregates

J-aggregates are ordered arrangements of highly polar and fluorescent cyanine dyes [32]. The highly polar monomers self-assemble under the influence of their mutual dipole interactions. Depending on the relative orientation of the monomers the aggregate can have a high degree of organization. This influences its optical properties as a result of the ordering. The self-assembly into chain-like crystallites is a susceptible process which is affected by various environmental changes. However, it can be controlled.

The optical properties of the J-aggregates depend on the relative orientation of the dye molecules. The partial overlap between the electron accepting and donating groups of

adjacent molecules will define its optical properties. The individual dipole moments of each molecule will couple to form a giant dipole oscillator, the so-called J-band. Upon optical excitation the oscillating electron density of one molecule induces oscillations to the electron density of the neighbouring molecules. Now the exciton is not localized over the monomer but is more delocalized and extends in size over all the aggregated state.

Generally, the dipole moments can be coupled in-phase or out-of-phase. This splits the energy levels into bands, the lower of which has concentrated most of the oscillator strength from all transitions. The red-shift observed upon aggregation is a direct consequence of that splitting.

The J-aggregates have distinct optical properties caused by the redistribution of the oscillator strength. For large number of N monomers the collective dipole moment of the aggregate is given by:

$$\mu_{J-Agg}^2 = 0.81(N+1)\mu_{mon}^2 \quad (2.4)$$

where, μ_{mon} refers to the dipole moment of the monomer unit [33]. Furthermore, the linewidth of the J-aggregate absorption band reduces significantly. The relative expression is described by equation (2.5).

$$\Delta E_{J-Agg} = \frac{\Delta E_{mon}}{\sqrt{N}} \quad (2.5)$$

2.4 Charge carriers in organic semiconductors

In organic light-emitting diodes electrons are injected from the cathode and holes are injected from the anode to the adjacent organic semiconductors. The efficiency of this current injection process depends on the energy barrier that exists between the respective materials. Before the electrical properties of an organic semiconductor are discussed an overview of charge carriers in organic materials will be given.

The interaction between a charge carrier and an atom of an organic molecule is stronger in an organic than in an inorganic semiconductor due to the low dielectric constant that organic materials possess. To start the charge transport process either the HOMO or the LUMO energy levels of an organic molecule must be half-occupied. This means that the molecule will be transformed into a radical ion. In the former case the ion is termed radical cation, whereas in the latter case the ion is termed radical anion.

Such charge carriers induce a lattice distortion within their surroundings. The interaction of electrons and holes with their surroundings (molecular vibrations) is described by a new quasi-particle which is referred to as polaron. The radical cation is termed hole-polaron, whereas the radical anion is termed electron polaron.

It is important to mention that the charge carriers cause a change in the geometry of the molecule compared to its ground state electronic configuration. The charged molecule

polarizes itself and also adapts to the charge redistribution within the molecule. This process is termed relaxation.

Figure 2-5 illustrates the energy levels for hole and electron polarons compared to the HOMO and LUMO levels of the uncharged molecule. This electron-phonon coupling results in the shift of the initial energy levels of the uncharged molecule. The amount of energy required to extract an electron from the HOMO is defined as ionization potential (IP), whereas the amount of energy that is gained by an electron when added to the LUMO level is defined as electron affinity (χ).

From Figure 2-5 it is observed that the actual energy level of IP lies lower in energy than the HOMO and the energy level of χ lies in higher energy compared to the LUMO; hence, the bandgap corresponding to the HOMO-LUMO is larger than the bandgap corresponding to the IP-χ.

However, the bandgap energy level is defined by the positions of HOMO and LUMO. All energy levels are considered in relation to the vacuum reference level that is taken as the zero energy level. Electrons fill the energy levels according to Fermi statistics. The work function ϕ is defined by the energy difference between the vacuum and the Fermi level.

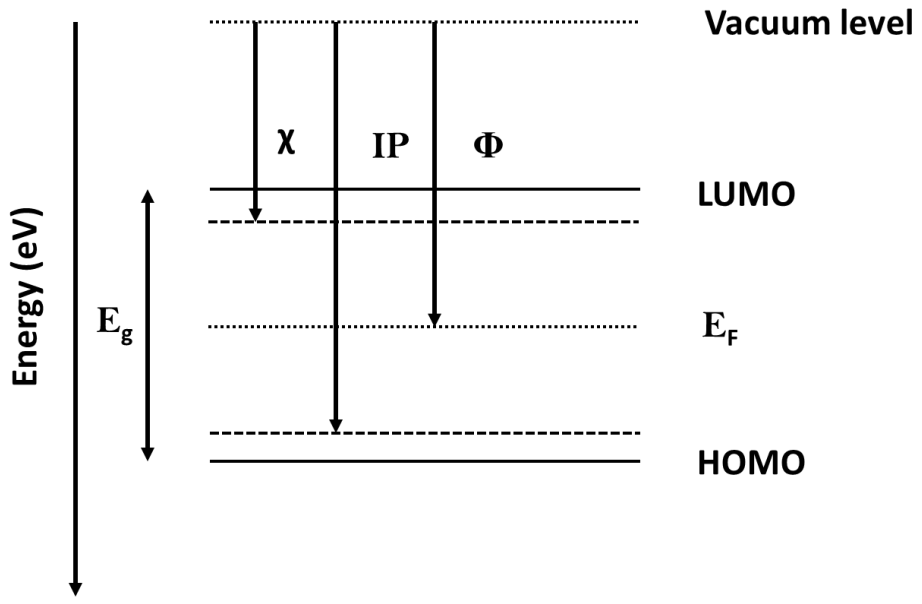

Figure 2-5 – A schematic energy diagram illustrating the HOMO and LUMO energy levels along with the ionization potential and the electron affinity. The work function and the vacuum (E_{vac}=0 eV) and Fermi energy levels are also presented. Figure based on Ref. [34].

2.5 Metal-organic semiconductor junctions

This section briefly discusses the energy level alignment at a metal-semiconductor interface. It also explains the nature of the energy barriers that are present at the interfaces and are responsible for prohibiting the efficient charge injection from the metallic electrodes. Figure 2-

6 illustrates the energy level shift that takes place when an organic semiconductor comes into contact with a metal.

Before contact, the metal and the organic semiconductor possess different Fermi energy levels as seen from Figure 2-6 (a). As an example, the HOMO and the LUMO of the organic material are located beneath and above the Fermi energy level of the metal, respectively. At the same time, the Fermi energy level of the organic material lies above the Fermi level of the metal.

Similarly to the inorganic semiconductor case, Fermi level alignment should be established between the two materials at contact. This means that band bending will occur in the space charge layer region and that the vacuum level will be aligned accordingly. Figure 2-6 (b) illustrates the relative energy levels of the two materials in contact. The two Fermi levels are aligned energetically. The HOMO and LUMO energy levels experience the same energy shift.

The vacuum level shift is not always achieved at the metal-organic interfaces. This is due to formation of interface dipoles that shift the vacuum level energy. These dipoles may have various origins, e.g. different arrangements of the electronic charge, interfacial chemical reactions or charge transfer across the interface. The energy shift due to dipoles is denoted as ϕ_d and can be as high as 1 eV; it is highlighted from the black stripe segment of Figure 2-6 (c).

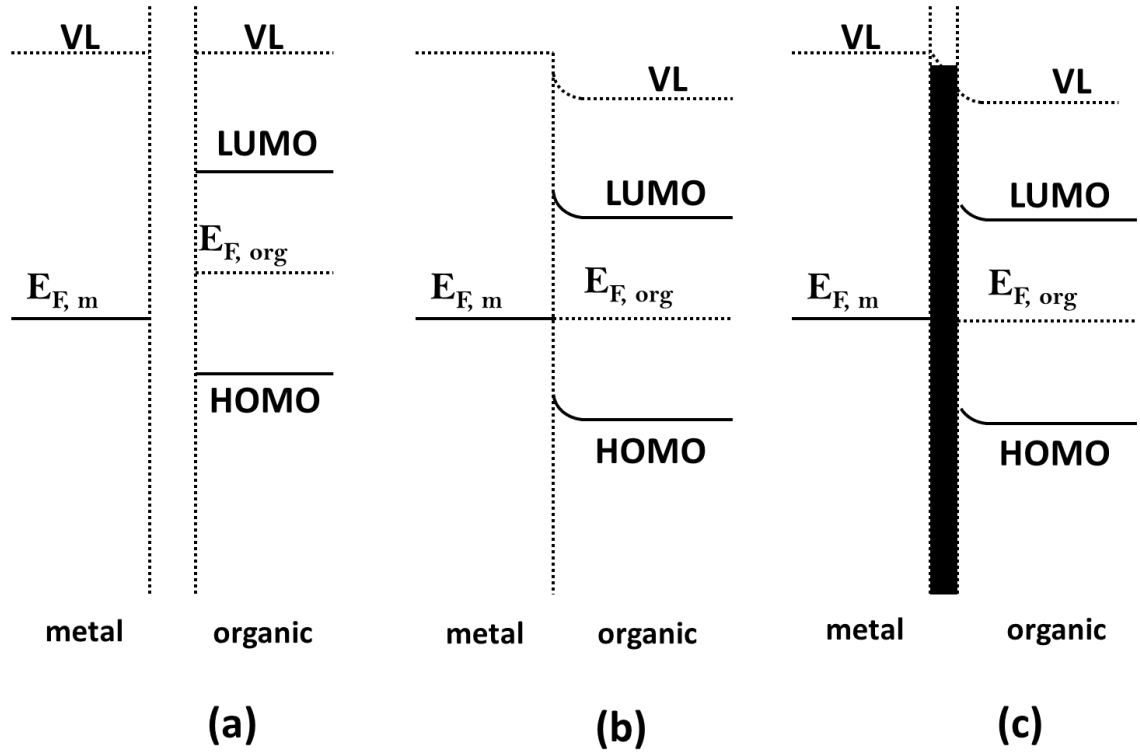

Figure 2-6 – Relative energy levels of the metal and the organic semiconductor: (a) before contact, (b) in contact, (c) in contact considering the vacuum level energy shift due to dipole formation.

Based on Figure 2.6 (a) the hole and electron injection barriers will be given by the following equations:

$$\Phi_{hole} = HOMO - \Phi_{anode} - \Phi_{d,anode} \text{ (Hole Injection Layer-HIL)} \quad (2.4)$$

$$\Phi_{electron} = \Phi_{cathode} + \Phi_{d,cathode} - LUMO \text{ (Electron Injection Layer-EIL)} \quad (2.5)$$

Here, Φ_{hole} and $\Phi_{electron}$ are the hole and electron injection barriers, respectively. Φ_{anode} and $\Phi_{cathode}$ are the work functions of the anode and the cathode materials. Finally, $\Phi_{d,anode}$ and $\Phi_{d,cathode}$ correspond to the vacuum level shifts related to the anode and the cathode, respectively.

Organic electronic devices such as OLEDs use electrodes based on different metals; therefore, the work function of the metals will be in principle different. The built-in voltage ($V_{bi}= \phi_{bi}/q$) is an important quantity that affects the charge carrier injection and is related to the work function of the metals through the equation:

$$\Phi_{bi} = \Phi_{anode} - \Phi_{cathode} \quad (2.6)$$

Generally, the anode work function is higher than that of the cathode. $\Phi_{anode} > \Phi_{cathode}$. That means that there is a built-in potential that exists in the system. The HOMO and LUMO energy levels are in the reverse bias conditions; this means that there is no flow of holes from the anode to the cathode and electrons from the cathode to the anode, respectively. To neutralize this built-in potential an external bias voltage $V=V_{bi}$ is required. $V> V_{bi}$ is required for charge injection and transport through the organic material.

2.6 Charge carrier injection in organic semiconductors

There are two main mechanisms that the carriers use to overcome the energy barriers and inject into the organic layer; namely, tunnelling through the energy barrier and thermionic injection. Figure 2-7 is a schematic representation of electron injection from a metal contact into an organic semiconductor.

Thermionic emission model: the thermionic emission is described by the Richardson-Schottky (RS) equation:

$$J_{RS} = AT^2 Exp[-\frac{\Phi_B - V_m(E)}{\kappa_B T}] \quad (2.7)$$

The parameters A and $V_m(E)$ are defined as follows: $A=4\pi mk_B^2/h^3$ that is called the effective Richardson constant and $\mathrm{V}_m(\mathrm{E}) = \sqrt{(\frac{qE}{4\pi\varepsilon\varepsilon_0})}$ is the lowering of the injection barrier which is caused by the attraction of the injected carrier and its mirror image. V_m depends on the applied electric field. Equation 2.7 suggests that the RS will be important at low fields and high temperatures.

Tunnelling model: Tunnelling through the energy barrier is possible for the charge carriers that are transferred from the metal to the organic semiconductor by the quantum mechanical tunnelling effect. This mechanism is described by the Fowler-Nordheim (FN) equation:

$$J_{FN} = \frac{Aq^2E^2}{\Phi_B C^2 k_B^2} Exp[-\frac{2C\Phi_B^{1.5}}{3qE}] \quad (2.8)$$

Here, A is the parameter defined in the thermionic emission model, $C = \frac{4\pi\sqrt{2m^*}}{h}$ and m* is the reduced charge carrier mass. J_{FN} varies with the applied field E=V/d, where d is the film thickness. The FN charge injection mechanism will be important at large fields and moderate temperatures.

The description of both mechanisms is based on the existing energy barrier for charge injection. There is also the case that no energy barrier exists for charge injection at the metal-organic semiconductor contact. This barrier-free injection it termed Ohmic. In this case the current density will be controlled by the carrier transport within the thin film.

Materials that have very low bandgap energy have HOMO and LUMO levels between the anode and cathode work functions, respectively. These materials have absorption resonances in the near infrared spectral region.

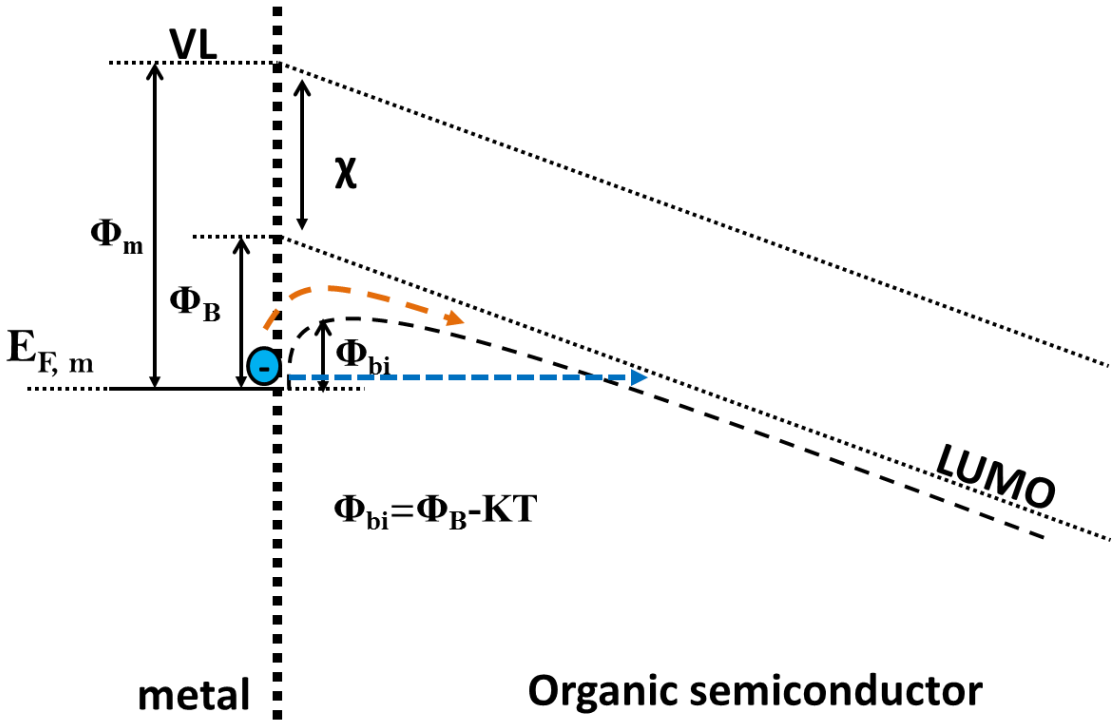

Figure 2-7 – Schematic diagram of the thermionic and tunnelling electron injection mechanisms. ϕ_m is the work function of metal, ϕ_{bi} is the applied bias, ϕ_B is the barrier for electron injection, VL the vacuum level and x the electron affinity of the organic semiconductor. The orange arrow curve relates to the thermionic emission mechanism, whereas the blue arrow line relates to the tunnelling mechanism.

2.7 Charge carrier transport in organic semiconductors

When the electrons and holes are injected into the organic semiconductor they will move across the film and in opposite directions. There are two types of motion depending on the crystallinity of the thin film. Firstly, there is the band transport model. This model describes charge motion in crystalline materials that have ordered phases. Secondly, there is the hopping transport model. This model describes the charge motion in amorphous disordered organic semiconductors [35].

The band transport mechanism describes both the organic and inorganic semiconductors. The coherent motion of charges is characterized by a wave vector k. There is a temperature-mobility relation that describes the band transport mechanism and is given by:

$$\mu \propto T^{-n},\ n>1 \tag{2.9}$$

here, μ is the charge carrier mobility in units cm^2/Vs, T is the temperature and n is a constant which is defined by experiment and also depends on the material.

In the hopping transport model k is not a good quantum number to describe the system. The high disorder that is found in amorphous thin organic films makes the charges to be localized; therefore, they can be transported through the film by hopping among molecules. These molecules have a distribution of energy states. This distribution is caused by the random orientation of the deposited molecules in the amorphous phase. Between these energy states there is a small energy barrier for hopping from one molecule to another; this renders the hopping process as thermally activated. The mobility can now be described by the following equation:

$$\mu \propto Exp[-E_{act}/k_B T] \tag{2.10}$$

where E_{act} is the activation energy for hopping, T the temperature and K_B the Boltzmann Constant.

2.8 Energy transfer mechanisms

The fabrication of organic polariton devices is not an easy task. It requires a careful consideration of the various parameters that the system depends on. Energy transfer between molecules of the same or different molecules can influence the design considerations. Therefore, it is important to describe the energy transfer processes within an OLED.

As was described in sections 2.7 and 2.8, a charge carrier can be injected from the metal electrode into an organic semiconductor passing first through an energy barrier for injection. Subsequently, the charge carriers are transported in the form of polarons across the organic material. Two energy transfer schemes are described in this section; namely Förster and Dexter energy transfer [31].

2.8.1 Förster energy transfer

In this process a high energy donor molecule and a lower energy acceptor molecule are required. The energy is transferred from the donor to the acceptor. This form of energy transfer has been described by Förster in 1948. Only neutral excitations are transferred from one molecule to the other. The Förster transfer relies on the Fermi's Golden rule for energy transfer between states which is given by the following relation:

$$K_{mn}=4\pi^2|V_{mn}|^2\delta(E_n-E_m) \quad (2.11)$$

Here, K_{mn} is the transfer rate of a donor energy state (E_m) to an acceptor energy state (E_n), V_{mn} is the interaction potential matrix element, and δ is the δ-function which is required for matching the donor and accepting states. Based on the above function the rate for the total energy transfer rate is given by the relation:

$$k_{DA}=\frac{1}{\tau_D}\left(\frac{R_0}{R}\right)^6=8.8\times10^{17}\frac{k^2}{n^4\tau_D R^6}\int g_A(E)g_D(E)dE \quad (2.12)$$

In the above equation, τ_D is the lifetime of the donor, k is a parameter that depends on the dipole orientation, n is the refractive index and R is the donor-acceptor separation distance. $g_A(E)$ and $g_D(E)$ are the normalized spectra for the absorption corresponding to the acceptor species and the emission corresponding to the donor species. R_O is termed Förster radius and is given by the relation:

$$R_0=\left(8.8\times10^{17}\frac{k^2}{n^4}\int g_A(E)g_D(E)dE\right)^{1/6} \quad (2.13)$$

The Förster energy transfer mechanism is a long range dipole-dipole interaction mechanism in the range 1-10nm.

2.8.2 Dexter energy transfer

The Dexter energy transfer can only be achieved if there is a physical orbital overlap between the donor and the acceptor molecules. This is a short-range mechanism where both charge carriers are transferred simultaneously.

An electron is transferred from the LUMO level of the donor into the LUMO level of the acceptor. At the same time, a hole is transferred from the HOMO level of the donor molecule to the HOMO level of the acceptor molecule. The respective rate for Dexter energy transfer is given by equation 2.14.

$$k_{Dex}=\hbar P^2 J exp[-\frac{2r}{L}] \quad (2.14)$$

Here, r is the donor-acceptor distance, ħ is the Planck's constant, P and L are constants, J is the donor-acceptor spectral overlap integral. Because the Dexter energy transfer decreases exponentially with distance, it is a short-range process in the range 0.5-2 nm.

2.9 OLED operation principles

Organic light-emitting diodes are devices that convert electrical current to optical power [36]. A typical conventional OLED is composed of a glass substrate, a hole transport layer (HTL), an electron transport layer (ETL), an emissive layer (EML), and both anode and cathode electrodes (electron and hole injection layers have been omitted for device simplification).

Figure 2-8 (a) represents the architectural characteristics of a multilayer OLED device. In this figure the top layer is the negatively charged cathode layer (pink layer with negative sign). Below this layer is the electron transport layer (green layer) where electrons are injected from the cathode electrode and move until they reach the light emitting layer. The ETL can be chemically engineered to have a deep HOMO energy level so as to block the transport of holes towards the cathode; therefore, it acts as hole blocking layer (HBL). The emissive layer (red layer) is where electrons and holes form excitons and emit light. The hole transport layer (blue layer) is associated with the movement of holes injected from the anode electrode. The HTL material can be chemically engineered to have a shallow LUMO energy level and act as an electron blocking layer (EBL). The positive electrode (pink layer with positive sign) is associated with hole injection and lye above the substrate were the whole device is built.

There are two types of OLEDs based on electroluminescent materials, namely the small-molecule OLEDs and the polymer LEDs. Appropriate layers are used between the anode and cathode electrodes and the emissive layer so as to lower the barriers for hole and electron injection, respectively. Conventional OLED structures use ITO (ϕ_{ITO}=4.7 eV) as the anode material, and a low work function cathode metal such as in the combination of Calcium (ϕ_{Ca}=2.9 eV) with Silver (ϕ_{Ag}=4.7 eV) deposited by thermal evaporation.

Figure 2-8 (b) depicts the operation mechanism of an OLED device. This is split into three steps:

Step 1: Under forward bias, charges are injected into the anode and cathode electrodes. Charges accumulate at the metal-organic interface where they overcome the interface barriers for injection into the organic semiconductors. Holes are injected into the HOMO level of the HTL/EBL and electrons are injected into the LUMO energy level of the ETL/HBL.

Step 2: Under the influence of the electric field, electrons are transported across the ETL and holes across the HTL were they meet the EML interface. Due to different HOMO and LUMO levels of the organic semiconductors charge carriers accumulate at the two interfaces.

Step 3: Next, electrons and holes are injected into the emissive regions. Due to the low dielectric constant and high binding energy that is found in the organic materials they experience a mutual coulomb attraction; they are forced to fuse together and create a molecular excited state termed an exciton. The exciton will recombine releasing energy in the form of electromagnetic radiation. The light emission is current driven and is called electroluminescence.

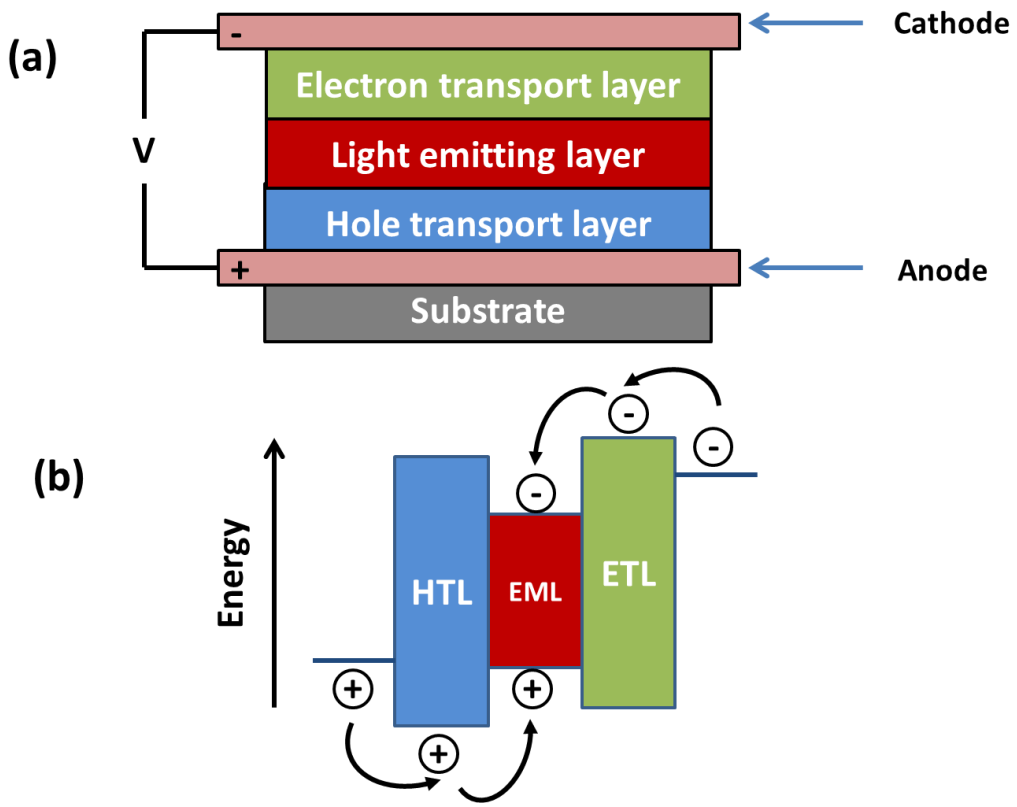

Figure 2-8 – (a) Schematic representation of a multilayer OLED architecture under forward bias. (b) Electron and hole transport across the ETL and HTL, respectively. Exciton formation occurs in the EML region.

2.10 Device architecture parameters

The engineering of an organic light-emitting diode is a multi-functional task. It is impossible to control all the parameters of the device that are responsible for the emission characteristics. The task becomes extremely complicated when there are dependencies amongst all the variables of the system. In the following, some of the parameters that can affect the performance of an organic light-emitting diode will be briefly discussed.

2.10.1 Orthogonal solvents

The deposition of alternative layers of various organic semiconductors is based on the ability of these materials to be dissolved into orthogonal solvents. The organic layers in the device have to be tolerant to swelling from the various solutions that are being processed on top of them.

If the same solvent is used then the underlying material will swell unless it is engineered to exhibit tolerance. The cross-linkable hole-transport organic semiconductor TFB that will be discussed in the following chapters is a good example of this category.

2.10.2 Active layer thickness

For organic light-emitting diodes the layers' thickness play a significant role in the performance of the device. However, it is very complicated to derive a relationship between the film thickness and the device properties.

The overall thickness of the organic layers can be split into two parts: Firstly, the thickness of the emissive layer, and secondly, the thickness of the non-emissive layers. Although an optimization process is required to maximize the ultimate performance of the device, it should be considered that as the thickness of the overall organic stack increases, this will lead to higher operating voltages.

2.11 Losses

There are losses associated with organic light-emitting diodes. The contribution of each mechanism weights differently to the overall performance of the OLED. This thesis is not focused on the quantitative analysis of such losses; however, an overview will be given in this section.

2.11.1 Losses quantified by the external efficiency of the device

The general external efficiency of an OLED device informs for the various losses that are responsible for the low conversion of electrical to optical power. The equation that describes the external quantum efficiency is given by:

$$\eta_{ext} = \gamma \cdot \eta_{S/T} \cdot q \cdot \eta_{out} \tag{2.15}$$

In this equation, γ is the charge balance factor, $\eta_{S/T}$ is the singlet/triplet ratio, q is the radiative quantum efficiency of the emitter semiconductor, and η_{out} is the out-coupling factor.

The value of the charge balance factor is defined in the range $0 \leq \gamma \leq 1$. If the number of electrons and holes are equal in the device, then γ=1. The device performance is optimum and electrons and holes are injected at the same amounts from the cathode and the anode electrodes, respectively. In the other end where γ=0, one of the carriers in the device dominates. If there is an excess of the one or the other carrier, this cannot be used to generate light and is therefore lost. This in turn reduces the external quantum efficiency of the device.

The value of $\eta_{S/T}$ is defined by quantum mechanics. Excitons in organic light-emitting diodes are defined by statistics. They are either singlets (25%) or triplet (75%) states. Triplet states have non-radiative emission and the transitions associated with them are spin-forbidden ($T_1 \rightarrow S_0$). However, the introduction of heavy metals in the emitter material can influence the spin-orbit coupling and thus give a $\eta_{S/T}$=1 for a phosphorescent emitter.

The photoluminescence (PL) quantum efficiency q of the emitter material is given by the ratio of the emitted to the absorbed photons.

Finally, η_{out} is the out-coupling factor which depends on the refractive index of the organic materials (~$1/2n^2$) in the OLED. This factor indicates how many of the photons created will escape to the outside word due to internal reflection.

2.11.2 Exciton-species annihilation

A significant loss channel accounts in the exciton-exciton annihilation process [37]. This process becomes important at high exciton densities, especially when the population of other species become important and act as a source of reduction for the number of singlet excitons. Here, the term species refers to triplet excitons, hole-polarons, electron-polarons and interaction with vibrational modes.

2.11.3 Reabsorption losses

Reabsorption losses are present in systems of organic semiconductors that have small Stokes shift and with high concentration of the emissive organic material. This is due to the overlap between the absorption and emission transitions of the same organic semiconductor and act as a loss pathway for the singlet excitons.

2.11.4 Waveguiding losses

Waveguiding losses are present to all organic light-emitting diodes. This is due to the effect of the total internal reflection that guides light to a medium far away from the active region, where light escape the device through the edge regions. These losses are related to the η_{out} outcoupling factor and are difficult to be controlled.

Chapter 3

Polariton physics: Fundamentals.

In this chapter the microcavity physics fundamentals are explained with a strong emphasis given on the physics of the strong light and matter interaction. A historic review on polaritons is also given. This covers the most significant experimental demonstrations for both inorganic and organic semiconductor microcavities.

3.1 Metallic and Distributed-Bragg-Reflector mirrors

Optical microcavities are structures that are composed of two parallel and reflective mirrors. The mirrors can be either metallic or Distributed-Bragg-Reflectors (DBR). Metallic mirrors are associated with losses when the emissive organic semiconductor is close to the metal electrode. In this way the energy of the excited organic semiconductor will be transferred and excite the surface plasmons (electromagnetic surface waves) that reside at the metal and semiconductor interface. The surface plasmons will move along this interface to end up in heat dissipation or waveguide losses [38].

Alternatively, a DBR mirror is composed of alternative layers of high and low refractive index dielectric materials (Figure 3-1). When light impinges at the interface of two dielectric materials of different index of refraction, this refractive index contrast will cause the light waves to be reflected at the interface of the two.

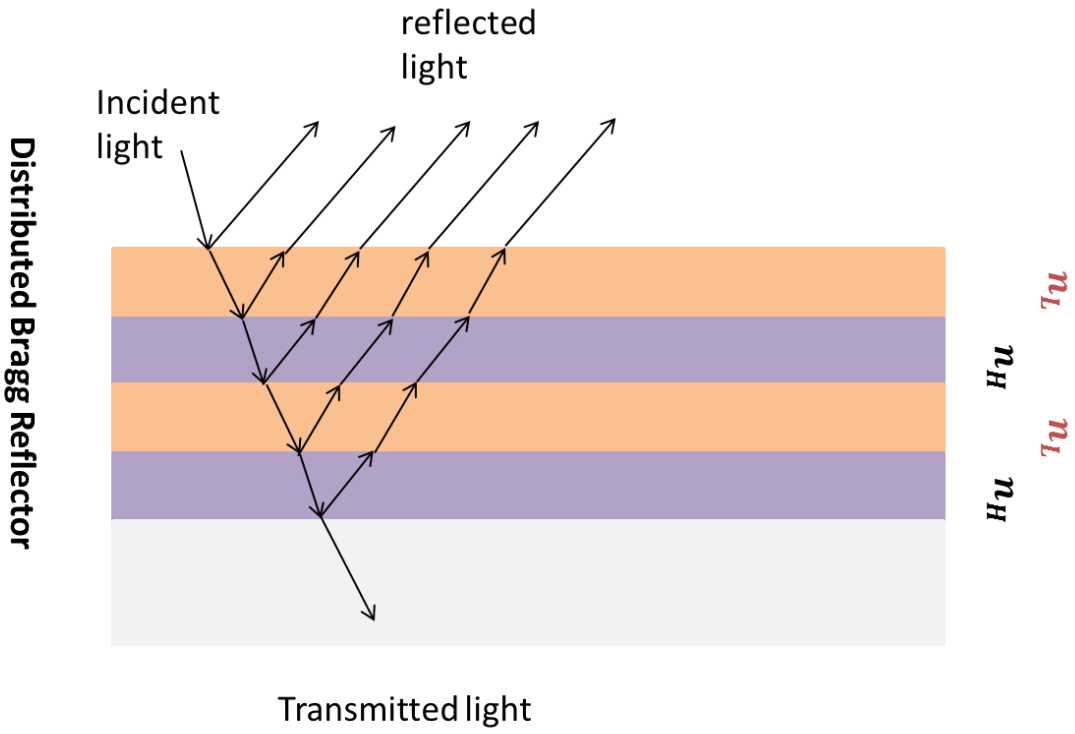

Figure 3-1 – Schematic representation of the DBR mirror that is commonly used in optical microcavities: n_H represents the high refractive index material such as Ta_2O_5 or TiO_2 and n_L represents the low refractive index material such as SiO_2.

On every interface in the layer stack part of the incident light is reflected and part of it is transmitted. The phase shift of the reflected light is 180^0 (π) when light propagates from the low to the high index material. This in turn causes a phase difference of all the reflected light beams to be zero or multiple to 360^0 which leads to constructive interference.

Constructive interference of all the reflected light waves results in high reflectivity. The strongest interference occurs when the thickness of the dielectric layers is chosen to be a

quarter of the light wavelength [39]. Therefore, the thickness of the low n_L and high n_H refractive index materials in a bragg stack is chosen according to the relations:

$$t_L = \frac{\lambda}{4n_L} \tag{3.1}$$

$$t_H = \frac{\lambda}{4n_H} \tag{3.2}$$

where λ is the wavelength of interest.

Assuming that the absorbance of the dielectric materials is negligible, the reflectance (intensity) of the DBR mirror comprised by 2m layers is given by the equation [40]:

$$R = \left(\frac{n_0(n_H)^{2m} - n_S(n_L)^{2m}}{n_0(n_H)^{2m} + n_S(n_L)^{2m}}\right)^2 \tag{3.3}$$

Here, n_0 and n_s are the respective refractive indices of the surrounding medium (n_0=1, in air). Alternatively, the transmittance is given by the relation (neglecting absorption A):

$$T = 1 - R \tag{3.4}$$

The stopband created from the high reflectivity of the DBR has a spectral width Δλ that is given by the relation [40]:

$$\Delta\lambda \approx \frac{4}{\pi}\lambda_B arcsin\left(\frac{n_H - n_L}{n_H + n_L}\right) \tag{3.5}$$

Where, λ_B is the central wavelength of the DBR. Transfer matrix calculations are usually used to calculate reflectivity as a function of the wavelength of light [39]. In this thesis we are only concerned for the TE mode of the EM field and therefore the TM mode will be neglected. Figure 3-2 (a) depicts the reflectivity of a DBR structure calculated for n=5 and n=10 bilayers of high (n_H=1.9) and low (n_L=1.5) refractive index materials, at θ=0^0 and central wavelength λ_B=550 nm. It can be seen from this plot that as the number of bilayers increases the reflectivity becomes higher and the stopband narrower. Figure 3-2 (b) shows the reflectivity of a DBR structure consisting of n=8 bilayers of high and low refractive index materials by varying the difference Δn= n_H-n_L of their indices, with n_L=1.5=const. The effect of increasing the refractive index difference is that the stopband becomes broader. It is also observed in the same graph a shift towards longer wavelengths. This can be understood from equations (3.1) and (3.2). A change in the refractive index will correspond to a change of the wavelength as the thickness of the layers during calculations was not changed. Therefore, by increasing the refractive index difference the DBR redshifts to longer wavelengths as seen from the graph.

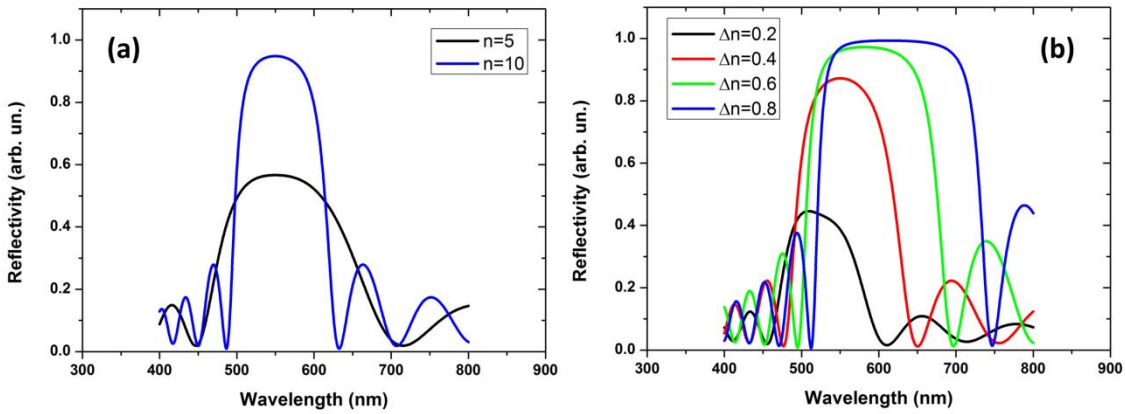

Figure 3-2 – (a) DBR reflectivity of n=5 bilayers (black line) and n=10 bilayers (blue line) of high (n_H=1.9) and low (n_L=1.9) refractive index materials. (b) Reflectivity of a DBR structure consisting of n=8 bilayers of low and high refractive index materials by increasing the refractive index difference of the two.

There is an associated penetration depth that light infiltrates into these structures which depends on the refractive index contrast between the two materials. The respective equation that describes the mirror penetration depth is given by [40]:

$$L_{DBR} = \frac{\lambda_B}{2n_{cav}} \frac{n_L n_H}{n_H - n_L} \tag{3.6}$$

where n_{cav} is the average cavity refractive index.

3.2 Optical microcavities

When two mirrors are brought in close proximity and are separated by distance of the order of the wavelength of light, a microcavity system is formed. The microcavity structure is essentially a Fabry-Perot resonator. Electromagnetic waves can be trapped inside the microcavity in the form of standing waves. The standing waves are associated with the dimensions of the structure and form a series of optical modes. The wavelength and structure of such are dependent on the intracavity thickness. Usually a single mode is chosen in the cavity. Equation 3.7 gives the wavelength of the allowed modes within the cavity:

$$\lambda_C = \frac{2nL_C}{m} cos\theta_{int} \tag{3.7}$$

Here n is the refractive index of the intracavity layer, L_C is the mirror separation, m is an integer number and θ_{int} is the angle formed between the propagation wavevector (k) with the normal. Figure 3-3 (a) shows the three lowest energy modes of the cavity along with the splitting of the wavenumber into vertical and horizontal components. The wavelength relation of equation 3.7 can be converted into a wavenumber relation:

$$k = \frac{2\pi}{\lambda_C} = \frac{\pi m}{nL_C} \frac{1}{cos\theta_{int}} \tag{3.8}$$

Only the vertical to the mirror surface wavenumber component is important; therefore the equation that describes $k_\perp$ is given by:

$$k_\perp = \frac{\pi m}{n L_C} \tag{3.9}$$

In terms of energy, equations 3.8 and 3.9 become:

$$E_\gamma = \frac{hck}{2\pi} = \frac{hcm}{2nL_C}\frac{1}{\cos\theta_{int}} = E_0(1-\sin^2\theta_{int})^{-1/2} \tag{3.10}$$

$$E_\perp = \frac{hcm}{2nL_C} = E_0 \tag{3.11}$$

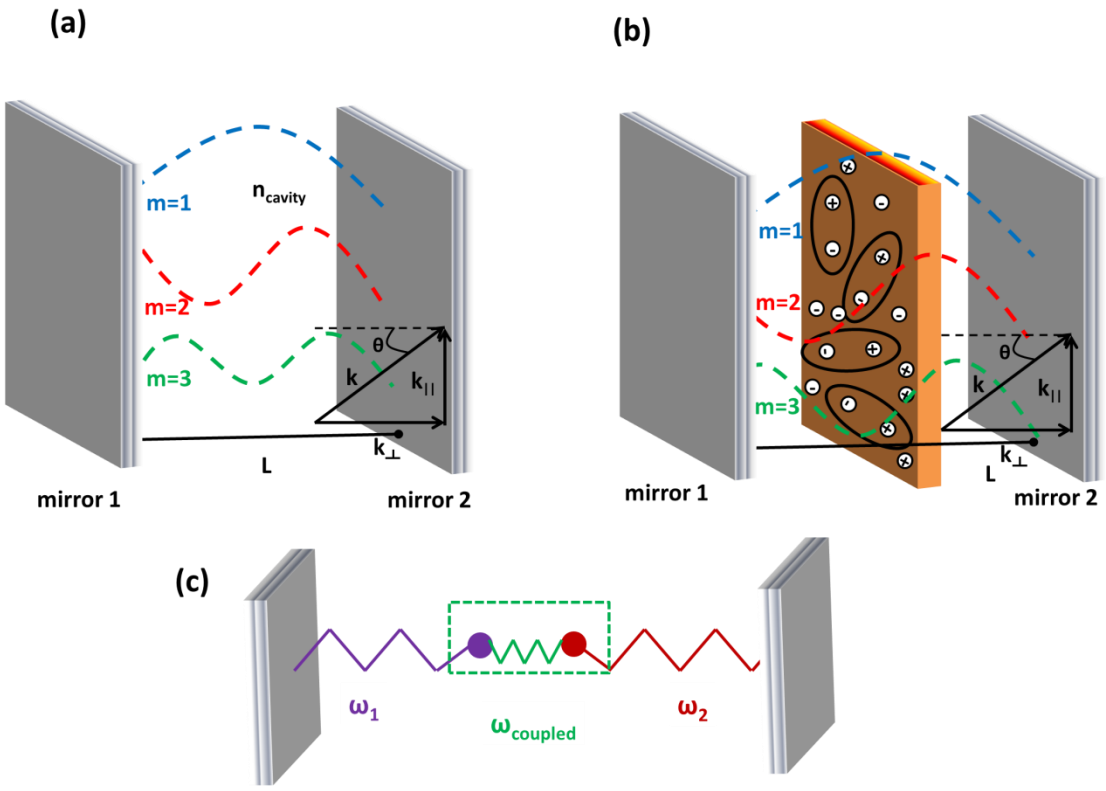

Figure 3-3 – (a) Microcavity structure that can support a number of modes depending on the intracavity mirror separation. (b) Organic semiconductor embedded in a microcavity configuration. The organic semiconductors in microcavity OLEDs can support Frenkel excitons, free electrons and free holes simultaneously as a result of charge injection. (c) Mechanical analogue that considers the energy exchange between two oscillators coupled by a third spring.

Here, h is the Planck's constant and c the speed of light in vacuum. To observe the photon energy E_γ in the out-of-cavity region a relation between the internal and external viewing angles has to be established. The angles of incidence (θ_1) and refraction (θ_2) for light passing through the boundary between two materials with refractive indexes n_1 and n_2 respectively are related through Snell's law:

$$n_1 sin\theta_1 = n_2 sin\theta_2 \quad (3.12)$$

Assuming that: a) medium 1 refers to the outside-of-the cavity region (air) with $\theta_1=\theta_{ext}$ and $n_1=1$, b) medium 2 refers to the intracavity region with $\theta_2=\theta_{int}$ and $n_2=n>1$, then the external viewing angle is related to the internal viewing angle through the equation:

$$\theta_{int} = arcsin\left(\frac{sin\theta_{ext}}{n}\right) \quad (3.13)$$

Using equation 3.13, the energy of the cavity mode can be observed as a function of angle and is termed as cavity mode dispersion:

$$\mathrm{E}_\gamma = \mathrm{E}_0\left(1 - \frac{\sin^2\theta_{ext}}{n^2}\right)^{-1/2} \quad (3.14)$$

Figure 3-3 (b) depicts an organic semiconductor that is placed inside a microcavity OLED. The organic thin film can support Frenkel excitons as well as free electrons and free holes that are present in the case of charge injection in OLEDs. Depending on the strength of the interaction between the photon component and the exciton component, two regimes are established. These are termed weak and strong coupling regimes.

The notion of coupled oscillators is frequently used to describe the interaction between a Frenkel excitation in an organic semiconductor and a confined photon mode. The mechanical analogue that describes the mechanism is shown in Figure 3-3 (c). The cavity photon and the exciton are represented by springs that are attached to two bodies of masses of m_1 and m_2, with the two springs resonating at slightly different frequencies, ω_1 and ω_2, respectively. The two oscillators are connected together by a third spring ($\omega_{coupled}$). The third spring can mediate energy transfer between the two oscillating bodies. Depending on the damping rates of the two oscillators and the energy transfer rate of the third coupling spring, two regimes are established. The strong coupling regime is characteristic of the fast energy transfer compared to dephasing processes (heat and photon dissipation). The second case is characteristic of the weak coupling regime where the dephasing processes dominate over the energy transfer process.

3.3 The weak and the strong coupling regimes

The mechanical analogue that was discussed in the last section briefly introduced the two regimes of operation. However, whether the strong QED regime will be reached or not strongly depends on the parameters of the system and will be qualitatively described in the next section. Next, the weak and the strong coupling regime are described and distinguished from each other based on the exciton and photon dephasing rates. A description of the difference between the two regimes based on the coupled oscillator model that includes losses is given in pages 36-37.

3.3.1 Weak Coupling regime:

When an organic semiconductor is placed at the antinode of an optical microcavity the exciton and the photon will interact. The strength of this interaction depends on three fundamental rates by which the nature of the system will be determined. The first is the exciton dephasing rate γ_{ex} (is the total broadening of the exciton resonance), the second is the photon damping rate γ_{ph} (is the total broadening of the exciton resonance) and the third is the rate Ω by which light and matter exchange energy. If the system loses energy more rapidly than it exchanges energy between the two components then the condition Ω<<γ_{ex}, γ_{ph}, applies. This is called the week coupling regime.

The Fermi Golden rule essentially states that the probability for transition between the initial and the final state in a weakly coupled system is proportional to the final states of that system. A microcavity can sustain only a number of modes. Therefore, the density of states (DOS) is altered in comparison to the free space case. Consequently, the DOS is increased when the dipole energy is resonant with the cavity field and suppressed otherwise. Other weak cavity effects include the modification of the angular emission properties of the organic semiconductor and the modification of the spontaneous emission rates of Frenkel excitons. The latter can be described by the Purcell factor P and is given by equation 3.15:

$$P = \frac{3}{4\pi^2}\left(\frac{\lambda}{n}\right)^3 \frac{Q}{V} \tag{3.15}$$

Here, λ is the selected wavelength of light in the cavity, n is the refractive index of the intracavity material; V is the volume of the cavity and Q the cavity quality factor. The Purcell factor P essentially states that the spontaneous emission rate of a transition in a cavity can be enhanced in respect to free space. The maximum value it can take up is adjusted by the Purcell factor. Other non-resonant transitions will be supressed.

The cavity quality factor is a measure of the photon confinement within the cavity and is given by equation 3.16:

$$Q = \frac{E_o}{\Delta E} \tag{3.16}$$

Here, E_0 is the energy that corresponds to the selected wavelength of light. ΔE refers to the FWHM of the energy mode. Microcavities with high Q-factors are associated with longer photon lifetimes. This is of great importance since it defines the polariton lifetime.

3.3.2 Strong Coupling regime:

If the exciton component of an organic semiconductor in a microcavity exchanges energy with the photon component of the cavity field more rapidly than all the other dephasing mechanisms of the system then the condition Ω>> γ_{ex}, γ_{ph} will hold. The system will be described as operating in the strong coupling regime.

A pictorial representation of the mechanism that dominates in the strong coupling regime is that of a periodic energy exchange between the photon and the exciton components in the microcavity. The organic material essentially absorbs, emits, reabsorbs, and reemits etc. many times before the energy is lost. This scenario is qualitatively described by considering the Maxwell's equations.

An incident electromagnetic wave will induce polarization in the form of dipoles for an organic semiconductor in a microcavity structure. The polarization will not be uniform across the thickness of the cavity but it will vary. The varying polarization will create a magnetic field according to the Ampere's law:

$$\nabla \times \bar{H} = \bar{J} + \frac{\partial \bar{D}}{\partial t} \tag{3.17}$$

Here $\bar{H}$ is the magnetic field strength, $\bar{D}$ is the electric displacement, $\bar{J}$ is the current density and t signifies derivation with respect to time. The created magnetic field will be varying with time. Consequently, this will produce an electric field via the Maxwell's equation:

$$\nabla \times \bar{E} = -\frac{\partial \bar{B}}{\partial t} \tag{3.18}$$

The organic medium will emit the electromagnetic radiation back to the cavity that will produce polarization in the microcavity region and this cycle will be repeated many times before the energy is lost. Before this occurs the energy will be stored in the resonator both as exciton and as a photon at the same time.

The resonant exchange of energy between the Frenkel excitons and the cavity photons modify the energy levels of the system as seen characteristically from Figure 3-4. Dispersion curves are commonly used to plot the reflectivity, photoluminescence or electroluminescence energy as a function of the angle or the wavevector. The exciton-photon energy separation (E_γ-E_{exc}) is termed as detuning (δ) at $\theta=0^0$ and defines three possible outcomes of a strongly-coupled system. Here the focus will be on the interaction of a photon mode with an exciton resonance. The exact mathematic definition will be given in the next section.

The system can be either positively detuned, negatively detuned or it can exhibit zero detuning. Figure 3-4 (a) depicts the dispersion curve for a positively detuned organic microcavity. In this case the angle-dependent photon mode (red dashed parabola) is energetically located above the dispersionless exciton energy (red dashed line). The relation E_γ-E_{exc} =δ>0 applies. The strong coupling condition modifies the energy levels as seen from the blue curves in the graph. The higher energy blue curve is called upper polariton branch and the lower energy blue curve is called lower polariton branch.

Similarly, for δ=0 detuning, the new eigenstates of the system are the newly formed polariton states as seen characteristically from the blue curves of Figure 3-4 (b). A negatively-detuned microcavity is formed when the exciton energy is located energetically at higher energy than the energy of the photon mode at $\theta=0^0$. Here, the E_γ-E_{exc} =δ<0 relation applies. The angle-dependent photon mode crosses the exciton energy at an angle θ. The two polariton modes

will appear to anti-cross at the same angle. This is seen in Figure 3-4 (c). Last, figure 3-4 (d) shows the dispersion curve that corresponds to the weak coupling regime.

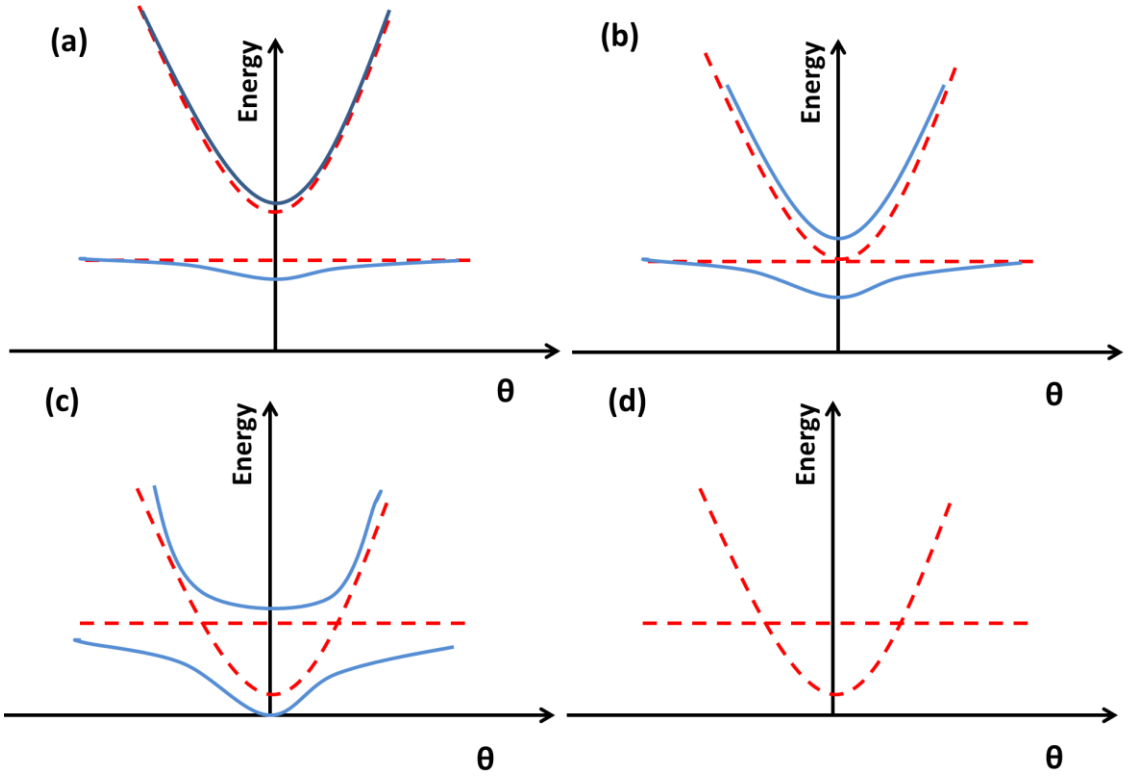

Figure 3-4 – Dispersion curve for a: (a) Positively detuned microcavity (δ>0), (b) zero-detuned microcavity (δ=0) and (c) negatively-detuned microcavity (δ<0), in the strong coupling regime. (d) A dispersion curve that corresponds to the weak-coupling regime. Red curves correspond to the exciton (dispersionless red line) and the photon (red curve parabola) modes. Blue curves correspond to the newly-formed polariton modes.

Classical treatment of a two-level model of coupled oscillators

The coupling of two classic oscillators (exciton and photon) can be given by equation 3.19 which describes a 2x2 Hamiltonian [41]. V, E_{ph}, and E_{ex} are the interaction matrix element, the photon energy and the exciton energy, respectively. The parameters $-i\gamma_{ph}$ and $-i\gamma_{ex}$ are included to describe photon damping and exciton dephasing losses, respectively.

$$\begin{bmatrix} E_{ph} - i\gamma_{ph} & V \\ V & E_{ex} - i\gamma_{ex} \end{bmatrix} \tag{3.19}$$

The time-independent Schrodinger can be written as [41]:

$$\begin{bmatrix} E_{ph} - i\gamma_{ph} & V \\ V & E_{ex} - i\gamma_{ex} \end{bmatrix} \begin{bmatrix} \alpha \\ \beta \end{bmatrix} = E \begin{bmatrix} \alpha \\ \beta \end{bmatrix} \tag{3.20}$$

where $\begin{bmatrix} \alpha \\ \beta \end{bmatrix}$ represents the eigenvector of the system. Equation (3.20) is referred to as the coupled harmonic oscillator model including dephasing. The characteristic polynomial of equation (3.20) can be solved to yield the eigenvalues of the system. More specifically:

$$det\begin{vmatrix} E_{ph}-i\gamma_{ph}-E & V \\ V & E_{ex}-i\gamma_{ex}-E \end{vmatrix}=0 \Rightarrow E_{pol}=$$
$$\frac{E_{ph}+E_{ex}-i(\gamma_{ph}+\gamma_{ex})}{2}\pm\frac{1}{2}\sqrt{(E_{ph}-E_{ex}-i(\gamma_{ph}-\gamma_{ex}))^2+4V^2} \quad (3.21)$$

As shown in equation (3.21) there are two solutions corresponding to the polariton energy. Both solutions depend on the photon energy; therefore they should exhibit strong angular dependence. The solution baring the positive "+" sign creates a continuum of energy levels and is termed as upper polariton branch (UPB). On the other hand, the solution that bares the negative "-" sign creates a continuum of negative energy levels and is termed as lower polariton branch (LPB). The LPB states are of importance since they are connected to a cut-off lower energy frequency of the system where organic polariton condensates are expected to be spontaneously formed with proper cavity engineering. The exciton and photon linewidths γ_{ex}, γ_{ph} along with the exciton and photon character of the polariton define the upper (γ_u) and lower (γ_l) polariton linewidths. Moreover, at the point of the exciton-photon degeneracy ($E_{ph}=E_{ex}$) and at a resonant angle of $0^0 \leq \theta_{Res} < 90^0$, the energy of the two branches is equal to

$$E=\frac{2E_{ex}-i(\gamma_{ph}+\gamma_{ex})}{2}\pm\frac{1}{2}\sqrt{4V^2-(\gamma_{ph}-\gamma_{ex})^2} \quad (3.22)$$

The energetic separation of the two branches is termed Rabi splitting; it includes dephasing and is given by equation (3.23).

$$\hbar\Omega_{12}=\hbar\sqrt{4V^2-(\gamma_{ph}-\gamma_{ex})^2} \quad (3.23)$$

Based on equations (3.23) and (3.24) there are two regimes of operation that depend on the $\sqrt{4V^2-(\gamma_{ph}-\gamma_{ex})^2}$ factor. In the first case the square root value of that factor is imaginary when $2V<|\gamma_{ph}-\gamma_{ex}|$. This is the weak coupling regime where dephasing dominates the system. In the second case where $2V>|\gamma_{ph}-\gamma_{ex}|$ the value is real and is associated with the strong coupling regime. In this scenario the exciton-photon interaction is stronger than the losses.

The eigenvector $\begin{bmatrix}\alpha\\ \beta\end{bmatrix}$ contains the relative mixing coefficients α and β of photon and exciton of the polariton quasi-particle in total, the squares of which describe the relative weight of each component and exhibit strong angular dependence. Since the total contribution of the exciton and photon character of polaritons should be 1, expressed as $\alpha^2+\beta^2=1$ (3.24), the solution of the system lead to the following set of equations for the coefficients (Appendix B):

$$a^2=\frac{V^2}{V^2+(E-E_{Ph}+i\gamma_{ph})^2} \quad (3.25)$$

$$\beta^2=\frac{(E-E_{Ph}+i\gamma_{ph})^2}{V^2+(E-E_{Ph}+i\gamma_{ph})^2} \quad (3.26)$$

Classical treatment of a three-level model of coupled oscillators

A model that contains more than one exciton resonances, as is in the case of mixing organic dyes sustaining two non-degenerate exciton resonances [42] or in the case that an organic semiconductor that contain both electronic (0,0) as well as a (0,1) vibrational transitions coupled to the cavity mode [24], the eigenvalue problem can be written in the following form:

$$\begin{bmatrix} E_{ph}-i\gamma_{ph} & V_1 & V_2 \\ V_1 & E_{ex1}-i\gamma_{ex1} & 0 \\ V_2 & 0 & E_{ex2}-i\gamma_{ex2} \end{bmatrix} \begin{bmatrix} \alpha \\ \beta \\ \gamma \end{bmatrix} = E \begin{bmatrix} \alpha \\ \beta \\ \gamma \end{bmatrix} \quad (3.27)$$

where γ_{ph}, $\gamma_{ex1}$and γ_{ex2} correspond to photon, (0,0) and (0,1) dephasings, respectively. The eigenvalues of the system describe the appearance of three polariton branches that can be obtained once the characteristic polynomial of equation (3.27) is solved:

$$det \begin{vmatrix} E_{ph}-i\gamma_{ph}-E & V_1 & V_2 \\ V_1 & E_{ex1}-i\gamma_{ex1}-E & 0 \\ V_2 & 0 & E_{ex2}-i\gamma_{ex2}-E \end{vmatrix} = 0 \Rightarrow E_{pol} \quad (3.28)$$

Again the eigenvector $\begin{bmatrix} \alpha \\ \beta \\ \gamma \end{bmatrix}$ contains the relative mixing coefficients, for the photon α and the two exciton resonances β and γ. The equation $\alpha^2+\beta^2+\gamma^2=1$ (3.29) is now required in the set of equations that describe the relative fraction of each polariton branch. The solution of the system lead to the following set of equations for the coefficients (Appendix B):

$$\alpha^2 = \frac{(E(\theta)-E_{ex1}+i\gamma_{ex1})^2(E(\theta)-E_{ex2}+i\gamma_{ex2})^2}{(E(\theta)-E_{ex1}+i\gamma_{ex1})^2(E(\theta)-E_{ex2}+i\gamma_{ex2})^2+V_1{}^2(E(\theta)-E_{ex2}+i\gamma_{ex2})^2+V_2{}^2(E(\theta)-E_{ex1}+i\gamma_{ex1})^2} \quad (3.30)$$

$$\beta^2 = \frac{V_1{}^2(E-E_{ex2}+i\gamma_{ex2})^2}{(E(\theta)-E_{ex1}+i\gamma_{ex1})^2(E(\theta)-E_{ex2}+i\gamma_{ex2})^2+V_1{}^2(E(\theta)-E_{ex2}+i\gamma_{ex2})^2+V_2{}^2(E(\theta)-E_{ex1}+i\gamma_{ex1})^2} \quad (3.31)$$

$$\gamma^2 = \frac{V_2{}^2(E-E_{ex1}+i\gamma_{ex1})^2}{(E(\theta)-E_{ex1}+i\gamma_{ex1})^2(E(\theta)-E_{ex2}+i\gamma_{ex2})^2+V_1{}^2(E(\theta)-E_{ex2}+i\gamma_{ex2})^2+V_2{}^2(E(\theta)-E_{ex1}+i\gamma_{ex1})^2} \quad (3.32)$$

Classical treatment of a multi-level model of coupled oscillators

Extension of the model to a simultaneous multi-exciton, non-degenerate strong coupling to a single cavity mode can be written in the form:

$$\begin{bmatrix} E_{ph}-i\gamma_{ph} & V_1 & \cdots & V_n \\ V_1 & E_{ex1}-i\gamma_{ex1} & 0 & 0 \\ \vdots & 0 & \ddots & \vdots \\ V_n & 0 & \cdots & E_{exn}-i\gamma_{exn} \end{bmatrix} \begin{bmatrix} \alpha_{ph} \\ \alpha_1 \\ \vdots \\ \alpha_n \end{bmatrix} = E \begin{bmatrix} \alpha_{ph} \\ \alpha_1 \\ \vdots \\ \alpha_n \end{bmatrix} \quad (3.33)$$

$$det \begin{vmatrix} E_{ph}-i\gamma_{ph}-E & V_1 & \cdots & V_n \\ V_1 & E_{ex1}-i\gamma_{ex1}-E & 0 & 0 \\ \vdots & 0 & \ddots & \vdots \\ V_n & 0 & \cdots & E_{exn}-i\gamma_{exn}-E \end{vmatrix} = 0 \Rightarrow E_{pol} \quad (3.34)$$

The eigenvector $\begin{bmatrix} \alpha_{ph} \\ \alpha_1 \\ \vdots \\ \alpha_n \end{bmatrix}$ signifies the simultaneous strong-coupling of one photon mode (α_{ph}) to a series of non-degenerate exciton resonances ($\alpha_1 \cdots \alpha_n$). To solve these equations that contain multiple excitons coupled to a single cavity mode numerical simulation methods are required.

3.4 Theoretical description of polaritons in organic microcavities

In this section the main mechanisms for populating polariton branches will be based on Refs. [43-45] in which a set of rate equations is used to describe the excitation dynamics in microcavities containing J-aggregates. The same model is used to simulate microcavity rates in Chapter 5. Basically, the model treats J-aggregates as 1-D excitonic system of N_d dye monomers. The monomers are characterised by energetic disorder and are coupled to each other via dipole-dipole interactions. This coupling forces excitons to be delocalised forming J-aggregates.

The rate equations developed describe the relaxation dynamics based on the absorption and emission of molecular vibrations. The molecular vibrations are classified into two categories. The first refers to a continuum spectrum of low energy vibrations with energies E<30 meV and the second refers to a discrete spectrum of molecular vibrations with high energies. In the model developed the molecular vibrations of the J-aggregates of the TDBC molecule were used which were identified via Raman spectroscopy [46]. The energies included had a value of E_v=40, 75, 120, 150 and 187 meV. The Fermi Golden rule was used to calculate scattering rates between initial and final states. However, the model does not distinguish between excitons formed by optical or electrical pumping. According to the solution of the rate equations polariton branches are populated based on the following two-step processes (figure 3-5):

Firstly, high energy excitons relax to the lowest J-aggregate state via emission of molecular phonons. This creates the so-called exciton reservoir, which is a quasi-thermalized population of excitons in the J-band density of states (time scale ~1ps).

Secondly, the LPB is populated by polaritons either by interactions with low energy molecular vibrations or by interactions with high energy molecular vibrations. In the first case polaritons are trapped close to the exciton reservoir since multiple scattering events are not possible due to the short polariton lifetime (10s-100s fs). In the second case the energy of the molecular vibrations is high enough to scatter polaritons down to the bottom of the lower polariton branch. In this way direct population of the minimum state of the system might be possible through proper cavity engineering, when the energetic separation of the exciton and the minimum of the LPB correspond to a specific high energy molecular vibration.

Upper branch polaritons cannot be populated since room temperature is not sufficient to activate the high energy Raman modes for exciton promotion into the UPB, therefore only the low energy vibration modes can contribute to the population of the UPB. The time scale of the second step is of the order of picoseconds.

Polariton branches can also be populated via the optical pumping mechanism. In this mechanism a weakly-coupled organic semiconductor has an emission spectrum that overlaps with the polariton branches of the strongly-coupled material. Since polaritons are part-excitons and part-photon quasi-particles, the light that is emitted from the weakly-coupled organic semiconductor will populate the photon part of the polariton and thus polaritons will be directly created. It was shown by Lodden et al [47] that populating polariton branches with this mechanism might be advantageous in circumventing the bottleneck effect in strongly-coupled systems in order to generate a high population at the bottom of the LPB.

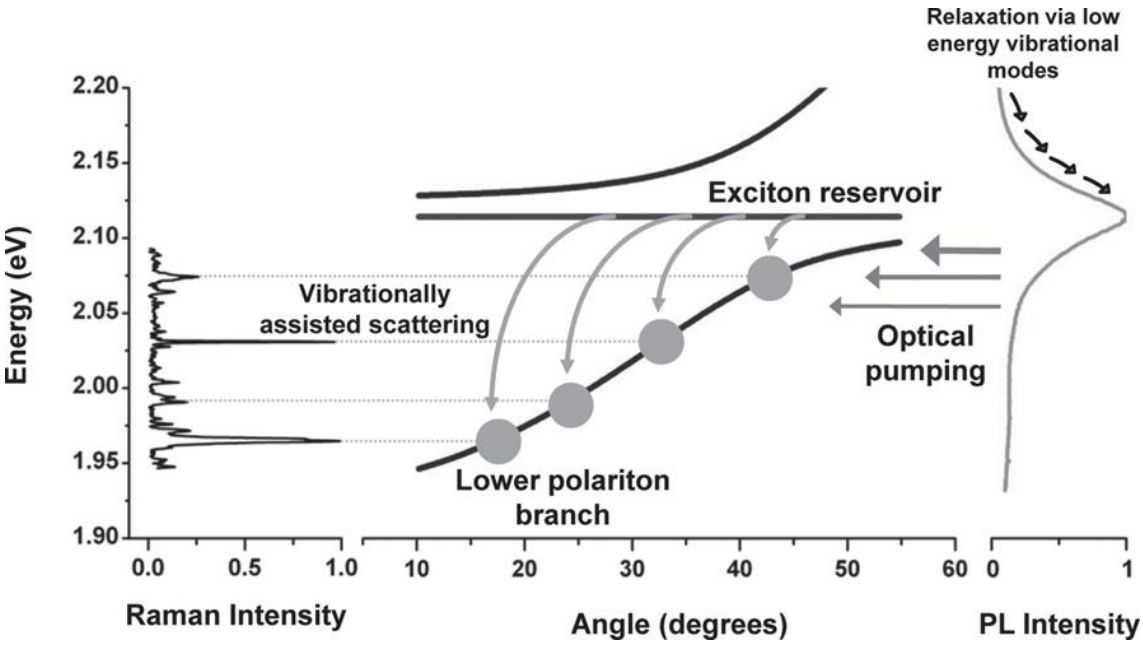

Figure 3-5 – Mechanisms responsible for populating the polariton branches, namely vibrationally assisted scattering and optical pumping. Left hand side: Vibrational spectrum taken for the J-aggregates of TDBC via Raman spectroscopy. Middle figure depicts the upper polariton branch, the exciton reservoir and the lower polariton branch. Arrows indicate scattering and population of the lower polariton branch. Right hand side: depicts the PL spectrum of the J-aggregates where is used to radiatively pump the lower polariton states. From Refs [46].

The mechanisms explained in this section are seen in Figure 3-5. In the left hand side of this figure the vibrational levels of the J-aggregate are shown taken via Raman spectroscopy. The

energy position of the strong discrete peaks of the spectrum coincides with the exciton-lower polariton branch energetic separation in the dispersion curve depicted in the middle of the figure. The grey arrows indicate that excitons are scattered down the lower polariton branch at this energy equivalence. In the right hand side of the figure the PL spectrum of the J-aggregates is shown. As explained the radiative pumping of a small number of uncoupled excitons is responsible for populating the LPB at high angles.

3.5 Historic review

In this brief historic review the most important demonstrations of inorganic and organic-based microcavity systems are given. Strong-coupling in inorganic semiconductor microcavities was demonstrated in 1992 [48] and since then it has dominated the field. An enormous amount of scientific reports were submitted to describe polariton phenomena related to inorganic semiconductor physics.

Alternatively, the use of organic materials in microcavity systems reported for the first time in 1998 [49]. Since then various organic semiconductors have been used in optical microcavities. Major advances in equipment manufacturing which is a major demand for making high quality structures has been progressing fast, allowing for the rapid growth of this field of research.

3.5.1 Inorganic microcavities

Inorganic semiconductors are in the heart of our technology. The invention of the integrated circuit based on transistors, triggered the research of inorganic semiconductors for optoelectronic applications. Since then, applications such as the VCSEL laser [50] that combines both aspects of the optical and electrical properties of these materials, was successfully demonstrated leading to a variety of new products that are today commercially available.

The term polariton was introduced in 1958 by Hopfield to describe the resonant interaction between photons and excitons in bulk crystals [51]. The first experimental demonstration of bulk polaritons was achieved in a ZnO crystal in 1965 by Hopfield and Thomas [52].

However, bulk polaritons can travel through the crystal in any direction with high velocities and therefore only a small fraction of them can reach the surface and be observed due to dissipation. In quantum wells control of the exciton decay in the growth direction can be achieved. When a quantum well is embedded in a microcavity then the excitons will couple with photons that have the same wavevector. This allows polaritons to be observed from the leakage of their photon component through the cavity mirrors.

A new era in the field of solid state physics started after the successful realization of the first strongly-coupled inorganic microcavity in 1992 by Weisbuch et al. [48]. In this report a planar GaAs-based semiconductor microcavity was fabricated and placed in between two highly reflective dielectric mirrors made of GaAlAs and AlAs. Performing reflectivity measurements in these structures the authors realised that there was a splitting in the reflectivity spectrum, as a result of the formation of new energy states, as seen from figure 3.6.

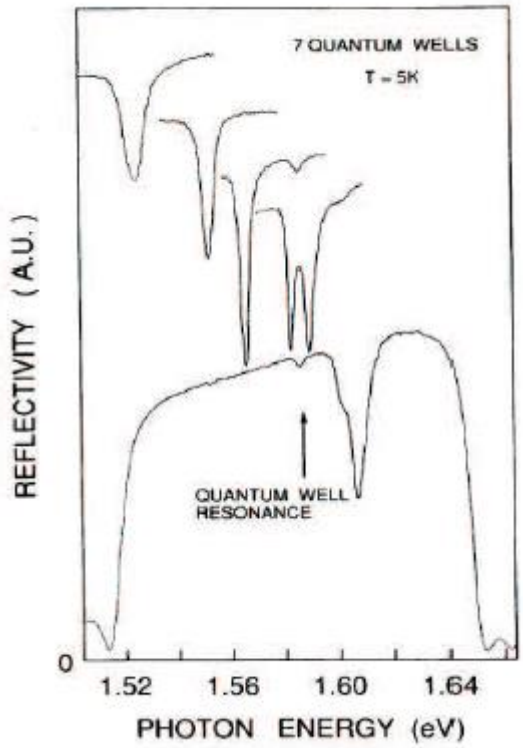

Figure 3-6 - Reflectivity spectra based on a planar semiconductor microcavity, depicting the energy level splitting at different photo-exciton detunings, from Ref.[48].

In 1996 Immamoglu and co-workers put forward a remarkable idea [28]. It was proposed that low-threshold, laser-like emission could be realised utilising these polariton quasi-particles by the direct condensation to the lowest energy state of the system. This effect which is termed Bose-Einstein Condensation is based on the property of any bosonic system, and under certain conditions, to have a collective behaviour and, therefore, to be described by a macroscopic quantum wavefunction. Such an experimental evidence was awarded with a Nobel prize in physics to Wolfgang Ketterle, Carl Wieman and Eric Cornell in 2001 for demonstrating BEC in dilute vapour atoms at ultra-low temperatures [53, 54].

The work of Houdre et al. [55] was first to study the photoluminescence properties of quantum well excitons in inorganic microcavities in the strong-coupling regime. Figure 3-7 shows the photoluminescence emission spectrum as a function of energy for a series of angles. This work was significant because it highlights for the first time the possibility that light can be emitted from populated polariton states.

Subsequent work investigated the mechanisms that are responsible for populating polariton states [56]. Then the focus was shifted in the understanding of the bottlenecks [57, 58] that prohibit such systems for achieving nonlinear light emission.

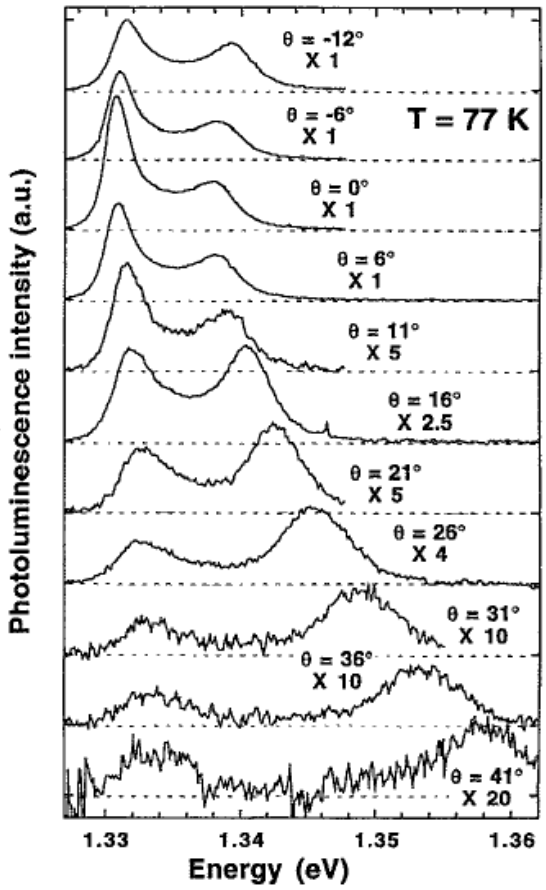

Figure 3-7 – Photoluminescence emission spectra of an InGaAs–based semiconductor microcavity, as a function of energy, for a series of angles in the strong-coupling regime, from ref. [55].

Le Si Dang et al. [59] was the first to observe coherent nonlinear emission from lower branch polariton states following non-resonant excitation in 1998. Two major breakthroughs in the field followed, namely demonstration of Bose-Einstein condensation, room temperature lasing in QW inorganic microcavities [60, 61], and nonlinear emission under electrical excitation [23, 62].

Under non-resonant excitation, strongly-coupled inorganic microcavities containing CdTe quantum wells can undergo a macroscopic phase transition (BEC) at very low temperatures (T=5.4 K) [60]. This is seen in figure 3-8 (a) where the emission intensity increases at the bottom of the lower polariton branch as a function of an increasing pump power (lower part). The upper part shows the respective population build-up at the angle of 0^0.

In 2007 Christopoulos et.al [61] observed room temperature lasing in bulk GaN microcavities. It was shown that inorganic materials such as GaN due to the high binding energy of their Wannier-Mott excitons can undergo lasing at room temperature [61]. Under pulsed, non-resonant excitation low-threshold coherent light emission was observed at 300 K compared to the VCSEL based on the same material and a blue shift which is characteristic of the polariton-polariton interaction. This is seen in figure 3-8 (b).

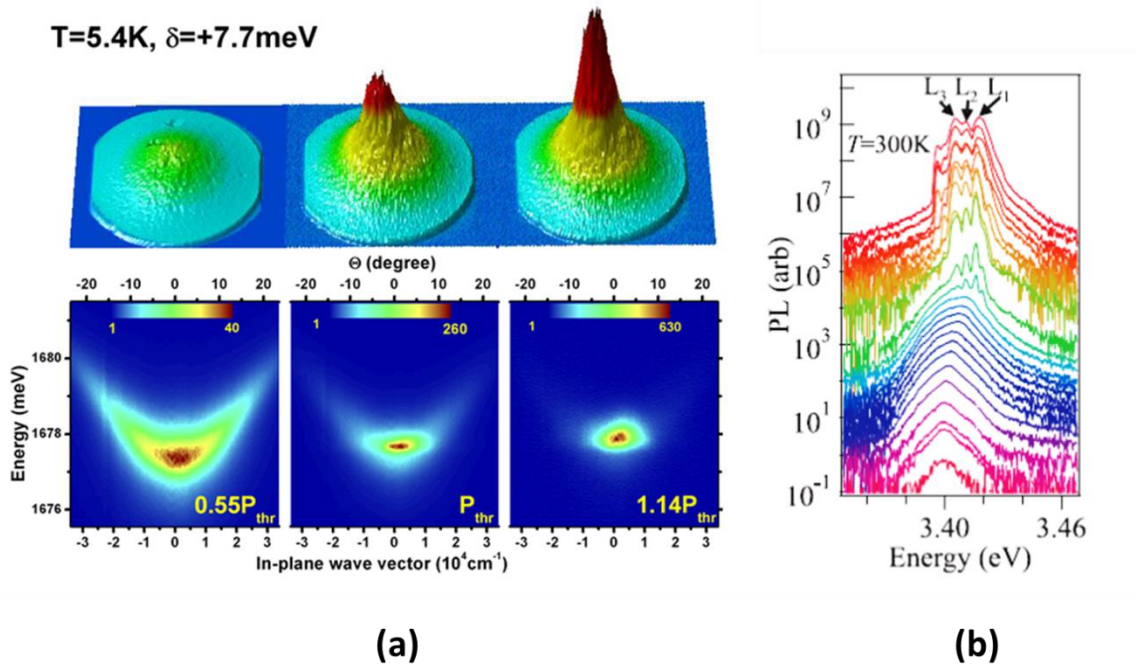

Figure 3-8 – BEC in a (a) CdTe based negatively-detuned microcavity at low temperature (T=5.4 K). The upper part signifies the build-up of the polariton population at the ground state and the lower part shows the increase of polariton emission intensity as a function of the pump power. From ref. [60]. (b) Emission spectra for the GaN-based microcavity for a series of increasing pump power, collected at an angle of 0^0, at T=300 K. From ref.[61].

The possibility of realising electrically driven polariton devices based on inorganic semiconductors was demonstrated for the first time by Tsintzos et al. [63] and then followed by others [64]. In their paper Tsintzos et al. showed that under electrical excitation polariton electroluminescence was observed for two cavity detunings, δ=0 meV and δ=-7 meV. This is shown in figure 3-9. Figures 3-9 a) and c) correspond to a zero detuning inorganic microcavity LED, and figures 3-9 b) and d) to a negatively-detuned inorganic microcavity LED. The authors demonstrated an excellent fit to the data using a two-level coupled harmonic oscillator model showing that the GaAs-based microcavity LED fabricated operate in the strong coupling regime. This is a very significant result suggesting that a polariton LED laser could be possible.

Following these reports, Schneider et al. [23], and Bhattacharya et al. [62] have demonstrated independently the creation of coherent light emitters based on exciton-polaritons in inorganic LEDs.

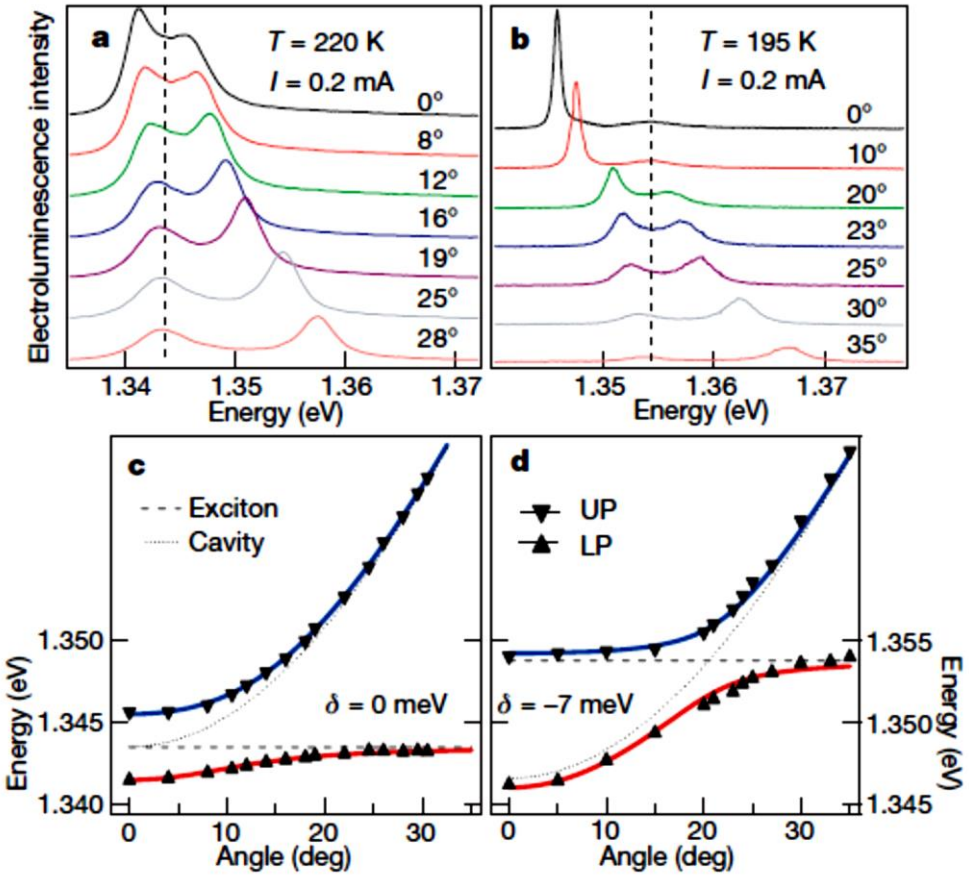

Figure 3-9 – (a) and (c) refer to a zero-detuned inorganic microcavity LED fabricated that operates in the strong-coupling regime, the emission spectrum as a function of angle at a driving current of I=0.2 mA and operating temperature of T=220K (a), and the respective dispersion graph (c). (b) and (d) refer to a negatively-detuned inorganic microcavity fabricated that operates in the strong-coupling regime, the emission spectrum as a function of angle at a driving current of I=0.2 mA and operating temperature of T=190K (b), and the respective dispersion graph (d). Based on ref. [63].

Figure 3-10 (upper part), based on the work of Schneider et al. [23] shows an electrically driven micropillar microcavity with four quantum wells (QWs), sandwiched between two distributed Bragg reflectors (DBRs). The DBRs were p-doped and n-doped to allow charge transport to the quantum wells which were placed at the antinodes of the electric field. The lower part of this figure plots the emission intensity as a function of the current density for two values of the magnetic field, 0 and 5T, respectively. The magnetic field serves as to enhance the polariton scattering efficiency and thus to show a clear lasing threshold (j_{th}) than in the case of zero magnetic field (0T).

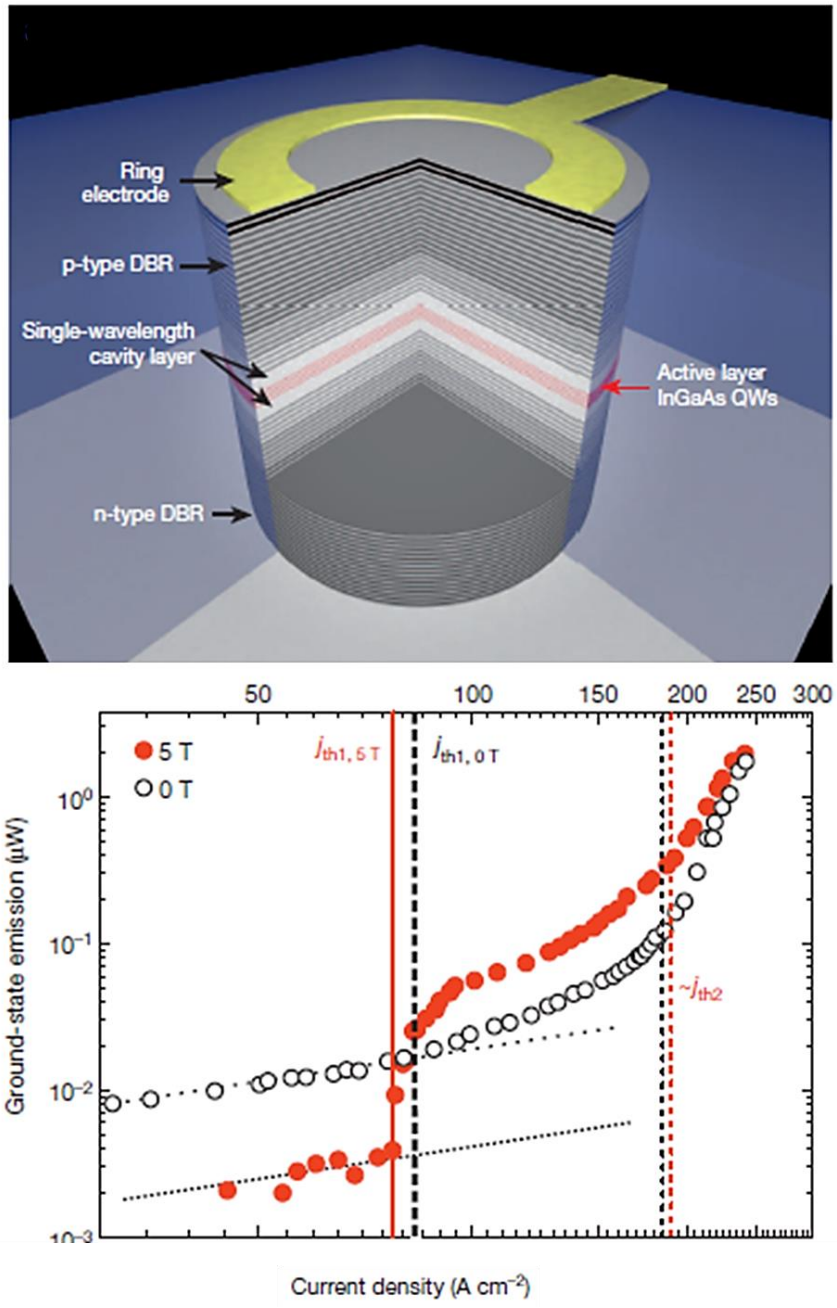

Figure 3-10 – Lasing behaviour in a micropillar-based microcavity in the strong-coupling regime. By the application of a magnetic field a clear threshold is observed for lasing as is described in ref. [23].

The demonstration of polariton lasing from inorganic LEDs [23, 62] is a significant step in creating electrically driven non-linear emitters with low-lasing threshold for commercial applications. The low-lasing threshold that can be achieved in the strong-coupling regime compared to that in the weak-coupling regime [65, 66] would be beneficial for achieving non-linear light emission in organic light-emitting diodes.

There is a large body of work done reporting strongly-coupled inorganic microcavities. This historic review only summarizes the most influential steps of the field. A more general overview can be found in ref. [67, 68]. A historic review of organic microcavities and OLEDs operating in the strong-coupling regime will be given in the following section.

3.5.2 Organic microcavities

Organic materials possess interesting physical properties compared to their inorganic counterparts which are of great interest especially in strongly-coupled systems. For example, Frenkel excitons are tightly bound possessing binding energies of the order of 1 eV, compared to binding energies of a few meVs found in weakly bound Wannier-Mott excitons. Furthermore, the high oscillator strength of the organic semiconductors renders the observation of the strong-coupling regime possible at room temperature.

The use of organic semiconductors in microcavities reported for the first time by Lidzey et al. [49] in optical microcavities containing a zinc-based porphyrin (4TBPPZn) as the strongly-coupled organic material. Porphyrins are organic compounds with very intense absorption bands. Particularly, the Soret band of these molecules has a relatively narrow absorption linewidth and high oscillator strength, two of the requirements for achieving the strong-coupling regime.

The material was dispersed in a polystyrene matrix and spun cast on top of a dielectric DBR mirror. The second mirror in the cavity was metallic silver that was evaporated on top. The reflectivity spectra as a function of angle revealed a Rabi splitting of more than 100 meV as shown in figure 3-11 (a). An energy splitting is observed by the appearance of two reflectivity dips that anti-cross near the Soret band resonance. The polariton dispersion extracted from these data shows anti-crossing around resonance (Figure 3-11 (b)).

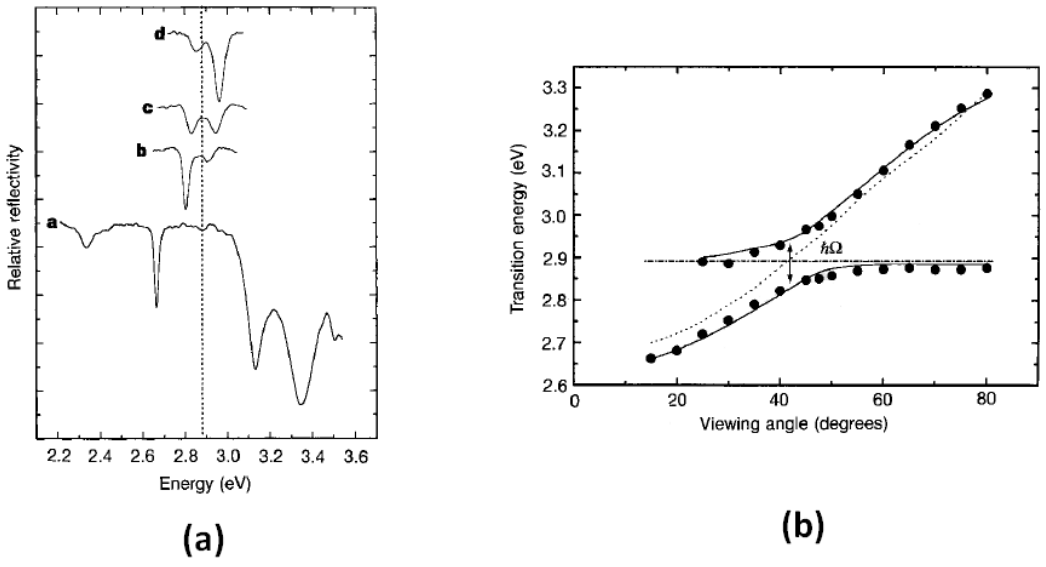

Figure 3-11 – (a) Reflectivity spectra of the 4TBPPZn-based organic microcavity, and (b) dispersion curve of the polariton dips as a function of the viewing angle. The fits are obtained by using a transfer-matrix reflectivity model. From ref. [49].

The use of the Soret band in Porphyrin dyes has the advantage of achieving a high Rabi splitting but has the disadvantage of being non-radiative. To observe the radiative emission of polariton states luminescent cyanine dyes were employed.

J-aggregates are a class of photoluminescent organic molecules that in highly polar environments can self-assemble into well-ordered structures. The aggregate exhibits narrow absorption and emission transitions compared to their monomers and the oscillator strength of the aggregate is the collective of all the monomeric units. For this reason, Lidzey et al. first observed polariton emission from microcavities containing J-aggregates of cyanine dyes in a polyvinylalcohol (PVA) matrix [69]. The photoluminescence spectrum is shown in figure 3-12 (a) and was obtained under non-resonant excitation. The polariton dispersion from reflectivity (with a Rabi splitting of approximately 80 meV) and PL measurements is seen in figures 3.7 (b) and (c), respectively.

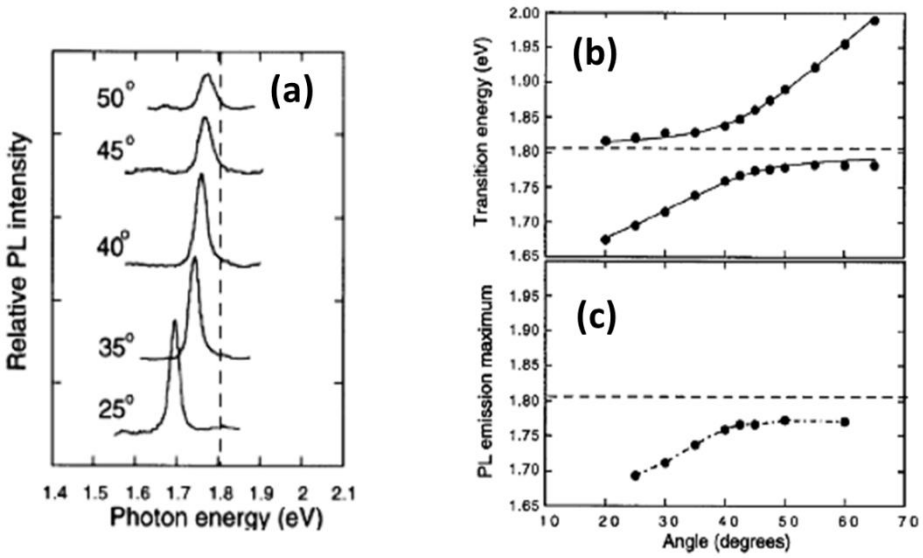

Figure 3-12 – (a) Polariton emission for a series of angles following non-resonant excitation, (b) reflectivity and (c) PL dispersion curves.

Other authors have reported the use of different organic materials to show strong-coupling in microcavities. For example, the use of the σ-conjugate polysilane polymer PBPS showed that the strong-coupling regime can be reached even if the transition linewidth of the absorption resonance is high (190 meV) [70, 71]. A range of Rabi splittings from 210 to 430 meV have been observed in these structures.

Instead of being solution processed, small-molecule organic materials can also be thermally evaporated. With this process materials such as polycrystalline 3,4,7,8 napthalenetetracarboxylic dianhydride (NTCDA) can be deposited as neat films with high control over morphology [72]. What is interesting about this organic semiconductor is that except from the main 0-0 absorption transition, other vibronic transitions with well-resolved absorption characteristics are present in the absorption spectrum. This creates the possibility of coupling multiple exciton transitions with the same photon mode, and it has been successfully demonstrated by the work of Holmes et al. [73].

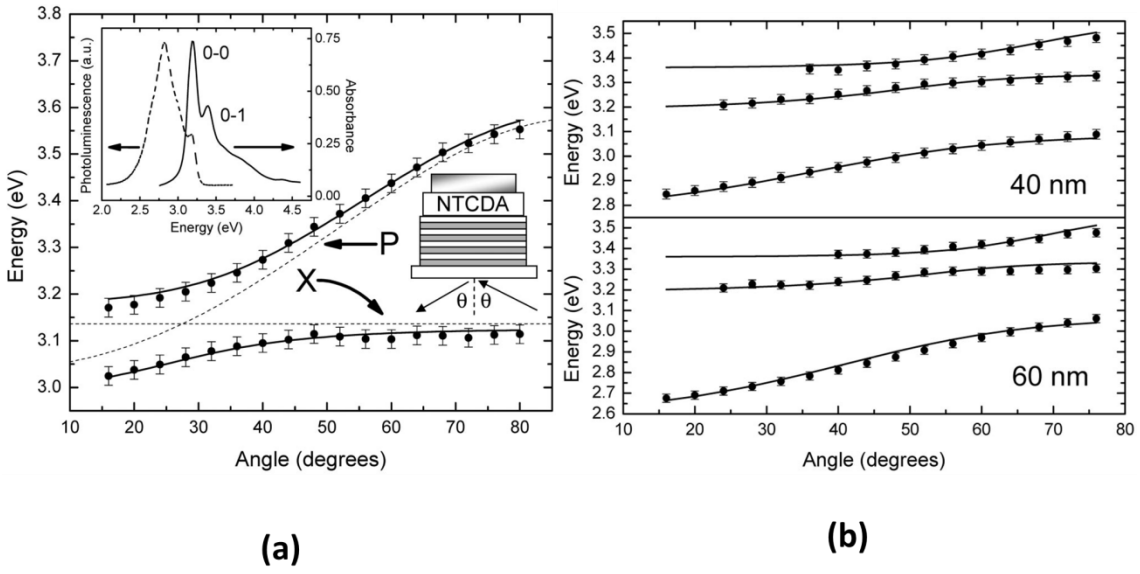

Figure 3-13 – (a) Polariton dispersion obtained by reflectivity measurements from a microcavity containing 20 nm of evaporated NTCDA. Inset: room temperature absorption and emission taken from a 50 nm thin evaporated film of NTCDA. (b) Polariton dispersion obtained by reflectivity measurements from a microcavity containing 40 nm (upper) and 60 nm (lower) of evaporated NTCDA. From ref. [73].

In this report, subsequent evaporation of a thin film of NTCDA and metallic aluminium onto a dielectric DBR mirror formed the microcavity. Figure 3-13 (a) shows the absorption and emission spectrum of NTCDA (inset) and the dispersion graph that was obtained by performing reflectivity measurements. It has to be mentioned that only 20 nm of the organic semiconductor required to exhibit strong-coupling. By increasing further the thickness of the evaporated film (Figure 3-13 (b)) it was shown that the 0-1 vibronic transition can be coupled as well. The result is the appearance of three polariton branches in the dispersion graph. In other microcavity systems NTCDA has been shown to exhibit strong-coupling through organic-inorganic hybridization where both Wannier-Mott and Frenkel excitons co-exist, at room temperature [74].

An alternative method of coupling multiple transitions with the same photon mode in an organic microcavity is to use two or more organic materials with characteristic narrow exciton transitions and high oscillator strengths. This was first reported by the work of Lidzey et al. [75] where two spatially separated organic semiconductors (seen in Figure 3-14 (a)) were simultaneously coupled to a single photon mode. The hybrid organic microcavity described has three polariton branches that are all well separated by the exciton transitions, as seen in Figure 3-14 (b). Each of the three branches has different contributions of the two excitons and the photon. The relative coefficient of each of the polariton constituents is shown in the lower part of figure 3-14 (b). Most recently it was shown that hybridization in organic microcavities can act as a pathway for ultra-fast energy transfer between exciton states [42].

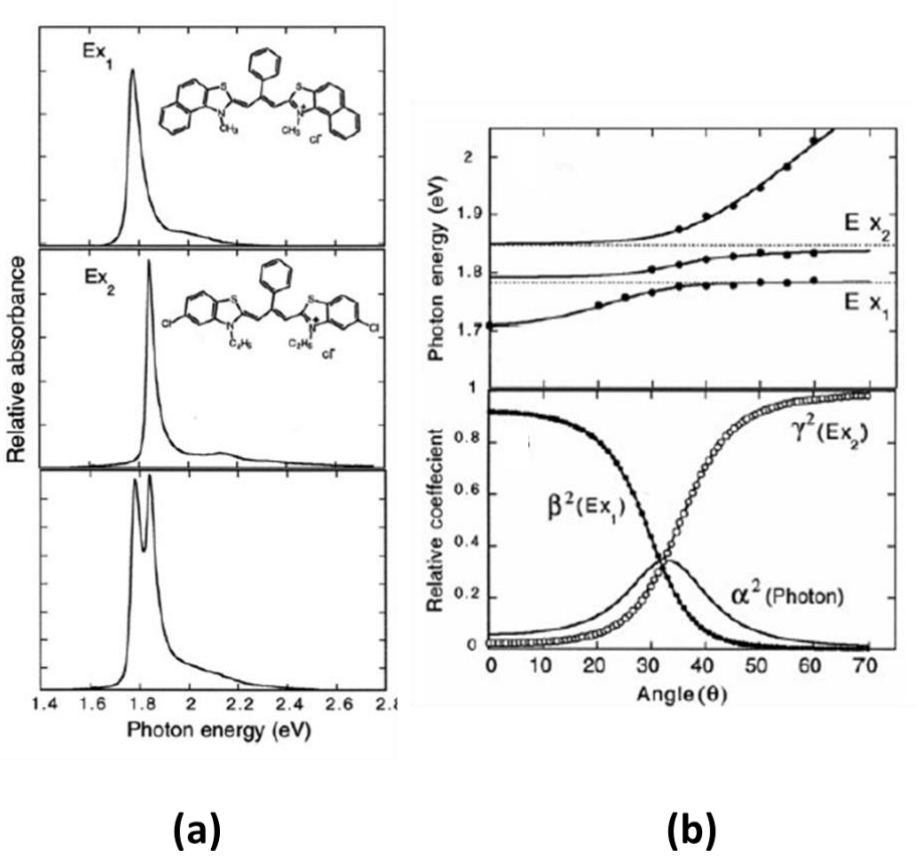

(a) **(b)**

Figure 3-14 – (a) Absorption spectra and structures of J-aggregate dyes. (b) Upper part: polariton dispersion obtained from reflectivity measurements, Lower part: relative component coefficient that corresponds to the lower polariton branch of the fabricated microcavity.

To understand the polariton dynamics in organic microcavities Lidzey et al. [76] studied the photoluminescence of a DBR-metal microcavity containing J-aggregates of a cyanine dye as the strongly-coupled organic semiconductor, through non-resonant excitation. The results were compared with a model based on the scattering of excitons from the exciton reservoir by molecular vibrations into polariton states, interbranch polariton transfer through absorption and emission of vibrational quanta, and radiative decay of polaritons. These agreed well with previous considerations published by Tetrakovskii et al. [77] regarding the interaction of polaritons with molecular vibrations.

The interaction of polaritons with molecular vibrations and the mechanism by which polariton branches are being populated were intensively studied both theoretically and experimentally. In a series of publications, Agranovich, Litinskaya and co-workers have theoretically studied the properties of polaritons, such as polariton localization, propagation, relaxation, and disorder [78-82].

Moreover, the work of P. Michetti and G.C. La Rocca focused on polariton dynamics [43-45, 83, 84]. A set of rate equations was used to describe the interaction of exciton-polaritons with molecular vibrations as the main mechanism to populate polariton states. This theoretical approach was experimentally verified by the work of D. Coles at al [46] in which it was observed that the polariton population was increased in the LPB when the energetic

separation of the exciton and the LPB state was equal to the energy corresponding to a high energy molecular vibration of the J-aggregate.

Cavity engineering is also one of the most important aspects of fabricating high quality organic semiconductor microcavities. The mirrors that are commonly employed in the fabrication of organic microcavities are either metallic or distributed bragg reflectors or both. P. A. Hobson et al [85] showed that a microcavity that consists of two metallic mirrors has a larger Rabi splitting and a lower quality factor compared to cavities containing a DBR and a metallic mirror. The Rabi splitting as a function of the square root of the oscillator strength for all-metal or hybrid cavities is seen in Figure 3-15.

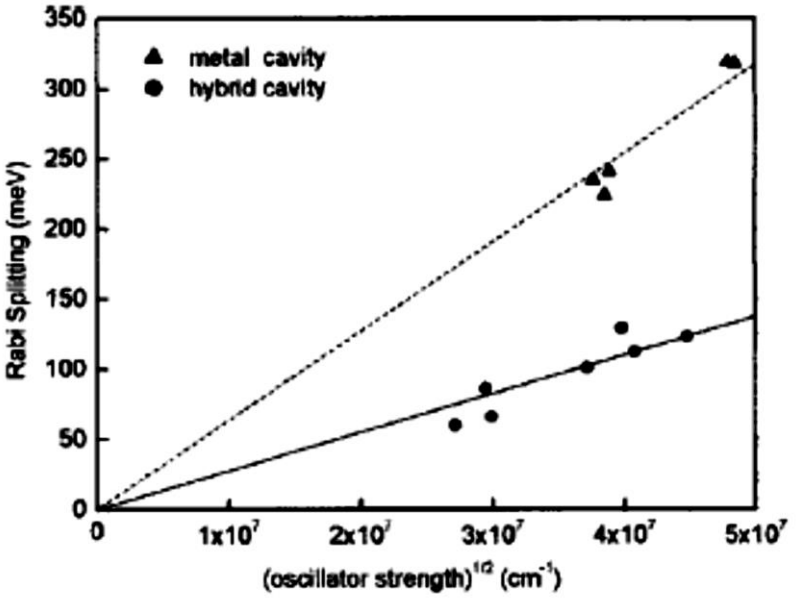

Figure 3-15 – (a) Rabi splitting as a function of the square root of the oscillator strength measured for metal-metal and DBR-metal organic microcavities.

The fabrication of a high quality organic microcavity having two DBR mirrors was already a challenge since sputtering or plasma enhanced chemical vapour deposition on top of organic layers usually damages the underlying organic material. Moreover, there is limited availability of thermally evaporated materials with high refractive index difference. Connolly et al [86] fabricated a double DBR organic microcavity. The bottom DBR was deposit via PECVD and consisted of SiO_2 and Si_3N_4 and the top DBR was deposit via thermal evaporation of LiF and TeO_2. Zinc porphyrin (ZnTPP) was used as the strongly-coupled organic semiconductor dispersed in polystyrene in order to create high quality factor microcavity structures. The microcavities fabricated with this method had a Q-factor in the range Q=420-600.

An alternative way of fabricating a double-DBR organic microcavity was explored by Wenus et al [87]. A wedged-shaped cavity was formed when two DBR mirrors grown via PECVD were laminated together at an angle. Initially, J-aggregates dispersed in gelatine matrix were spun cast on the bottom DBR (9 pairs of Si_3N_4/SiO2). A second DBR (9 pairs of Si_3N_4/SiO2) was separately grown onto a quartz glass. Then it was pressed at one side of the substrate forming a wedge-shaped microcavity structure. The quality factor obtained for this graded cavity

structure was Q=130. With this method the polariton dispersion can be plotted as a function of position instead of angle of incidence.

High Q-factor cavities are required in order to increase the polariton lifetime. An alternative way of creating high Q-factor cavities which led to the first observation of polariton lasing was demonstrated by the work of S. Kena-Cohen et al [88]. In this microcavity the top and bottom DBR mirrors consisted of 12 pairs of SiN and SiO_2 dielectric layers which were grown by plasma enhanced chemical vapour deposition on quartz substrates [89]. The 70 nm thick gold was evaporated on top of the DBR mirrors. Photolithography and lift-off was then used to create stripes of 0.5 mm wide and 30 mm long with 0.5 mm separation. By positioning the gold-coated DBR substrates face-to-face and by applying high pressure the two substrates were hold together by cold welding. The empty microcavity that was formed was filled with melted anthracene molecules that filled the empty microcavity (140 nm) through capillary forces. Crystallization was achieved by slowly decreasing the temperature rate. Figure 3-16 shows the measured photoluminescence as a function of pump fluence at $\theta=0^0$. In the inset of the figure the LPB FWHM and the integrated intensity as a function of the pump fluence indicate a lasing threshold at the intersection between sublinear and superlinear regimes.

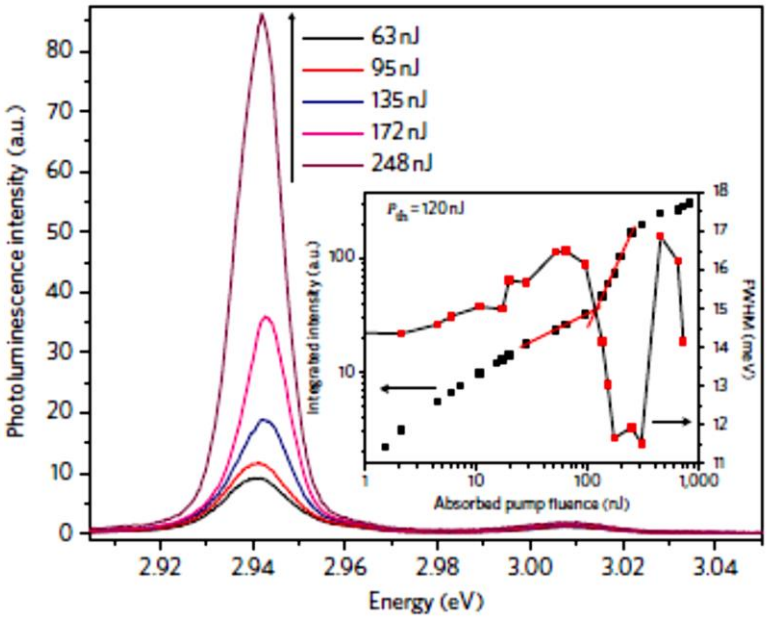

Figure 3-16 – LPB emission intensity measured at $\theta=0^0$. In the inset of the figure the integrated intensity and FWHM of the LPB at $\theta=0^0$ indicates a lasing threshold as seen by the crossover between the sublinear and superlinear regimes. From ref. [88]

The organic semiconductors used till that point consisted of small molecules. An alternative approach was the use of polymers to exhibit strong coupling in organic microcavities. Firstly, in the work of Takada et al [70] the polymer PBPS was used as the strongly-coupled organic semiconductor. With a linewidth of approximately 15 nm this polymer exhibited strong-coupling and a large Rabi splitting of 430 meV. This polymer has also been used in polymer light-emitting devices [90].

A different conjugated polymer that was used to show strong coupling in microcavities was the ladder-type polymer meLPPP [24]. This organic semiconductor has well-resolved absorption

transitions, characteristic of the rigid backbone of the ladder-type materials synthesized [91, 92]. The microcavity structure consisted of DBR mirrors made of SiO_2 and Ta_2O_5 via magnetron sputtering. Demonstration of room temperature Bose-Einstein Condensation utilising a conjugated polymer was achieved for the first time. Figure 3-17 shows the emission intensity in the momentum space of the microcavity at excitation densities below, near and above the lasing threshold. A characteristic blue-shifted from the polariton dispersion due to polariton-polariton interaction appears in the spectrum.

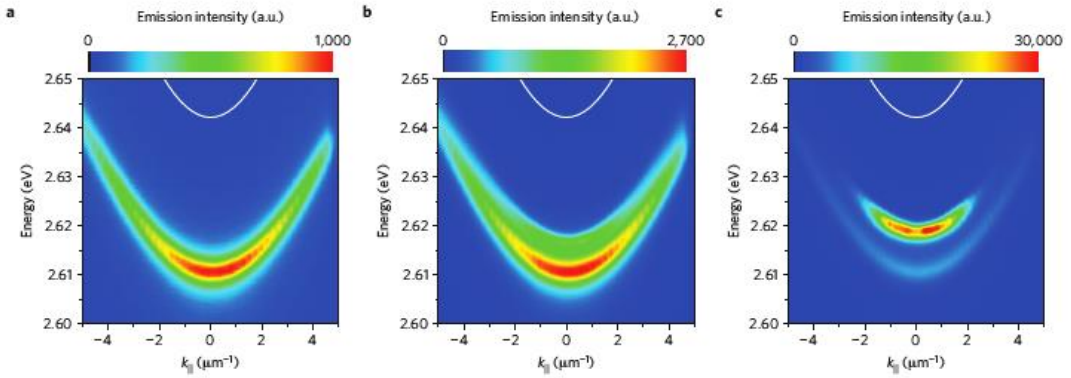

Figure 3-17 – Photoluminescence spectrum in the momentum space recorded for a double-DBR microcavity structure containing the ladder-type polymer mLPPP, below, near and above the lasing threshold. From ref. [24].

A second demonstration of room temperature Bose-Einstein Condensation was achieved in the work of Daskalakis et al [25]. The optical microcavity fabricated consisted of a top and a bottom DBR mirrors made of SiO_2 and Ta_2O_5 via magnetron sputtering enclosing a single layer of the organic semiconductor TADF. TADF are oligomer molecules that were used to exhibite ultra-strong coupling in all-metal microcavities with a Rabi-splitting of the order of 1 eV [93]. The Q-factor for this cavity was approximately 600. Nonlinear emission from the bottom of the LPB was observed with a characteristic blue-shift due to polariton-polariton interactions.

Apart from being optically excited polariton modes can also be excited through charge injection in strongly-coupled OLEDs. The first demonstration of polariton electroluminescence was demonstrated in the work of Tischler et al [94]. The microcavity OLED consisted of two metallic Ag mirrors of which one was semi-transparent in order to allow light to escape from the cavity and be observed. The strongly-coupled organic semiconductor was based on J-aggregates of a cyanine dye that was deposit via the layer-by-layer technique (LBL) [95]. Figure 3-18 shows (a) reflectivity, (b) EL emission spectra and (c) the respective dispersion curves for this OLED microcavity showing good agreement in all cases.

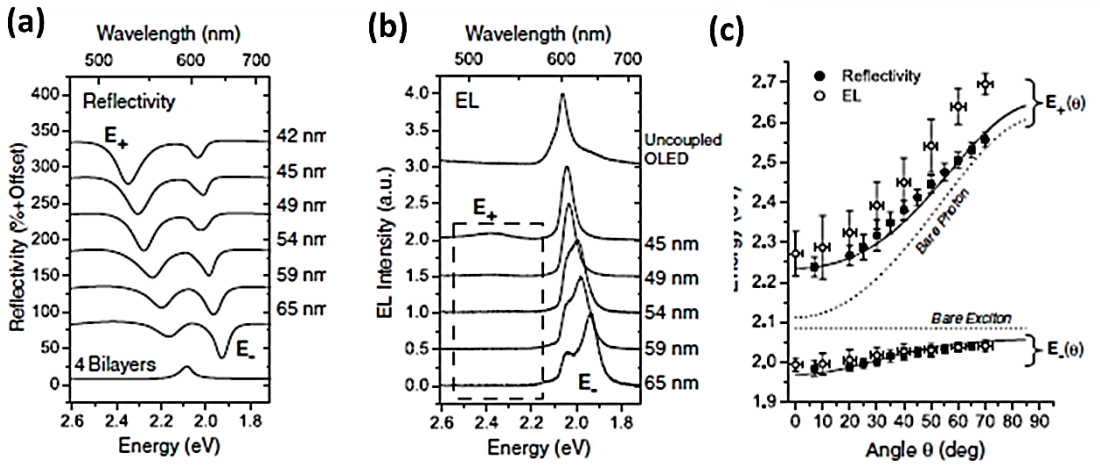

Figure 3-18 – (a) reflectivity, (b) electroluminescence and (c) dispersion curved for the OLED microcavity fabricated based on J-aggregates of the dye TDBC. From Ref. [94]

An alternative way to electrically excite polariton modes was shown in the work of Lodden et al [47]. The material tetraphenyl porphyrin TPP was used as the strongly-coupled organic semiconductor placed between Ag and Al metallic mirrors. By utilising Alq_3 as the weakly-coupled and emissive organic material in the same structure, with its emission spectrum overlapped with the upper and the lower polariton branches, direct population of the branches was achieved via the optical pumping mechanism in order to circumvent the bottleneck effect that prohibit significant polariton population to be achieved at the bottom of the LPB. The Q-factor achieved for this cavity was Q~28. TPP was also studied from the same author in terms of populating polariton states via thermal activation [96].

Finally, polariton electroluminescence was observed from all-metal microcavities operating in the ultrastrong coupling regime due to the high interaction strength of these materials, containing organic semiconductors such as the organic semiconductor TDAF [97] and a squarrilium dye (Sq) [98]. This regime has been previously explored in various systems including intersubbund quantum wells in the infrared [99] and THz [100] regions, as well as using organic molecules [93, 101].

Particularly, a very interesting result was obtained in the work of Gubbin et al. [97] where the OLED devices fabricated had different thicknesses and therefore de-tunings. The turn-on voltage measured was the same (3.1 V) for all the devices reported and below the exciton energy of TDAF (3.5 eV) as seen from figure 3-19. The same turn-on voltage observed suggests that lower polaritons do not form directly by the injection of charge carriers from the electrodes but follow a two-step process where excitons are created first and then scatter into polariton states. It also contradicts previous results that suggest work function modification by changing the detuning [102].

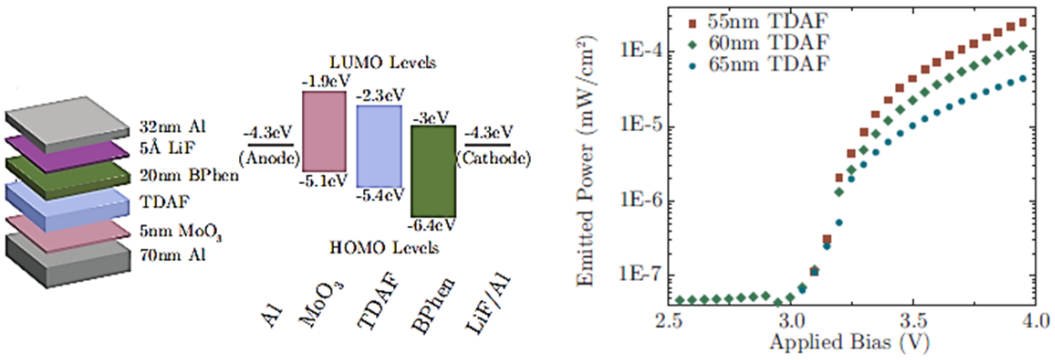

Figure 3-19 – Microcavity structure, energy levels of the materials used in the polariton OLED and the emitted optical power as a function of the applied bias showing the same turn-on voltage for all devices fabricated. From Ref. [97].

Chapter 4

Experimental Methods

In this chapter an overview of the various experimental techniques that were employed during this study is provided. A description is given for the device fabrication processes and the characterization measurements which were employed under both optical and electrical excitation. The motivation behind the selection of the device architectures is discussed and the procedure of fabricating two distinct sets of device structures is detailed. The first set examines organic polariton LEDs and is related to the EL emitted from strongly-coupled states, whereas the second control device set is fabricated to examine the EL emitted from uncoupled Frenkel exciton states. Moreover, various techniques were used for spectroscopic investigations. These include thin film and solution-based absorption and emission spectroscopy as well as reflectivity, photoluminescence and electroluminescence angle-resolved spectroscopy. The simplified version of the set up that was used to electrically characterize the samples and to perform efficiency comparisons for the two sets of devices is presented here. Finally, a brief description of the time-resolved emission measurement technique that was carried out at the University of Southampton is given.

4.1 Introduction

The fabrication and characterization of strongly-coupled OLEDs is motivated by the need to understand the physics behind the operation of these devices that could potentially lead to the realization of the organic laser diode. This chapter is focused on three main parts.

Firstly, a description of the materials that were used in the fabrication process is detailed. These include metals, metal oxides, fluorescent and non-fluorescent organic semiconductors.

Secondly, the device fabrication part with the fabrication of two sets of devices is detailed. The first refer to control (or conventional) OLEDs and the second refer to microcavity OLEDs with either two metallic mirrors or the combination of a metal and a DBR mirror.

Thirdly, the rest of the chapter is dedicated to the experimental techniques that were used to characterize them.

In terms of terminology, control or conventional devices refer to OLED devices that lack the microcavity configuration. Microcavity OLEDs are based on a double mirror configuration which may operate in the weak or in the strong coupling regime. Microcavity OLEDs that work in the strong coupling regime are termed polariton OLEDs, organic polariton LEDs, or strongly-coupled OLEDs. Alternatively, OLED devices that operate in the weak-coupling regime are simply referred as OLEDs. Compartment material is defined as the non-emissive organic semiconductor in devices; mainly, the organic hole-transport and electron-transport materials.

4.2 Materials used in OLED devices

The materials used in this thesis in the fabrication of OLEDs are the hole- and electron-transport organic semiconductors, fluorescent materials, insulating materials, metal-oxides and metal electrode materials. The structure of these materials is given in the following sections alongside with a brief explanation of their function in the device.

4.2.1 Hole-transport materials

Figure 4-1 depicts the chemical structure of the solution processable hole-transport materials used in this thesis. These materials are characterized by high hole mobilities and may or may not act as electron blocking layers. This depends on the position of the LUMO energy level they possess.

Another important characteristic of the hole transport semiconductors is that they can be processed from different polar or non-polar solvents. For example, PEDOT:PSS is soluble in water but insoluble in toluene. This allows multiple layers to be deposit on top of each other without swelling of the underlying organic layer.

Organic materials such as the cross-linkable TFB add an extra functionality to the processing steps as it can be thermally annealed to form an impenetrable solid organic layer that is resistive against the attack from other organic solvents.

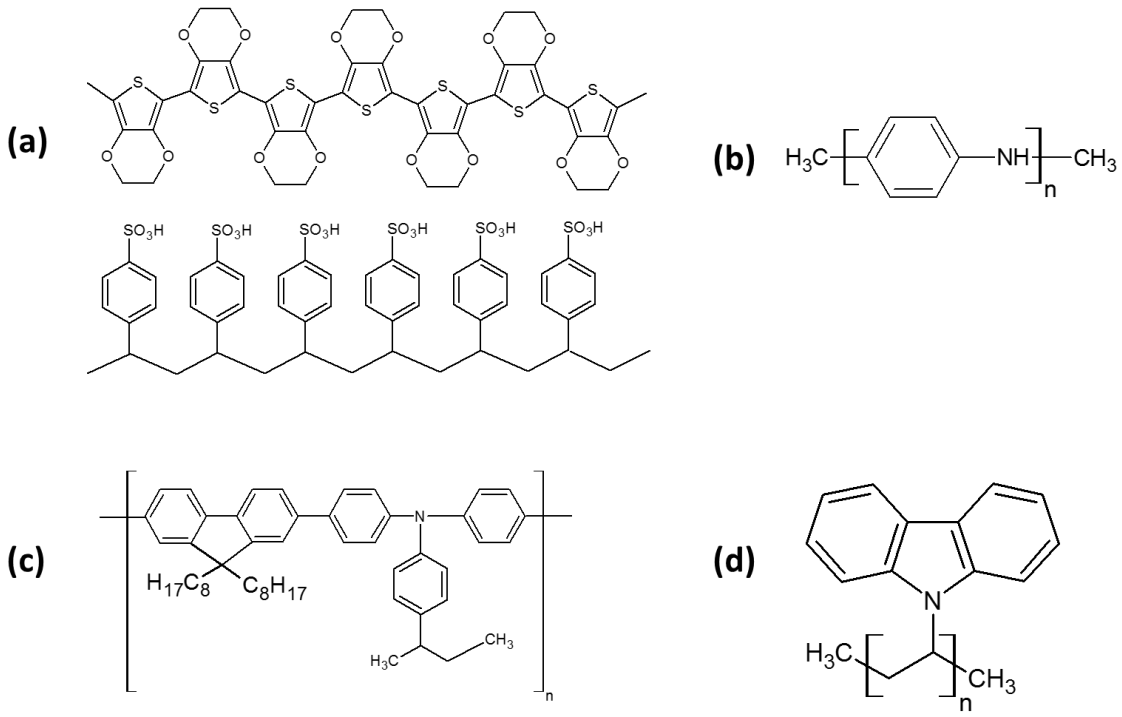

Figure 4-1 – A schematic representation of the molecular structure of the hole-transport organic semiconductors used in OLEDs: (a) PEDOT:PSS, (b) Polyaniline(PAni), (c) Poly[(9,9 –dioctylfluorenyl -2,7 diyl))-co-(4,4'-(N-diphenylamine)]-butylphenyl))(TFB), and (d) Poly(9-vinylcarbazole) (PVK).

Characteristically, PEDOT:PSS was purchased from H.C. Stark and is a water-based organic semiconductor material that was used as received. PAni is a conductive polymer similar in device function to PEDOT:PSS, it was purchased from ORMECON in the form of nanoparticles dissolved in water and was used without any further purification. A high temperature cross-linkable TFB polymer was used in devices on top of the PEDOT:PSS layer and was provided by Cambridge Display Technology. Poly(9-vinylcarbazole) (PVK) is another hole transport polymer. The material PVK was purchased from Sigma-Aldrich. The function and the characteristics of each material in the device will be detailed in the fabrication section.

An inorganic hole transport material that was used in this study was the inorganic semiconductor MoO_3. This material functions similarly to the solution processable PEDOT:PSS and can be either solution-processed or thermally evaporated. In this study thermal evaporation of the MoO_3 was used. The material was purchased from the company Kurt J. Lesker.

4.2.2 Electron-transport organic semiconductors

Organic semiconductors that transport electrons are electron-transport materials. These materials are associated with high electron mobilities and they can act as effective hole blocking layers depending on the energy position of their HOMO level.

The main electron-transport material that was used in this study was BCP. Bathocuproine (BCP) is an electron transport molecule that was deposited in devices via thermal evaporation. This organic semiconductor was purchased from Sigma-Aldrich. The chemical structure of the molecule is shown in Figure 4-2.

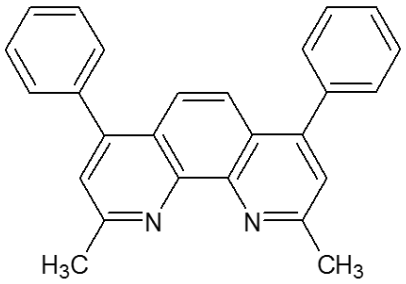

Figure 4-2 – A schematic representation of the molecular structure of the electron-transport organic semiconductor used in OLEDs: Bathocuproine (BCP).

4.2.3 Emissive organic semiconductors

There is a wide range of emissive organic semiconductors used in this thesis. The fluorescent materials can be divided into small molecules and polymers.

The small-molecule organic semiconductors include the R-substituted molecules of the acene family such as 2-methyl-9,10-di(2-naphthyl) anthracene (MADN), 9,10-diphenylanthracene (DPA), and 5,12-diphenyltetracene (DPT), which were purchased from Sigma Aldrich. They can easily be processed from organic solvents such as toluene and can be used in blends with other small molecules or polymers. Another family of small molecules are the self-assembled cyanine dyes. The material used in this study is the 5,5',6,6'-tetrachloro-1,1'- diethyl-3, 3'-di(4-sulfobutyl)-benzimidazolocarbocyanine (TDBC) salt. The Lumogen F Orange 240 (LumF) is a light emitting small molecule that was provided by BASF. Figure 4-3 shows the chemical structure of the fluorescent small molecules.

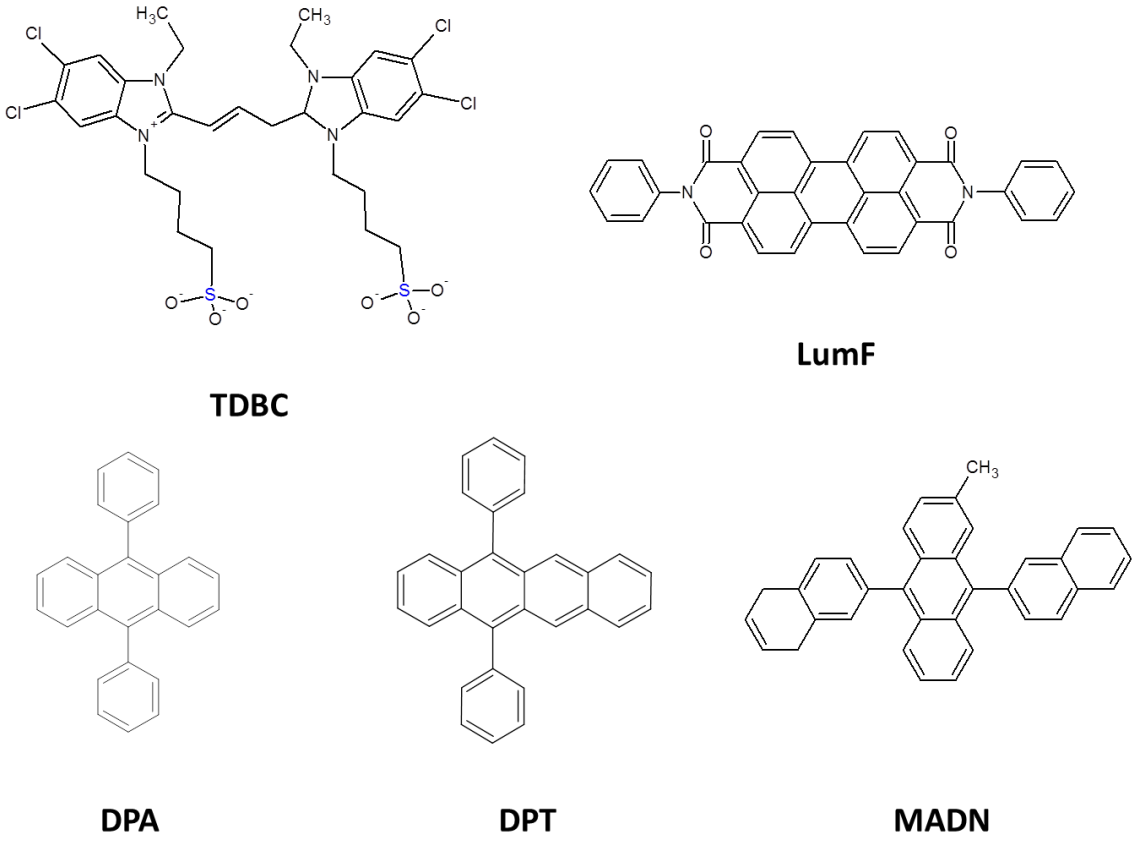

Figure 4-3 – A schematic representation of the molecular structure of e 2-methyl-9,10-di(2-naphthyl) anthracene (MADN), 9,10-diphenylanthracene (DPA), 5,12-diphenyltetracene (DPT), Lumogen F Orange 240 (LumF), and 5,5',6,6'-tetrachloro-1,1'- diethyl-3, 3'-di(4-sulfobutyl)-benzimidazolocarbocyanine salt (TDBC).

Light emitting polymers were also used in this study. The blue emitting polymer meLPPP was synthesised by Dr Hunan Yi in the chemistry department of the University of Sheffield. The conjugated polymers F8BT and PFO were purchased from Sigma Aldrich. The conjugated polymer ADS128GE (NP) was purchased from American Dye Source. Figure 4-4 shows the chemical structure of the fluorescent polymers.

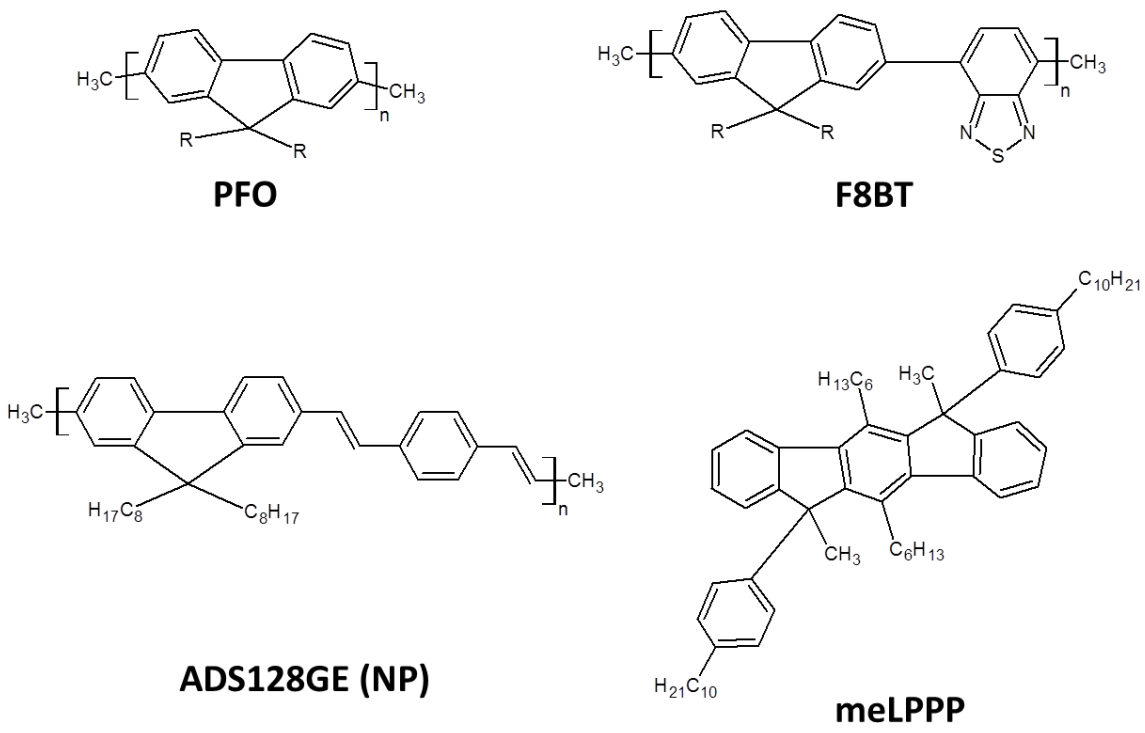

Figure 4-4 – A schematic representation of the molecular structure of the fluorescent polymers PFO, F8BT, ADS128GE (NP) and meLPPP.

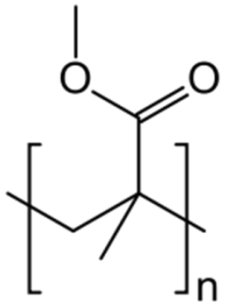

Figure 4-5 – A schematic representation of the molecular structure of the insulating polymer: poly(methyl methacrylate) (PMMA).

4.2.4 Insulators

Insulating polymers were used in this study as host materials for OLED fabrication (Chapter 7), namely, the poly(methyl methacrylate) (PMMA). This material was purchased from Sigma Aldrich and its chemical structure is depicted in figure 4-5.

4.2.5 Metals

Three metals were used during the fabrication process, namely Calcium (Ca), Silver (Ag) and Aluminium (Al), all in a pellet form with length of about 2-6 mm. All of them purchased from Sigma Aldrich and were kept in inert atmosphere to prevent oxidation.

4.3 Preparation of material solutions

Various fluorescent organic semiconductors were dissolved in both polar and non-polar solvents prior to thin film deposition. Polar organic materials can easily dissolve in polar solvents. Therefore, self-assembled J-aggregates of organic dyes that bear a permanent dipole moment, can readily be dissolved in highly polar solvents, such as H_2O and MeOH.

All other solution processable organic materials that were prepared have strong affinity towards dissolution into common organic solvents. Specifically, chlorobenzene, dichlorobenzene, chloroform, toluene and tetrahydrofuran were selected and tested. Different combinations of organic semiconductor-solvent systems were investigated.

There are three cases of miscibility of an organic material into an organic solvent. The material can be dissolved, partly-dissolved or undissolved, denoted as D, PD and UD, respectively, to indicate the resulted solubility. In undissolved solutions the organic material remains in the solid state phase. In the partly-dissolved case a part of the organic material dissolves; with some remain as undissolved aggregates. In the third case all of the organic material is dispersed uniformly within the organic solvent. Materials dissolve better in solvents when stirred or heated or the combination of both.

Two different vials were used to prepare solutions, namely transparent or amber based vials. The former was selected to handle mainly transparent materials, such as PMMA. The later was used for fluorescent dyes or conjugated polymers to strongly inhibit any photo-activated response. Amber glass vials are specifically designed to prevent from initializing any kind of light induced chemical activity between the material and the solvent, or the material itself.

Vials of 2, 4, 8, and 20 ml of volume were used depending on the desired amount of the final solution. The vials had been rinsed first with IPA and then gun-dried using pressurized N_2 at ambient conditions. Organic materials were weighted out into the vials, typically few milligrams at a time.

Solution concentrations are commonly quoted in milligrams of dissolved substance per millilitre of solvent. Suitable solvents were selected for each material and added, spanning a wide range of concentrations from 0.5 mg/ml to the highest 100 mg/ml for the host-guest blended systems. In the later, host polymers were separately prepared from guest dyes where they were mixed stoichiometrically in a third, pre-cleaned vial.

The mixing of materials within solvents is highly enhanced when assisted by heating or by magnetic bar stirring processes. The temperature assisted process is affected by two limiting factors:

The first considers the boiling point of the solvent used. Care was taken for auto-ignition at elevated temperatures. The second considers the organic semiconductor dissolved. If the temperature applied is high, unexpected degradation prior to thin film deposition might occur. The temperate range that the solutions were thermally treated in this work was safely selected at the range 60^0-90^0 C.

The process of dissolution assisted by agitation using a magnetic bar stirrer is straight-forward. Commonly, higher spin speeds are required when preparing high concentration solutions. In this work a range of 400-800 rpm (revolutions per minute) was used. A combination of the two dissolution assisted processes was available by using a thermostatically-controlled hot plate in a clean room.

HPLC grade solvents were used at all times in all organic-based solutions and de-ionized water was used for water based solutions. A micropipette or conventional gradual pipette was selected according to the low or high volatility of the respective solvents.

Organic semiconductors can exist in a crystalline phase. Higher mobilities in organic field effect transistors have been reported [103] when processed from slow evaporated organic solvents. A microcrystalline phase is usually formed by the relatively slow solvent evaporation during spin coating. Volatile solvents such as chloroform are associated with fast evaporation rates, which are non-ideal to induce crystallinity.

4.4 Thin film deposition

4.4.1 Spin coating

Thin films of materials can be deposited using various techniques. A highly accurate and reproducible technique is that of spin coating. Thin films of solution processable organic materials were cast using a Semitec or a Laurell technologies spin processor. Prior to deposition, non-polar based solutions were filtered using 0.45 μm x 13 mm PTFE syringe mounted filters, whereas for solutions based on polar solvents, 0.45 μm x 13 mm PVDF syringe mounted filters were used.

The rotating part of the spin-coater is called the “chuck” and is the main part where all substrates are placed prior to spinning. In the central part of the chuck a pipe exists that is connected to a rotatory vacuum pump. The role of the pump is to keep the substrates in one place during spinning by exerting a force created by the vacuum. A selected amount of substance is cast onto the substrates using pipettes.

There are two spin casting methods. In the static deposition method, solution deposition is done prior to the onset of spinning. In the dynamic deposition method, solution deposition is done during the spinning of the substrate.

The spin speed defines the layer thickness of the thin film through the equation:

$$t \propto \frac{c\eta(c)}{\sqrt{\omega}} \tag{4.1}$$

According to equation (4.1), the thickness of the deposited film (t) is proportional to the concentration (c) and the viscosity η of the solution and inversely proportional to the square root of the rotatory spin speed (ω). The spin speed, the acceleration, the spin time and a possible selected dual-phase spinning (sequential slow and fast spin speeds) can all be adjusted by the electronic controller of the spin coater.

To measure film thickness a small scratch was made into the film surface. A Dektak 3ST surface profilometer, using a stylus force of 15 mg was used to scan across the scratch and thereby measure the film thickness. The tip of the profilometer was gently cleaned when required in order to prevent any unwanted materials being attached to it.

In each measurement there is an associated uncertainty of about 1-5 nm in the total thickness. This error is based on the total cumulative error of every individual step in the measurement.

4.4.2 Thermal evaporation

Most of the organic light-emitting diodes presented in this study used thermal evaporation as the technique to depositing various layers within the device, especially the electron transport semiconductor and the metallic cathode. The basis pressure for the evaporation process was of the order of 10^{-6} Torr.

4.5 Fabrication of optical microcavities and devices.

The fabrication of organic light emitting devices is a multi-step process. The overall procedure differs according to the selected architecture (mirror selection). The general processing steps entail: 1) substrate preparation, 2) anode evaporation, 3) organic thin film deposition and 4) cathode thermal evaporation.

4.5.1 ITO etching procedure for DBR-based microcavities.

Fused quartz polished plate substrates were purchased from the company UQG Ltd. [104] with dimensions: 20mm x 15mm x 0.7mm. Then the quartz substrates were sent to Bte Bedampfungstechnique GmbH, for deposition of the DBR mirror and the ITO electrode by magnetron sputtering. The Distributed-Bragg-Reflectors were made by sputtering alternative layers of SiO_2 and TiO_2, having low and high refractive indexes, respectively.

The thickness of each layer was selected by optical simulations to create an appropriate stopband. Each layer had thickness based on the following relation: $T=\lambda/4n$, were λ is the refractive index of the centre of the stopband and n is the refractive index of the material.

ITO was deposited on top of the final and high refractive index TiO_2 layer of the DBR mirror having a thickness of 200 nm and a sheet resistance of 17 Ω/□. ITO substrates without the DBR

mirror and thickness of 200 nm had the same sheet resistance. Other substrates with 100 nm of ITO had a sheet resistance of>30 Ω/□. The ITO was then etched into pixels for subsequent device fabrication. This is described below:

A) ITO surface cleaning

The substrates were placed into an IPA bath were they were ultrasonic cleaned for 5 minutes. Pressurized Nitrogen gas was then used to dry the substrates.

B) Applying the photoresist cover.

Each sample was placed on the chuck of the spin processor. A layer of HMDS (hexamethylisilazane) adhesion promoter was spin coated onto the surface at 4000 rpm for 1 minute followed by heating to 100 ^{0}C for 1 minute on the hot plate to dry the surface. Next, a layer of the positive photoresist SPR350 was spin coated at 4000 rpm a process again followed by heating at 100^{0}C. All processes were made in yellow windows to avoid any exposure to UV light.

C) Exposure and development.

The samples were exposed to UV light for 1min 90s through a shadow mask and an optical aligner. The UV exposed substrate was then developed in de-ionized (DI) water:PLSI(for one minute) in a ratio of 3:1 to remove the unexposed areas. The patterned photoresist was again baked at 100 ^{0}C for 1 minute to remove any residual solvent.

D) Acid etching

The substrates were submerged in a hydrochloric acid (36% v/v) bath for 10-13 minutes to remove the ITO from the unexposed areas. A resist meter was used to check if the ITO had been removed. If not the sample was put back in the HCl solution for two minutes, and then re-tested.

E) Photoresist removal and cleaning

To remove the photoresist and to clean the samples the etched substrates were immersed in warm butyl acetate for two minutes. Then they were immersed for 1 minute in acetone followed by warm IPA for two minutes.

4.5.2 Wet cleaning process

All substrates were cleaned using the following four-step procedure: a) Removal of large contaminants, b) Hellmanex cleaning, c) deionized water cleaning, and d) isopropyl alcohol cleaning.

To remove large particles adhered to the surface, a tissue dipped in IPA was run across the surface. Next, the substrates were sonicated for 10 minutes in a Petri dish containing an alkaline aqueous solution (1% v/v) of Hellmanex detergent in de-ionized water. After DI water and IPA cleaning the substrates were N_2 gun dried.

4.5.3 Oxygen plasma cleaning process

To remove residual molecules adsorbed on the surface of the substrates, the samples were cleaned using an oxygen-plasma process. The substrates were placed on a glass holder, maximum 10 at a time and inserted in a vacuum chamber. Here an oxygen gas was used to produce oxygen plasma. Impurities and contaminants were subsequently removed from the surface. The total application time was 10 minutes.

This treatment was also used in order to modify the surface of the ITO layer. By this treatment the energy level of the ITO is slightly shifted (from 4.2 eV to 4.7 eV) assisting the injection of holes to the adjacent material [105, 106].

4.6 Device fabrication

In this section the two strongly-coupled OLED architectures are presented and discussed. The fabrication process for the OLEDs is identical to that used to fabricate strongly-coupled OLEDs. However, weakly coupled devices usually do not include a bottom mirror for light confinement. The fabrication of the devices can be split into four main processes: 1) anode deposition, 2) organic thin film deposition, 3) cathode evaporation and 4) encapsulation. The metal anode deposition on top of the ITO layer is considered only for the metal-metal microcavity devices.

4.6.1 DBR-metal based organic polariton LEDs

A standard set of procedures were used to deposit a multi-layer material stack. This section describes the fabrication of DBR-metal based organic microcavity LEDs. Device structure 1 is shown in Figures 4-6 and 4-7. The structure is composed of a DBR mirror and an ITO layer that was sputtered onto quartz crystal as described in previous section.

Three ITO anodic legs are protruding out from each side of the substrate. One long ITO stripe that is spatially distanced from the three ITO anodes is formed to create the electrical connection between the deposited metal cathode and a test fixture.

A film of self-assembled TDBC J-aggregates was used on the active medium in the strongly-coupled OLED. The device contains the following organic layers: A) PEDOT:PSS, B) TFB, C) J-aggregates, and D) BCP.

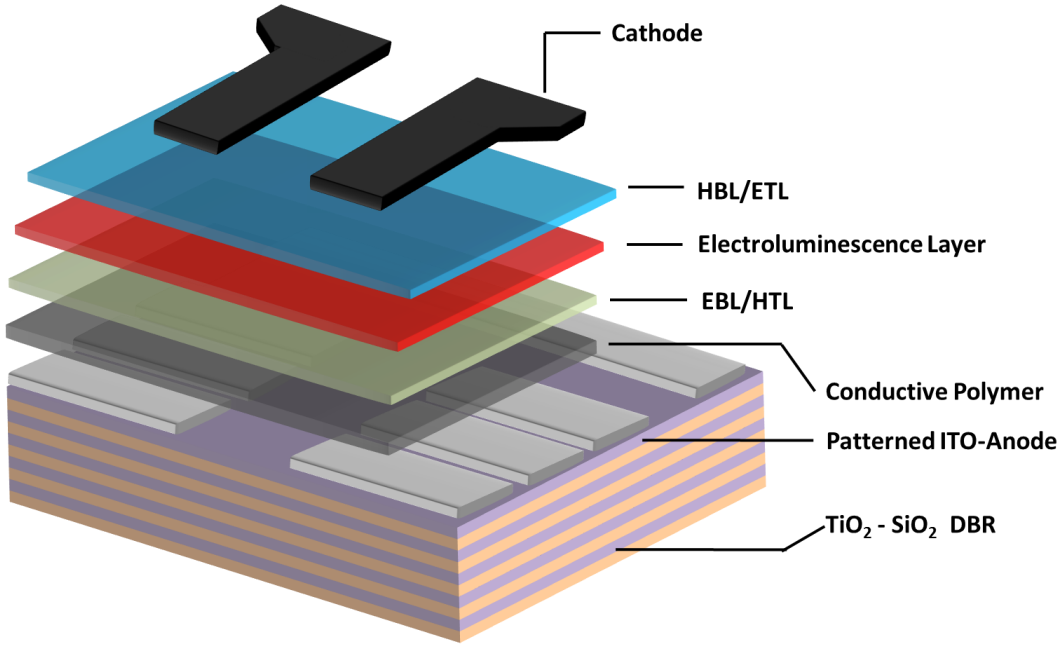

Figure 4-6 – Graphical representation of the multi-layer device structure 1 of a strongly-coupled organic light emitting diode.

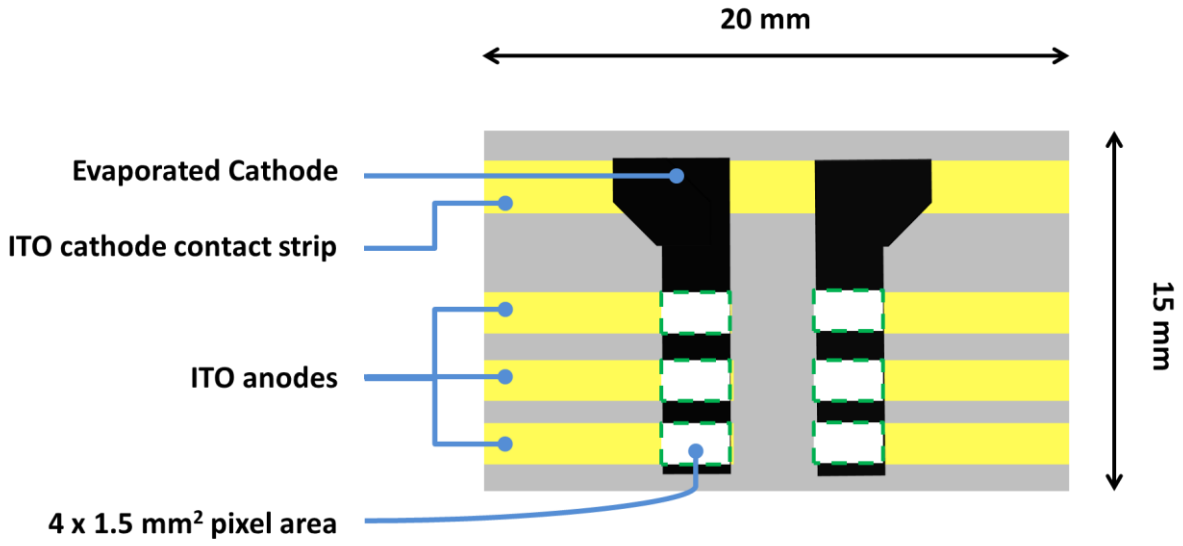

Figure 4-7 – Graphical representation of the strongly-coupled OLED structure 1 depicting the active area of the bottom emitting pixel defined as the overlap between the ITO fingers and the metallic cathode.

PEDOT:PSS

A hole injection and transport polymer was utilized to extract holes from the ITO. Poly-(3,4-ethylenedioxythiophene) polystyrene sulfonate, commonly known as PEDOT:PSS is a two-component composite polymer. The first component, poly-(3,4-ethylenedioxythiophene), known as PEDOT, is a polythiophene derivative. This component is responsible for transporting holes. The second component, the polystyrene sulfonic acid electrolyte (PSS) is a polystyrene derivative that is functionalised with sulfonate groups.

$PEDOT^+$ cations are mixed stoichiometrically and bonded with anionic PSS^- [107]. The morphology of the PEDOT:PSS dispersion is dependent on its concentration a property that affects its thin film electronic properties [108, 109].

The material used was purchased as an aqueous solution from either H. C. Stark or Ossila. The solution has a distinct dark-blue colour and was dissolved in H_2O in the form of nanoparticle dispersion. A syringe mounted with a 0.45 µm x 13 mm PVDF filter was used to transfer the solution onto the substrate. A film was then cast using a spin coater at 5000 rpm. The resulting Dektak measured thickness was approximately 30 nm.

A cotton bud wetted with DI water was used to strip off PEDOT:PSS from the cathode connection region. Any unremoved material that remained attached to the surface, could result in current leakage. The samples were then transferred to a warm plate where they were baked at 130 ^{0}C for approximately 15 minutes to remove any traces of trapped moisture. Due to its hygroscopic nature, the samples were stored in nitrogen-filled glovebox prior to deposition.

PEDOT:PSS plays a significant role in the operation of the device. Firstly, the polymer is used to smooth out any roughness introduced from the underlying ITO layer. Spikes on the ITO layer result in the formation of local shorts in the OLED. These in turn result in local non-emissive parts of the pixel (black spots) or complete pixel failure. The PEDOT:PSS act as a buffer layer to reduce the effect of such spikes.

Secondly, PEDOT:PSS prevents chemical interaction between the ITO and the semiconductor. The direct contact of the ITO with the organic semiconductor will result in the chemical interaction of the two when are in contact [110].

Thirdly, the PEDOT:PSS acts as a hole injecting layer as its work function is approximately 5.2 eV [111]. This increased value of the work function facilitates more efficient hole injection into materials having high ionization potential.

Poly[(9,9 –dioctylfluorenyl -2,7 diyl))-co-(4,4'-(N-diphenylamine)]-butylphenyl))

The polymer Poly[(9,9 –dioctylfluorenyl -2,7 diyl))-co-(4,4'-(N-diphenylamine)]-butylphenyl)), commonly known as TFB, is a hole transport and electron blocking material. It has a characteristic HOMO and LUMO energy levels of 5.3 eV and 2.3 eV, respectively. The polymer was provided by Cambridge Display Technology and was dissolved in common organic solvents such as toluene and chlorobenzene. A solution of 10 mg/ml in toluene creates a 50 nm thin film when spin coated at 3000 rpm spin speed.

The material that covered the area of the cathode connection was again removed by using a cotton bud that was previously immersed in toluene. Next, the substrates were placed on a warm plate were thermally annealed at 180 ^{0}C for one hour. The material was chemically designed to undergo thermally induced cross-linking. The cross-linked TFB is insoluble to organic solvents such as toluene.

5,5',6,6'-tetrachloro-1,1'- diethyl-3, 3'-di(4-sulfobutyl)-benzimidazolocarbocyanine salt (TDBC)

J-aggregates of the cyanine dye TDBC was used as an electroluminescent material. TDBC was dissolved in water at a concentration of 10 mg/ml. Spin coated thin films have a thickness of approximately 30 nm in devices. The substrates were placed on a warm plate at 70 ^{0}C for 5 minute to remove any trapped water remained within the film. Cyclic voltammetry was used to determine the HOMO (3.25 eV) and LUMO (5.03 eV) levels for TDBC with the help of Dr. Hunan Yi, of the Chemistry department of the University of Sheffield.

Bathocuproine

Bathocuproine, commonly known as BCP, is an organic semiconductor that transports electrons. The material has a LUMO energy level of 3.2 eV and a HOMO level at 6.4 eV, which is a very effective hole blocking material.

Thermal evaporation was used to deposit thin films of BCP. Films of 50 nm were used to confine holes and to limit the charge losses to the cathode electrode.

Cathode thermal evaporation

The material selected as the electron-injecting was decided by the wavelength at which the device was designed to operate. Generally, for UV and blue opacity devices, aluminium was used, whereas for visible and NIR devices silver was preferred. To facilitate more efficient electron injection, calcium is used on top of the EIL/HBL as a low work function metal, prior to coating with silver or aluminium.

Ca/(Ag or Al) cathode were deposited by thermal evaporation forming a film of 105 nm in total. This created 6 addressable LEDs.

Calcium (Ca)

Metallic calcium was used as an electron injection layer between silver (or aluminium) and the organic semiconductor. Calcium has a work function of 2.89 eV [112] making it suitable for injecting electrons to the LUMO energy level of many organic semiconductors. The evaporation rate was kept constant at 0.3 Å/s. In most devices an ultra-thin Ca film was used (5 nm) to inject electrons.

Calcium reacts strongly with oxygen and water creating various forms of calcium oxides or hydroxides that have insulating properties. Moisture permeation can severely affect the lifetime of the device as it penetrates into and reacts with the calcium layer [113]. Devices that were kept in N_2 environment for more than 6 months were remaining functional. All the devices made in this study used Calcium in combination with silver or aluminium.

Silver (Ag)

Silver was used as a cathode contact material for the OLEDs; it was also used as a mirror in optical metal-based microcavities. Silver was thermally evaporated on top of Ca and acted both as a metallic mirror and as an electrode contact.

Silver has a work function of 4.26-4.7 eV [112] and is highly reflective, making it suitable for device applications. The source material comes in form of beads. An Al_2O_3 crucible was used as a heating element for thermal evaporation. The evaporation rate ranged from 0.3 Å/s to the highest 1 Å/s which was reached after 10 nm of operation.

4.6.2 Device encapsulation

The final step of the device fabrication is the process of encapsulation. A small drop of a light-curable epoxy was then dropped onto the middle of the device using a glass pipette. A glass slide was then placed on the top by the help of tweezers, touching the side edge first. By applying a small amount of pressure the epoxy was evenly distributed in the space between the glass slide and the evaporated cathode.

Encapsulation is significant for the improvement of lifetime and reliability of organic light-emitting devices [114]. Most of the research done so far has been focused on their barrier performance as a need to retain low level permeation of water and oxygen inside the device. Other aspects include the thermal stability and glass transition temperatures of the active layers. This limits the processing temperatures at which the encapsulation layers can be deposited.

4.6.3 Metal-metal based organic polariton LEDs

Microcavity OLEDs were also fabricated based on metallic mirrors that also act as anode and cathode electrodes. The quality factor of the cavity is lower; however polariton devices can be fabricated and tested.

The device is based on ITO legs designed to create the electrical connection between the deposited metal cathode and a test fixture. One large ITO stripe is used as a basis to the active area of the device. This structure is shown in Figures 4-7 and 4-8.

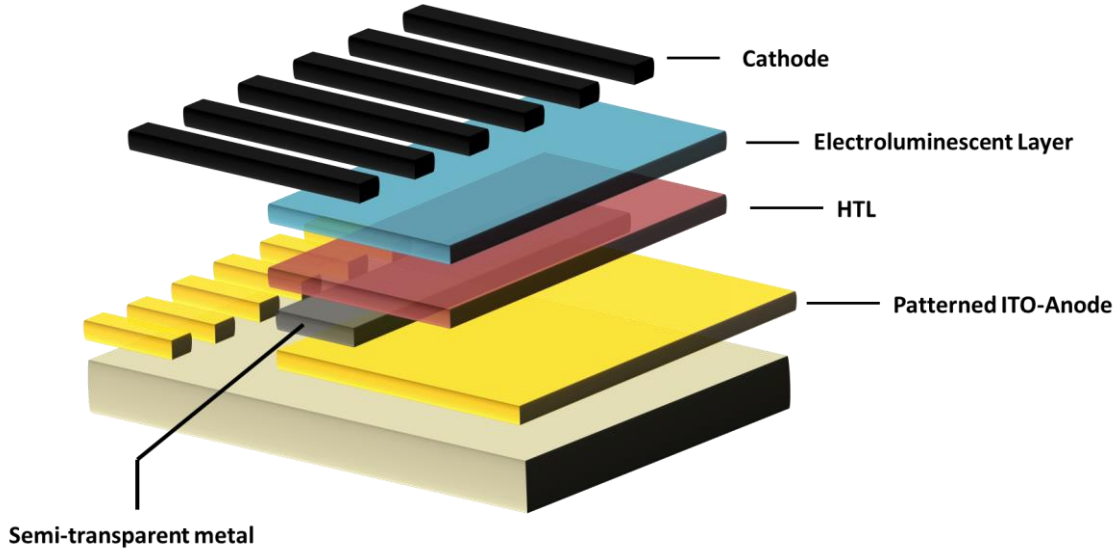

Figure 4-8 – Graphical representation of the multi-layer device structure 2 of a strongly-coupled organic light emitting diode.

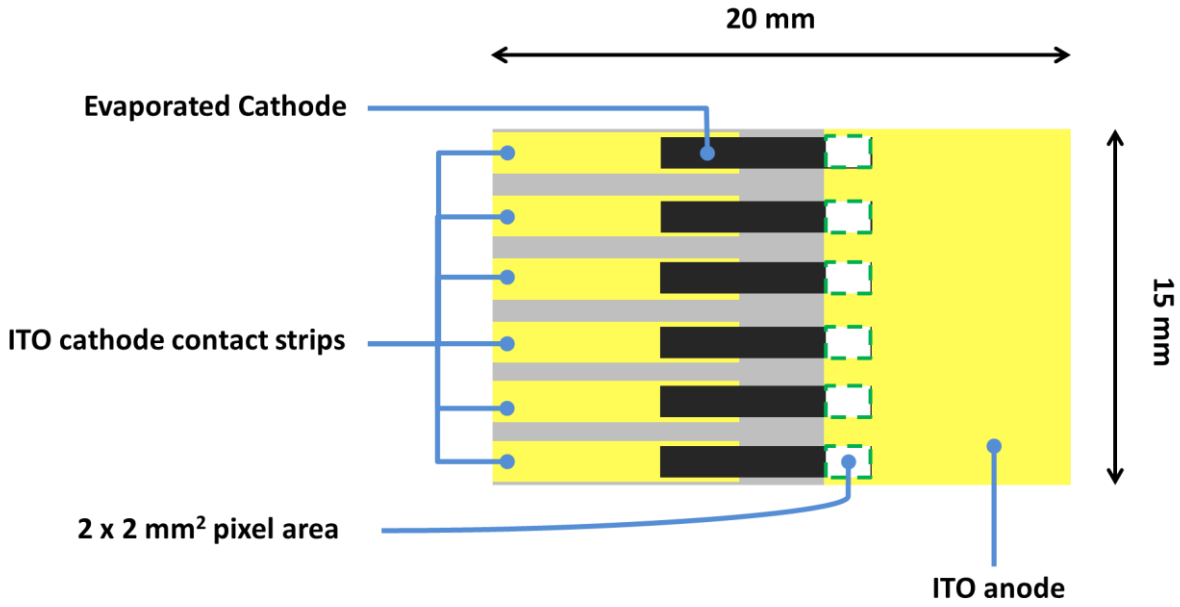

Figure 4-9 – Graphical representation of the strongly-coupled OLED structure 2 depicting the active area of the bottom emitting pixel defined as the overlap between the ITO fingers and the metallic cathode.

In the next section, the device fabrication steps are described; these include: A) aluminium deposition, B) MoO3 thermal evaporation, C) PAni spacer layer thin film deposition, D) electroluminescent layer deposition, E) cathode deposition, and F) encapsulation. Parts C(PEDOT:PSS), E) and F) will not be described as they were already discussed in previous section.

Anode deposition

On top of the ITO layer, a metallic stripe of aluminium was thermally evaporated. This semi-transparent contact allows light to pass through the layer. The experiments performed in this study indicate that 30 nm is approximately the upper limit for which the devices remained electrical functional as at higher thicknesses short circuits led to current leakage.

Despite that aluminium has a lower work function than that of silver, it was favoured in devices where the fluorescent material had absorption peaks in the UV or blue region of the spectrum.

Aluminium (Al)

Aluminium has high reflectivity that extends to the near-UV region of the spectrum. This makes aluminium suitable for UV optoelectronic applications. The reported work function is 4.28 eV [112] and thus it can be used both as anode and cathode contact. To improve its work function it must be covered by a thin layer of MoO_3.

Thermal evaporation of molybdenum oxide (MoO_3)

MoO_3 was used as a hole transporting (HTL), and was deposited onto ITO/metal and ITO anode contacts. The energy level for hole injection is 5.2-6.9 eV. MoO_3 is a n-type metal oxide with its Fermi level close to the conduction band. When used in conjunction when an organic semiconductor hole injection is achieved by electron extraction from the HOMO-level of the organic semiconductor [115]. The energy level alignment between MoO_3 and other organic semiconductors can be found in recent publications [116].

MoO_3 comes in the form small (4-6mm), high purity, chunks (Lesker). An Al_2O_3-based crucible was used to hold 2-3 pieces of MoO_x and act as a heating element. Evaporated MoO_3 was at a rate of 0.3 Å/s, with a shadow mask being used to pattern the MoO_3 onto the ITO or metal contact.

Thermal evaporation of the MoO_3 semiconductor results in a reduction of oxygen with the material having a MoO_{3-x} stoichiometric form. x denotes the fraction of oxygen found in the deposited layer.

Studies have shown that in metal-oxides, oxygen can be controlled by the process of sputtering, where Mo and O_2 are stoichiometrically mixed. There is a transition from semiconducting (3-x~3) to metallic behaviour($x \approx 3$) when the oxygen concentration is gradually reduced [117, 118].

MoO_3 has a significant role in the engineering of the device structure. Firstly, it is used as a hole injection thin film. The reported work function for the MoO_3 layer on top of ITO was 5.2 eV [119], which is close to the HOMO energy level of most fluorescent organic semiconductors that were considered in this study.

Secondly, the material can be used to smooth out any roughness caused from the underneath metallic layer. Thirdly, a PEDOT:PSS and PAni spacer layers can be easily spincoated on top of MoO_3 taking advantage of its hydrophilic nature; thermal evaporation of the metal-oxide followed the Al deposition without breaking the high-vacuum conditions between successive evaporations.

Polyaniline (PAni)

Polyaniline was used as a spacer layer between MoO_3 and the electroluminescent thin film. PAni is a hole transport polymer, similar in function to PEDOT:PSS but with distinct absorption features. The HOMO and LUMO energy level position are energetically located at 4.6 eV and 3 eV, respectively [120].

The material was purchased dissolved in NMP from ORMECON. For λ-cavity structures, a thick film of approximately 90 nm is required.

A thick film of PAni was intentionally selected to smooth out any imperfections in the form of spikes that were unintentionally introduced during metal thermal evaporation. The substrates were placed on a hot plate were heated at 80 ^{0}C for 5 minutes to remove any residual water. Any material remained on the cathode surface area was removed by the use of a cotton bud which was previously wetted in water.

4.6.4 Electroluminescent layer

Two different thin film concepts were examined; pure films and host:guest blended systems. The organic material used for strong coupling studies in this device structure was the ladder-type polymer meLPPP which was introduced in a previous section.

4.7 Optical characterization

In the following sections the techniques that were used to detect polariton energy states in organic-based microcavities, are explored. The techniques are based on populating the strongly-coupled states using various methods. These methods include: angle-resolved reflectivity or transmission spectroscopy, electroluminescence (EL) and photoluminescence (PL) angle-resolved spectroscopy.

Before the techniques are explained a description of the optical spectroscopy measurements will be given. The measurements were performed to record the absorption and emission spectra of the organic semiconductors in thin films and solutions.

4.7.1 Absorption and emission spectroscopy of thin films and solutions

Two setups were used to record the optical properties of organic semiconductors and devices. Firstly, an optical-based setup was used for light absorption and emission studies, as shown schematically in Figure 4-8.

The system uses an excitation rail (OR1) that can support various optical elements. O1 denotes the optical fibre that directs white light emitted from a tungsten lamp to a pinhole element (L1), of either 50 μm or 100 μm diameter. The light is then collected by a lens (L2) that collimates the beam. The beam then passes through a lens (L3) that focuses it into a spot of the order of a few hundreds of μm in diameter, as the small spot size assures that the absorption measurement will reduce the effect of thickness variations.

The middle sample holder spatially rotates on an axis through the sample position. When the sample is placed in the sample holder the substrate is positioned perpendicular to the impinging light.

A second optical rail is used to support a series of lenses and collection optics. The reflected by the sample light passes through a (L4) lens that again collimates the incident light. A collection lens (L6) focuses light onto a second optical fibre (O2). A polarizer (L5) was adjusted to selectively permit the TE light polarization. Then the light passes through the fibre (O2) that is coupled to an Andor Shamrock 303i imaging spectrometer, equipped with air cooled charge-coupled device camera (CCD).

For absorption measurements the probe passes through the sample. In emission measurements, laser light is focused on the sample at some incident angle to generate emission. Two laser light sources were used. A 405 nm GaN CW laser of 5 mW power and a 473 nm blue CW laser of 200 mW power. A filter was used to reduce the high power of the laser beam as such high power would be destructive for the organic materials.

For emission measurements a long-pass filter was used to prevent from scattered laser light entering the spectrometer. Care was taken for not to direct the laser light beam into the optical fibre as this could severely affect the CCD camera.

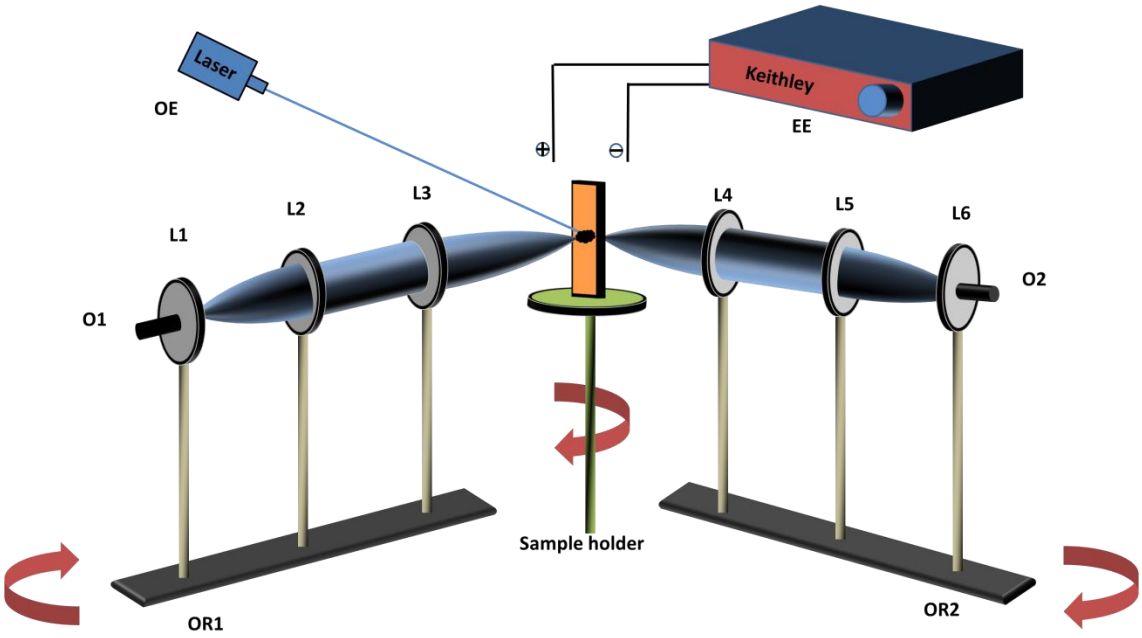

Figure 4-10 - Absorption and emission spectroscopy measurements of organic semiconductors in thin films and solutions.

Secondly, absorption and emission measurements of organic semiconductors in thin films or dissolved in solutions were also made using a Fluoromax-4 Spectrofluorometer (HORIBA JOBIN YVON).

In both cases, the recorded absorption spectra were used to simulate the refractive index (n) and the absorption coefficient (k) values of the organic materials. These are required as input parameters for transfer matrix simulations.

4.8 Electrical characterization

The light-emitting diodes fabricated were characterized electrically. The method includes: a standard test fixture to establish electrical connection, a Keithley source measure unit to record the current-voltage characteristics and a luminance meter to quantify the light emitted from the OLED device.

4.8.1 Test-fixture

Figure 4-11 depicts an image of the standard test fixture that was used to mechanically support and electrically connects the DC source and the OLED device. All measurements were made in dark to avoid any ambient light affecting the measurements.

To establish connection with the OLED a test fixture was assembled. It is compromised by the design of the ITO pattern. The required components include two ZIF sockets, a Veroboard and electrical connection legs. The Veroboard is a pre-formed circuit board of copper strips on an insulating board. Two ZIF (Zero Insertion Force) sockets were used positioned on the Veroboard at a distance dictated by the length dimension of the OLED substrate.

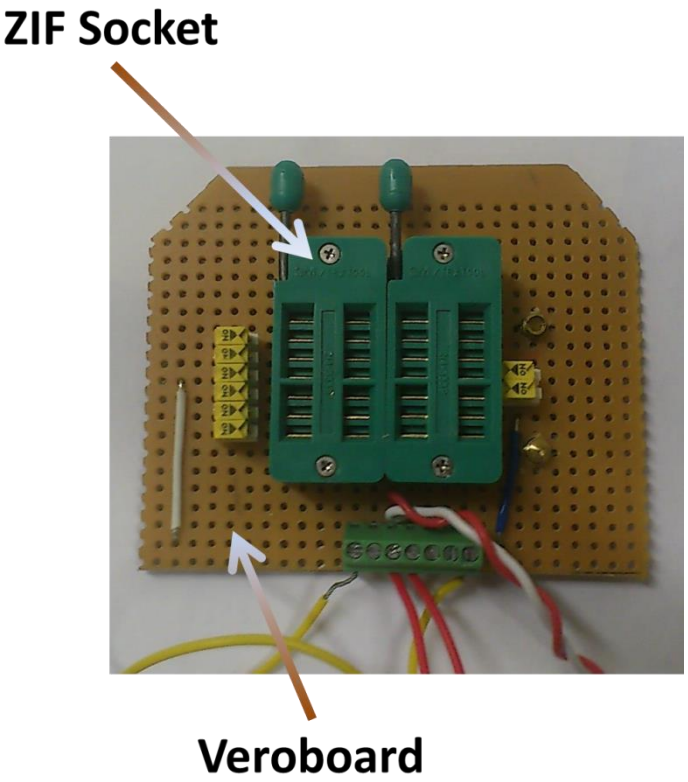

Figure 4-11 – Image of a custom made test fixture based on (a): DBR-metal architecture design explained in section.

Electrical connection between the OLED device and the circuit electronics was established by the use of electrical connection legs. The legs were designed for use with 0.7 mm or 1.1 mm thick glass making an electrical attachment to the ITO layer of the device.

The combined current-voltage-luminance characteristics were recorded by a computer automated Labview program through a GPIB interface.

4.9 OLED and polariton OLED efficiency comparison technique

To gain a deeper understanding of the physics that govern the strongly and weakly-coupled devices their relative efficiency was measured and compared. A liquid light guide (NA=0.59) was placed onto the active pixel. The EL emitted was integrated over wavelength and angle into a forward, solid angle cone of 36^0 using an Andor CCD spectrometer. JVL characteristics were also recorded using either a photomultiplier tube or a Luminance meter. The last two measurement setups used are described in the next two subsections.

For degradation measurements of OLEDs (Chapter 7) EL recordings were collected within 5 minutes of operation by mounting an optical fiber at a working distance of approximately 10 cm above the active area of the pixel.

4.9.1 Photomultiplier

Figure 4-10 shows a schematic representation of the assembly that was used to record the JVL characteristics. A disadvantage of using the TDBC dye as the active medium is its low quantum yield of ~ 1.1% [42]. Therefore, a photomultiplier (PMT) tube was used to record the EL emission signal. The same setup was used for both strongly-coupled and weakly-coupled J-aggregate OLEDs. Figure 4-11 depicts a J-aggregate based OLED emitting in the red spectral region. The emission is visible in the dark.

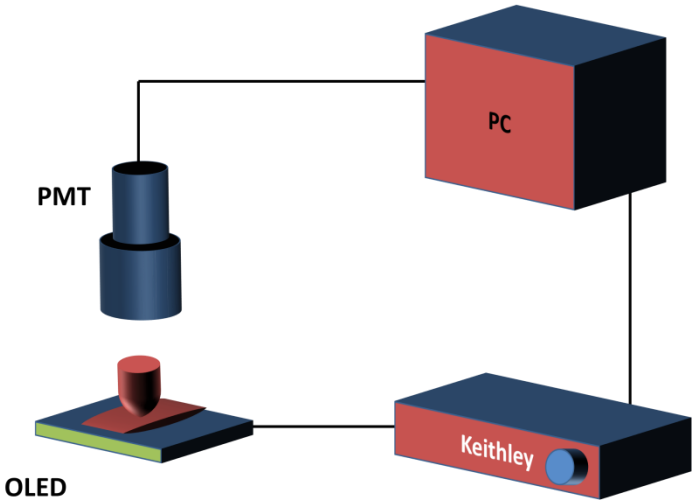

Figure 4-12 – A schematic representation of the apparatus used to perform Current-Voltage-Luminance characteristics of the OLEDs.

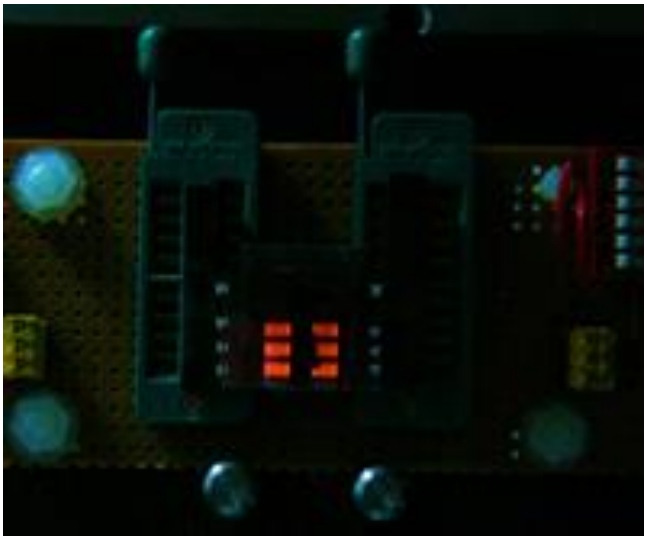

Figure 4-13 – A j-aggregate based OLED emitting Red light. The photo was taken in the dark due to the low quantum efficiency of the J-aggregate.

4.9.2 Luminance meter

The power efficiency of an OLED can be quantified as the ratio of the luminous power out, as detected by the human eye, to the electrical power in. The lumen (lm) unit is introduced to quantify the luminous power due to eye variations across the visible spectrum. The photopic curve [121] depicts the response of the human eye as seen in figure 4-12 [122]; however, the blue and red response is much weaker than the green response [39]. Characteristically, the eye has a maximum efficiency of 683 lm per incident optical Watt at λ=555 nm. Given an arbitrary spectrum ϕ(λ) of incident light, the responsivity Φ can be calculated by using the following equation:

$$\Phi = \frac{\int \varphi(\lambda) P(\lambda) d\lambda}{\int \varphi(\lambda) d\lambda} \tag{3.2}$$

where P(λ) is the photopic response.

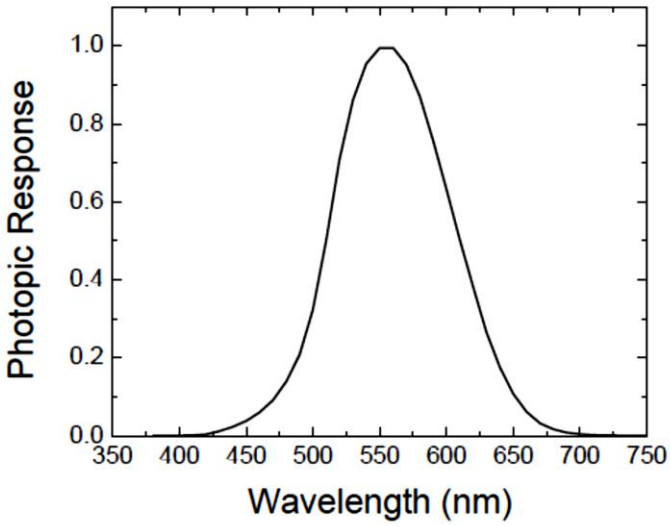

Figure 4-14 – Photopic response of the human eye.

The unit Candela (Cd) defines the related luminous intensity, which is the luminous flux per solid angle in steradians (1 cd=1 lm/sr). A Konica Minolta Luminance meter LS-100 was used to record the J-V-L characteristics of the devices. The same setup was used to measure the samples as depicted in Figure 4-10, with the only difference that the PMT was replaced by the Luminance meter.

4.10 Time resolved emission measurements.

Figure 4-13 illustrates a schematic representation of the setup that was used to record the temporal response of the OLEDs and the polariton OLEDs. 2 μs square pulses of amplitude 18 to 24 V and 10 KHz frequency were applied across the devices. Light, integrated over wavelength was collected by a 0.7 NA objective lens. Thereafter, it was focused onto the entrance slit of a Hamamatsu streak camera (C5680) having a resolution of 2 ps. The emission from the exciton reservoir and the UPB state was cut by the use of a 600 nm long pass filter.

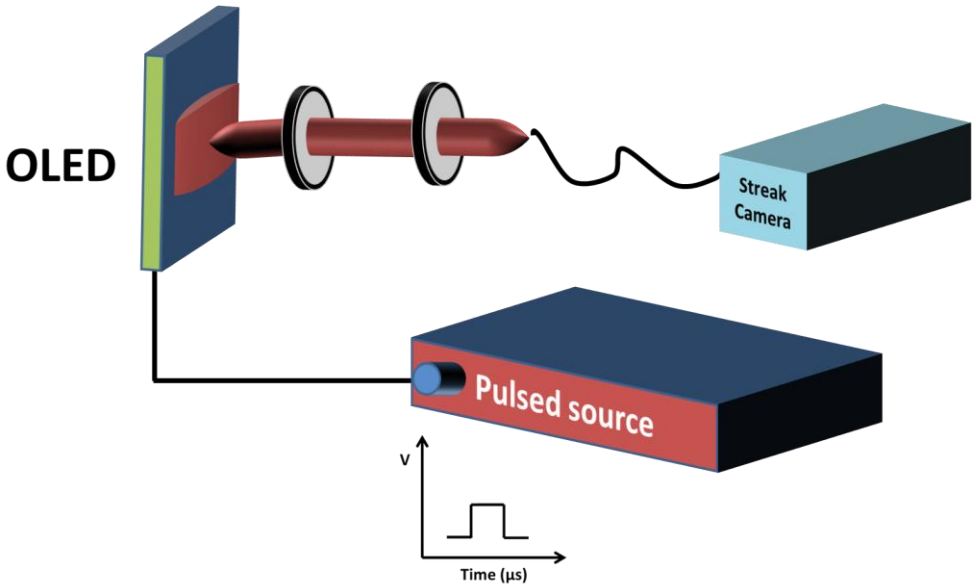

Figure 4-15 – A schematic representation of the setup used to record the temporal response of the devices.

4.11 Conclusions

In this chapter the various methods for the fabrication and characterization of organic light-emitting diodes in the strong and the weak coupling regimes were described. The strongly-coupled devices can be either DBR-metal or metal-metal bottom emitting OLEDs. Engineering such devices is a challenging task and a proper selection of both the strongly-coupled material as well as the compartment organic semiconductor has to be thoroughly examined. The techniques reviewed here were used to collect experimental data that are followed.

Chapter 5

Polariton electroluminescence based on J-aggregates of self-assembled cyanine dyes.

In this chapter thin films of J-aggregates of TDBC cyanine dye molecules have been under investigation for application in strongly-coupled electroluminescent systems. A structure employing a microcavity configuration with a DBR and a metallic mirror placed either side of and a thin film of J-aggregates as the active organic layer is primarily used in calculations in order to determine the potential of the system to reach the strong-coupling regime. Experimentally, two sets of devices were fabricated; namely, conventional OLEDs and microcavity OLEDs. For MCOLEDs reflectivity, PL and EL angular dependent spectroscopy were used to characterize the samples in order to explore the polariton population density as a function of angle. Experimental and theoretical efficiency calculations are then compared in order to elucidate the processes that affect the population of polariton states in both electrical and optical devices. This chapter concludes that for the realization of efficient organic polariton LEDs, materials with higher quantum yields and with higher mobilities that can sustain higher injection densities are required.

5.1 Introduction

One interesting aspect of cyanine dyes is their ability to self-assemble in polar environments such as water [123]. These molecules share the common functionality that the relative orientation of the dipole moments upon aggregation defines their red-shift and the narrowing of their absorption and emission spectra compared to that of the monomer.

Depending on the deposition technique, the aggregated species can be extended over a large area or over a small area. The former is met when aggregation is induced by the layer-by-layer (LBL) technique [95], whereas the second is usually produced by spin casting [32]. The layer-by-layer deposition technique is based on sequential immersion of a substrate into solutions containing oppositely charged materials. In between immersions a washing step is required to remove any residual material that is not electrostatically attracted. This results in the formation of oppositely charged monolayers. In the case of J-aggregates the aggregation covers a large region, whereas the aggregation that is induced by techniques such as spin casting over few monomeric units.

In this study a thin film of J-aggregates is placed between a hole transporting semiconductor (TFB) and an electron transporting semiconductor (BCP). The charge transport materials possess energy levels that are suitable for confining electrons and holes within the J-aggregated layer. Hence, excitons that are generated interact with the confined photon field of the cavity allowing the combined system to reach the strong coupling regime.

This chapter is separated into four parts. In the first section, a basic calculation is performed in order to determine the thickness of the organic layers that are required in order to construct a negatively-detuned microcavity OLED. Next, the fabrication of the microcavity OLED is briefly discussed along with the material thicknesses and the energy levels of all the organic materials in the device. Moreover, reflectivity, PL and EL measurements are presented with polariton populations being extracted from theory and experiment. In the last section, basic JVL characteristics and time-resolved measurements are presented for coupled and uncoupled OLEDs. The later measurements are important in order to understand whether the emission dynamics is affected by strong light and matter interaction or not.

5.2 Reflectivity transfer-matrix calculations

The process of fabrication of a microcavity OLED commences by making calculations based on the optical properties of the entire system. Such calculations are important as they can indicate the conditions needed to achieve strong-coupling by adjusting the thickness of the organic semiconductors within the cavity.

Figure 5.1 shows the absorption spectrum of the TDBC monomers and their J-aggregation taken from a spin coated thin film of the TDBC dye blended with Polyvinyl alcohol in a H_2O-based solution. PVA was diluted in water at a concentration of 30 mg/ml. It was subsequently blended with 3 mg of the dye per ml of the PVA/H_2O solution. Only the central feature of the J-

aggregated state is observed indicating that the monomers have self-assembled in the polyvinyl alcohol transparent matrix. The main absorption transition of the monomer is at 2.39 eV with a shoulder located at 2.55 eV. The J-aggregate absorption transition peaks at 2.11 eV.

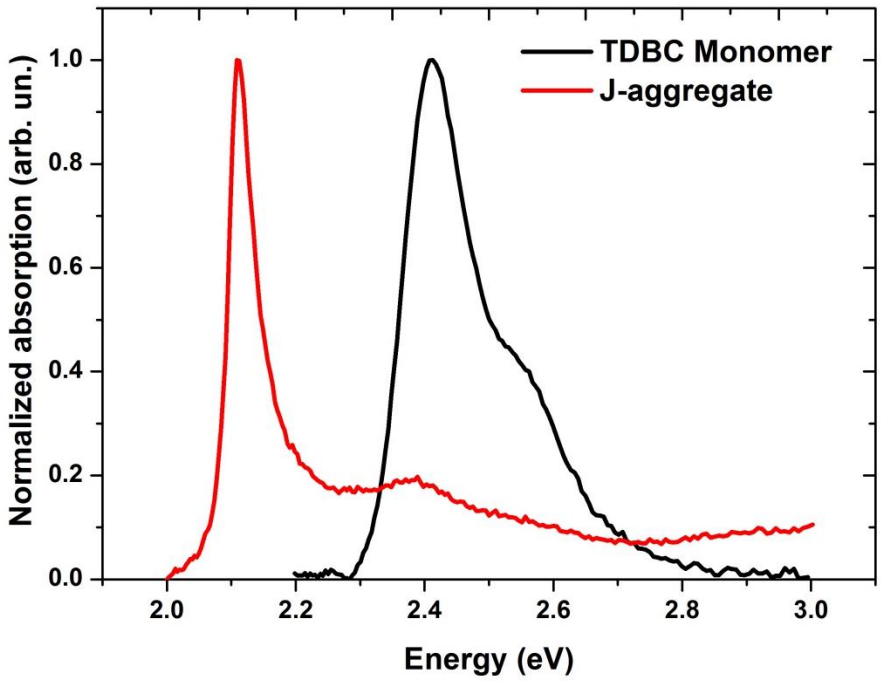

Figure 5-1 – Normalized absorption spectrum of the TDBC dye dispersed in polyvinyl alcohol.

Reflectivity transfer-matrix calculations were performed based on the following structure: Glass/DBR(5 pairs of SiO_2/TiO_2)/ ITO (200nm)/ PEDOT:PSS (30nm)/ TFB (50nm)/ J-aggregates (10nm)/ BCP(40nm)/ Ca(5nm)/ Ag(100nm). It should be mentioned at this point that the incorporation of a DBR-based mirror in the structure was selected in order to achieve a high Q-factor cavity.

Previous studies of polariton electroluminescence utilising j-aggregates of the TDBC molecules with two metallic mirrors, reported quality factors of about 10 [124]. Other studies that used different organic semiconductors as the strongly-coupled medium, such as meso-TPP achieved quality factors of Q~28 [47, 96]. Since DBR mirrors increase the quality factor of the cavity, and high Q factors are required to achieve increased polariton lifetime it is more advantageous to fabricate devices incorporating DBR mirrors in the structure.

The development of a negatively-detuned optical microcavity is ideal for the study of the scattering mechanisms of excitons toward the lower polariton branch via interaction with vibrational modes by which polariton states are being populated [46]. Therefore, the study of the properties of lower branch cavity polaritons at negative de-tunings will potentially lead to an understanding of the factors that determine the establishment of a macroscopic population at the bottom of the LPB.

Figure 5-2 shows the calculated reflectivity spectra for a typical structure using transfer matrix simulations [39]. The calculated n,k values were extracted and seen in Appendix A. The calculations were performed for a range of angles between 0^0 and 60^0 with a step size of 5^0.

Two dips are clearly visible within the DBR stop band; the first is at lower energy and the second at higher energy, respectively. The two dips undergo a shift to higher energies as the external viewing angle is increased with a simultaneous change of their relative positions. The blue curves in the plot are used to highlight this spectral shift. The red vertical line reflects the energetic position of the exciton transition which is located at 2.11 eV.

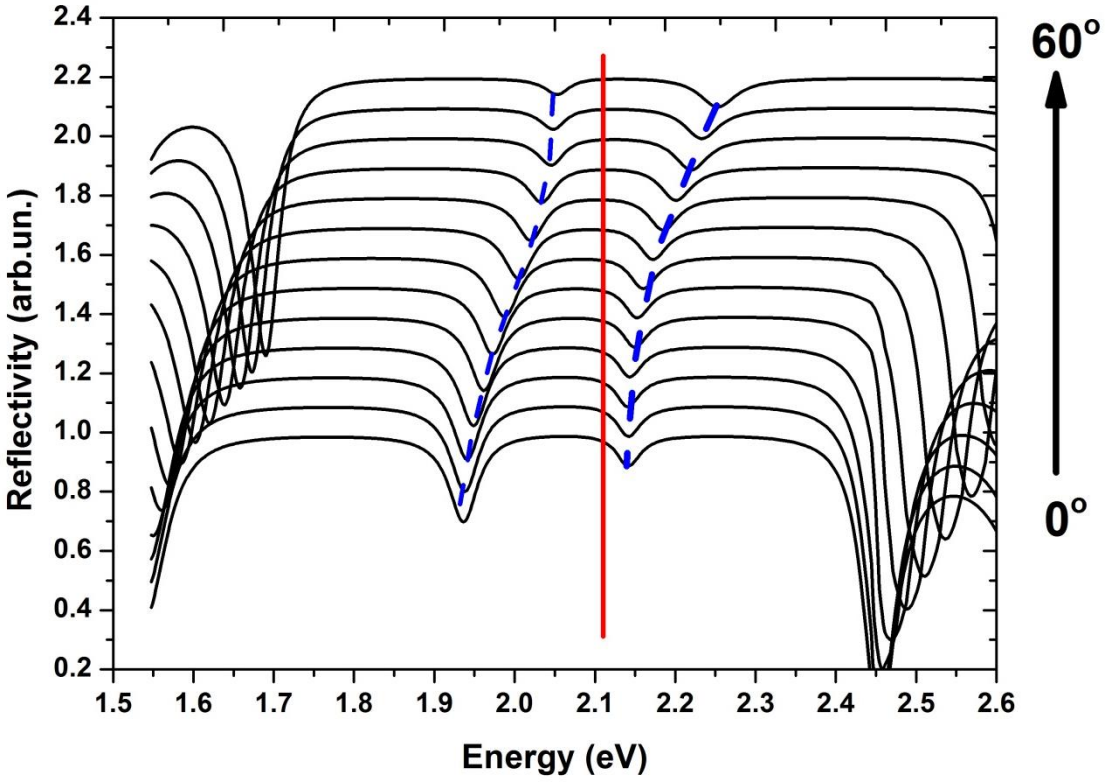

Figure 5-2 – Reflectivity matrix calculations for strongly-coupled organic microcavity system.

The energetic positions of the dips in figure 5-2 are plotted against the external viewing angle θ as is shown in figure 5-3 in the so-called dispersion diagram. The calculated LPB and UPB branches are marked in the figure and can be seen to anti-cross to an angle of $\theta_{Res}= 40^0$ which corresponds to the crossing point between the bare exciton (black dash line) and the bare photon (blue curve) modes.

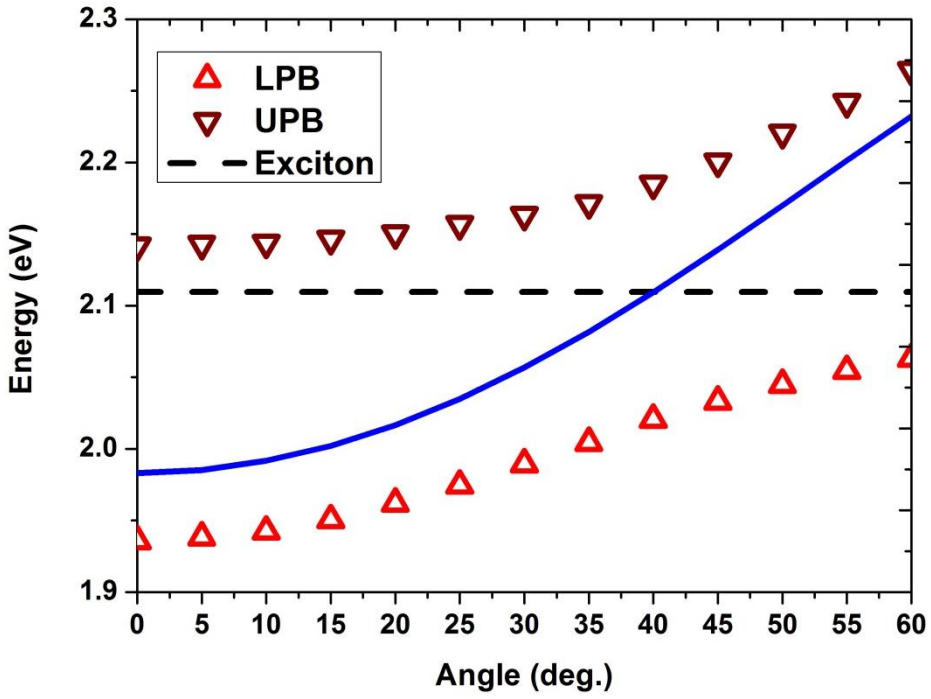

Figure 5-3 – Dispersion diagram showing the calculated reflectivity dips corresponding to the LPB (red upper case triangles), the UPB (brown lower case triangle), the exciton (dashed black line) and the photon (blue line) mode.

5.3 Cavity fabrication

The fabrication of the microcavity OLED was detailed in Chapter 4. Figure 5-4 (a) briefly summarizes the microcavity design and figure 5-4 (b) the associated HOMO and LUMO energy levels of each of the organic materials used through which the positive and the negative charge carriers travel in order to meet, undergo coulombic capture and then recombine. The work functions of the electrodes are also shown in the same figure.

The charge carriers travel through the various organic layers under the influence of the electric field. Particularly, holes are injected from the ITO anode to the PEDOT:PSS layer. Subsequently, holes travel through the TFB layer until they reach the TFB/TDBC interface. They eventually enter the J-aggregated organic thin film where they remain confined.

Electrons are injected from the Ca/Ag cathode into the electron transport semiconductor BCP. The electrons then drift into the TDBC-based film as a result of the applied field where they are coulombically attracted by the holes that coexist within the same layer. The energy levels of BCP and TFB are suitable for confining holes and electrons, respectively, to the J-aggregated layer. Light emission follows the formation of excitons in the emissive layer.

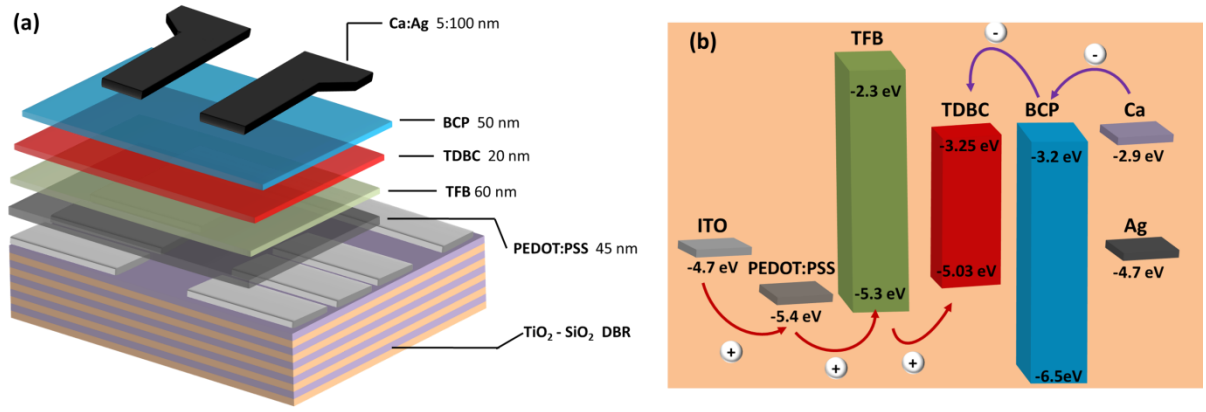

Figure 5-4 – (a) Microcavity OLED structure, (b) Energy level diagram showing the charge carriers travelling through the HOMO and LUMO energy level of the organic layers after electrode injection.

5.4 Results and discussion

5.4.1 Reflectivity measurements

Reflectivity and transmission measurements use white light by means of populating the energy levels of the system without considering any relaxation dynamics. Upon exciting the system with a white light source, the incident light is stored in the resonator as the cavity mode. The microcavity is angularly tuned towards higher angles; therefore, changes in the absorption can be easily detected and analysed, as seen characteristically from figure 5-5. In transmission measurements a peak appears in the spectrum, whereas in reflectivity measurements a characteristic dip appears in the recording spectrum.

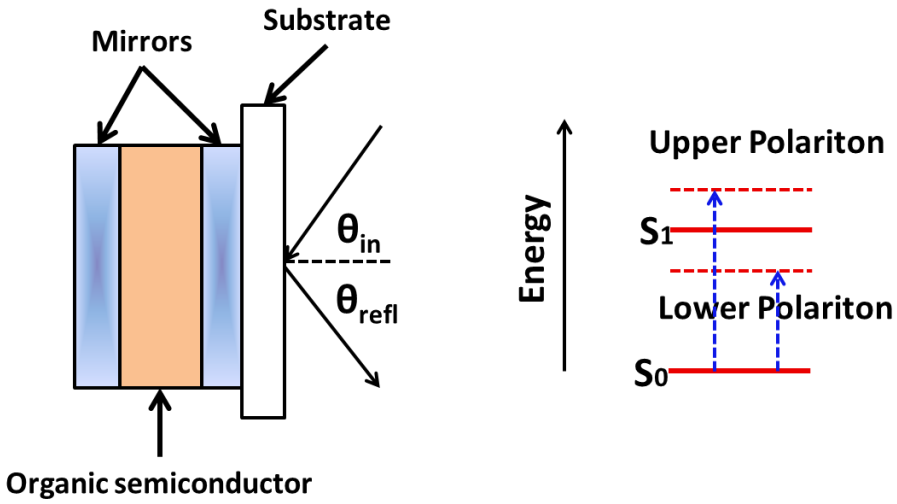

Figure 5-5 – (Left side): A simplified representation of the organic microcavity structure used for reflectivity or transmission measurements. (Right side): Modified energy level diagram taking into account the newly formed polariton states.

Figure 5-6 reveals the reflectivity spectra that were recorded from a strongly-coupled microcavity OLED at a range of angles between 7.5^0 and 50^0. As is seen from the figure there are two dips in the spectra that shift their energetic positions as the angle of observation increases. The vertical red line corresponds to the exciton resonance. The dips do not cross the exciton transition but instead "repel" each other. This suggests that the strong-coupling regime is reached. Again, the location of the dips is highlighted by two blue curves. There are also dips appearing at low energies and high angles, as well as at higher energies. These correspond to dips due to the DBR mirror. To confirm the establishment of the strong-coupling regime, the data are fitted to a 2-level coupled harmonic oscillator model as is shown in the dispersion graph of Figure 5-7.

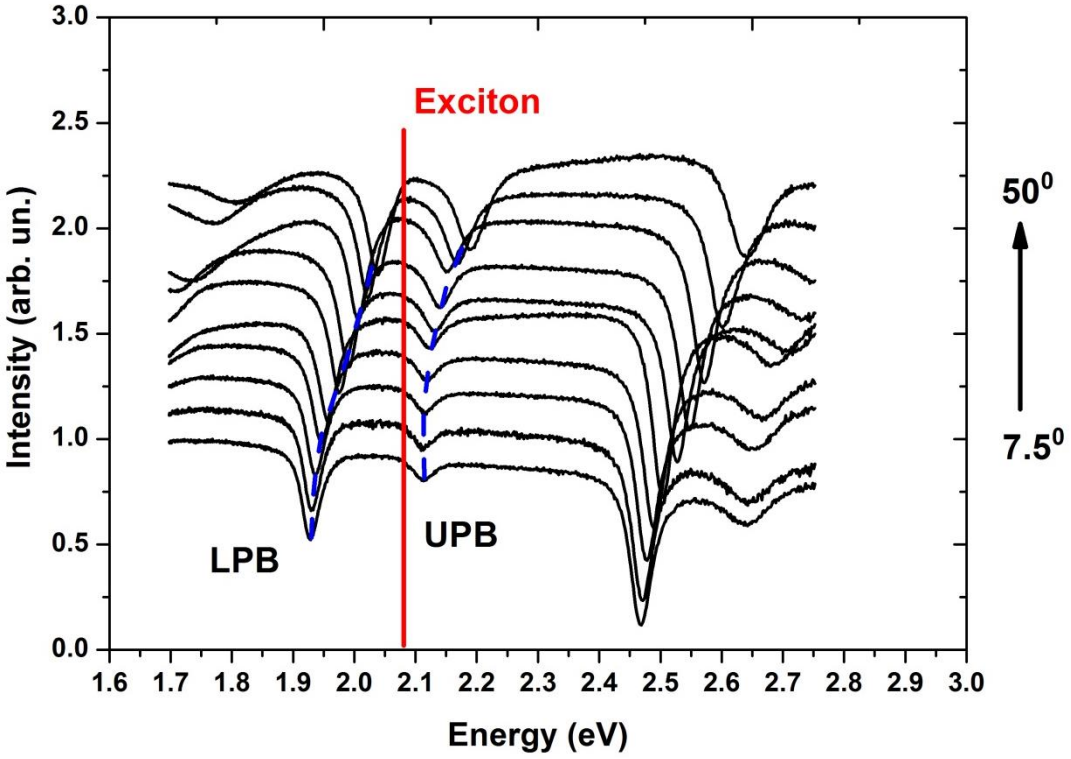

Figure 5-6 – White light reflectivity spectra that were obtained in the range of angles between 7.5^0 and 50^0. The two dips that are depicted in the spectrum correspond to the LPB and UPB minima. The red vertical line is positioned at the energy of the exciton resonance. The blue curves are used as a guide to the eye for highlighting the spectral shift of the dips.

The dispersion plot in figure 5-7 (a) depicts the angle-dependent data of the reflectivity dips (red circles for the LPB data and blue circles for the UPB data), the exciton (black line) and the photon (purple curve) modes, as well as the fits obtained by the 2-level coupled harmonic oscillator model for the two branches. The excellent agreement between the fit and the data clearly demonstrate that the strong-coupling regime is reached. Simultaneously, the fit provides information regarding the parameters of the system. The extracted parameters are the photon mode at E_0=1.962 eV, the exciton mode at E_{ex}=2.085 eV, an effective refractive index of n_c=1.871 and an interaction potential of V_0=73.7 meV. The resonant angle is located at 39^0 (grey vertical line). By using the extracted parameters for the photon energy at $\theta=0^0$ and the refractive index n, and by using equation (3.14) the photon dispersion was calculated as a function of angle, seen as purple curve in Figure 5-7.

In Figure 5-7 (b) the LPB fraction of the polaritons as a function of angle is shown. The LPB is more photonic (>0.8) than excitonic (<0.2) at observation angles close to zero, whereas at higher angles the LPB is more excitonic than photonic. Any disagreement between model fit and experiment most likely come from errors in the organic film thickness, the film morphology, and the cathode electrode deposition.

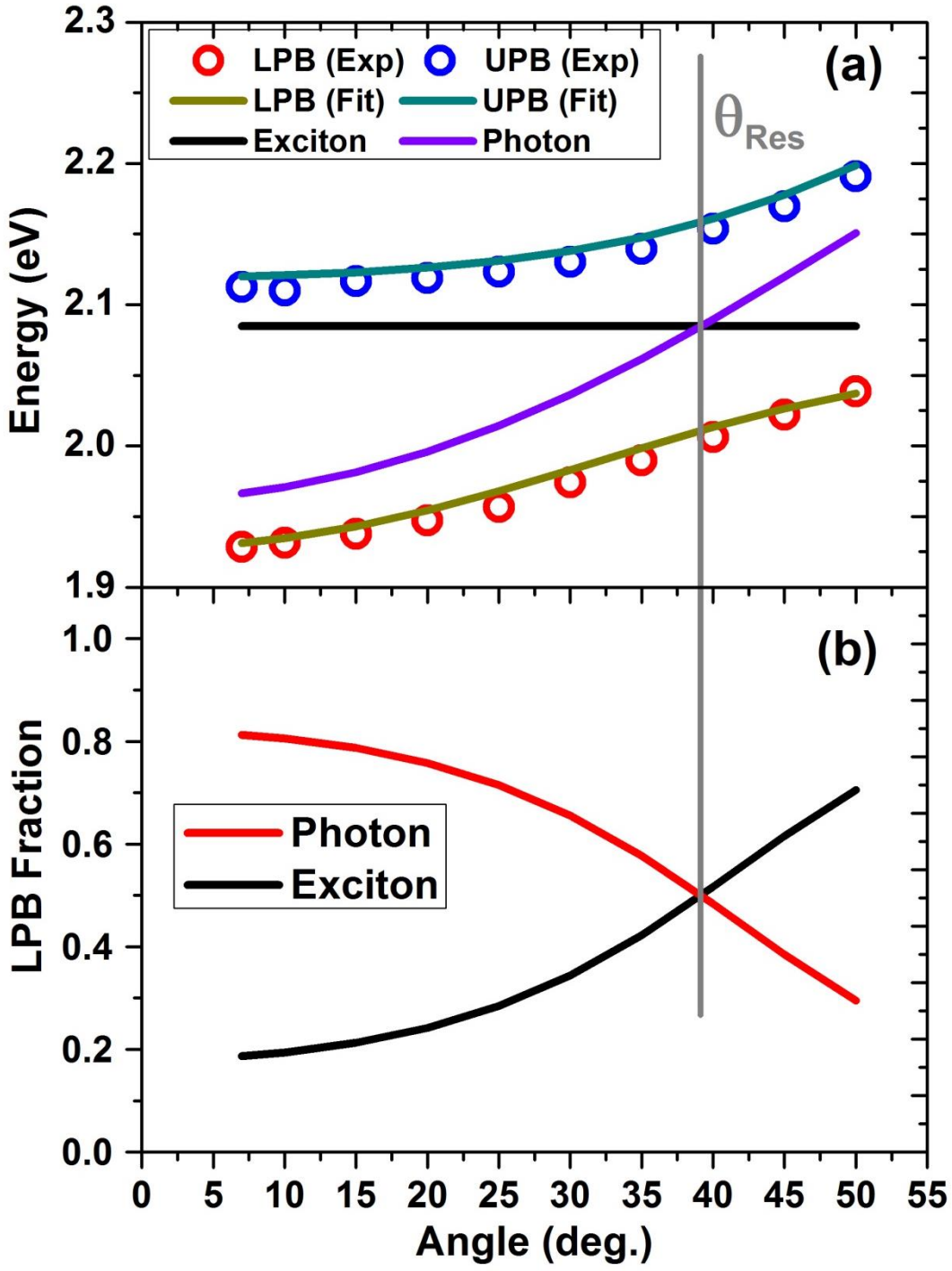

Figure 5-7 – (a) Energy dispersion diagram showing the experimentally obtained reflectivity dips corresponding to the LPB (red circles), the UPB (blue circles), the exciton (black line), the photon (purple curve), and the LPB (dark yellow curve) and UPB (Dark cyan curve) fits based on a two-level harmonic oscillator. (b) Relative fraction of the LPB as a function of the external viewing angle.

5.4.2 EL and PL measurements

As discussed in previous section, the reflectivity and transmission measurement techniques can probe polariton states which are created by storing the incident white light in the resonator geometry.

Alternatively, EL and PL measurements are based on probing the states via recording the angle-dependent emission spectrum. In both scenarios the excited state dynamics of the system must be carefully considered.

In photoluminescence studies, a laser light source is used guided by a set of optical elements and focused onto a small size spot. The diameter of the spot is defined by the focal length of the lens and the area of the light beam. The energy of the impinging photons is higher than the excitonic transition of the strongly-coupled material. This is called non-resonant excitation. High energy states are initially populated by optically pumping the organic semiconductor with high energy laser light. Next, rapid vibronic relaxation from higher to lower energy states creates a high density exciton reservoir. This subsequently leads to the emission from the strongly-coupled states.

In electroluminescence measurements the organic semiconductor undergoes excitation when electrical current passes through the body of device. Only singlet states are considered as triplet states cannot be coupled to the system. By varying the angle of detection the electrically excited states can be mapped and analysed. Figure 5-8 depicts the excitonic energy diagram of polariton PL and EL.

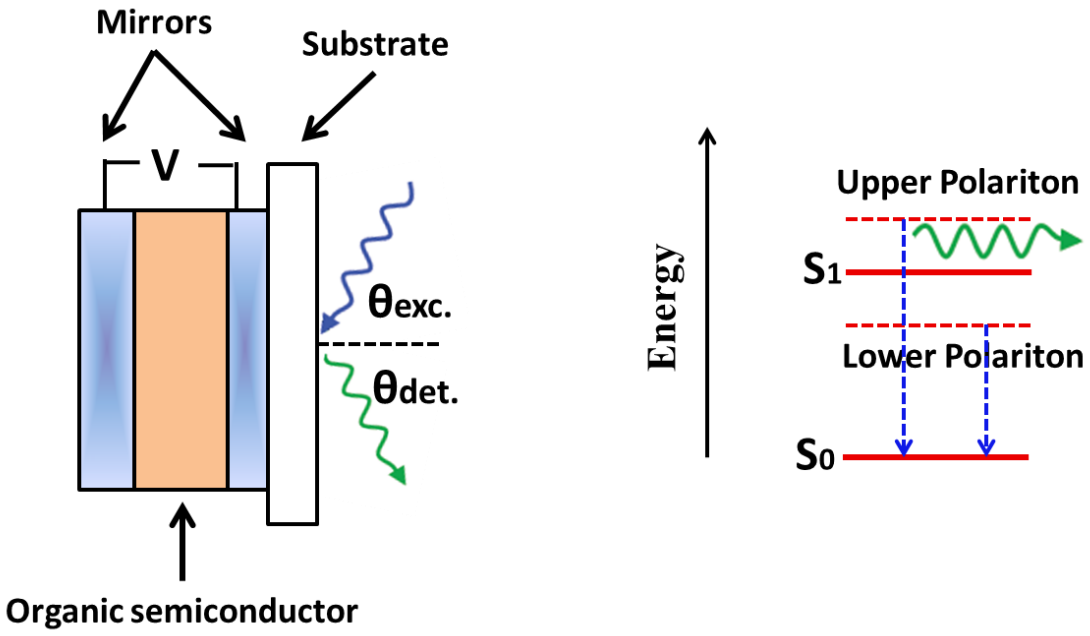

Figure 5-8 – (Left side): A simplified representation of the organic microcavity structure used for EL and PL measurements. (Right side): Modified energy level diagram showing the emission from the polariton states under EL or PL excitation.

Figure 5-9 depicts the normalized and Lambertian corrected PL and EL plots of the microcavity OLED fabricated. The laser was focused to a spot size of a 8 x 10^{-5} cm^2 at an excitation density of 1.3 x 10^5 mW/cm^2. The laser power was set at 10.4 mW. The emission intensity for both plots is normalized at high angle. The upper and lower polariton branches are fitted based on a 2-level model again demonstrating that the device operates in the strong-coupling regime. Based on the coupled oscillator model it is calculated that the PL and EL Rabi splitting energy is $\hbar\Omega_{PL}$=117 meV and $\hbar\Omega_{EL}$=104 meV, respectively. The resonant angle determined for both PL and EL is at 50^0. Moreover, the extracted detunings are δ_{PL}=-157 meV and δ_{EL}=-152 meV.

There is a small difference between the two sets of data measurements. This can be seen both in the extracted Rabi splitting and the detunings. The accuracy in these values can be explained by the method the fits to the data is done. The UPB signal is very weak at high angles but it can be obtained by fitting with Lorentzian lineshapes the data, where exciton emission and UPB signal overlap. The UPB peak position at high angles is used to generate the UPB data seen as lower case triangles in the two plots of Figure 5-9. Since both data are extracted in the same way the accuracy can be justifies with reference to each other. This difference in the data originates from the emitting area of the two structures. Specifically, the optical excitation and emission area is defined by the spot size area of the laser beam, whereas the emission that is collected under electrical excitation originates from the whole pixel area. Therefore, there is a range of angles that are collected from the EL but not the PL measurements which causes this parameter dissimilarity.

In both cases the upper polariton branch emits weakly and is observable only at high angles. To confirm this, EL and PL normalised emission spectra at $\theta=0^0$ and $\theta=50^0$ taken from figure 5-9 are shown in Figure 5-10 (a) and (b). As seen from the figure (a) at $\theta=0^0$ the lower polariton branch PL emission peaks at 1.927 eV. The lower polariton branch of the EL spectrum peaks at 1.935 eV. Both of these spectra have a second peak at 2.1 eV for PL and EL at $\theta=0^0$. The UPB overlaps with weak emission from uncoupled J-aggregates that escape through the cavity mirror at low angles.

At $\theta=50^0$ as seen from figure 5-10 (b) the LPB EL emission peak is located at 2.054 eV, whereas the LPB PL emission peak is located at 2.043 eV. The UPB for both EL and PL are indicated by red and black arrows. The UPB EL peaks at 2.192 eV and of PL at 2.171 eV. In both spectra the UPB signal is very weak. There is also a broad peak collected in the EL spectrum that peaks at 1.927 eV. This peak coincide with the LPB at $\theta=0^0$ and is caused by waveguiding effects.

Weak UPB emission in strongly-coupled optical microcavities containing J-aggregates of the TDBC dye has been observed by the experimental work of Coles et. al [125] which is in a good agreement with the theoretical model that has previously developed [44, 45, 83] . According to this study there are two main mechanisms responsible for populating upper polariton branch states. Firstly, emission from weakly-coupled excitons that optically pump the upper polariton states and secondly, thermal scattering of excitons from the exciton reservoir to upper polariton states via a continuous bath of low vibrational energies. The discrete vibrational energies do not play a significant role in the population of the upper polariton branch states because their energy is much higher than the thermal energy required for activation.

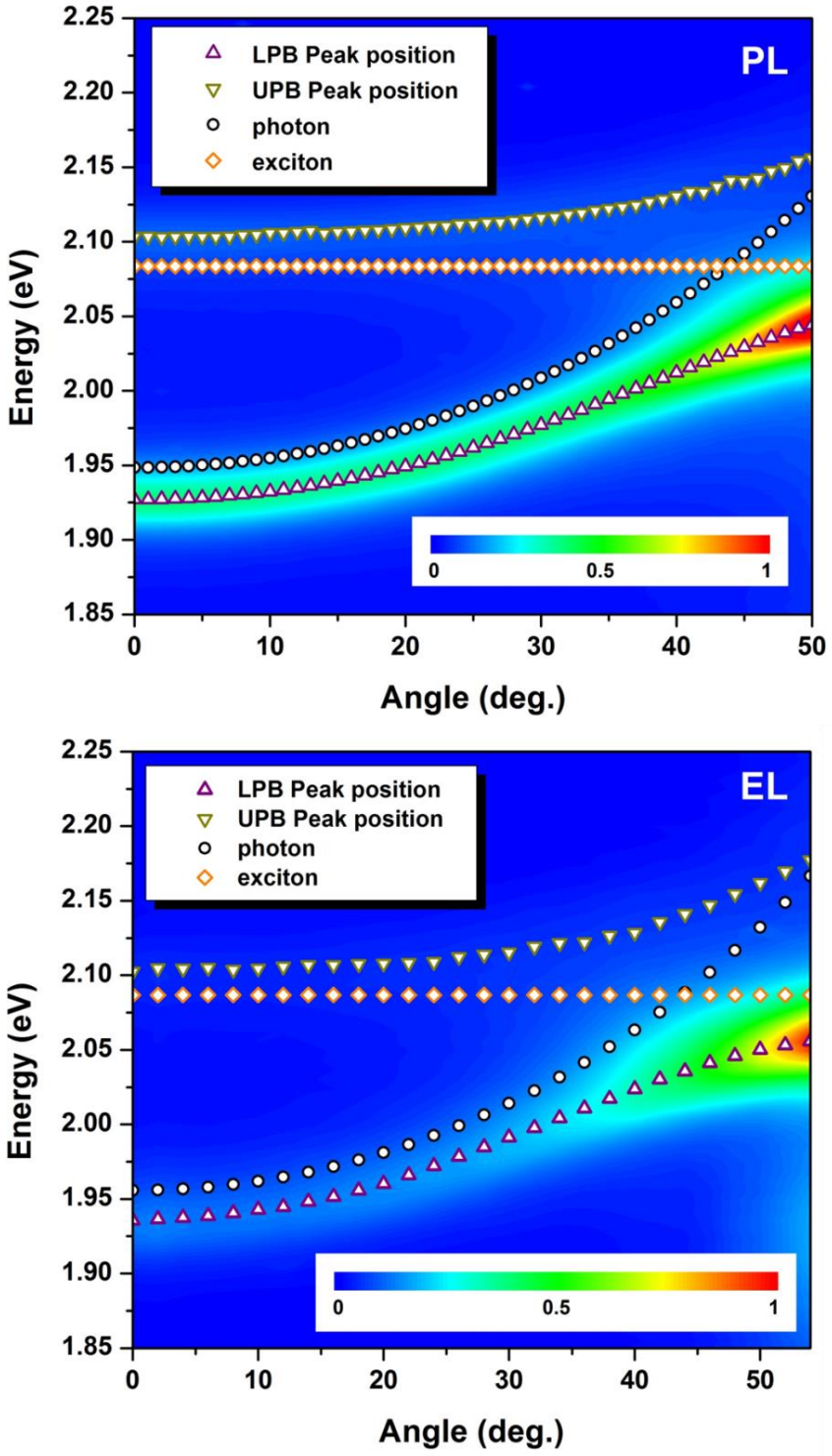

Figure 5-9 – Normalized and Lambertian corrected PL and EL contour plots of the strongly-coupled microcavity OLED.

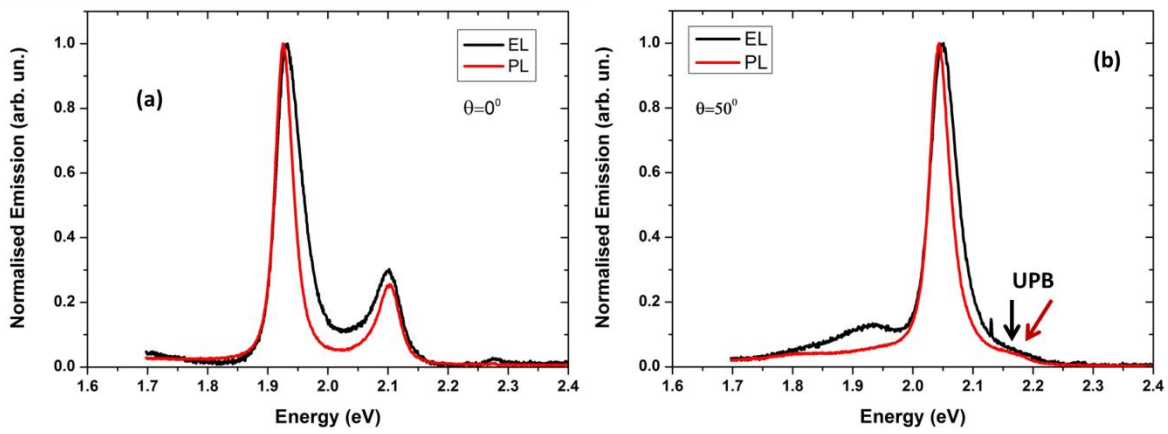

Figure 5-10 – Normalized EL and PL emission intensity at (a) θ=0⁰ and (b) θ=50⁰ from measurements taken from the same microcavity OLED.

The emission intensities can be converted into relative polariton population densities based on the following relation:

$$P = \frac{I(\vartheta)}{\alpha^2} \tag{5.1}$$

where $I(\theta)$ is the angular dependent intensity of the emission following both optical and electrical excitation, and α^2 is the photonic fraction of the exciton-polariton. Figure 5-11 depicts the polariton population density of the experimental data (open circles) and the data that were extracted from theoretical simulations (solid curves). The later were provided by Dr. Paolo Michetti for both optical and electrical excitations.

The model that was used to simulate polariton population distributions is discussed in Refs. [43-45, 83]. A brief description of the main assumptions that the model was based was given in chapter 3 and will not be further discussed here since it remains outside the scope of this thesis.

The solution of the full set of equations provides with the following picture for the population dynamics of the polariton branches: 1) in the first step the high energy excitons relax rapidly (~1 ps) to the lowest J-band states by emitting molecular phonons. 2) The J-band forms a quasi-thermalized "exciton reservoir" with excitons then scattered via interactions with local molecular vibrations to the polariton states. The second step is slower (hundreds of picoseconds) than the first step. Due to the fact that the polariton lifetime is of the order of 10-100 fs [126], the scattering events will not be sufficient to populate lower angle polaritons and thus the populations of the polariton branches will be more closely located towards the exciton reservoir.

As is depicted in Figure 5-11 the UPB and LPB populations are almost equal at low angles, whereas at higher angles the LPB has higher population density for both optical and electrical excitation. This is due to the fact that polaritons accumulate closer to the exciton reservoir. The energy separation of the exciton and the LPB $|E_{ex}-E_{LPB}|$ is larger than the energy separation between the exciton and the UPB $|E_x-E_{UPB}|$ at higher angles. This means that at room temperature there is insufficient thermal energy available to populate upper branch polaritons at high angles.

In contrast however, low energy molecular vibrations can be emitted by excitons as they scatter down to the LPB, populating states close to the exciton reservoir. Higher energy molecular vibrations, typically of J-aggregates [127], can contribute to the population at the bottom of the LPB. Finally, polaritons on the UPB and LPB close in energy to the reservoir can be via the "optical pumping" mechanism [47]. Here, a small number of uncoupled molecules with an emission spectrum (Figure 5-12) that overlaps with the UPB or LPB can contribute to the creation of UPB and LPB polaritons. This optical pumping mechanism has been explored in strongly-coupled microcavity OLEDs utilising meso-TPP as the strongly-coupled organic semiconductor [47]. It is shown that potential loss mechanisms in the exciton reservoir that populate the polariton states could be circumvented by direct optical excitation of the polariton branches.

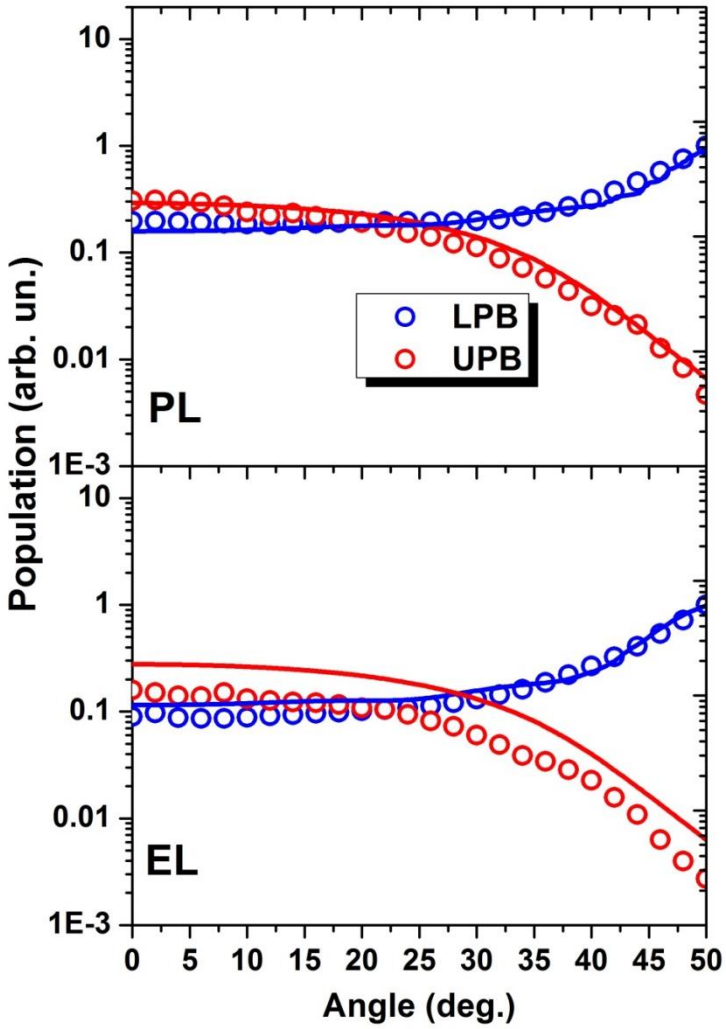

Figure 5-11 – Theoretical (solid curves) and experimentally (open circles) obtained polariton population densities of the UPB (red) and LPB (blue) corresponding to both optical and electrical excitations.

In Figure 5-12 the EL emission profile of a conventional OLED and a microcavity OLED that was recorded at normal incidence are shown. The OLED emission (red curve with offset) peaks at 2.08 eV with a lower energy peak positioned at 1.89 eV. The emission from the microcavity OLED spectrum (blue curve) is fitted by three Lorentzian lineshapes to take into account the UPB, LPB and bare exciton emission. The lower energy peak located at 1.94 eV is assigned to the LPB (green curve), whereas the weak exciton-like emission observed at 2.09 eV is an overlap of the uncoupled exciton emission (orange curve) leaking out from the cavity at 2.08 eV and weaker emission from the UPB (purple curve) located at 2.1 eV. Based on the Lorentzian fit it is calculated that the ratio of the intensity of the LPB to the UPB is 4.6.

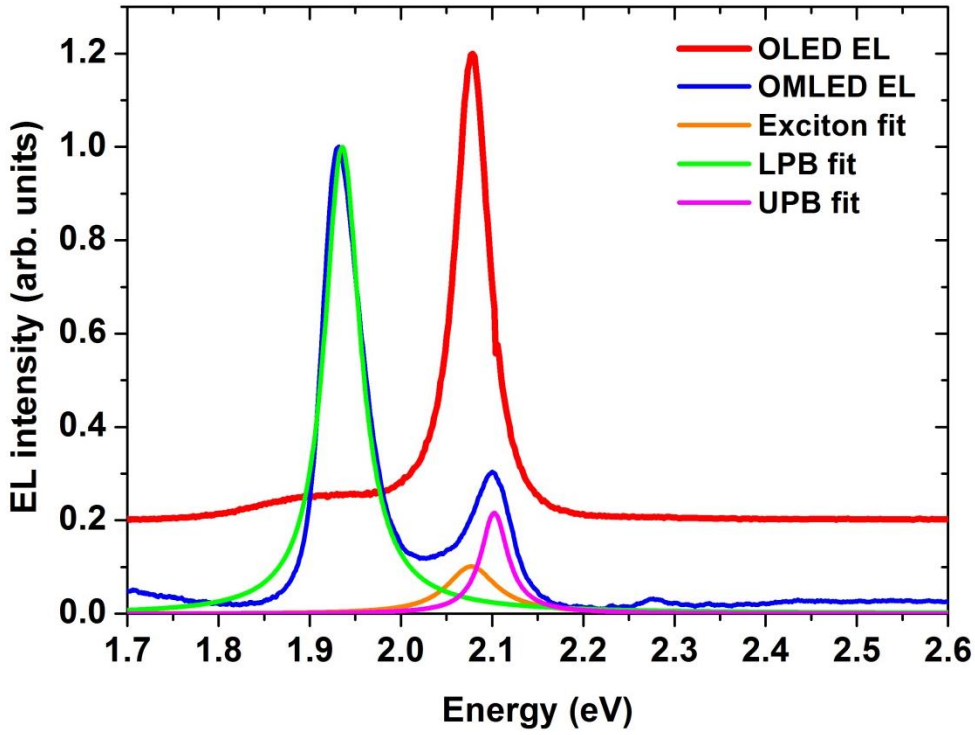

Figure 5-12 – Electroluminescence spectrum of an OLED device (red curve) and a microcavity OLED device (blue curve). The later is a superposition of the LPB spectrum (green curve), the UPB spectrum (purple curve) and the exciton spectrum (orange spectrum).

5.4.3 Electrical measurements

The OLED performance was studied by measuring the Current-Voltage-Luminance (J-V-L) characteristics at room temperature. Figure 5-13 (a) shows that the emission intensity recorded for the uncoupled and the coupled OLEDs is different. Particularly, the emission intensity of the uncoupled device is approximately 6 times higher than that observed from a coupled device over a range of applied voltages (5V -10 V). Moreover from figure 5-13 (b) it is observed that the electrical properties of the devices have the same electrical characteristics. The noise floor is below 4 volts and therefore the noise data are omitted from the graphs. A high voltage was used In these measurements since the QY of the TDBC dye is very low and in order to get a higher signal intensity. Also, the nature of the JVL characteristics requires having a range of measurements.

Here, optical measurements were recorded from 10 microcavity OLEDs and conventional OLED devices integrated over a half-angle of 36^0. An average of the measurements shows that the OLED devices are 6.1 ± 2.1 times more efficient at 10 V than the MCOLED ones. Additionally, it was observed that the OLED device is more efficient over the range 5 V-10 V of all measurements.

The structure of the MCOLED and the OLED devices are identical apart from the DBR mirror in the MCOLED. Therefore, it is expected that the current density-voltage characteristics will have similar electrical properties, whereas the difference in the emission intensity should originate

from the incorporation of the DBR mirror in the strongly-coupled OLED. Since the MCOLED operates in the strong coupling regime it is reasonable to assume that the modified EL spectrum will account for this dissimilarity. Specifically, the difference in the brightness is due to the rates of relaxation that are different in the two cases. In the case of the strongly-coupled MCOLED the emission is determined by the slow relaxation of the scattered excitons from the exciton reservoir that populate the LPB states. In the case of the OLED device, the weakly-coupled spontaneous radiative decay determines the emission dynamics. In both types of devices any waveguiding or light trapping losses due to the DBR mirror and the corresponding losses in the OLED have been ignored.

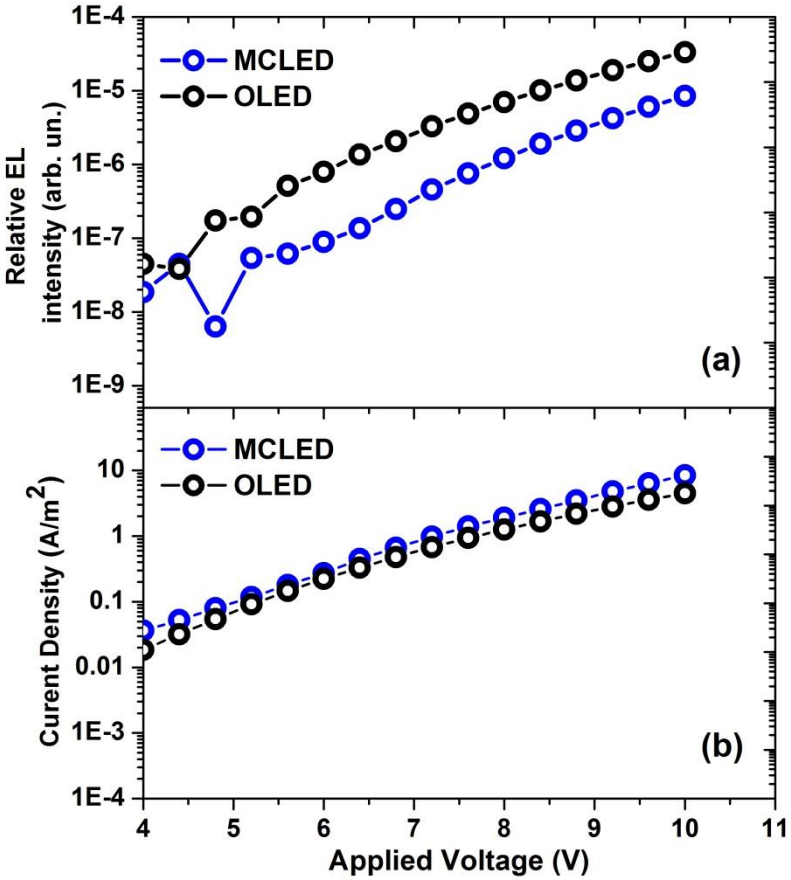

Figure 5-13 – (a) Luminance-Voltage and (b) Current density-Voltage characteristics of the MCOLED and conventional OLED devices.

5.4.4 Efficiency comparisons

In order to understand the reduced efficiency of the microcavity device compared to the conventional OLED device, the PL emission of the microcavity OLED was modelled using numerical simulations that were performed by Dr. Paolo Michetti at the University of Wurzburg. An overview of the model that is used in these simulations covered in Chapter 3. The most important points regarding this calculation are summarized below:

The numerical calculations for the microcavity OLED emission rates of the lower and upper polariton branches were parametrized based on the fits to the EL dispersion curve (figure 5-9).

The efficiency ratio η_{eff} of a MCOLED and a conventional OLED is an important parameter to describe the difference in the emission intensity of the two devices. In order to make this calculation, an assumption was made that the ratio of the microcavity (calculated with the model) and the exciton decay rates correspond to the efficiency ratio η_{eff}. Due to the fact that J-aggregates of the TDBC dye have low room temperature quantum yield, the non-radiative decay of the weakly-coupled excitons in the MCOLED and the weakly coupled excitons in the OLED is the same, which suggests that the above assumption is justified.

The above assumption is based on the low PL quantum yield of the J-aggregates at room temperature and does not take into consideration any waveguiding or light trapping losses within the devices. The calculation does not also take into consideration any triplet or polaron states and their interactions.

Figure 5-14 summarizes the simulation results and depicts on a logarithmic scale the microcavity emission rates for the upper and the lower polariton branches for a range of angles between 0^0 and 75^0. A larger emission rate is seen at all angles for the LPB compared to the UPB. Furthermore, the LPB emission rate exhibits a significant increase for angles within the range 40^0 to 50^0. This increase is caused due to the close proximity of the LPB states to the exciton transition which results from a more efficient scattering. The respective UPB emission rate drops for angles above 36^0.

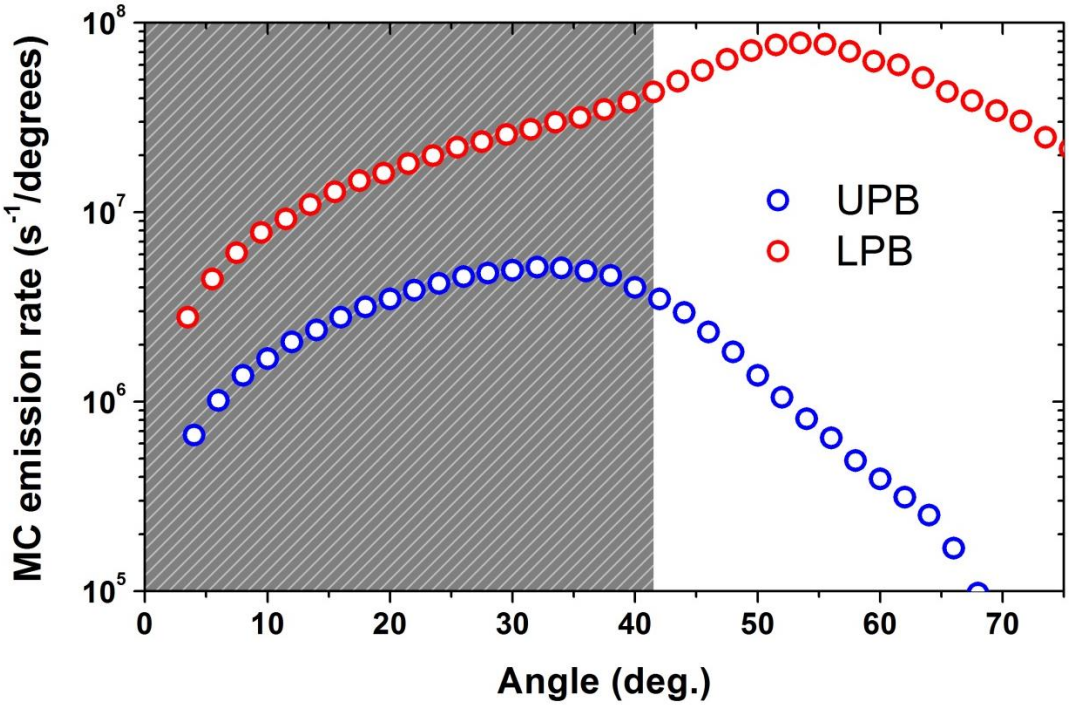

Figure 5-14 – The upper and lower polariton PL decay rates of the microcavity OLED as a function of angle calculated using numerical simulations.

To calculate the theoretical efficiency ratio of the MCOLED and the conventional OLED device the PL emission rate for the upper ($\int_{0^0}^{36^0} \Gamma_{UPB} d\theta = 5.2 \times 10^7\ s^{-1}$) and lower ($\int_{0^0}^{36^0} \Gamma_{LPB} d\theta = 1.6 \times 10^8\ s^{-1}$) polariton branches over the angular region of 0^0 to 36^0 was calculated which coincides with the integrated emission into a forward cone of 36^0 that was recorded using a liquid light guide, with a total polariton emission rate being $\int_{0^0}^{36^0} \Gamma_{Pol} d\theta = 2.12\ x\ 10^8\ s^{-1}$. The integration area is seen by the grey shaded area of figure 5-14. It is found that the model predicts the ratio of the emission rates close to zero degrees to be approximately 3.5, a value in a good agreement with the experimentally obtained intensity ratio of 4.6 at normal incidence.

By assuming a radiative decay rate of Γ_{ex}=5.4 x 10^{-9} s^{-1} (τ_{ex}=185 fs) [128] for the J-aggregates and by using a scaling factor $\eta = \frac{2\pi(1-Cos(36^0)}{2\pi(1-Cos(90^0)}$=0.19, to account for the integration area under consideration, it is found that the theoretical efficiency ratio of the MCOLED and the conventional OLED to be approximately $\eta\Gamma_{ex}\left(\int_{0^0}^{36^0} \Gamma_{Pol} d\theta\right)^{-1} \approx 4.8$, a value in good agreement with the experimentally obtained value of 6.1± 2.1.

The main conclusion of this calculation is twofold. Firstly, this value is in the same order of magnitude and therefore in good agreement with the experimentally obtained efficiency value 6.1± 2.1. Secondly, it is concluded that the reduced efficiency of the strongly-coupled devices results from the slow scattering rate of excitons from the exciton reservoir to the polariton states. Since the injection density in these devices is relatively low such scattering events cannot contribute to the building of a significant population on the lower polariton branch. This renders this system incapable of establishing a macroscopic population for the LPB at $\theta=0^0$.

Therefore, systems that use non-emissive materials with high charge-carrier mobilities and strongly-coupled organic semiconductors with high quantum yields are needed in order to increase the scattering rates towards the bottom of the LPB. The demonstration of lasing under current injection in inorganic quantum-well microcavity devices by Schneider et al. [23] exhibited a threshold current density of approximately 0.065 mA/cm^2. Such current densities are easily attainable in OLEDs [129], however, there is still a lot of challenges to overcome, in terms of quality factor, organic semiconductor and degradation. These issues will be discussed in subsequent chapters.

5.4.5 Time resolved measurements

Time dependent dynamic studies in OLEDs have been used previously in OLEDs. In the work of Kaseman et al. [130] the emissive layer was comprised of the host:guest system Alq3:DCM. In these studies short pulses were used in order to investigate the role of the various quenching mechanisms in OLEDs and compared with optical simulations.

Here, the time resolved emission of the MCOLED and the conventional OLED devices were measured in order to investigate whether device emission dynamics are significantly modified

in the strong coupling regime or not under current injection. An electrical ps pulsed generator was used with the characteristics of 2μs square pulses, of amplitude 18 to 24 V, and frequency of 10 kHz. The rise and the decay times were then recorded.

In figure 5-15 (a) and (b) OLED and microcavity OLED devices are compared. The time dependent emission intensity obtained is depicted as black circles in the graphs. The exponential fits for the rise time τ_{rise} (orange fit), and the decay time τ_{decay} (blue fit) following a voltage pulse are almost identical. The slow rise time (≈200 ns) is probably due to the low mobilities of the organic semiconductors used which transport charges to the emissive layer as well as in the energy level mismatch of these organic materials.

Furthermore, the EL decay time being approximately 50 ns is long compared to the lifetime of the TDBC molecules (ps scale). This is caused by the high amount of free and trapped charges that remain in the J-aggregate layer that recombine only slowly once the driving pulse has been removed.

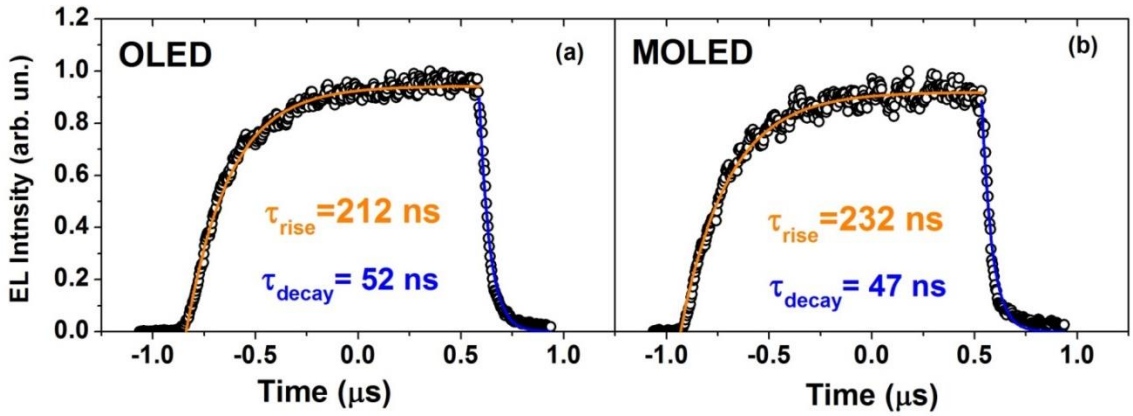

Figure 5-15 – Streak camera-recorded EL intensity for (a) a conventional OLED and (b) a microcavity OLED devices under pulsed applied excitation.

5.5 Conclusions

Until now, studies on strongly-coupled organic light-emitting diodes were mainly focused on the device fabrication and on demonstrating EL and PL in such devices [47, 96-98, 124, 131]. This is the first time that a comprehensive study is done that quantifies properties of the system that have not been previously assessed by other investigations.

A number of important conclusions were deduced from this study. Firstly, reflectivity electroluminescence and photoluminescence measurements show that the system based on J-aggregates of the TDBC dye operate in the strong coupling regime. There is a small difference in the extracted parameters of the EL and the PL spectra which is potentially caused by the collection area of the sample in the two methods.

Secondly, direct conversion of the recorded EL and PL intensity into polariton population shows that the system is populated equally at $\theta=0^0$, whereas at high angles there is an asymmetry with the density of the lower branch polaritons being higher than the respective population density of the upper branch polaritons. The LPB is populated due to the scattering of reservoir excitons with low energy molecular vibrations or high energy discrete vibrations. In contrast, the thermal energy at room temperature cannot populate the upper branch at high angles. Direct radiative pumping of uncoupled emission in the exciton reservoir can populate both branches if there is an overlap between the emission spectrum of the uncoupled excitons and the UPB or LPB states.

Thirdly, the intensity of the LPB is 4.6 times higher than the intensity of the UPB at $\theta=0^0$. The lower intensity of the UPB in EL has been observed in other studies containing J-aggregates [124] as the emissive material as well as in strongly-coupled OLEDs containing the organic semiconductor meso-TPP [96]. A more effective way of generating higher density of upper branch polaritons can be achieved if the device incorporates a weakly-coupled emitter whose emission spectrum overlaps with the upper (and/or lower) polariton states. This radiative pumping mechanism is very efficient in generating increased emission of the upper branch polaritons [47].

Fourthly, two sets of devices were fabricated, namely strongly-coupled microcavity OLEDs and weakly-coupled conventional OLEDs and they were compared in terms of their efficiency. It was found that the MCOLED is 6±2.1 times less efficient than the conventional OLED device. This value is close to the theoretical predicted value of 4.8. This results from the slow scattering rates of reservoir excitons towards the bottom of the lower polariton branch.

To increase these scattering rates strongly-coupled organic semiconductors with higher luminescence quantum yield and materials with high mobilities that can sustain higher injection densities should be used. In this scenario to harness non-linear scattering processes is possible but can only occur in significant exciton and polariton densities.

Finally, time-resolved measurements reveal that there is a little difference in the rise time (~200 ns) and the decay time (~50 ns) of the OLED and MCOLED. The charge injection and transport in both devices are very slow processes compared to the exciton or the polariton lifetimes and therefore cannot affect the system's dynamics.

Chapter 6

Exploring organic semiconductors in optical microcavities and LEDs.

In this chapter three different organic semiconductors are explored with special emphasis given to their ability to form polariton states when each is placed inside an optical microcavity structure. The three organic materials under investigation are the luminescent dye Lumogen F Orange 240 (LF), the organic semiconductor 5,12-diphenyltetracene (DPT) and the conjugated polymer meLPPP. The material selection is mainly based on optical properties such as high quantum yield and their ability to be processed into thin films from organic solvents. It is shown that despite the fact that specific semiconductors have relatively broad absorption linewidths they are still able to reach the strong coupling regime due to their high oscillator strength. Finally, it is concluded that in order to observe polariton electroluminescence, both the material and the optical microcavity must satisfy two requirements; namely limited dissipation of Frenkel excitons and significant light confinement.

6.1 Introduction

To observe polariton electroluminescence in organic light-emitting diodes, the devices must be able to confine light within the structure with limited optical losses due to scattering or other waveguiding effects. At the same time, the active, emissive and strongly-coupled electroluminescent material within the cavity must be able to generate sufficient singlet states that are coupled to the confined photons, since the forbidden triplet states cannot be coupled to the photon field.

The efficient generation of excitons is closely associated with the device structure. For example, a single emissive organic layer or a layer made by blending different organic materials with different functionalities can be selected. Indeed, a strongly-coupled material can be used as part of a blend with two other organic semiconductors that act as electron and hole transporting materials. This broadens the range of available materials used having different mobilities and emissive properties.

The fabrication of efficient microcavity OLEDs that operate in the strong-coupling regime is not straightforward. Some reasons for this include the nature of the organic semiconductor itself, its position inside the microcavity or other effects that can prohibit the device undergoing strong-coupling.

This chapter details three different organic semiconductors that have been incorporated in devices in order to generate polaritons following electrical injection. Each organic material is examined in detail. It is concluded that in order to achieve high density of polaritons, substantial modification in device structure is needed to overcome various optical losses.

6.2 Lumogen F Orange 240

Historically, the dye Lumogen F Orange 240 (LF) was extensively studied for light management in Luminescent Solar Concentrators due to its environmental stability at ambient conditions [132]. Here, the selection of the organic material is based on two main characteristics. Firstly, the LF dye has a high quantum yield which approaches the absolute value of unity at very low concentrations [132]. Secondly, the organic dye is characterized by well-resolved and narrow absorption transitions. Further details of the structure of the LF dye were given in Chapter 4.

6.2.1 Absorption and PL spectrum

A number of several solvents were used to dissolve the LF dye. In chlorobenzene solution it exhibited enhanced dissolution forming fewer aggregates as observed from spin coated thin films. Other solvents such as toluene were only capable of dissolving the dye well at lower

concentration (2% w/v). The absorption spectrum of the dye suggests that the dye is suitable to undergo strong-coupling in a microcavity.

To record its absorption spectrum, the LF dye was blended with the optically-transparent polymer PMMA at a concentration of 16.7 % w/w in a chlorobenzene solution and then spin coated on a transparent glass to form a thin film having a thickness of approximately 60 nm. The absorption spectrum of the Lumogen F Orange 240 dye is shown in Figure 6-1 (a). The spectrum is characterized by a main 0-0 transition ($E_{0\text{-}0}$ = 2.36 eV) alongside the 0-1 ($E_{0\text{-}1}$ = 2.53 eV) and 0-2 ($E_{0\text{-}2}$ = 2.7 eV) vibronic transitions. The 0-3 vibronic transition ($E_{0\text{-}3}$ = 2.88 eV) is not clearly resolvable. From a Lorentzian fit, it is determined that these transitions have linewidths of 92.2 meV (0-0), 115.8 meV (0-1), 117.3 meV (0-2) and 341.6 meV (0-3), respectively.

To measure the emission spectrum of LF, the dye was blended at different concentrations with the insulating polymer PMMA. Figure 6.1 (b) shows the emission of the dye as its relative concentration component is increased. Here, the relative concentration is defined as η_C=[dye]/[PMMA], for dye concentrations of 0.5, 1, 2.5, 5, 7.5 and 10 in chlorobenzene solutions.

It can be seen that as the concentration of the dye in the PMMA host polymer is increased the main 0-0 emission band becomes suppressed. A high reduction in the main 0-0 emission can be caused by self-absorption. This can be significant in high concentration thin film solutions. However, there is no spectral shift in the corresponding absorption profiles. Furthermore, each individual vibronic peak becomes superimposed on a featureless broadband. This emission background shifts to lower energy levels, with the large broadband centered at approximately 2 eV. It is apparent that there is an overlap of the absorption and emission spectra that decreases by increasing the dye content. Reversely, the Stoke's shift is increased from 39.8 meV recorded at 16.7 % w/w, to 60.3 meV recorded at 33.3 % w/w of the relative concentration.

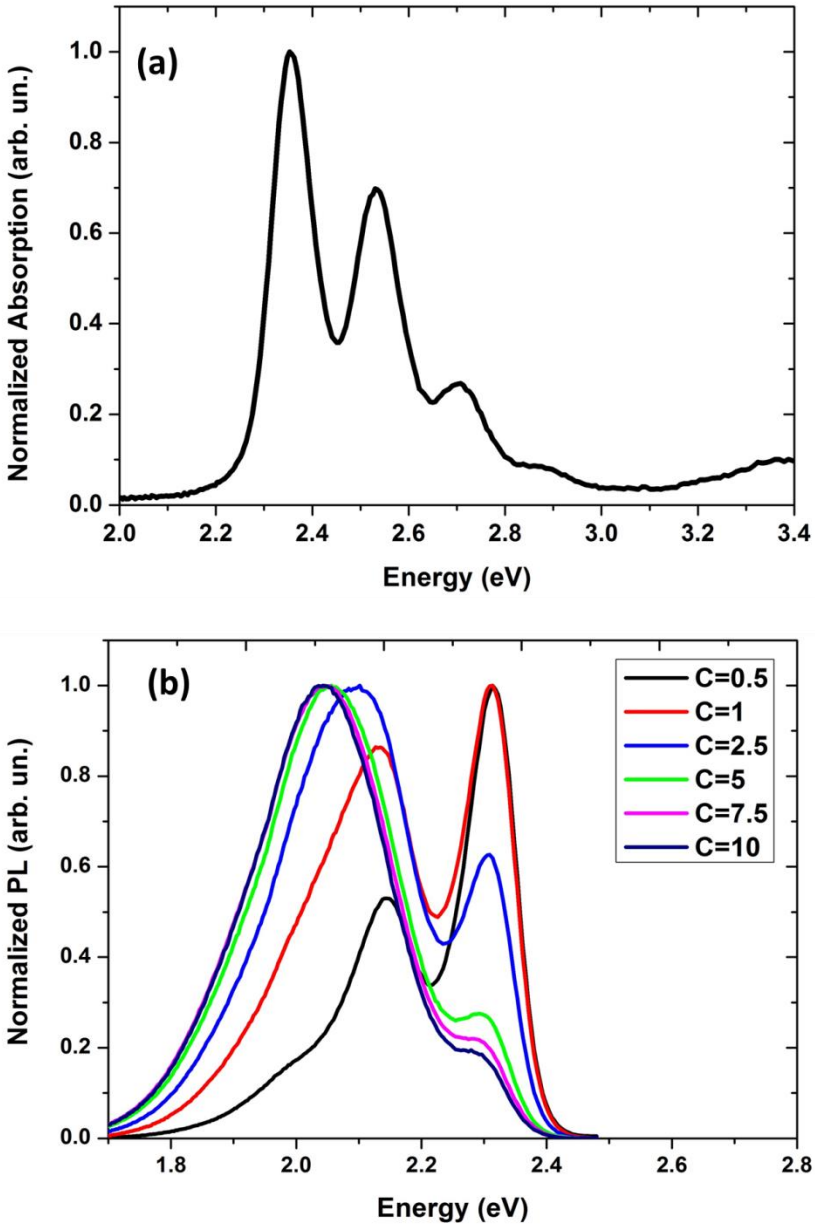

Figure 6-1 – (a): Normalized absorption spectrum of a spin coated film of Lumogen F Orange 240 dye dispersed in PMMA. (b): Normalized PL spectrum of the dye depending on concentration.

6.2.2 Strong coupling in an optical microcavity

In order to investigate the behaviour of the LF dye inside an optical microcavity structure the dye was blended with PMMA at a concentration of 33.3% w/w in a chlorobenzene-based solution. The λ/2 optical microcavity fabricated consisted of a 50 nm semi-transparent Ag mirror that was evaporated onto a glass substrate. Next, the blend was spin coated on top of the silver layer having an approximate thickness of 160 nm. The structure was completed by thermal evaporation of a second 100-nm-thick Ag light-confining mirror.

With this simple cavity geometry the ability of the system to form polariton states can be experimentally assessed. A laser light source emitting at 3.06 eV was used to excite the LF

through the semi-transparent side of the cavity mirror. The photoluminescence emission from the cavity was then recorded by mapping the angle-dependent emission spectrum with light escaping through the semi-transparent cavity mirror.

Figure 6.2 shows reflectivity and PL spectra recorded from the optical microcavity for a series of angles. For low energies, the reflectivity dips and the PL peaks for each angle correspond approximately to the same energy, having a small difference caused by probing the system with different techniques. At higher angles of observation only reflectivity dips can be seen from the spectra but not PL emission. The PL spectra at high angles (44^0 and 54^0) are noisy due to the low emission intensity recorded at these angles.

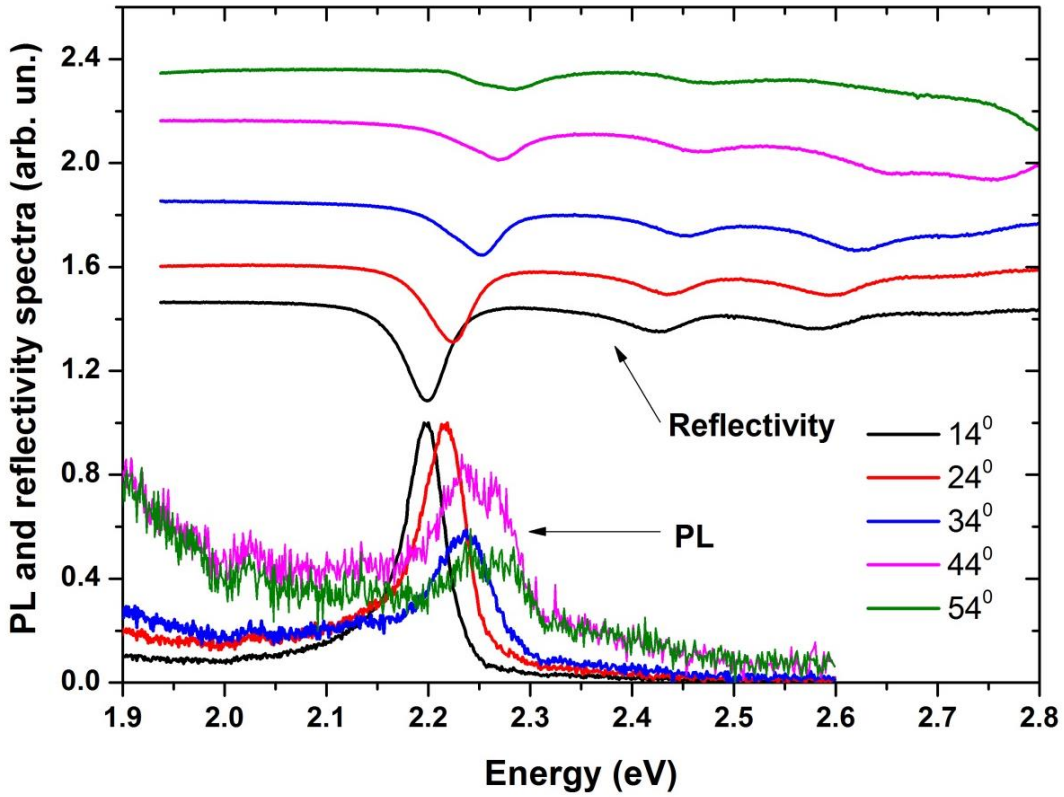

Figure 6-2 – PL and reflectivity spectra recorded for a series of angles of the LF-based optical microcavity.

A more detailed analysis of the angular-dependent PL emission spectrum following optical excitation is shown in the plot in Figure 6-3. It can be seen that most of the emission intensity is concentrated in the lower polariton branch at lower angles and decreases as the angle of observation increases. Furthermore, there is a shift in the emission energy towards high energies at higher angle. A lower limit for the quality factor of this cavity was estimated by fitting a Lorentzian spectral line shape to the observable emission at $\theta=0$, with a Q factor of 52 determined from the emission peak located at 1.182 eV.

On the same figure is plotted data taken from reflectivity measurements as shown using the red-white triangles. It can be seen that the reflectivity minima anti-cross at each exciton transition and exhibit angle dependence. It is found that in this case there are four distinct branches. Therefore, the use of a 4x4 matrix Hopfield Hamiltonian describing the interaction between a photon and three excitonic oscillations is needed for the quantitative fitting.

The positions of the reflectivity minima determined by fits to the spectra are shown as black curves in the contour plot. Here, the excitonic resonances are shown with black-white circles and correspond to the three main absorption transitions $E_{ex}(i)$, with i=1,2,3 referring to the lowest-to-highest energy resonances. Particularly, $E_{ex}(1)$ refers to the electronic transition (0,0), whereas $E_{ex}(2)$ and $E_{ex}(3)$ refer to the vibrational transitions (0,1) and (0,2), respectively. The photon mode is shown on the same graph and is indicated by grey circles. The fitted data show an excellent agreement with both the reflectivity and the PL angle-dependent spectra. This indicates that the three transitions, one electronic (0,0) and two vibrational (0,1) and (0,2), are simultaneously coupled to the photon mode of the cavity. The strong-coupling regime was reached.

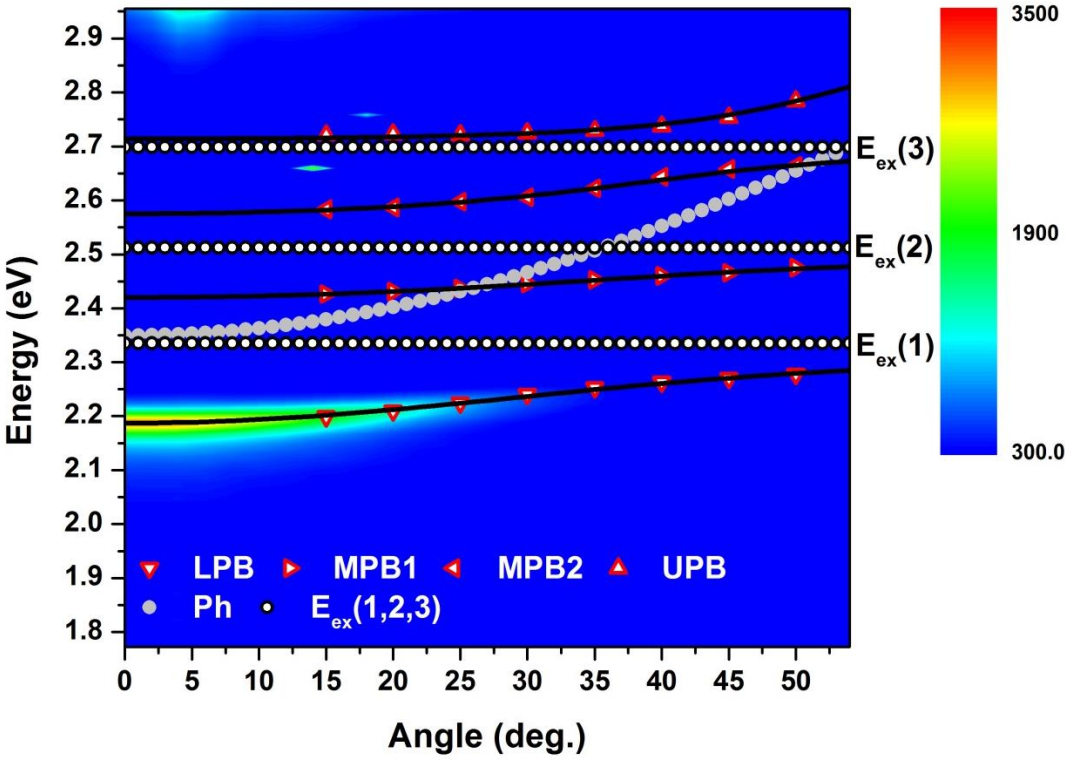

Figure 6-3 – Plot of an all-metal microcavity containing the Lumogen F Orange 240 dye dispersed in PMMA.

Four polariton branches can be identified in the spectrum: A lower polariton branch (LPB), two middle polaritons branches (MPB1 and MPB2) and an upper polariton branch (UPB). The extracted values from the coupled oscillator that describe the cavity are the photon mode, having a normal incidence energy of E_{ph}=2.349 eV, the exciton modes $E_{ex}(1)$=2.336 eV, $E_{ex}(2)$=2.512 eV and $E_{ex}(3)$=2.699 eV, the effective refractive index n_{eff}=1.65, and finally the interaction potentials V_1=0.133 eV, V_2=0.107 eV, and V_3=0.063 eV. The later correspond to branch splittings of $\Omega_{0\text{-}0}$=266 meV, $\Omega_{0\text{-}1}$=214 meV and $\Omega_{0\text{-}2}$=126 meV, respectively.

It is apparent that the 0-3 transition does not couple to the cavity mode due to its broadband absorption linewidth and lower oscillator strength. A system with four absorption transitions simultaneously coupled to the cavity mode would require five polariton branches to be

described properly three of which would be middle polariton branches with highly mixed excitonic character.

Figure 6-4 depicts the mixing coefficients of the four polariton branches. The relative weights are $|\alpha|^2$, $|\beta|^2$, $|\gamma|^2$, and $|\delta|^2$, corresponding to the photon, and the $E_{ex}(1)$, $E_{ex}(2)$ and $E_{ex}(3)$ fractions, respectively.

It can be seen that the LPB is principally composed of a superposition of the cavity photon and the lowest energy exciton $E_{ex}(1)$. At small angles the lowest excitonic and photonic components contribute almost equally. As the angle of observation increases, the LPB becomes more excitonic. At 15^0 the LPB has equal contributions from its two main components. In addition to $E_{ex}(1)$, the LPB also contains a small fraction of $E_{ex}(1)$, although this is less than 10 % of all angles, with the fraction of the Ex_3 transition being less than 1 % for all angles of observation.

The MPB1 however exhibits a more mixed excitonic character, with contribution of the $E_{ex}(2)$ resonance becoming more significant in this branch. It can be seen that it goes from almost 30 % at low k states to the maximum value of 83 % at the highest k observable state. An equal contribution from $E_{ex}(1)$ and $E_{ex}(2)$ resonances is observed at the angle of 22^0.

Turning to the MPB2, it is found that there is a considerable reduction in the $E_{ex}(1)$ component. However, the $E_{ex}(3)$ contribution now becomes very significant with a maximum value of $|\delta|^2=0.79$ at 55^0. At 38^0, the middle polariton exhibits the maximum mixing of all components, with the components of photon, $E_{ex}(1)$, $E_{ex}(2)$, and $E_{ex}(3)$ being 0.34, 0.1, 0.28, and 0.28, respectively.

The UPB case is more straightforward. At low angles, the UPB is more $E_{ex}(3)$ in nature, whereas at high angles the photon fraction is more significant. An equal mixing of the two occurs at an angle of 46^0. The $E_{ex}(1)$ and $E_{ex}(2)$ components contribute less than 10 % to the UPB each at all angles.

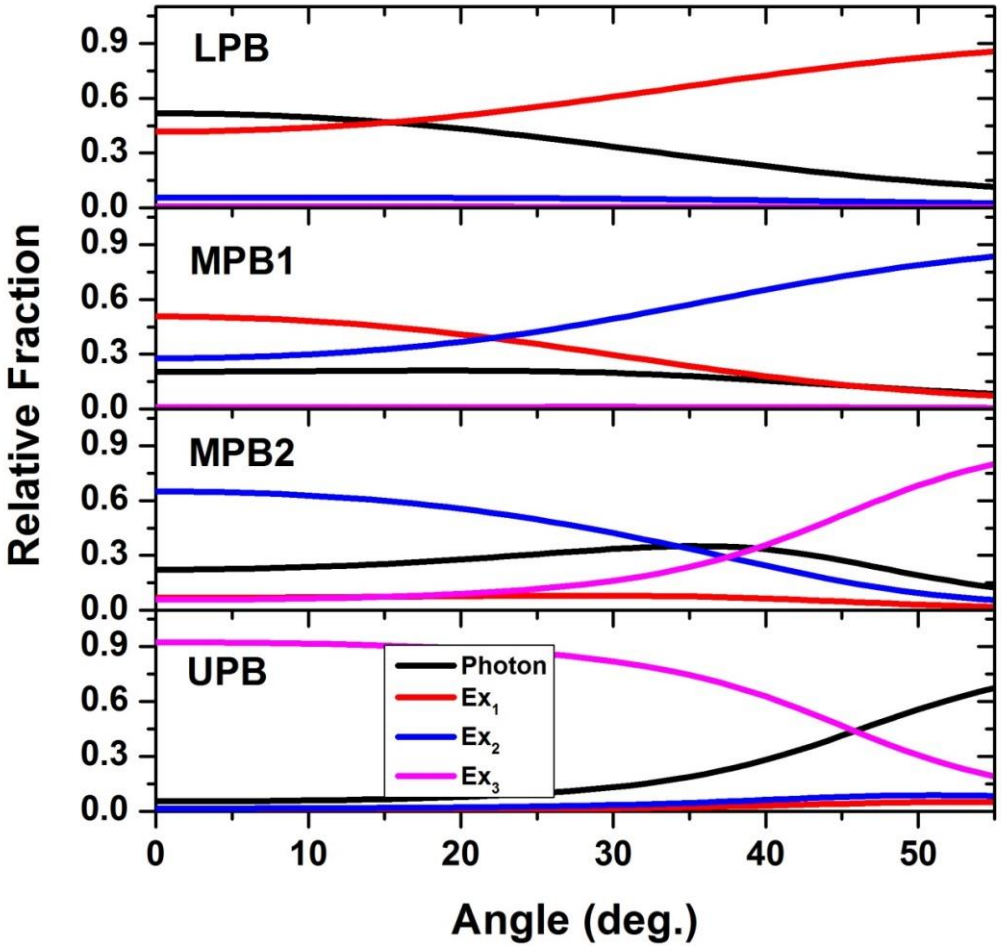

Figure 6-4 – Relative exciton-photon character of the four polariton branches.

6.2.3 Host:guest systems for efficient energy transfer.

The organic microcavity system presented in Figure 6-2 was based on a blend of the LF dye with a transparent and insulating polymer matrix (PMMA). To generate polariton luminescence, it was necessary to excite the LF dye directly by high energy photons. However, in order to move towards a device applicable structure, it was decided to explore a Förster-energy transfer mechanism utilizing a host:guest system to excite the LF excitons.

There are two main criteria for selecting the appropriate host polymer. Firstly, to fulfil the requirements for efficient energy transfer, the absorption spectrum of the LF dye should overlap significantly with the emission spectrum of the conjugated host polymer. Secondly, the absorption spectrum of the guest molecule and the absorption spectrum of the host polymer should not overlap. Conjugated polymers have broad absorption features and concentrate the majority of the oscillator strength. These broad inhomogeneous transitions are responsible for small Rabi-splittings that forces the system to go into the weak coupling regime.

A number of light emitting polymers were used in this study. Their chemical structure was shown in chapter 4. Their emission spectra exhibit significant spectral overlap with the

absorption spectrum of the Lumogen F dye. This is shown in Figure 6-5. Each host:guest system has its own characteristics and will briefly described in this section.

System (a): meLPPP is a blue emitting polymer with distinct absorption and emission spectra. There is a significant overlap with the LF dye as shown in Figure 6-5 (a). It should be noted that a pure film of meLPPP can form polariton states in optical microcavities and this will be described separately in section 6.4. Therefore, it is expected that this system will exhibit strong coupling from the (0-0) transition of both materials in a blend, and with higher vibronic transitions, or even mixed exciton or vibronic states contributing to the formation of a multiple branch system. This scenario is clearly more complicated than the other host:guest systems.

System (b): This system is shown in Figure 6-5 (b). The polymer NP is a conjugated polymer that emits in the blue-green region of the spectrum. Its narrow emission is different from its broad band absorption. There is a small overlap between the absorption spectra of the host and the (0-2) transition of the LF dye. This overlap suggests that the (0,0) and (0,1) transitions of the LF dye will be more likely to operate in the strong-coupling regime.

System (c): Here a blue emitting polymer called PFO is used, having an absorption spectrum that is well spectrally separated from the absorption spectrum of the LF dye. There is a good spectral overlap that fulfils the Förster energy transfer scheme. This suggests that four well resolved polariton branches will be possible.

System (d): This blend utilises a green emitting polymer called F8BT. As can be seen in Figure 6-5 (d), F8BT has a broad absorption that overlaps with all the vibronic transitions of the LF dye. This suggests that only the (0,0) electronic transition will be strongly-coupled. However, in this system, both Förster energy transfer mechanism and direct population of the LPB by the F8BT emission are expected to populate states at the LPB. In the second case, polaritons can be generated directly due to the 'optical pumping' mechanism. Due to the fact that in its lifetime a polariton oscillate between its photonic and its excitonic components in the form of Rabi oscillations [133], emission of photons from F8BT, that overlap in energy with LPB states, will directly excite states in the lower polariton branch. A similar example was studied in the work of Lodden et al. [47] where a weakly-coupled organic semiconductor (Alq_3) directly populated the polariton states of the strongly-coupled organic semiconductor (TPP) by radiative pumping.

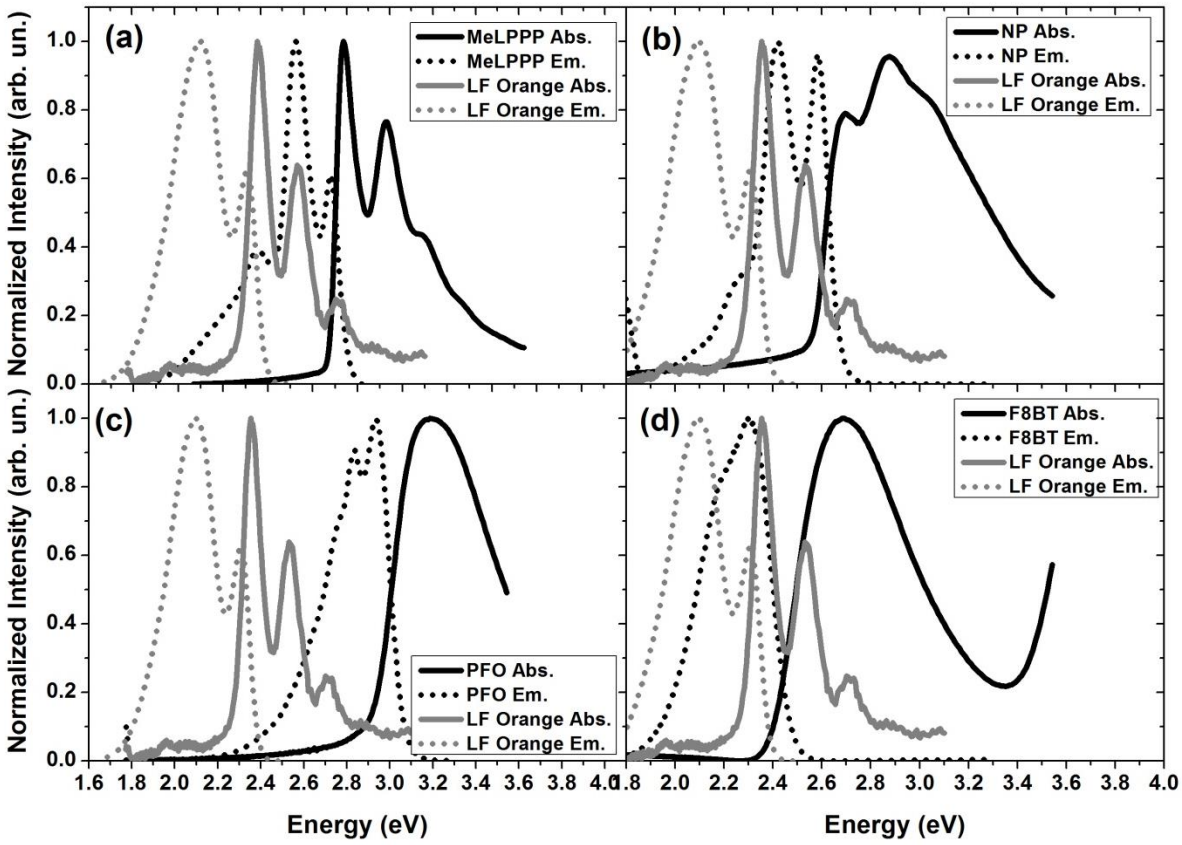

Figure 6-5 – Host:guest systems for the study of Forster energy transfer scheme utilizing the following polymers: (a) MeLPPP, (b) ADS128GE (NP), (c) PFO, and (d) F8BT. Lower part: The chemical structure of the conjugated polymers PFO, F8BT and NP.

To explore whether polariton electroluminescence can be realised based on these host:guest systems, it is first necessary to fabricate conventional non-cavity OLED devices and study their optoelectronic properties.

Two sets of devices were fabricated. In the first set, only the host polymers were used as the active EL material. The devices fabricated are composed of: ITO/PEDOT:PSS (30 nm) /polymer (70 nm)/Ca (5 nm)/Ag (100 nm). In the second set of devices, a host:guest blend was used as the active layer. Here, structures fabricated were composed of: ITO/PEDOT:PSS (30 nm) /polymer:LF (90 nm)/Ca (5 nm)/Ag (100 nm). The concentration of the polymer:LF blend was varied from 1:0.1 to 1:1 w/w for the highest LF concentration.

Devices that did not incorporate LF dye were operational as can be seen from the recorded JVL characteristics shown in Figure 6-6. Brightness above 1000 cd/m^2 is achieved for polymers NP and F8BT at 6 V, whereas meLPPP and PFO exhibit lower brightness (approximately 100 cd/m^2) at the same voltage.

However, the second set of devices that included the LF material was non-operational for all concentrations of guest molecules explored. This result demonstrates that unfortunately, Lumogen F Orange 240 is not a suitable material to be used in a host:guest system under electrical operation. The most obvious explanation is that this dye creates a series of various

trap states that are localized and sufficiently deep that are highly detrimental in organic semiconductor devices explored. Although, to my knowledge, there are no references of using the Lumogen F orange 240 dye directly in OLED devices, PTCDI [134] which is a similar dye with the same core structure as LF but different side groups has been reported to have a HOMO energy level at 6.2 eV and a LUMO energy level at 4.4 eV. If LF has similar energy levels, then the deep LUMO level will affect the electrical properties of the device. A study of the various perylene diamine derivatives and their properties can be found in Ref. [135].

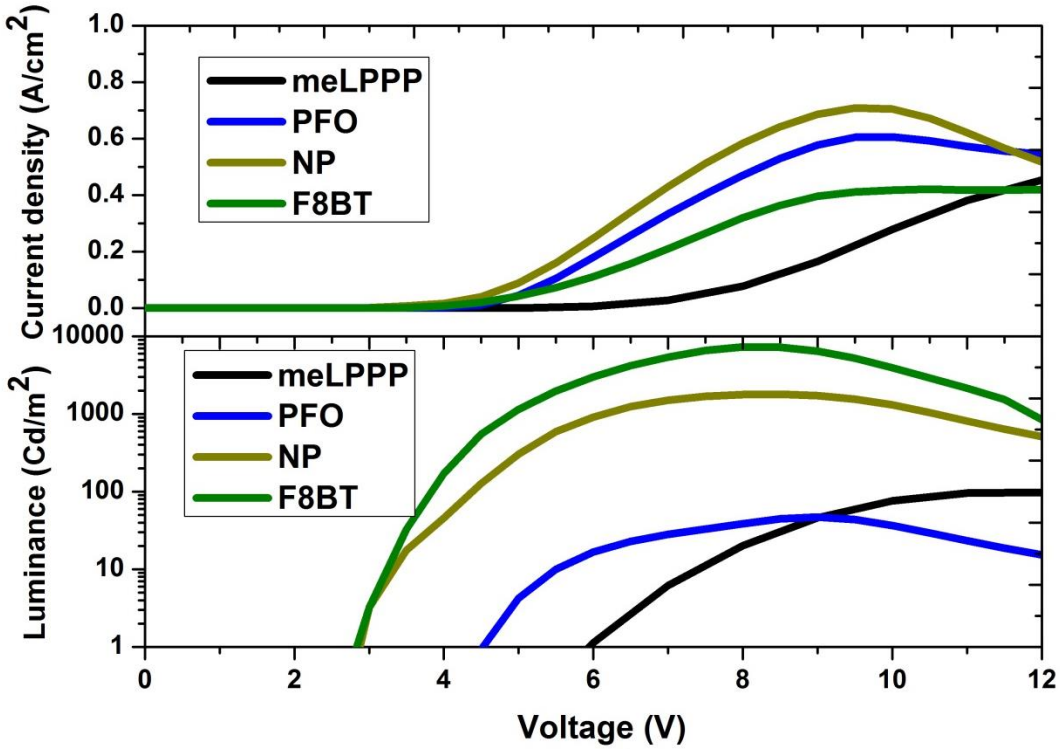

Figure 6-6 – JVL characteristics for OLEDs containing different host conjugated polymer as the emissive layer.

An alternative approach is to use a conjugated polymer that is transparent in the optical spectral region and transports only one type of charge carrier (holes). To investigate this, Polyvinylcarbazole (PVK) was used to host the Lumogen F dye. It has been shown that PVK can be a good host matrix for small molecules, especially for the iridium-based complexes in OLEDs [136]. Therefore, PVK was tested as a host polymer for the dye LF.

For EL measurements, devices with the structure ITO(100nm)/PEDOT:PSS(30nm) /PVK(150nm)/Ca(5nm)/Ag(100nm) were fabricated. The same structure was used for devices that incorporated the LF as a dopant material with a concentrations of 30:3 w/w and 30:10 w/w PVK:LF used. A comparison of the EL and PL spectra of the LF dye is illustrated in Figure 6-8. Here, the PVK electroluminescence, the PVK:LF electroluminescence and the photoluminescence from a control film of PMMA:LF thin film are compared.

Due to the fact that PVK has a HOMO and a LUMO energy levels located energetically at 5.5 eV and 2 eV, respectively [137] the devices have a high operational voltage. The device turns on above 9 Volts, as a result of the high LUMO energy of the PVK. The relative energy levels of the OLEDs fabricated are shown in Figure 6.7.

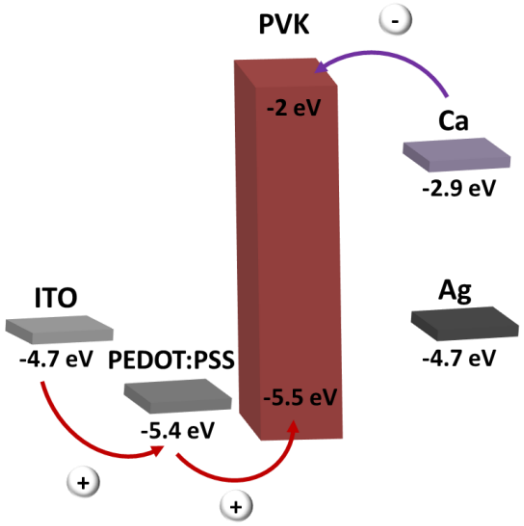

Figure 6-7 – Energy level scheme of various materials in the OLED

The EL spectrum was recorded both at 11 Volts (purple curve) and at 15 Volts (blue curve). At 11 Volts, there are two major peaks observed. One is located at high energy (2.96 eV) and the second at lower energy (2.13 eV). The high energy peak is related to the fully overlapping conformation (f-PVK), where both carbazole groups are aligned face to face in adjacent positions along the polymer backbone. The lower end peak is due to several different mechanisms including aggregation [138]. Upon increasing the applied bias, the low energy peak becomes more intense, whereas the higher energy peak becomes less pronounced and slightly shifts 42 meV, towards higher energies.

The PL emission spectrum of the PMMA:LF blend is shown in the red curve of figure 6-8. It can be seen that the spectrum overlaps significantly with the lower energy component of the EL spectrum of PVK.

The EL spectrum of the PVK:LF blend of lower and higher concentrations reveal one dominant peak at both blends (plotted using brown and orange curves) that is red shifted in comparison to all other recorded spectra.

The electroluminescence emission peak measured for the two different dye concentrations is located at 1.76 eV (705 nm), and neither coincide with PVK nor LF emission. We speculate that this emission is most likely charge transfer state created by both PVK and LF.

The JVL characteristics of the various devices were recorded. Figure 6-8 shows typical data For the PVK:LF (30:10 w/w) device to assess the potential of being used in polariton OLEDs. The maximum luminance (black curve) was recorded at 18 Volts with a value of 1 Cd/m^2. This very low brightness indicates that the PVK:LF system is impractical for use in organic polariton LEDs.

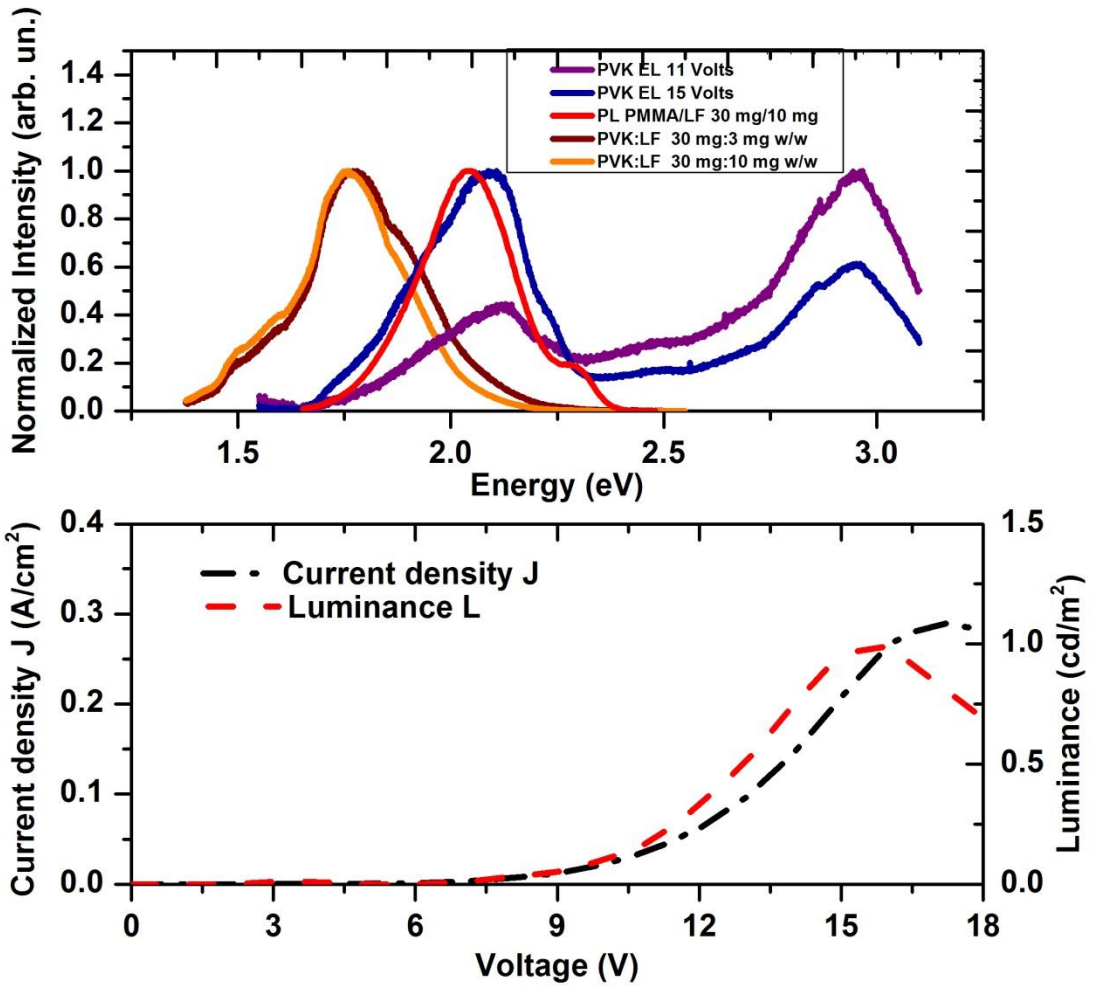

Figure 6-8 – (Upper part) EL and PL emission spectra of PVK and Lumogen F Orange 240. (Lower part) JVL characteristics of the PVK:LF 30:10 w/w blend OLED.

6.2.4 Conclusions

In this section the dye Lumogen F Orange 240 was studied due to its narrow exciton transitions and its high quantum yield. It was shown that when the dye is inserted in a microcavity structure the strong-coupling regime can be reached. However, incorporation of the dye in OLEDs is not sufficient in generating efficient devices. It was shown that if the host matrix is a fluorescent polymer then the device is not operational. Alternatively, if the host matrix is a transparent conjugated polymer (PVK) the device becomes operational, but the brightness is extremely low. Therefore, the Lumogen F Orange 240 cannot be used in OLEDs to directly generate electroluminescence.

6.3 5,12-diphenyltetracene

As shown in Chapter 4 the elementary core of 5,12-diphenyltetracene is tetracene. The material is chemically tailored with two phenyl side-rings that make the molecule highly soluble into common organic solvents. 5,12-diphenyltetracene is commonly referred to as DPT and has been previously used in OLED devices as a green emitting material [139]. It has a high quantum yield of approximately 80% in solution [140], and due to the energetic position of the singlet and triplet energy levels, it has been investigated for its potential use as an efficient singlet fission organic semiconductor targeting OPV applications [141]. Due to the high quantum yield, the high solubility into several organic solvents and the narrow absorption linewidths, the ability of DPT to form polariton states in organic microcavity light-emitting diodes has been explored.

6.3.1 Absorption and PL spectrum

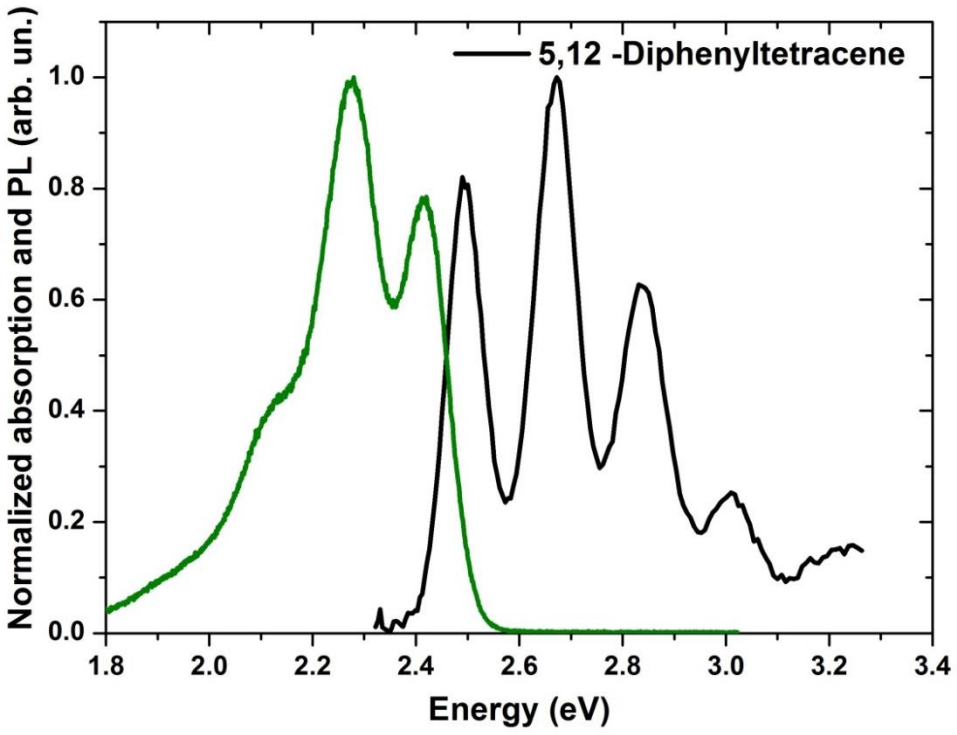

Figure 6-9 – Normalized absorption and PL spectrum of DPT dispersed in Poly(methyl methacrylate).

Figure 6-9 plots the absorption spectrum (black curve) and the emission spectrum (green curve) of 5,12-diphenyltetracene. The measurement was made on a thin film of DPT that was blended into a transparent and insulating PMMA matrix at a concentration of 3 % w/w and spin-cast from a toluene-based solution.

It can be seen that DPT has a well-resolved absorption spectrum. The main 0-0 transition is located at $E_{0\text{-}0}$=2.52 eV. The other absorption peaks are vibronic in nature and possess transitions that are energetically located at $E_{0\text{-}1}$=2.67 eV, $E_{0\text{-}2}$=2.84 eV and $E_{0\text{-}2}$=3.00 eV. The 0-0

absorption has a FWHM of 84.3 meV. The other 0-1, 0-2 and 0-3 of the vibrational replicas have characteristic linewidths of 93.4 meV, 105.1 meV and 199.9 meV, respectively.

The photoluminescence spectrum of DPT is plotted using a green curve in Figure 6-9. A small overlap with the absorption spectrum is observed. Moreover, a corresponding Stokes shift of 79.6 meV was determined. It can be seen that the photoluminescence spectrum is dominated by three emission peaks that are energetically located at 2.41 eV, 2.28 eV and 2.11 eV; within the green-yellow area of the visible spectrum.

6.3.2 Strong coupling in optical microcavities

To determine whether DPT can form polariton states in an optical microcavity, the organic semiconductor must be positioned close to the antinode of the optical field either in a pure form or as a dopant in a polymer matrix. This requires a deposition technique such as thermal evaporation or spin coating. Here, spin-coated was used where the matrix semiconductor was that of a conjugated polymer doped with a guest material. In this way more effective control over the dopant concentration and the layer thickness of the deposited film can be simultaneously achieved.

Two optical microcavities were investigated. The first is based on the blue-emitting conjugated polymer PFO and the second is based on the hole-transport polymer PVK. DPT is used as the strongly-coupled organic semiconductor in both systems. The comparison of the two types of approach is a necessary step towards the realization of a strongly-coupled OLED.

6.3.3 PFO:DPT host:guest system

The organic semiconductor microcavity fabricated consisted of a DBR mirror and a metallic mirror. The bottom DBR was deposited on a quartz crystal substrate by plasma enhanced physical chemical deposition (PECVD). It has composed of 10 λ/4 pairs of silicon dioxide (n=1.49) and silicon nitride (n=2.03). Its normal incidence transmission is shown in Figure 6-10. The DBR has a peak reflectivity of 98.9% at 2.52 eV (490 nm) which was determined via transmission measurements. PFO was doped with the molecular dye DPT at 3:10 w/w and was deposited onto the DBR via spin coating. This resulted in the creation of a 136 nm thick layer. To complete the structure a metallic silver mirror was deposited on top via thermal evaporation.

The center of the DBR reflectivity was designed to be close in energy to the 0-0 absorption transition of DPT. PFO was selected in order to facilitate efficient Förster energy transfer in analogy to the host:guest systems used in thermally evaporated organic semiconductor systems such as Alq_3:DCM [142]. In figure 6-10 (a) the PFO absorption (blue curve) and emission (dashed blue curve) spectra together with PL emission and absorption of DPT are shown in order to highlight the spectral overlap of the two species and to indicate their positions relative to that of the DBR mirror.

Both photoluminescence and reflectivity measurements were performed as a function of angle. For optical excitation, a 5 mW blue GaN CW laser was used. Light with energy 3.06 eV was imaged into the microcavity and was absorbed by the PFO:DPT blend. The angular dependent emission from the cavity is shown in Figure 6-10 (b). Superimposed in the same plot are data taken from reflectivity measurements as well as fitted data based on the coupled oscillator model. The fit is on the reflectivity spectrum and not on the PL. There are three polariton branches that are the result of the coupling of a photon with two excitonic (0-0) and (0-1) oscillator states.

The normalized photoluminescence contour plot shows light emitted mainly from the LPB states. A noticeable emission is as well observed from the middle and upper polariton branches.

The appearance of the higher energy branch emission is only visible since the plot is logarithmically scaled.

Plots of reflectivity and PL emission are shown in Figure 6-10 (d) for a series of angles. There is a good correspondence between PL emission and reflectivity spectra. Both peaks shift at higher angles as the angle of observation increases. The vertical dashed lines are there to highlight the position of the LPB dips and the corresponding LPB PL emission peaks.

The experimentally obtained reflectivity minima are depicted in the plot as oriented red-white triangles. The reflectivity data are fitted via a 3x3 Hamiltonian model, due to the coupling between the photon, and the two exciton modes (0-0) and (0-1). The resulting dispersion curves (black curves) indicate that the microcavity works in the strong-coupling regime. The photon mode appears in the form of purple-white circles and the exciton modes as black-white circles.

The values that are extracted from the coupled oscillator model provide with information about the photon mode E_γ= 2.396 eV, the exciton modes (0-0) $Ex_{0\text{-}0}$= 2.497eV and (0-1) $Ex_{0\text{-}1}$= 2.669 eV, the interaction potentials V_1=36 meV, V_2=26.7 meV and the effective refractive index of the system n_{eff}=1.897.

It is interesting to observe that there is a small shift of about 1-3 nm between the reflectivity and the PL data for the LPB. This shift was observed in many microcavity systems and is not influenced either by the organic semiconductor or the mirror alone. There are two reasons to explain this. Firstly, the area of the excitation spot that is probed each time is not the same. This may cause a small shift in the PL, reflectivity and EL measurements. Second, upon EL or PL excitation, the dielectric properties of the semiconductor change. This in turn can change the dispersion curve.

In the cavity fabricated the LPB is negatively detuned (δ=-99.7 meV) with respect to the 0-0 exciton transition. As the energetic separation between the two increases the LPB around $\theta=0^0$ will possess a reduced exciton character. In designing microcavities for polariton-based organic laser applications the LPB minimum has to be sufficiently mixed with the excitonic transition in order to properly engineer high exciton-polariton scattering rates towards low polariton branch states [46].

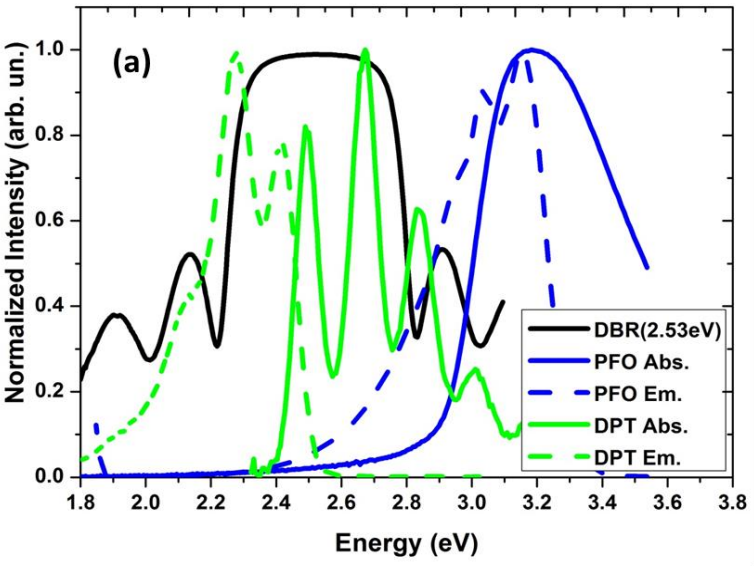
(a)
Normalized Intensity (arb. un.)
Energy (eV)
DBR(2.53eV)
PFO Abs.
PFO Em.
DPT Abs.
DPT Em.

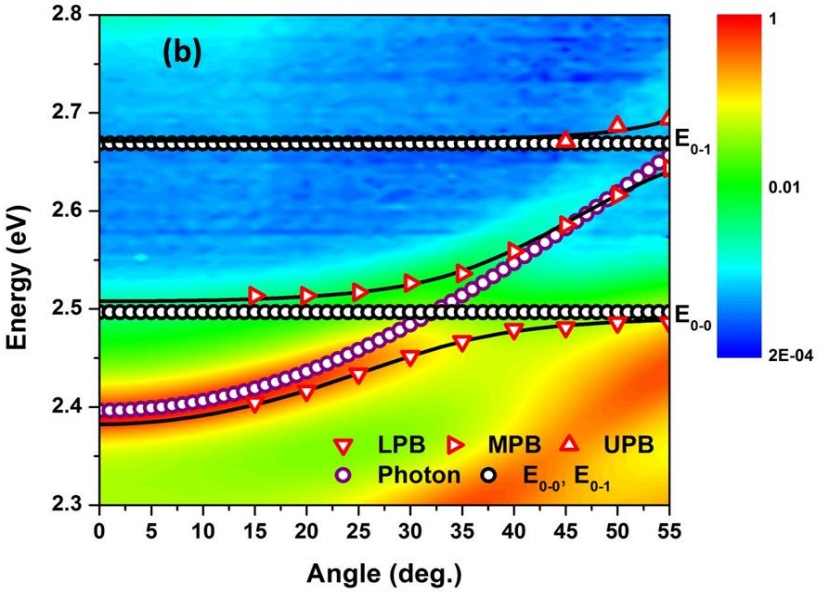
(b)
Energy (eV)
Angle (deg.)
E_{0-1}
E_{0-0}
LPB
MPB
UPB
Photon
E_{0-0}, E_{0-1}
1
0.01
2E-04

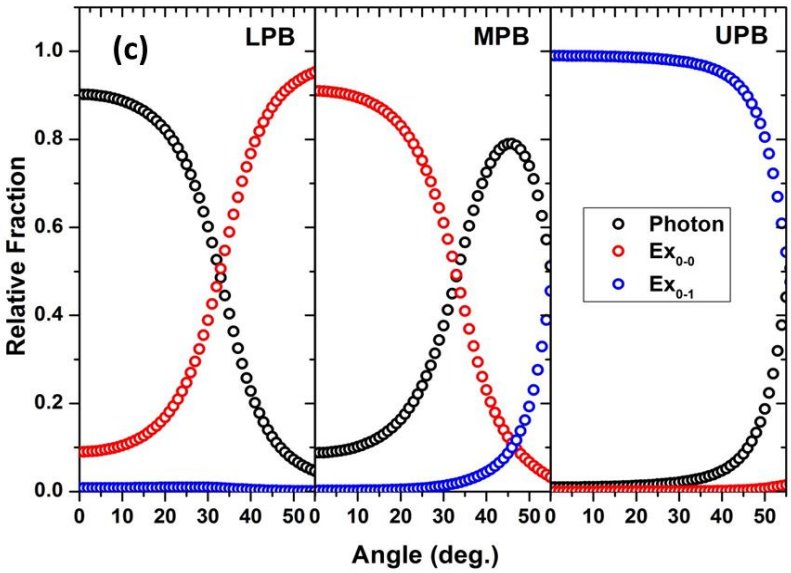
(c)
LPB
MPB
UPB
Relative Fraction
Angle (deg.)
Photon
Ex_{0-0}
Ex_{0-1}

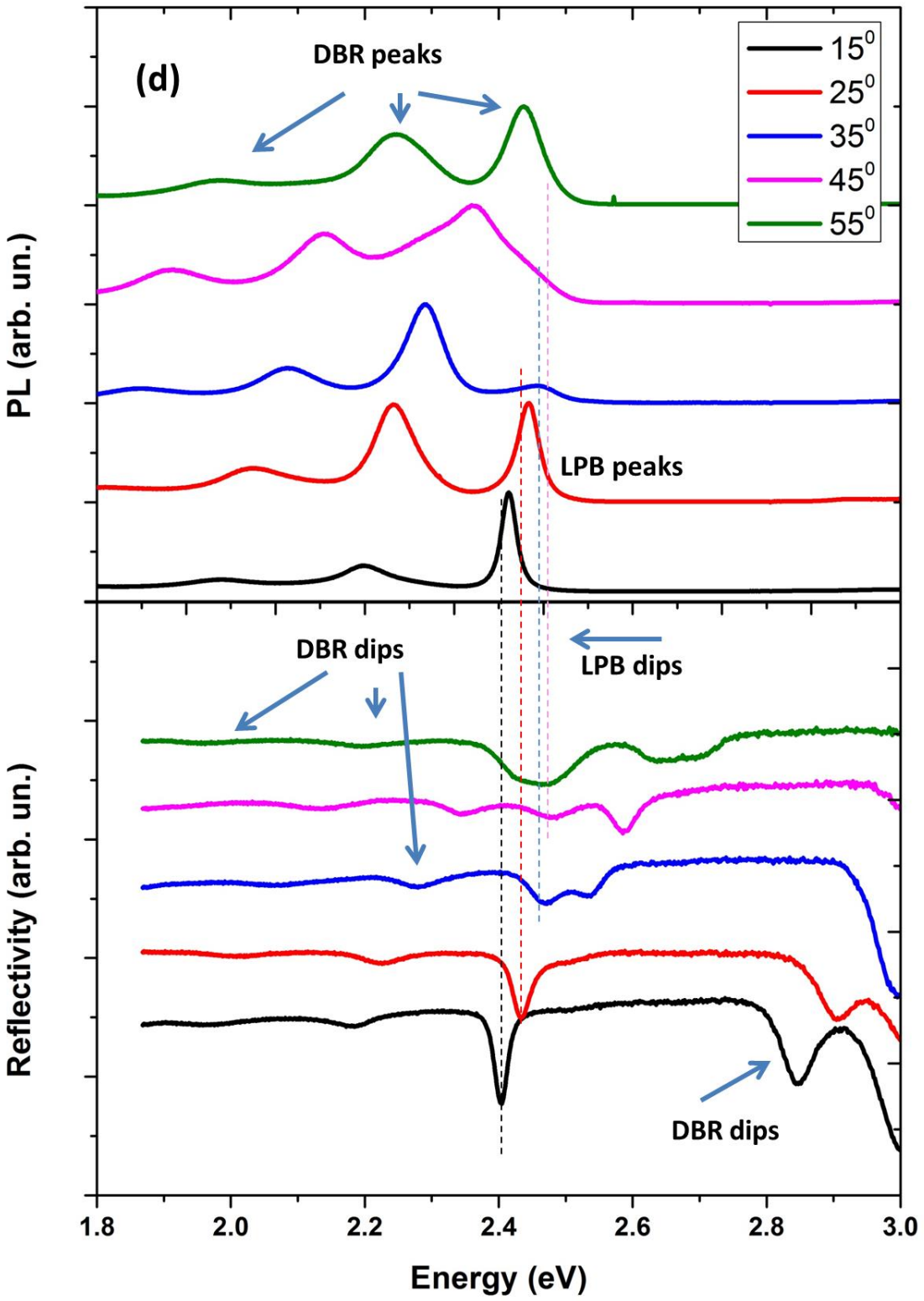

Figure 6-10 – (a): Normalized absorption and emission spectra of 5,12-diphenyltetracene and PFO along with the transmission spectrum recorded for the PECVD- fabricated DBR mirror having a 490 nm stop-band center. (b) A Lambertian corrected and normalized PL contour plot for the PFO:DPT host-guest system plotted on a logarithmic scale. (c) The fraction of the relative components for the three polariton branches. (d) Reflectivity and PL plots of the microcavity at 15^0, 25^0, 35^0, 45^0, and 55^0. The vertical dashed dips highlight the correspondence between the LPB reflectivity dips and LPB PL peaks.

The Hopfield coefficients of the polariton have been calculated and are shown in Figure 6-10 (c). In this cavity, a 3-level model was used to fit the interaction between the cavity photon

and the excitonic states. The model indicates that at 32^0, the photon (α^2), the exciton (β^2) and the vibronic (γ^2) fractions for the LPB are 0.495, 0.495 and 0.01, respectively. Similarly, at 57^0 the LPB is mostly excitonic (0.96), as seen from Figure 6-10 (c).

The middle polariton branch has a more excitonic character. At $\theta=0^0$ is composed of 91% (0-0) excitonic which then decreases at higher angle. The photon fraction of the MPB is 8.8% at $\theta=0^0$, and reaches a maximum value of 79% at 46^0. It then decreases at progressively lower angles in favour of the increasing (0-1) vibrational fraction.

Finally, the UPB fraction is 99% (0-1) and possesses only 1% of both photonic and (0-0) excitonic components at low angles. At the highest recorded angle, the (0-1) character reduces as the photonic fraction becomes more dominant.

6.3.4 PVK:DPT host:guest system

A second organic microcavity was fabricated without utilizing the blue emitting PFO conjugated polymer as the host system. Instead, a transparent PVK-based polymer was used as the host matrix for the DPT guest dye molecules. DPT was mixed with PVK at a concentration of 1:1 w/w in a toluene-based solution up to a total concentration of 20 mg/ml.

By employing either an emissive conjugated polymer or a non-emissive matrix polymer it is possible to explore the mechanisms responsible for populating the polariton states in a strongly-coupled system. In this way such systems can be compared and assessed prior to the fabrication of organic polariton LEDs.

To explore polariton emission a 5 mW CW GaN laser light source was used to populate the so-called DPT exciton reservoir. The reflectivity and PL recorded spectra are shown in Figure 6-11 (a) for a series of angles. The lower energy dip located at 2.22 eV in reflectivity spectrum and the respective PL emission that corresponds to this reflectivity dip is related to the DBR's dip position that shifts as the angle of observation increases. At low angles laser light leaks through the DBR dips. Additionally, at higher angles uncoupled light emission leaks through the cavity mirror and contributes to the observed signal.

At higher energies the first dip corresponds to the lower polariton branch. The dashed vertical lines highlight the PL and reflectivity energy position of the LPB. There is good correspondence between PL peaks and reflectivity dips, again with a small shift due to the area probed and the difference in the dielectric medium upon PL excitation. At the angle of 45^0 the DBR dip overlaps with the dip in the reflectivity spectrum which appears to be shifted at slightly lower energy.

The second reflectivity dip recorded at 2.51 eV (at 15^0) corresponds to the middle polariton branch that shifts to higher energies as the angle of observation increases. No PL was observed that corresponds to the middle polariton branch. The upper polariton branch dip minimum is clearly observed at high angles located at approximately 2.71eV. Again no PL emission was observed for the UPB.

The angle-dependent emission spectrum was recorded and it is shown in the logarithmically-scaled plot of Figure 6-11 (b). Superimposed are data recorded from reflectivity measurements and data corresponding to fitting parameters for this microcavity system. There are four main observations based on this plot:

The reflectivity data are shown by the red-white triangles and are well separated by the two absorption resonances Ex_{0-0} and Ex_{0-1} (white circles). The reflectivity data is based on a 3x3 Hamiltonian matrix. From the generated fits (black curves) based on the reflectivity data it is concluded that the system exists in the strong-coupling regime, with three polariton branches, namely the LPB, MPB and UPB.

The parameters that are extracted by fitting this system are the photon mode (blue-white circles) being an energy at normal incidence of E_0= 2.484 eV, the exciton resonances Ex_{0-0}= 2.463eV (0-0), Ex_{0-1}= 2.679 eV (0-1), and interaction potentials V_1=37.5 meV, V_2=36.4 meV and the effective refractive index n_{eff}=1.844.

It can be seen that the PL that is emitted under optical excitation is concentrated to the bottom of the LPB. No emission is observed from the other two polariton branches, in contrast to the experimentally observed emission that was recorded in the PFO:DPT strongly-coupled microcavity.

In the figure a small energy difference between the generated reflectivity LPB fit and the emission spectrum is observed due to the change in the dielectric properties of the organic semiconductor.

Figure 6-11 (c) shows the mixing Hopfield coefficients that are extracted from the three-level coupled oscillator model. The relative fraction is plotted versus the angle of observation for each polariton branch. The photon mode at $\theta=0^0$ thus the cavity is positively detuned. The lower polariton branch thus exhibits slightly higher excitonic (0.6) than photonic (0.39) character at $\theta=0^0$, and is less than 1% of the (0-1) transition. At higher angles this asymmetry increases.

The middle polariton branch contains significant contribution from all three components at all angles. Maximum mixing occurs at an angle of ~30^0, where the middle branch polariton character contains 10% (0,0) exciton and 10% (0,1) vibrational and ~80% photonic.

The upper polariton branch consists mainly of (0,1) vibronic and photonic character with some mixing of (0-0) excitonic character mainly at higher angles.

By evaluating the relative mixing coefficients of the polariton branches, the dye concentration in the microcavity and the energetic location of the bottom of the LPB, an engineering approach can be determined for designing polariton devices. The bottom of the lower polariton branch can be engineered to contain a higher fraction of excitonic character either by changing the exciton-photon detuning or by adding a higher content of the dye in the blend, or by both.

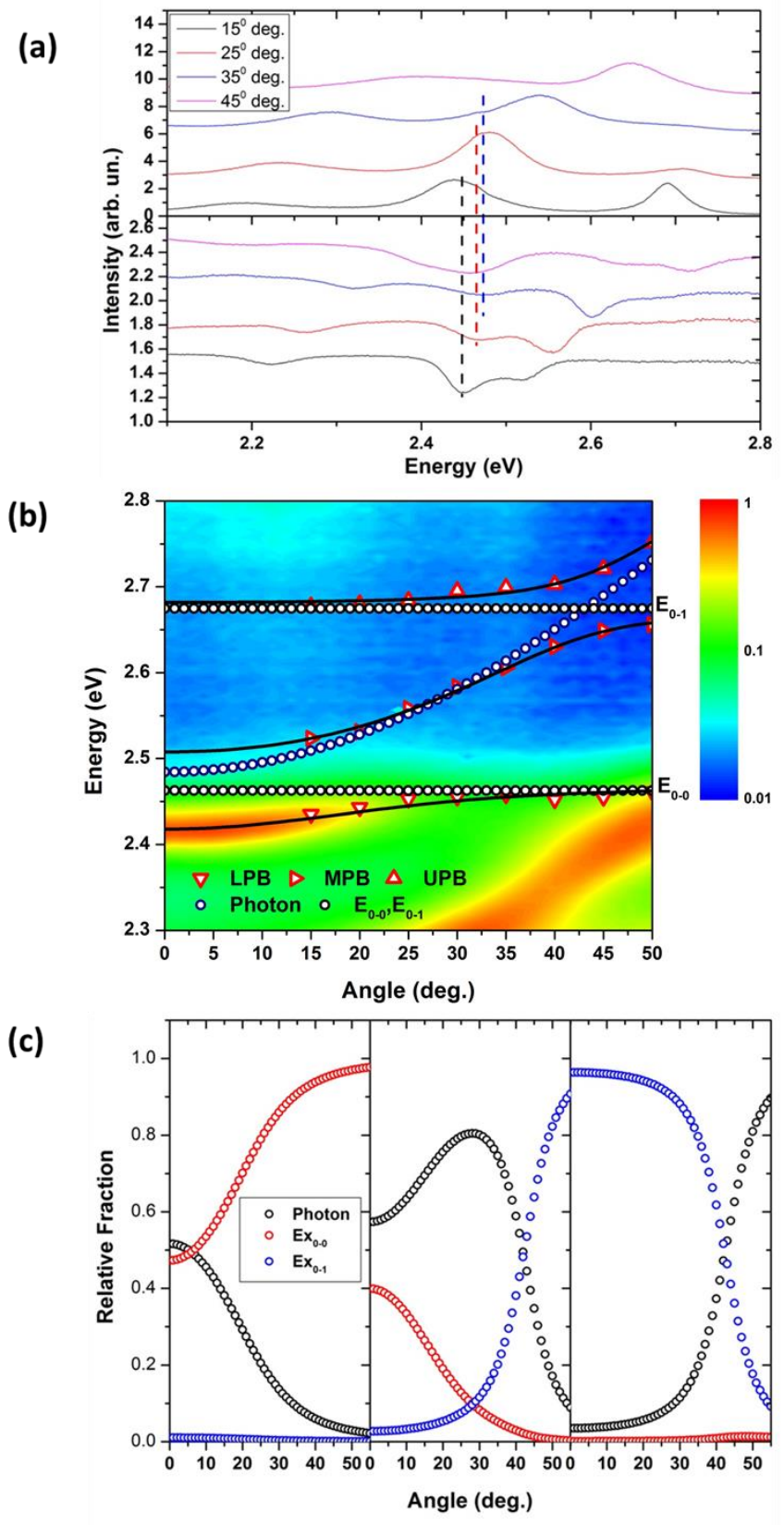

Figure 6-11 – (a): Reflectivity (lower part) and PL (upper part) recorded for a series of angles. Vertical dashed lines are there in order to highlight the energy position of the PL peaks and reflectivity minima correspondence. (b) Normalized and Lambertian corrected PL plot of 5,12-diphenyltetracene embedded in the PVK host matrix along with the reflectivity data and fitted dispersion curves. (c): The fraction of the relative components for the three polariton branches.

6.3.5 Main differences between the PFO:DPT to PVK:DPT systems

An important difference is observed between the two DPT-based microcavities. The PFO:DPT system exhibits a rather weak, but observable emission from the MPB and UPB. Instead, there is no emission observed from the middle or upper polariton branches for the PVK:DPT system.

The differences in the processes that are responsible for populating the polariton branches in the two strongly-coupled systems can be explained by considering the main available mechanisms of populating the polariton states in the PFO:DPT microcavity.

In Figure 6-10 (a) it is can be seen that the emission spectrum of PFO overlaps significantly with the DPT absorption spectrum. Therefore, through non-radiative Förster energy transfer from the PFO polymer to the DPT dye molecules, the DPT exciton reservoir can be populated.

Secondly, the uncoupled PFO polymer is able to undergo emission at energies that correspond to the two higher energy polariton branches of the system, allowing the population of the LPB and UPB via optical pumping.

Thirdly, a substantial amount of the GaN blue laser light emitting at 3.06 eV will be absorbed by the high energy absorption states of diphenyltetracene; therefore, populating directly the high energy k-states that correspond to the exciton reservoir.

Finally, a small amount of DPT molecules will be weakly coupled. Depending on the detuning the emission peaks of DPT will be energetically in the neighbourhood of the LPB where the 'optical pumping' mechanism will be responsible for some of the LPB content.

In the PVK:DPT strongly-coupled microcavity the first two mechanisms are absent; therefore, this is suggestive of the fact that these two processes are most important in making visible the MPB and LPB to the external observer.

6.3.6 Microcavity OLEDs based on PVK:DPT blends.

A microcavity OLED and a conventional OLED device were fabricated based on the procedures detailed in Chapter 4. As the active layer the devices contained a 50 nm of DPT embedded in PVK. The selection of PVK as the host for DPT was based on the fact that PFO:DPT-based OLEDs degrade fast at these high dye concentrations.

Two sets of devices were fabricated. OLED devices that incorporated a bottom-based DBR mirror are referred to as microcavity OLEDs and devices which did not incorporate this mirror and are referred to as conventional devices. The microcavity OLED device structure under investigation consisted of:

Glass(0.7mm)/DBR/ITO(200nm)/PEDOT:PSS(35nm)/PVK:DPT(240nm)/Ca(5nm)/Ag(100nm).
The DBR was made of alternative layers (10 pairs) of SiO_2 (n_L=1.49) and TiO_2 (n_H=2.65), with the center of the stop-band located at 2.3 eV (540 nm).

It should be noted that in addition to the inclusion of the DBR mirror in the microcavity OLED, the ITO anode thickness was 200-nm-thick in the microcavity OLED in order to achieve less sheet resistance allowing higher amount of charge carriers to be injected and thus to improve the device's performance. This is anticipated to induce additional absorption losses.

6.3.7 Microcavity-OLED

Figure 6.12 (a) shows the reflectivity spectrum at $\theta=20^0$ of the microcavity OLED fabricated. It is seen that the reflectivity is very high in the stop band to allow any observation of dips in the spectrum. Moreover, a plot of EL emission intensity as a function of angle is shown in Figure 6-12 (b). There are three main characteristics of this plot.

Firstly, there is a weak EL emission located around 2.36 eV that slightly shifts at higher energies as the angle of observation increases. This is close in energy to the emission peak of 2.4 eV observed in conventional OLEDs. Secondly, emission escaping through the DBR dips is observed at higher angles that shows angle dependence. Thirdly, EL emission stopped from being recorded at 42^0 where the devices exhibited current leakage. This is likely to be caused by the lack of a hole blocking material that can confine holes in the emissive layer region. All devices made similarly exhibited the same behaviour after a few minutes of operation.

Figure 6-12 (c) shows the EL spectrum recorded at $\theta=0^0$. As is seen from the plot there are two main peaks observed, one located at 2.36 eV and a second weaker peak located at 2.28 eV. The signal recorded was very weak.

Therefore, it cannot be concluded weather the system exists or not in the strong-coupling regime. A lower reflectivity DBR is required so as to observe dips in the reflectivity spectrum in order to examine if the system is strongly-coupled.

6.3.8 Conventional-OLED

The EL spectrum from the conventional device is significantly different from the MCOLED. This is shown characteristically in the linearly-scaled EL plot of Figure 6-13 (a). The bottom emitting OLED does not exhibit angle-dependent emission, but coincide with the emission spectrum of DPT, for the $0\rightarrow i$ transitions, with i=0,1. These correspond to the energies: $E_{0\rightarrow0}$=2.42 eV and $E_{0\rightarrow1}$=2.27 eV. The difference in the lower energy peak position between PL and EL as seen in figure 6-13 (b) that shows that the EL spectrum and the PL spectrum at $\theta=0^0$ of DPT have peaks corresponding to $0\rightarrow i$ transitions, with i=2,3. For EL these energy peak at $E_{0\rightarrow2}$=2.03 eV, $E_{0\rightarrow3}$=1.88 eV and for PL at $E_{0\rightarrow2}$=2.1 eV, $E_{0\rightarrow3}$=1.95 eV.

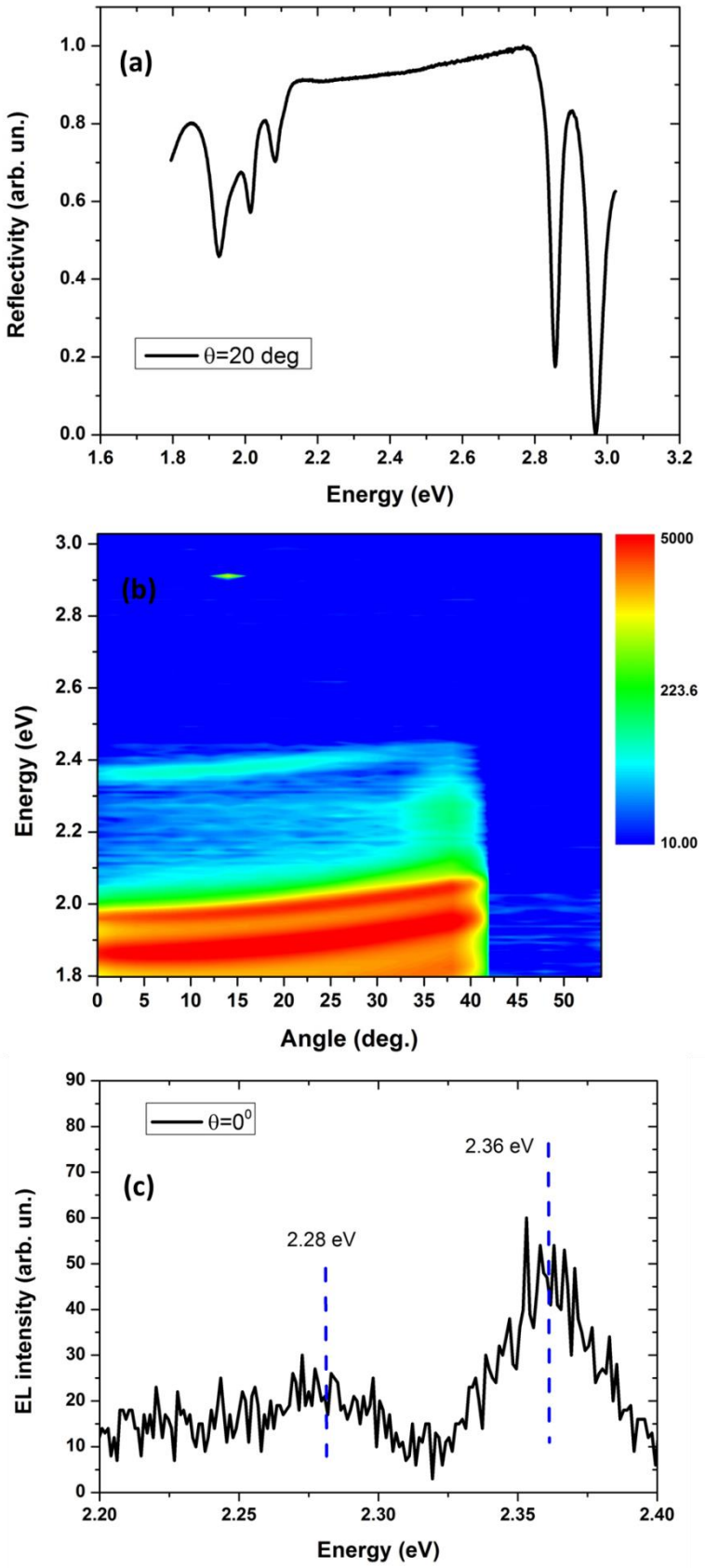

Figure 6-12 – (a): Reflectivity spectrum of the MCOLED fabricated at 20^0. (b) Logarithmically-scaled EL contour plot of MCOLED containing DPT molecules embedded in a PVK matrix. (c) Electroluminescence plot at $\theta=0^0$ of the MCOLED.

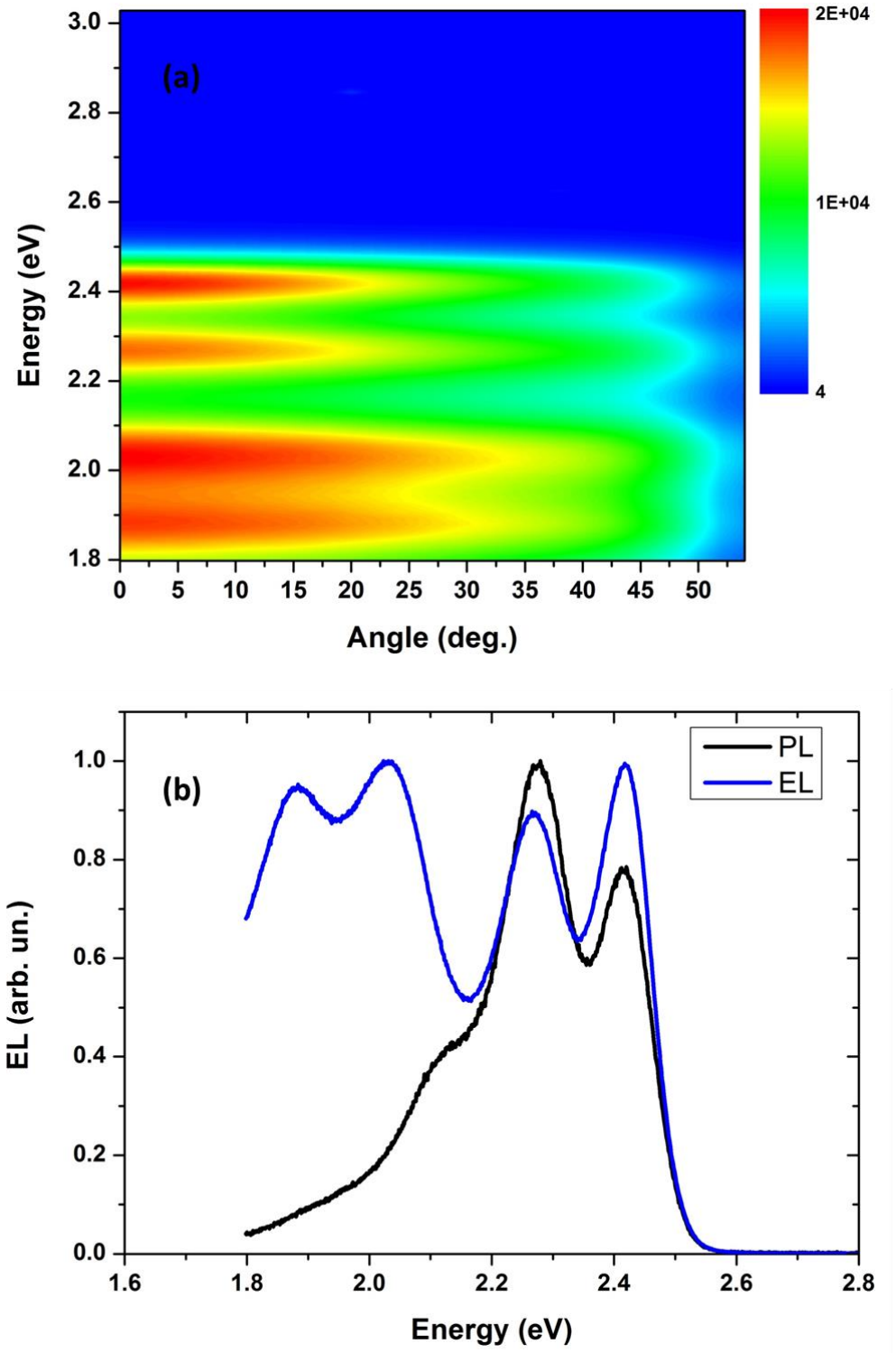

Figure 6-13 – (a): Linearly-scaled EL plot from a conventional OLED device. (b) EL spectrum and PL at $\theta=0^0$ of DPT

6.3.9 Conclusions

This section examined the dye 5,12-diphenyltetracene blended with the emissive conjugated polymer PFO and with the non-emissive conjugated polymer PVK in optical microcavities and OLEDs.

It was shown that DPT reaches the strong-coupling regime when embedded in microcavity structures with reflectivity and PL spectra corresponding well in each of the systems fabricated. Their dispersion curves are described by a three-level coupled harmonic oscillator model. Three branches appear as the lower, the middle and the upper polariton branches.

Emission from the middle and the upper polariton branches is only visible in microcavities based on the PFO:DPT blend. Their observation is more likely to be caused by the spectral overlap of the PFO emission with that of the middle and upper polariton branches. No such emission is observed in microcavities for PVK:DPT based blends.

In microcavity OLEDs fabricated, it cannot be resolved if the system exists in the weak- or in the strong-coupling regime due to the high reflectivity of the DBR mirror. The MOLED show limited lifetime due to current leakage. The combination of high charge imbalance, lack of hole blocking layer/electron transport layer, and the higher ITO conductivity may contribute to this device instability.

6.4 Ladder-type polymer meLPPP

All the organic materials discussed so far that have demonstrated strong light and matter interaction in an optical microcavity were based on small molecules either in the form of blends or in the form of self-assembled, J-aggregated thin films (e.g. see Chapter 5).

Polymers are macromolecular structures composed of a smaller repeating molecular unit. They have been used extensively in polymer light-emitting diodes (PLEDs) as the main electroluminescent component [143-145].

In this section attention turns to the use of the methyl-substituted ladder type poly(para-phenylene) conjugated polymer (meLPPP) as the active medium in both optical microcavities and LEDs, as meLPPP is the only polymer so far to form a Bose-Einstein Condensate at room temperature [24]. This is based on the narrow absorption spectrum of meLPPP and its high photoluminescence quantum yield which is approximately ~unity in dilute solutions [92].

6.4.1 Absorption and emission spectrum of meLPPP thin films

The absorption and the photoluminescence spectrum of meLPPP are plotted in Figure 6-14. The electronic (0,0) and vibrational transitions (0,1), (0,2) are observable in the absorption spectrum at 2.744, 2.927 and 3.118 eV. It can be seen that meLPPP has relatively narrow electronic and vibrational transition linewidths, with (0,0), (0,1) and (0,2) peaks having a FWHM of 160, 180 and 190 meV, respectively.

The PL spectrum is characterized by narrow emission with peaks located at 2.676, 2.523 and 2.354 eV. MeLPPP is also characterised by a small Stokes shift of 58 meV, with PL and absorption being approximate mirror images of one another. The small Stokes shift together with the relatively narrow electronic and vibrational transitions have been attributed to the molecular geometry of the polymer backbone. This arrangement strongly prohibits any steric effects in the molecular backbone and therefore reduces electronic disorder [91]. It is the existence of such narrow, well-defined, high oscillator-strength transitions that make meLPPP a good candidate for strong-coupling studies.

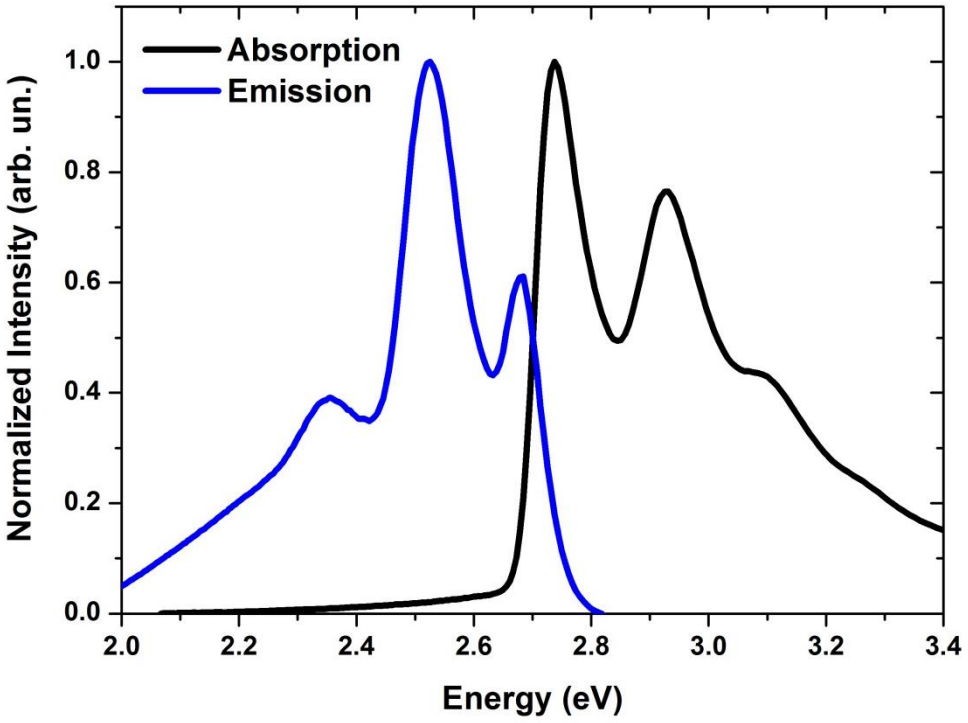

Figure 6-14 – Absorption (black curve) and photoluminescence (blue curve) spectrum of meLPPP from a spin coated thin film on quartz glass.

6.4.2 Optical microcavity system

To demonstrate that meLPPP can reach the strong-coupling regime, a DBR-metal mirror organic microcavity was fabricated. The bottom DBR mirror consisted of 10 pairs of SiO_2/SiN_x and was deposited by PECVD onto a glass substrate. The centre of the stop band was located around 2.63 eV (λ = 470 nm). The cavity medium consists of a 25 nm thick meLPPP film positioned between two 50 nm thick PVA optical spacer layers. The top cavity mirror consists of an evaporated 100-nm-thick silver film, forming a λ/2 microcavity, as seen in Figure 6-14 (a). PL measurements were obtained by optically exciting meLPPP by a 5mW GaN laser source, at 3.05 eV. Simultaneously, reflectivity measurements were carried out as a function of incident angle θ using a collimated white light source.

Figure 6.14 (c) shows the reflectivity and PL emission recorded for increasing angle of observation. 15^0 was the smallest angle that reflectivity could be measured. There is a good correspondence between reflectivity and PL emission. The reflectivity dip located at about 2.4 eV for 15^0 correspond to the DBR dip that shifts in energy as the angle of observation increases. Light can escape through the mirror as seen from the respective PL spectrum. A second dip observed approximately at 2.64 eV shifts in energy as the angle of observation increases for both reflectivity and PL spectra. At high angles of observation a third and a fourth deep appear in the reflectivity spectrum, however, no PL was observed at these energies. The pink dip at 45^0 and the PL seem to be slightly shifted. This is due the possible overlap with some uncoupled emission of the (0,0) transition.

Figure 6.15 (b) shows the PL plot of the recorded spectrum as a function of the angle of observation. Only the LPB emission is visible. Each spectrum is characterised by a number of dips in reflectivity (black, lower case triangles, circles and squares) that undergo a series of anti-crossing about the energies of the (0,0) and (0,1) meLPPP transitions as marked in the figure. Data were obtained by fitting the reflectivity dips based on a 3-level coupled harmonic oscillator (black solid curves) as the photon field is coupled to two exciton transitions, $E_{0\text{-}0}$ and $E_{0\text{-}1}$.

The fits to the polariton branches are based on a 3-level matrix Hamiltonian model. The parameters that are extracted for this system are the photon mode E_0= 2.671 eV, the exciton resonances $E_{0\text{-}0}$=2.724eV, $E_{0\text{-}1}$= 2.917 eV, the interaction potentials V_1=60.5 meV, V_2=49.4 meV and the effective refractive index n_{eff}=1.829.

Three polariton branches are identified; a lower polariton branch (LPB), a middle polariton branch (MPB) that results from photon-driven (white solid curve) mixing between the (0,0) and (0,1) transitions and an upper polariton branch that mainly consists of a mixture between cavity photon and the (0,1) meLPPP transition.

Emission is only observed from the lower polariton branch; there is no emission signal corresponding to the middle or the upper polariton branches.

There is an excellent agreement between the dispersion fits based on the reflectivity data and the PL emission spectrum.

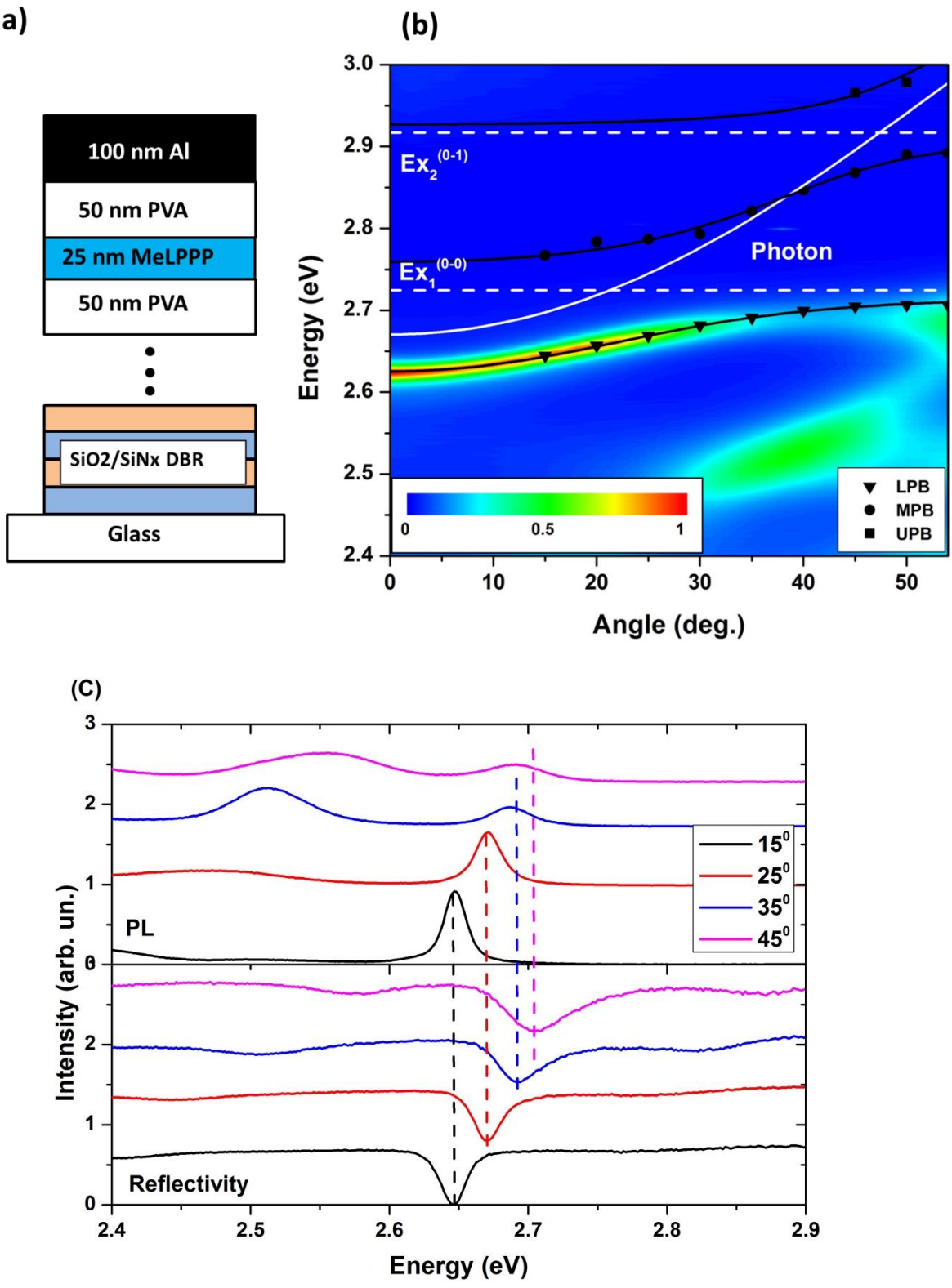

Figure 6-15 (a) – A DBR-metal organic microcavity that contains the ladder polymer meLPPP positioned at the antinode of the structure. (b) Normalized and Lambertian corrected PL plot recorded for the fabricated organic microcavity of Figure 6-14 (a). Reflectivity data and fits based on a coupled harmonic oscillator model are superimposed on the same graph as well. (c) PL and reflectivity data for different values of angle of observation.

Figure 6-16 details the Hopfield coefficients of the (0-0) and (0-1) transitions with that of the photon cavity mode. The lower polariton branch exhibits higher photonic (0.81) than excitonic

(0.16) character at θ=0. At the highest angle this asymmetry increases. At these angles the LPB is mainly excitonic (0.95) and less photonic (0.047). The LPB is more photonic and excitonic (0-0) at the angle of 49^0.

The middle polariton branch exhibits stronger mixing between the two excitonic transitions and the cavity mode. The highest amount of mixing is observed at an angle of 38^0. At this angle, the two excitonic resonances contribute equally (0.18), whereas the photon component has its highest value (0.64). At lower angles, the (0-0) transition dominates, but at higher angles the vibronic transition is more pronounced.

For the upper polariton branch, the mixing of the three components is more straightforward. The UPB mainly composed of $E_{0\text{-}1}$ at a range of angles between 0^0-40^0. The photonic coefficient becomes more significant for angles higher than 40^0 and contributes equally with the $E_{0\text{-}1}$ mode (0-1) at 49^0. At the highest angle of observation the UPB is mainly photonic (0.78) rather than excitonic (0.02) or $E_{0\text{-}1}$ (0.2).

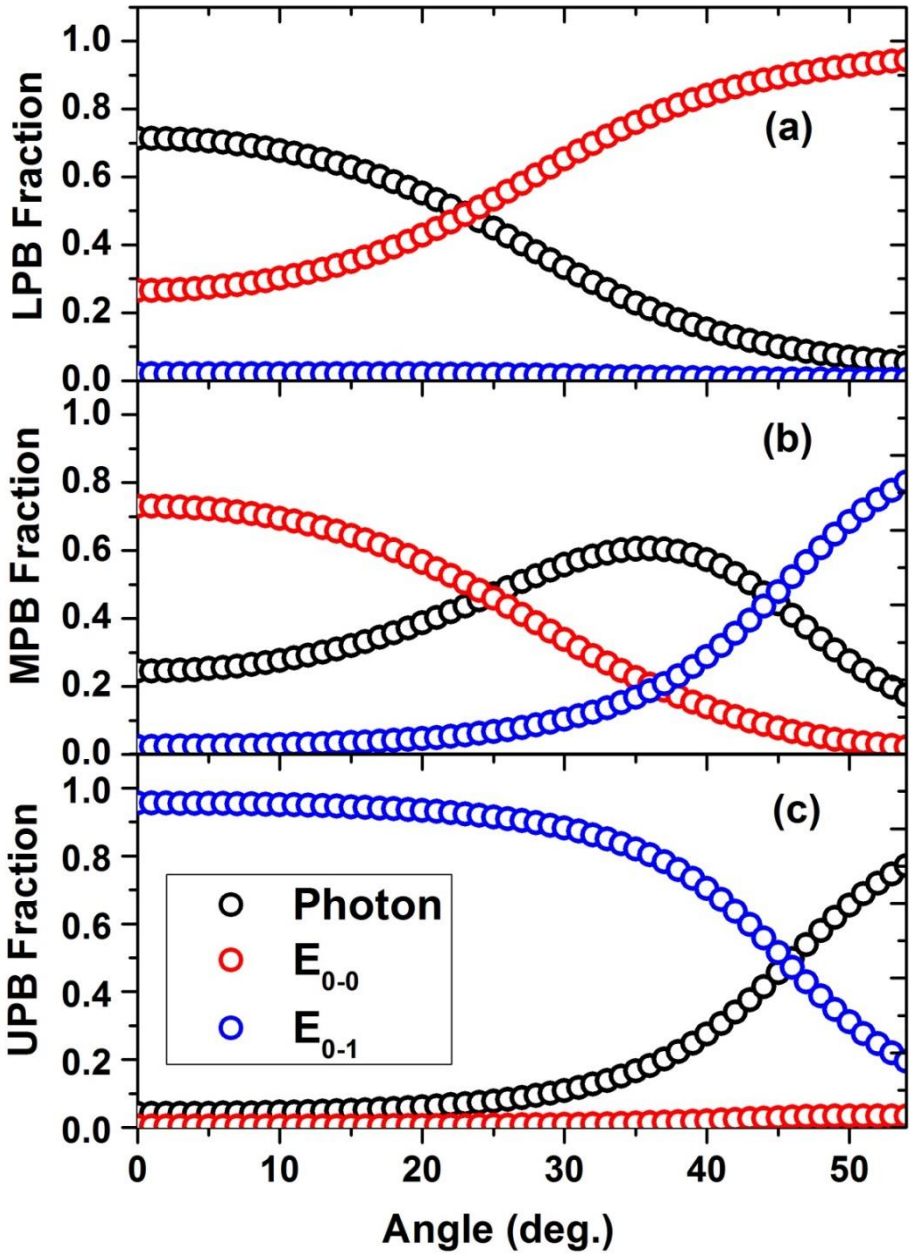

Figure 6-16 – Relative Fractions of the photon mode (black circles), the excitonic mode (0-0) (red circles) and the vibronic mode (0-1) (blue circles) that contribute to the LPB, the MPB and the UPB.

6.4.3 Organic microcavity LED

In section 6.4.2 it was shown that the ladder-type polymer meLPPP can be used as the strongly-coupled organic semiconductor in optical microcavities. Simultaneously, meLPPP can be used as the blue emissive material in organic light-emitting diodes, as has been previously reported [146]. Therefore, it can be assumed that the incorporation of meLPPP in an organic microcavity LED can also result in strong coupling and polariton electroluminescence.

The full process of fabricating a metal-metal mirror microcavity OLED was described in detail in Chapter 4. The device structure constructed is shown in Figure 6-16 (a) along with the thickness of each layer in the device. The function of each organic material is briefly explained.

On top of the ITO layer a 30-nm-thick and thermally evaporated aluminium layer was deposited as the bottom semi-transparent mirror. Aluminium has been selected over silver because it has slightly higher reflectivity in the blue spectral region and significantly higher reflectivity in the UV spectral region, respectively. On top of this, 30 nm of MoO_3 was thermally evaporated to both reduce the roughness of the metal electrode and to allow the spin coating of an alcohol-based spacer layer owing to its hydrophilic nature.

Following this, approximately 100 nm of the conjugated polymer PAni was deposited by spin coating. The selection of PAni over PEDOT:PSS was based on two main considerations. Firstly, the PAni film has a characteristic smooth surface after spin coating, in contrast to the high amount of undissolved PSS aggregates that are usually observed in spin coating PEDOT:PSS films. Secondly, the PEDOT:PSS solution used could only form good quality film having a thickness of around 40 nm. For higher thicknesses, the spin speed that was required was relatively low and consequently the film quality was very poor. PAni however formed smooth layers having a thickness of 100 nm. Finally the ladder polymer meLPPP was spin coated on the PAni HTL from a toluene-based solution. Thermal evaporation of a Ca/Al top mirror completed the device.

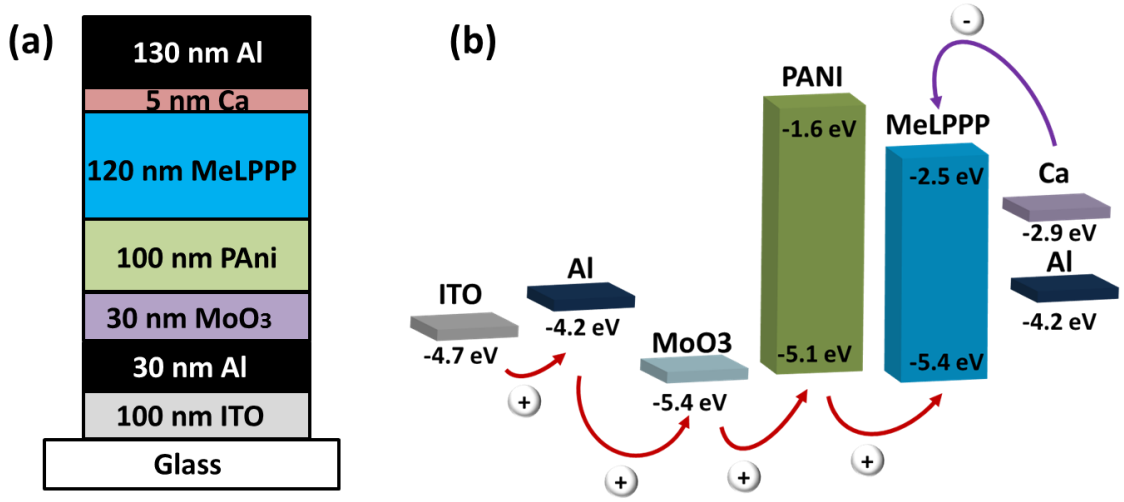

Figure 6-17 – (a) Microcavity OLED structure with the Ladder-type polymer mLPPP as the emissive layer, and (b) the energy levels of the corresponding materials along with the path of the charge carriers travelling through the organic layers.

Figure 6-16 (b) shows the flow of electrons and holes through the respective energy levels of each material in the microcavity OLED under electrical operation. Holes are injected from the ITO to the Al metal without any energy barrier. However, there is a large injection barrier for holes of about 1.2 eV that exists at the MoO_3/Al interface. Holes from the metal oxide will travel around 100 nm before they reach the PAni/meLPPP interface. Due to the relative HOMO

energy position of the two materials, holes are expected to jump to the meLPPP layer where they will meet with electrons to form excitons. Simultaneously, the injection of electrons from Ca/Al electrode to the LUMO level of meLPPP occurs by overcoming a small energy barrier (0.4 eV).

Figure 6.17 (a) shows the reflectivity spectrum and the EL emission spectrum from the cavity at 12 V of applied bias as a function of angle. In the reflectivity spectrum a dip appears that shifts in energy as the angle of observation increases. Three dips in the spectrum are also visible. These correspond to 2.72, 2.83 and 3.12 eV, but do not shift in energy. The peak at 2.72 eV coincides with the absorption resonance $E_{0\text{-}0}$. The peak at 2.83 eV does not correspond to a resonance of the meLPPP spectrum and must be the result of another material used in the structure or some structure imperfection. At 3.12 eV the peak is visible for increased recording angles and disappears at 50^0 where high light scattering of the optical array causes signal variations.

The EL spectrum of the MCOLED has two main characteristics. The first emission peak is located at 2.54 eV which coincides with the emission of the $E_{0\text{-}1}$ resonance of meLPPP. The second peak shifts in energy as the recording angle increases and overlaps with the $E_{0\text{-}0}$ emission peak. The EL spectrum was plotted as a function of angle as seen in figure 6.17 (b). In the same graph, the reflectivity dips recorded for the same structure are shown for comparison.

The PL emission plot that was obtained under optical excitation is shown in Figure 6.17 (c) for the same microcavity OLED. The plot is logarithmically-scaled to highlight that the peak emission as a function of angle does not shift. Three peaks are again observed. The 2.7 eV and 2.53 eV correspond to the emission peaks of the transitions (0-0) and (0-1). A third peak is observed at 2.64 eV that overlaps with that of 2.7 eV.

All these observations suggest that the system exists in the weak coupling regime. The peak that shifts in energy is caused by electroluminescence mainly of the 0-0 transition that leaks through the photon mode. The second EL peak in the spectrum that does not shift with angle is emission caused by the 0-1 transition. Reflectivity dips that do not shift in energy with angle and coincide with the location of the absorption transition (0-1), are typically met in weakly-coupled systems of microcavity structures.

It was shown in previous section that the ladder-type polymer meLPPP can be strongly-coupled in an optical microcavity. However, when a microcavity OLED was fabricated the system exists in the weak coupling regime. The MCOLED system incorporates PAni with absorption spectrum overlapping with the absorption spectrum of meLPPP as is seen in figure 6-18 (a).

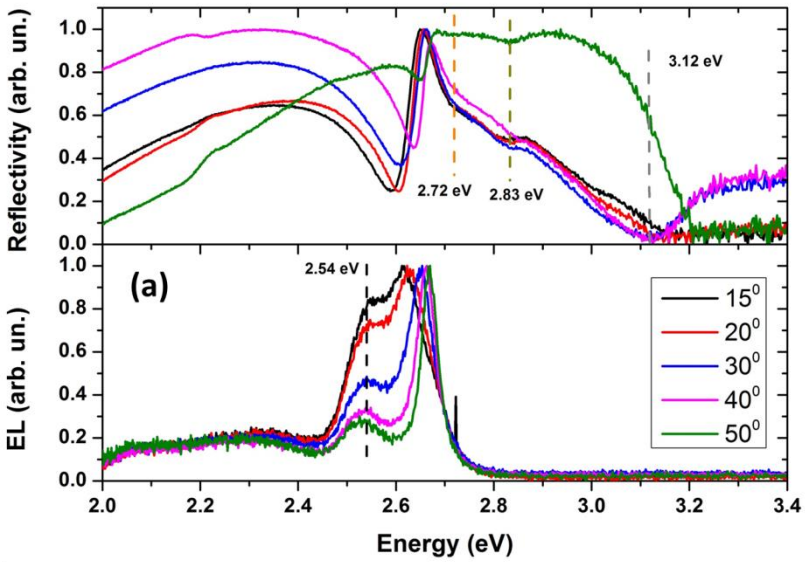
Reflectivity (arb. un.)
1.0
0.8
0.6
0.4
0.2
0.0
3.12 eV
2.72 eV
2.83 eV
(a)
2.54 eV
EL (arb. un.)
15⁰
20⁰
30⁰
40⁰
50⁰
2.0
2.2
2.4
2.6
2.8
3.0
3.2
3.4
Energy (eV)

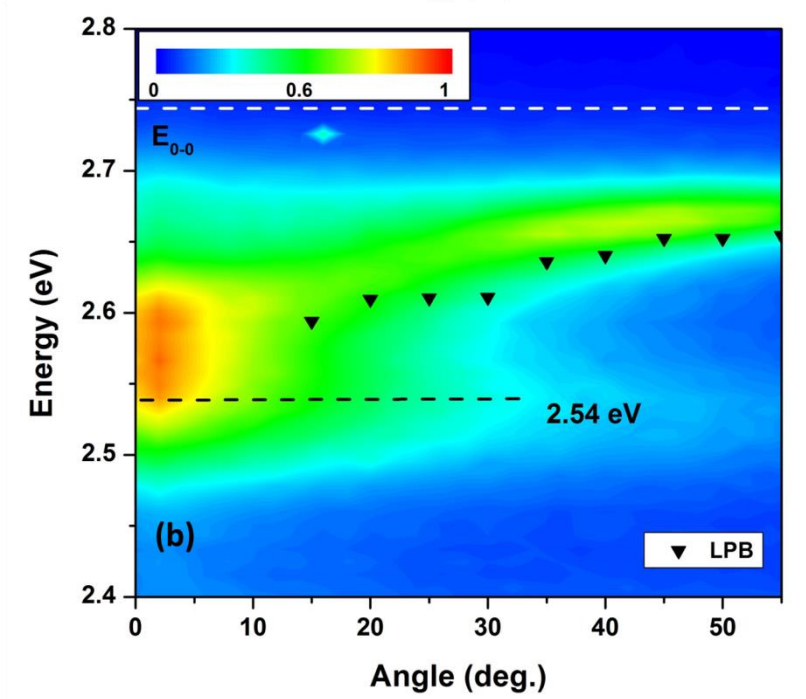
2.8
0
0.6
1
E0-0
2.7
Energy (eV)
2.6
2.54 eV
2.5
(b)
LPB
2.4
0
10
20
30
40
50
Angle (deg.)

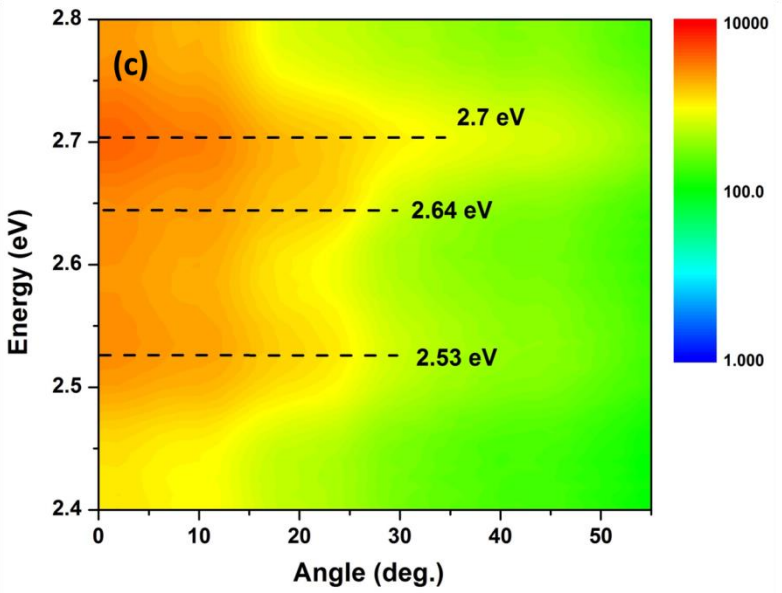
2.8
(c)
2.7 eV
2.7
2.64 eV
Energy (eV)
2.6
2.53 eV
2.5
2.4
0
10
20
30
40
50
Angle (deg.)
10000
100.0
1.000

Figure 6-18 – (a) Reflectivity and EL spectra as a function of angle for a MCOLED. (b) Linearly scaled EL as a function of angle under electrical excitation with reflectivity dips superimposed on the same graph. (c) Logarithmically scaled PL emission plot that was obtained under optical excitation.

To understand more of the role of PAni in the device, the absorption and PL spectra were recorded and shown in the upper part of Figure 6-18 (a). Pani has two absorption bands. The high energy band is composed of the two overlapping peaks. The first is located at 3.56 eV and the second at 2.91 eV. A lower energy band is located energetically at 1.58 eV. The PL spectrum is composed of a strong emission peak at 3.06 eV and a second peak at about 2.41 eV. The lower part of figure 6-18 shows the meLPPP/PAni bilayer absorption spectrum inside the MCOLED.

A second microcavity was fabricated by replacing the PAni layer with a 135 nm transparent polymer PVA with a refractive index of 1.5. If the PAni layer is responsible for the system existing in the weak-coupling regime then the microcavity that contains PVA will be strongly-coupled with angular-dependent PL emission stemming directly from the LPB under the same conditions of optical excitation.

Figure 6-18 (b) indicates that the system exists in the strong-coupling regime and the emission spectrum originates from the LPB. This emission plot shows the PL spectrum under optical excitation, the 0-0 absorption transition $E_{0\text{-}0}$, the reflectivity data corresponding to the LPB and the generated fit based on the 3-level model of coupled-harmonic oscillators. The extracted parameters for this system are the photon mode E_0= 2.99 eV, the exciton resonances $E_{0\text{-}0}$= 2.699eV, $E_{0\text{-}1}$= 2.919 eV, the interaction potentials V_1=125.5 meV, V_2=133.8 meV and the effective refractive index n_{eff}=1.73.

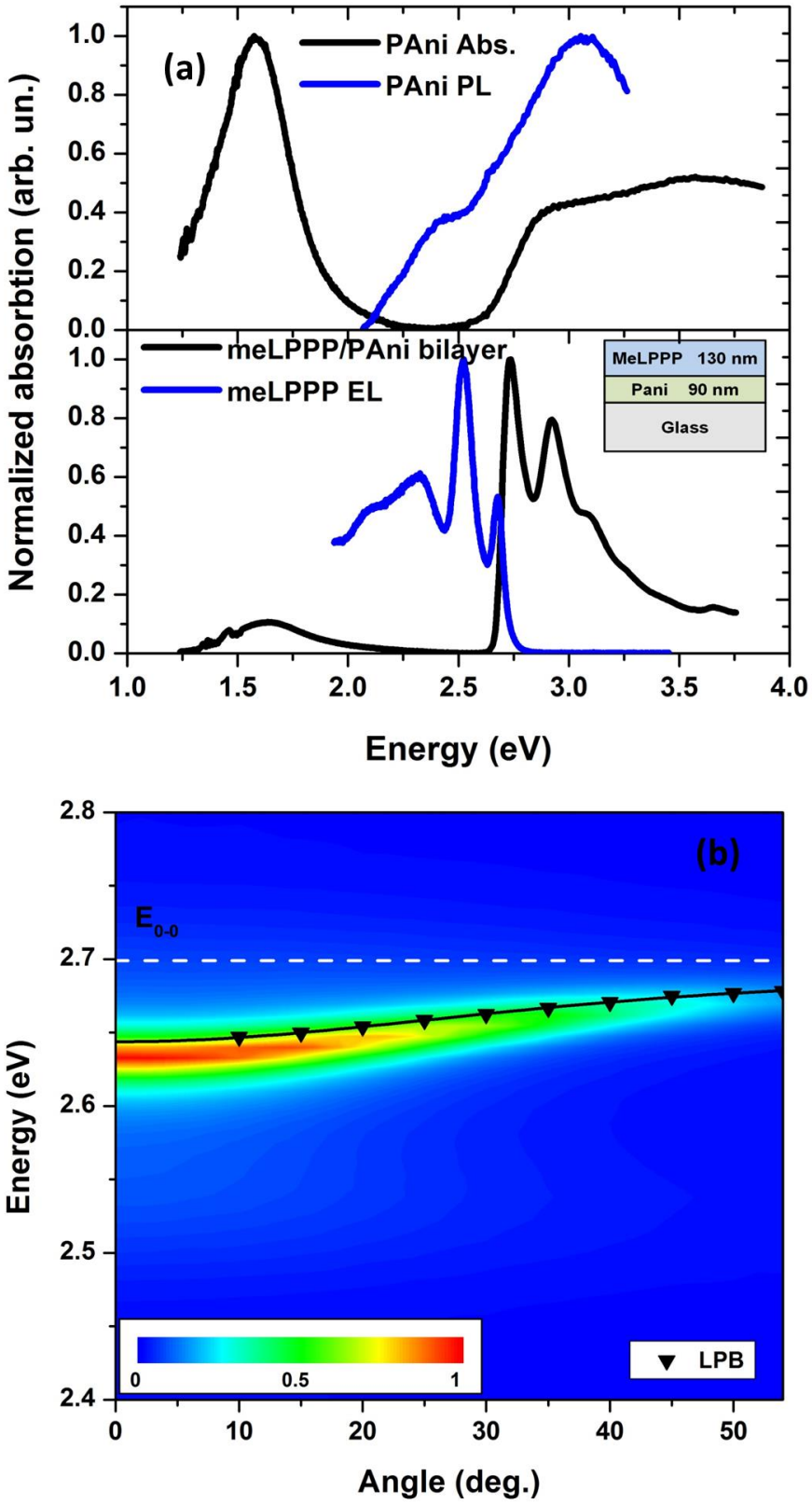

Figure 6-19 – (a) Absorption and emission spectra of PAni taken by spin coating a thin layer of 90 nm onto glass (upper part) and the absorption of the mLPPP/PAni bilayer (inset) and its corresponding electroluminescence taken from a control device having the same thickness as the structure: ITO/MoO3/PAni/mLPPP/Ca/Al (lower part). (b) The angle-dependent PL emission plot corresponding to the structure of figure-6.16 (a) by replacing PAni with PVA.

It is concluded that the incorporation of PAni whose absorption band at high energies overlaps with the absorption transition of meLPPP, changes the properties of the cavity and results in the system operating in the weak coupling regime.

6.4.4 JVL Characteristics

To acquire further insight into the optical and electrical properties of the devices fabricated the JVL characteristics were recorded and compared. Two devices were investigated: a control OLED device and a microcavity OLED device (MCOLED) as described in the last section.

Figure 6-20 (a) illustrates the brightness and current-density of the two devices as a function of the applied voltage. The turn on voltage (defined as the voltage that is required to obtain brightness of 1 Cd/m^2) is 10 Volts for the OLED and 10.5 volts for the MCOLED. The OLED device is slightly brighter than the respective MCOLED across a range of applied bias and reached at 100 Cd/m^2 at 14 volts, whereas the MCOLED reached at 10 Cd/m^2 at the same voltage.

The difference between devices can be explained by the additional Al layer (anode) that was added to create the microcavity device. The ITO hole injection electrode has a work function of ϕ=4.7 eV. Holes can easily be injected to the aluminium layer, due to the lower work function of aluminium (ϕ=4.2 eV). Subsequently, the energy level difference between the MoO_x layer (ϕ=5.4 eV) and Al introduces a barrier of 1.2 eV in the MCOLED device in comparison to the OLED device that does not incorporate the Aluminium layer, where the respective energy barrier is 0.8 eV between the ITO and the MoOx layers. This is shown schematically in Figure 6-19.

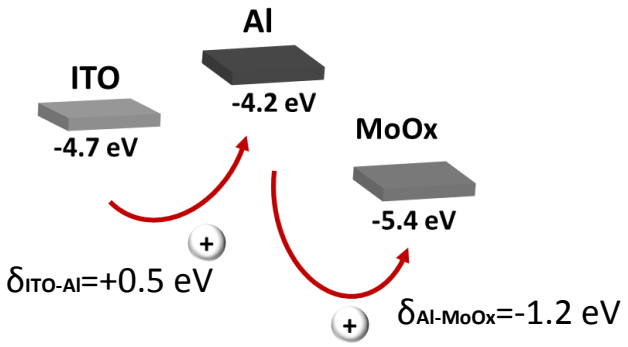

Figure 6-20 – Schematic representation of the position of the energy levels of ITO, Al, and MoO_x in the MCOLED and their respective energy barriers δ for hole injection under forward bias.

However, both types of devices had a turn on voltage around 10 volts. This can be attributed to a series of reasons.

Firstly, it can be caused due to the selection of the thick stack designed for a λ-microcavity structure having a total thickness (excluding electrodes) of 280 nm. Secondly, due to the lack of an ETL/HBL in the device which forces light to be emitted at high voltages; holes reach at the meLPPP/Ca interface where the injection of electrons occurs at high biases. Thirdly, the

exciton formation close to the metal cathode layer leads to the quenching of the emission as it is absorbed by the aluminium cathode electrode. Fourthly, the inclusion of many different layers with different energy levels cause various voltage drops at the interfaces were the charge carriers accumulate due to different barriers. Fifthly, due to the fact that the fabrication procedure was done outside the glovebox, oxygen and moisture or other impurities might have accumulated in the organic layers adding energy barriers or traps in the devices.

Figure 6-20 (b) depicts the current efficiency in terms units of Cd/A as a function of the applied voltage. As seen from the graph the OLED device reaches a maximum efficiency of 1.65 Cd/A at 13 Volts with a brightness of 35 Cd/m^2. On the other hand, the MCOLED reaches a maximum efficiency of 0.12 Cd/A at 12 volts with a brightness of 10 Cd/m^2.

Figure 6-20 (c) shows how the OLED and MCOLED efficiencies correlate as a function of the applied voltage. For this set of devices the efficiency (defined as the ratio of the OLED (η_{OLED}) and MCOLED (η_{MCOLED}) current efficiency η) is varied between $\Phi = 12$ and $\Phi = 18$ having an average value of 14.8 in the range of 9-15 volts. This means that the OLED device is 15 times more efficient than the MCOLED device. This agrees with findings in Chapter 5. However, the two systems are different in terms of structure and dynamics as meLPPP operates in the weak coupling regime.

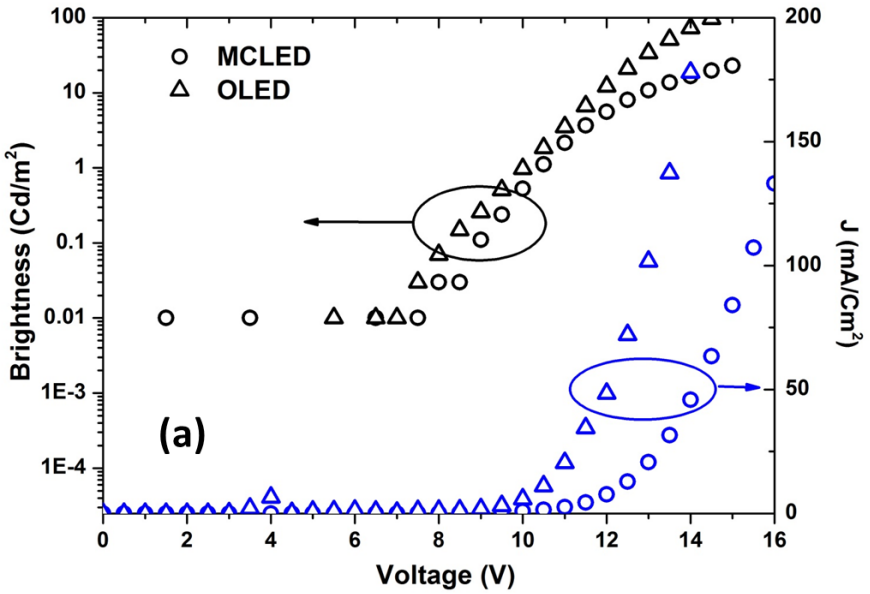
MCLED
OLED
Brightness (Cd/m²)
J (mA/Cm²)
Voltage (V)
(a)

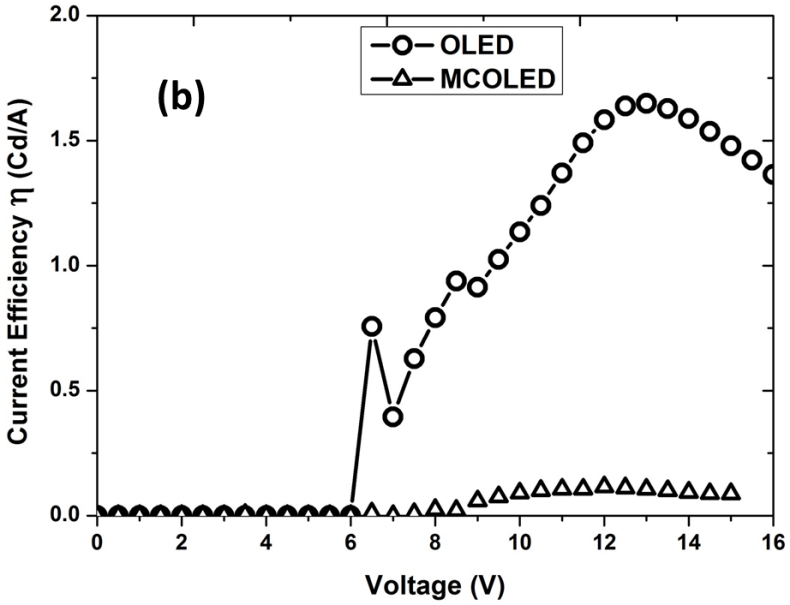
OLED
MCOLED
(b)
Current Efficiency η (Cd/A)
Voltage (V)

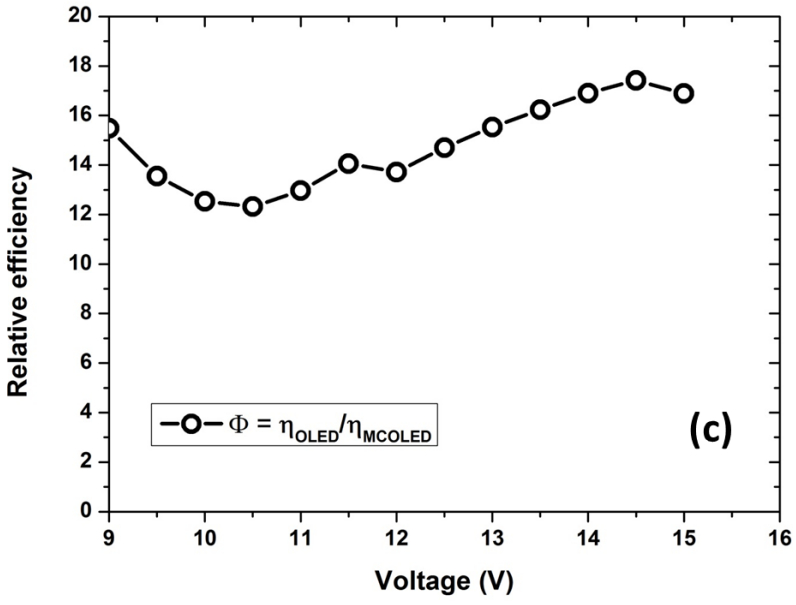
Relative efficiency
Φ = ηOLED/ηMCOLED
(c)
Voltage (V)

Figure 6-21 – (a) JVL measurements of a control OLED and a microcavity OLED device. (b) Current efficiency as a function of the applied bias showing the maximum efficiency and the roll-off region at high voltages. (c) Relative efficiency of the OLED and the MCOLED devices.

6.4.5 Conclusions

Three organic semiconductors were tested for their ability to emit polariton electroluminescence in an OLED microcavity device. The material Lumogen F Orange 240 was successfully incorporated in an optical microcavity acting as a guest in a transparent host polymer matrix. However, utilizing the dye as an electroluminescence material has proven to be challenging since it was not possible to realize an operational device. Only a combination with PVK proved successful, however, the very low brightness (1 Cd/m^2) reached render the material impractical for device application.

The organic semiconductor 5,12-diphenyltetracene was also successfully integrated into a blended system. The system based on this material was able to reach the strong coupling regime in optical microcavities and to exhibit electroluminescence in conventional OLEDs. However, the DBR of the microcavity structure selected for this study was highly reflective resulting in a limited amount of information especially at high angles. Moreover, all microcavity OLEDs were not operational within a short operation due to the imbalance of electrons and holes in combination with the absence of a hole blocking layer.

Finally, a ladder-type polymer meLPPP was able to reach the strong coupling regime. However, the fabricated devices operated in the weak coupling regime. The hole transport polymer PAni whose absorption band overlaps with the absorption spectrum of meLPPP changes the properties of the microcavity resulting in the device being operating in the weak coupling regime. Substituting PAni with PVA results in the system operating in the strong coupling regime.

The main conclusion from this study is summarized in three basic points: (a) the utilization of an electron transport/hole blocking layer is important to confine electrons in the electroluminescent layer and to limit the losses to the cathode, and (b) not all organic materials can be incorporated in devices in order to directly create excitons under charge injection. However, by altering the device structure and separate the strongly-coupled material this may be possible. (c) If the absorption spectrum of an organic semiconductor that can be strongly-coupled overlaps with the absorption spectrum of another organic material in the microcavity, this may result in the system operating in the weak-coupling regime and depends on their relative concentration.

Chapter 7

Degradation issues in small-molecule OLEDs.

This chapter details degradation issues related to the fabrication and operation of microcavity-based OLEDs. There are two main causes of degradation in the devices explored in the previous chapters. The first is related to the emissive material itself; a problem that is also met in conventional OLEDs. Here issues such as the relative concentration of the organic semiconductor in the active layer are explored. The second degradation mechanism relates the various interfaces within the device and the deposition techniques used. Here, the evaluations of short circuits or due to the loss of conductivity within the device are considered.

7.1 Introduction

OLED degradation is a generally complex problem that depends both on the materials selected and on the device stack. Various sources for luminance degradation exist in small-molecule-based OLEDs: Firstly, thermal stability of various organic semiconductors can have a detrimental effect in the device operation causing catastrophic failure [147]. For example, TPD is an organic semiconductor that is used as a hole transport material in OLEDs [148]. This material has a low glass transition temperature ($T_g \approx 63\ ^0C$). If the material is heated above this temperature morphological changes will occur. This can significantly reduce the electroluminescent characteristics of the OLEDs, especially if there is interdiffusion within the emissive layer.

Secondly, degradation due to interfaces [149]. In systems where the recombination zone is located near the interface between the emissive layer and the electron (or hole) transport layer, high local fields will be present due to charge accumulation at the heterojunction interface. This can cause degradation of the organic semiconductors and subsequently OLED failure. One way of circumventing this problem is to create emissive layers comprised of blends with both hole and electron transport materials where the emissive organic semiconductors are incorporated within.

Thirdly, various traps can influence the performance of the OLEDs [150]. For example, charge traps in the organic semiconductor can affect its mobility. Moreover, non-radiative recombination metal ions can diffuse in the interior of the device and accelerate aging.

Finally, degradation may include failure of encapsulation [151]. Moisture and oxygen are notoriously impeding the OLED lifetime. Usually, OLEDs incorporate a metallic cathode electrode. Diffusion of O_2 and H_2O can cause oxidation of the metal layer and lead to non-emissive regions. This progressively leads to OLED degradation. The permeation of oxygen and moisture can greatly affect devices made on flexible substrates rather than devices made on glass substrates [152].

Devices that suffer from such effects show decreased luminance as a function of time and current load, issues that clearly limit their lifetime.

In this thesis, deposition of the strongly-coupled organic semiconductor in devices is performed by the spin-coating technique, a solution processed method. Since J-aggregates of the TDBC molecules have low quantum yield [42] , the Lumogen F Orange 240 cannot be used in OLEDs, and because electroluminescence and stability of the ladder-type polymer meLPPP has been studied previously [153, 154], the focus of this chapter will be on R-substituted acene molecules. It will be shown that organic blends that utilize one of the low mass molecular dyes introduced in Chapter 4 can undergo severe degradation effects when incorporated in organic light-emitting diodes.

Specifically, it will be shown that MADN and DPA, two blue emitting molecules, exhibit electroluminescence when used in OLEDs, whose EL spectrum depends on the polymer matrix they are embedded in and their relative concentration. When these molecules are blended

with an insulating polymer matrix (PMMA) they exhibit change in their emission spectrum and rapid degradation.

It will also be shown that significant degradation can occur when thermal evaporation is used to deposit the emissive material. A number of processes can result in the quenching of the emissive species. In some small-molecule OLEDs degradation may result from the contribution of many effects acting simultaneously, rather than a single and dominant mechanism acting by itself. In the following sections, the influence of small-molecule concentration to the overall EL intensity of the acene-based OLED devices is under study. It will be shown that molecular dyes such as MADN, DPA and DPT exhibit similar degradation effects.

These effects have to be considered for the design of efficient strongly-coupled OLEDs. The stability of the strongly-coupled semiconductor is very significant. Changes in the absorption/emission characteristics of the OLEDs will signify potential loss pathways for lower branch polaritons that will prohibit the build-up of a substantial population at the bottom of the lower polariton branch. Therefore, the small-molecules used with the solution-processed method must be stable within the device.

7.2 Luminance quenching in small-molecule organic light-emitting diodes.

Most of the organic materials used in strongly-coupled organic microcavities are mainly based on small-molecules [42, 47, 73, 88, 155] rather than polymers [24], as polymers mainly have broad absorption profiles which prohibit the strong-coupling regime to be established. It was shown in Chapter 6 that 5-12 diphenyltetracene (DPT) can be used as a strongly-coupled organic semiconductor in optical microcavities. MADN and DPA are similar organic materials as they belong to the same R-substituted acene family. Therefore, fabrication of OLED devices can reveal some of their degradation characteristics. The fact that MADN and DPA each have a high quantum yield [156] and well-resolved absorption characteristics (more distinguished for DPA, Figures 7-2, 7-3) make these materials as good candidates for use in strongly-coupled OLEDs.

7.3 The role of the interfacial energy barrier

Efficient OLEDs based on small molecules typically employ materials with balanced electron and hole mobilities and small injection barriers. The height of the injection barrier is a consequence of the energy mismatch between the interfacial layers. MADN [156] has HOMO and LUMO energy levels at 5.5 eV and 2.5 eV, respectively. Similarly, DPA [157] and DPT [158] have a HOMO energy level at 5.81 eV and 3.1 eV, and a LUMO energy level at 2.87 eV and 5.54 eV, respectively. It is expected that since DPT emits in the green-red region of the visible spectrum, the energy barrier for injection of electrons directly from Ca to DPT will be less than the energy barrier for the Ca/MADN or Ca/DPA interfaces, as seen in Figure 7-1. In the devices

explored here the active material was either solution-processed via spin coating (MADN or DPT in TFB) or thermally evaporated (MADN or DPT) in a single layer.

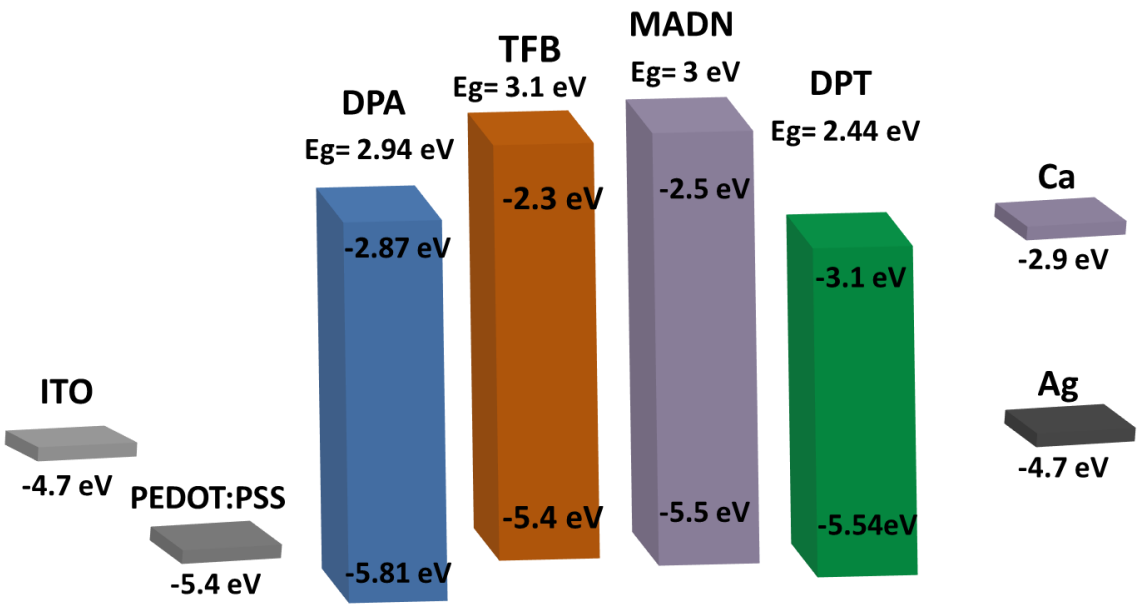

Figure 7-1 – Energy levels of the fluorescent materials used in chapter 7 for degradation studies along with the respective energy levels of the rest of the materials used in the fabricated OLEDs.

7.4 Absorption and EL spectra of MADN and DPA

Figure 7-2 shows the absorption and the electroluminescence spectra of MADN. The absorption spectrum of MADN was obtained by spin coating a MADN:PMMA blend having a relative concentration of 0.5:1 w/w from a toluene-based solution onto glass. As seen from the graph the absorption spectrum has four observable peaks. The main (0-0) electronic absorption transition is located at 3.106 eV. The other three vibronic peaks are located at 3.272 eV, 3.442 eV and 3.633 eV corresponding to (0-1), (0-2) and (0-3) transitions, respectively.

The EL spectra were recorded for two fabricated devices in which the emissive layer deposited either by thermal evaporation of a thin film of MADN or by spin coating a blended film of MADN:TFB at a ratio of 0.01:1 w/w. EL measurements were performed at the lowest possible operation voltage (V=6 Volts) for devices that feature the following structure: ITO/PEDOT:PSS(45nm)/active material(50-90nm)/Ca(5nm)/Ag(100nm).

It can be seen that the OLEDs have highly structured EL spectra with well resolved peaks in the range of 1.8-3.1 eV. The EL spectrum of the spin coated thin film features a main narrow transition at 2.86 eV and two lower energy emission features located at 2.71 eV and 2.49 eV. There is an extra shoulder slightly appearing at 2.27 eV.

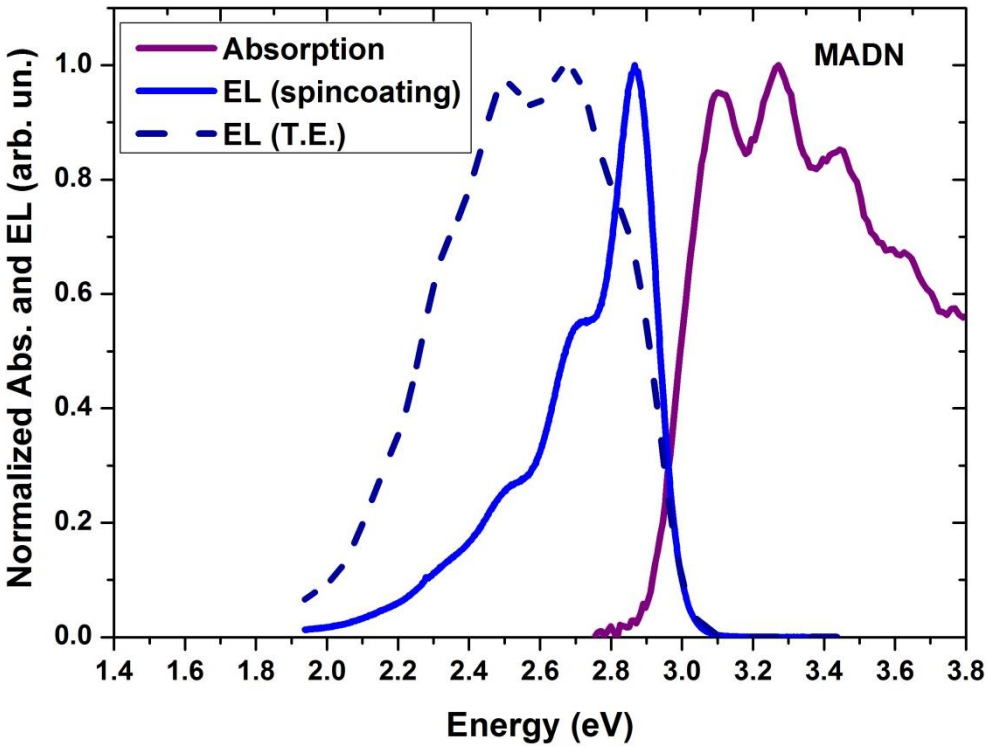

Figure 7-2 – Absorption and EL emission of MADN. The absorption spectrum (purple solid curve) was recorded from a MADN:PMMA (0.5:1 w/w) solution spin coated onto a glass substrate from a toluene-based solution. EL from a 90-nm-thin evaporated film is also shown in the dashed deep-blue EL curve, whereas EL from a 60-nm-thin spin coated film of MADN in TFB (MADN:TFB 0.01:1 w/w) is shown from the blue solid curve.

The OLED based on the evaporated thin layer of MADN has four transitions that correspond to the same energy levels as the OLED based on the spin-coating emissive blend. Here, the two middle transitions are more pronounced. In addition, the high energy transition peak is suppressed compared to the EL spectrum of the spin-coated layer, whereas the lowest energy shoulder exhibits enhancement. The main difference in the two OLEDs is the amount of dye used in the emissive blend, which suggests that the difference in the EL spectrum is caused by the mutual interaction of the MADN molecules. The Stokes shift was determined as 239 meV.

The absorption and EL spectrum of DPA is shown in Figure 7-3. DPA has a well-resolvable absorption spectrum which was obtained by spin coating a DPA:PMMA blend at a relative concentration of 0.5:1 w/w. The main 0-0 electronic transition is located at 3.122 eV, with vibronic progressions located at 3.297, 3.468 and 3.638 eV, corresponding to the 0-1, 0-2 and 0-3 transitions, respectively.

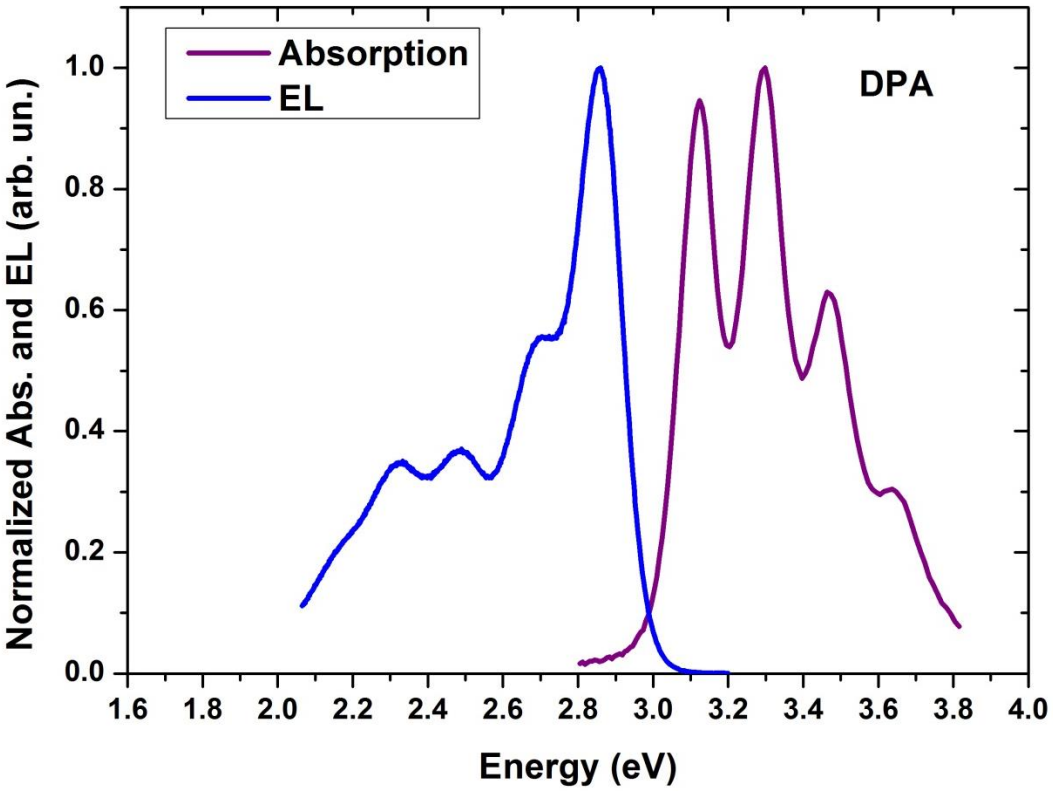

Figure 7-3 – Absorption and EL emission of DPA. The absorption spectrum (purple solid curve) was recorded from a DPA:PMMA (0.5:1w/w) solution spin coated onto a glass substrate from a toluene-based solution. The EL was recorded from a 85-nm-thin spin coated film of DPA in TFB (DPA:TFB 0.01:1) is shown from the blue solid curve.

The EL spectrum of DPA occurs predominantly in the blue part of the visible spectrum with the electroluminescence peaks located at 2.858, 2.696, 2.487 and 2.321 eV, respectively. A small observable shoulder is also located at 2.147 eV. There is a small similarity between the emission spectrum of MADN and that of DPA as their emission peaks are shifted only a few nanometres. This similarity results from the backbone of the two blue emitting materials being composed of anthracene. A Stokes shift was determined as 267 meV.

7.5 Degradation of DPA:PMMA based OLEDs.

Single layer devices incorporating DPA as the fluorescent dye blended with the transparent and insulating matrix PMMA were fabricated. This experiment was performed to assess whether the dye can emit light when disposed in an insulating matrix. The OLED had the following structure: ITO/PEDOT:PSS(45nm)/PMMA:DPA(85nm)/Ca(5nm)/Ag(100nm). The PMMA:DPA concentration was set at 1:1 w/w. Interestingly, blue emission from the active area of the PMMA:DPA OLED device was observed.

Figure 7-4 (upper part) plots the EL emission spectrum recorded from devices operating at two different values of applied bias (6 volts and 9 volts). The EL emission spectrum of the device at 6 volts is shown as the black solid curve of Figure 7-4 (upper part). It can be seen that initially

(t=0 min.) the spectrum is well resolved with the characteristic peaks of DPA visible. PMMA is expected to supress transport in the charge active region of the PMMA:DPA. In the first 10 minutes of operation an overall 7-fold reduction in the EL emission intensity is observed. After a period of 30 minutes the EL intensity becomes very weak.

For higher bias (9 volts) the emission again becomes weaker. Initially (t=0 min.) the EL emission is characterised by the same spectrum. After 10 (red curve) or 20 (blue curve) minutes the intensity shows a 16-fold reduction owing to the higher operating voltage that appears to accelerate degradation.

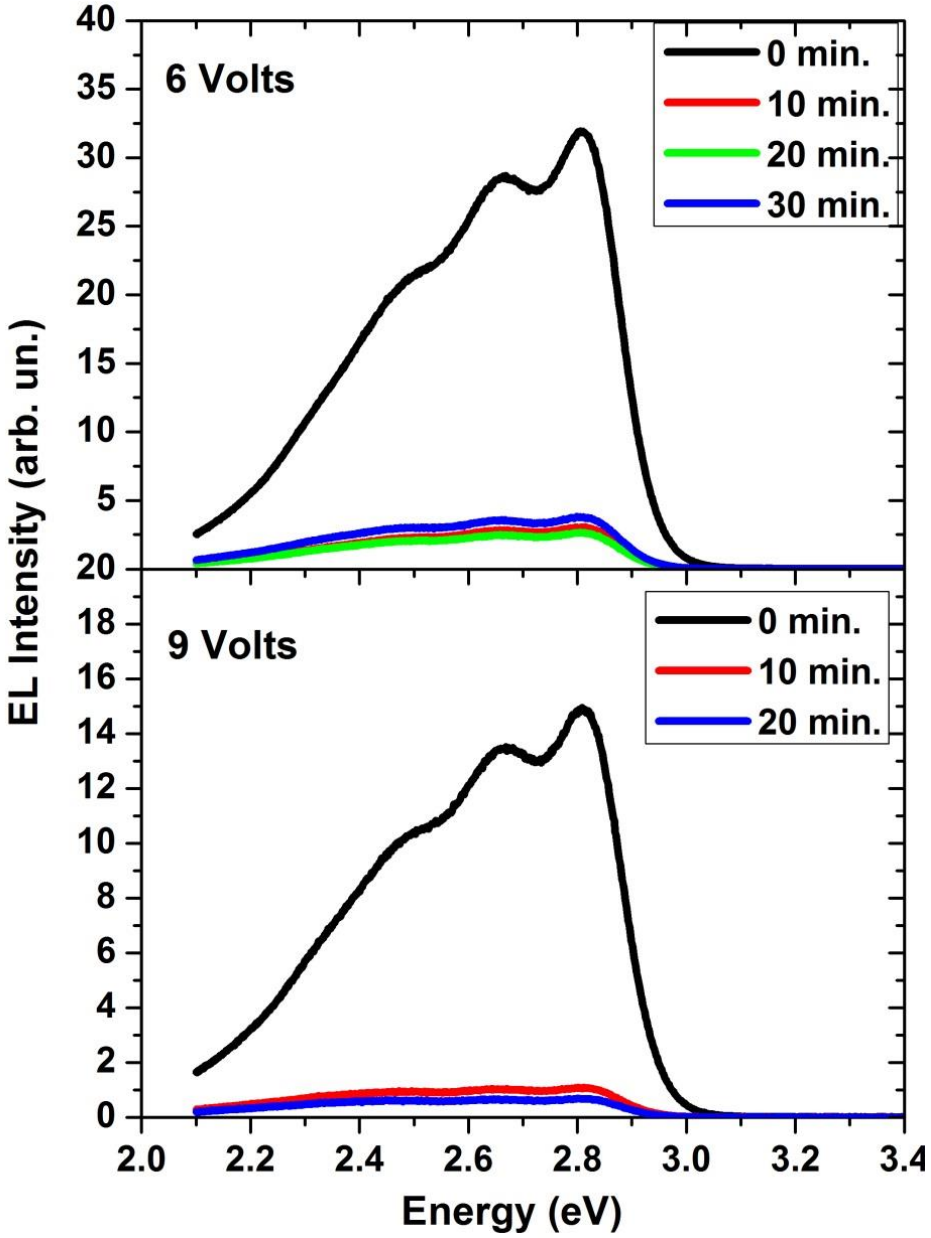

Figure 7-4 – Time evolution of the EL emission spectrum of diphenylanthracene embedded in PMMA, operating at 6 Volts (upper part) and at 9 Volts (lower part).

The experiment presented in this section was performed in order to investigate an alternative route of utilising guest molecules in OLEDs. DPA molecules embedded in PMMA which is an

insulating polymer behave differently from OLEDs that utilise a hole-transport polymer (TFB). The later shows current leakage that leads to catastrophic failure of the device as time progresses (Chapter 6). With this method a better control over the electron-hole imbalance may be achieved. Figure 7-4 informs of the following:

Firstly, devices that use PMMA as a host matrix and MADN as a guest molecule in the emissive layer exhibit light emission under applied bias, given the nature of the insulating matrix. Since the amount of MADN in the emissive blend is high, molecules are close together spatially as well as energetically to allow hopping of charge carriers from one molecule to another.

Secondly, the EL spectrum of DPA in PMMA is slightly different from OLEDs where DPA uses TFB as a host matrix (Figure 7-3). The peak positions remain the same whereas the relative intensity of the peak changes. The difference is possibly caused by the higher amount of the dye used in combination with the nature of the polymer matrix. PMMA might interact with local charges present in the dye molecules in a different way that TFB does resulting in a different EL spectrum.

Thirdly, it is shown that after a few minutes of operation the EL emission intensity becomes weak. This indicates that the blend of the dye molecules MADN cannot be used in combination with an insulating matrix to create a stable OLED.

7.6 Degradation in spin-coated thin film PVK:DPT based OLEDs.

To investigate the loss in luminance as a function of applied voltage, organic light-emitting diodes were fabricated based on the 5,6-diphenyltetracene (DPT). The molecular dye was blended with an optically transparent and active matrix of the conjugated polymer Polyvinylcarbazole (PVK). The OLED was structured as follows: Glass/ITO(100nm)/PEDOT:PSS(45nm)/PVK:DPT(40nm)/Ca(5nm)/Ag(100nm). The concentration for the PVK:DPT blend was set at 1:0.5 w/w. Figure 7-5 depicts the EL emission spectrum of the PVK:DPT based OLED.

During initial operation the applied bias was set to 5 Volts to generate electroluminescence. The EL recorded peaked at 2.42 eV, 2.27 eV, 2.04eV and 1.89 eV. The two higher energy peaks are assigned solely to the emission of DPT. However, two other peaks at 2.04 eV and 1.89 eV have a more mixed origin. Previous studies have shown that there is a complexity in the EL emission of PVK in OLEDs which can be attributed to several mechanisms [138]. Therefore, PVK can contribute to the lower energy emission spectrum.

The HOMO and LUMO energy levels of PVK are positioned at 5.7 eV and 2.2 eV, and that of DPT at 3.1 eV and 5.54 eV, respectively. It is therefore more likely that electrons will be injected from the metallic cathode to DPT at a low applied voltage. Furthermore, it is well known that PVK is a hole transport material. However, it is unclear whether DPT is a hole or electron transport material or has an ambi-polar transport nature.

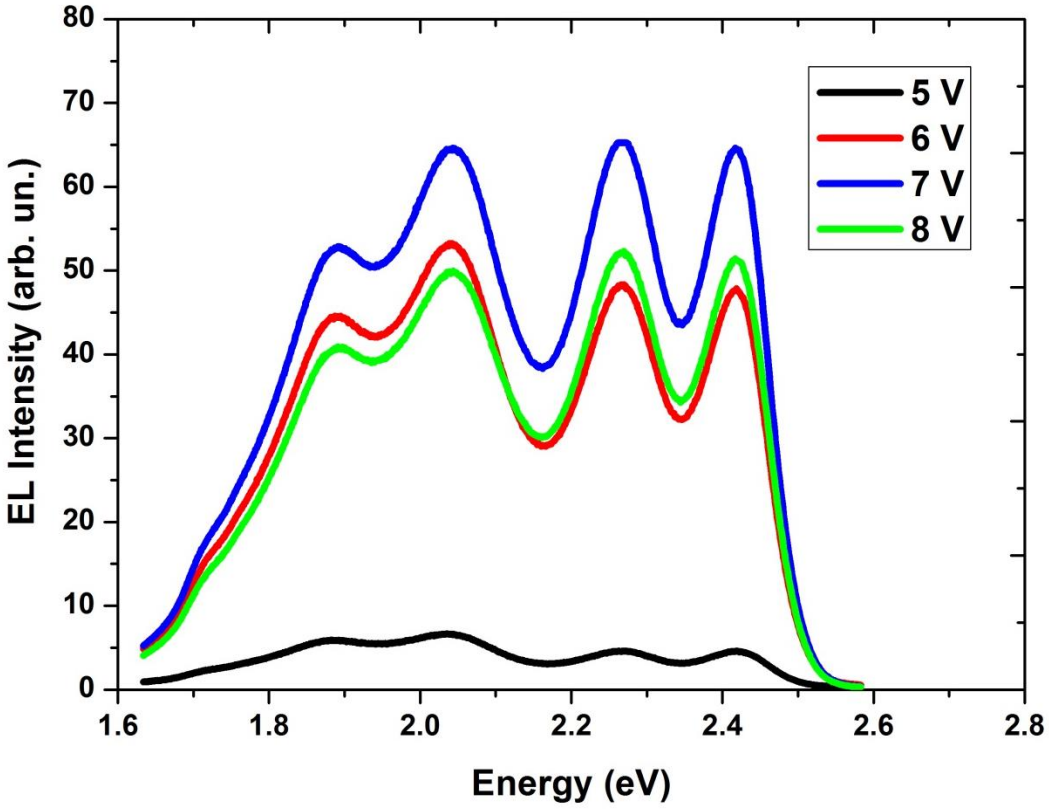

Figure 7-5 – EL emission spectrum of the PVK:DPT OLED device at an increasing applied bias. The overall integrated intensity changes are shown in the same graph.

It is observed from Figure 7-5 that the relative intensity of the two lower energy peaks is slightly higher than the two higher energy peaks of DPT which were recorded at 5 volts. By increasing the bias to 6 volts there is a significant increase in the EL spectrum. Within two minutes the EL intensity decreases and by increasing further the applied bias to 7 volts the higher energy and the lower energy emission transitions are comparable. At 8 volts the overall intensity of the EL spectrum remains the same as previously due to the fast degradation the system undergoes. The decrease of the high energy peaks is likely to be caused due to change in the recombination zone.

In Figure 7-6 the EL spectra of an OLED based on PVK:DPT (Figure 7-5), of an OLED based on TFB:DPT (1:0.83 w/w) and the PL spectrum of DPT are compared. As seen from the graph, there are no significant differences at the peak positions of the PL spectrum of DPT and the EL spectrum of the TFB:DPT. There is a small decrease in the intensity of the high energy peak located at 2.413 eV and an increase of the emission peak located at 2.11 eV of the TFB:DPT sample compared to the PL spectrum due to self-absorption.

The EL spectrum of the PVK:DPT device is similar to the other two spectra in the graph having higher emission intensities of the peaks located at 2.04 eV and 1.89 eV. There is only a small shift of the third observable peak which in the PL spectrum is observed at 2.11 eV that shifts

slightly to lower energies (at 2.041 eV). This may be caused by the difference in the PVK polymer matrix used that may contribute to the EL spectrum.

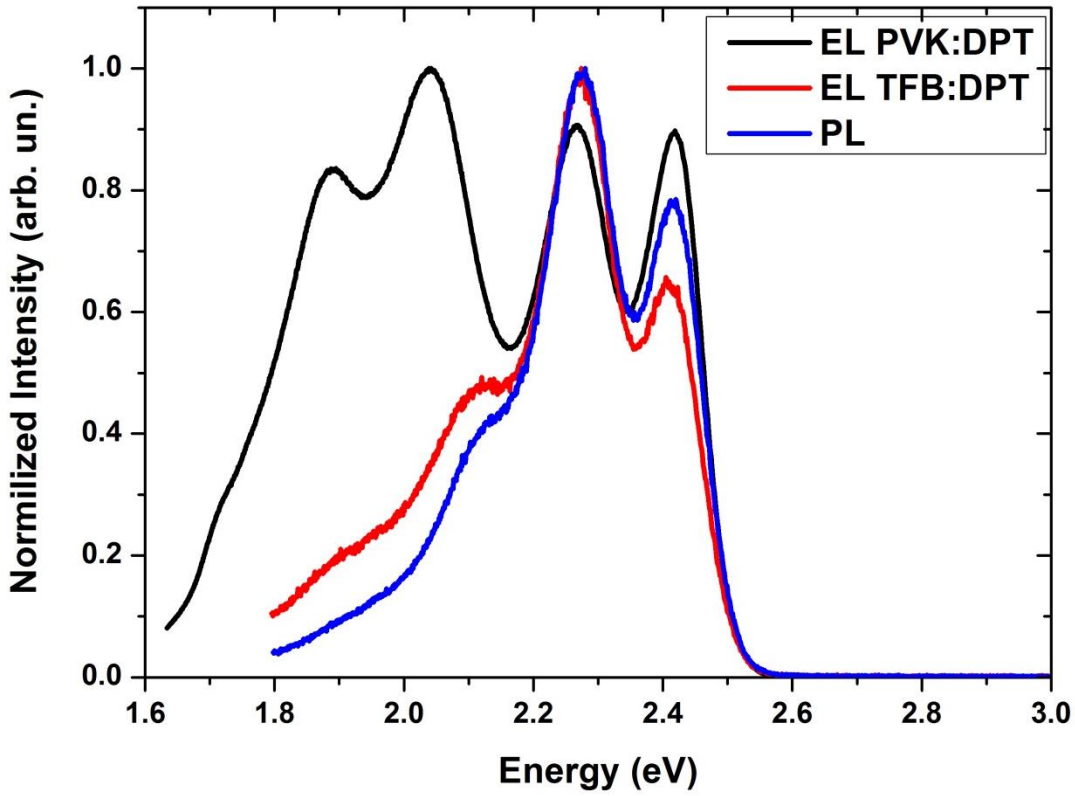

Figure 7-6 – Normalised EL emission spectrum of the PVK:DPT, TFB:DPT OLED devices and the PL emission spectrum of DPT.

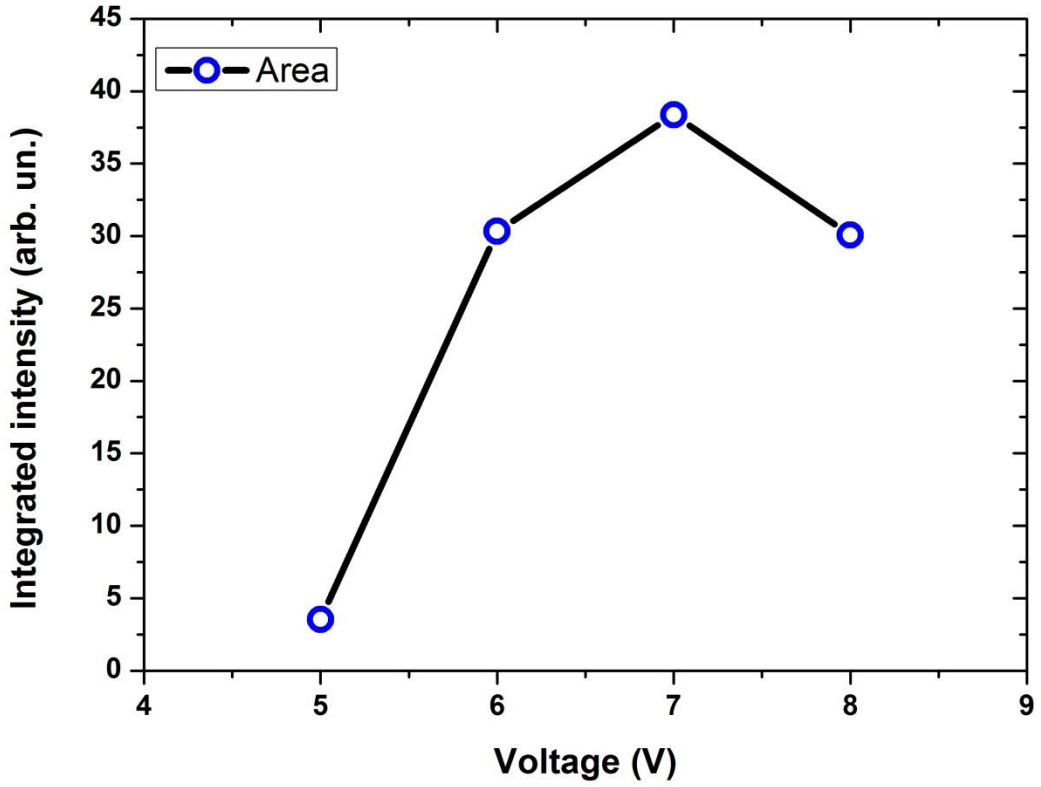

Figure 7-7 – Integrated EL intensity of the PVK:DPT spectra of figure 7-5 as a function of the applied voltage.

In Figure 7-7 the integrated emission intensity of the EL spectra of Figure 7-5 are shown for quantitative comparison (pink circles with black line interconnections). It is concluded, that upon increasing the applied voltage of the OLED the EL intensity increases, reaches to a maximum and subsequently reduces due to degradation. It is important to mention that organic semiconductors in strongly-coupled OLEDs, such materials will ideally not undergo rapid degradation as this will act as a fast depopulation channel of the LPB.

The time evolution of the total emission intensity as a function of time for such devices was also recorded and is shown in Figure 7-8. It can be seen that the total integrated intensity reduces linearly as a function of time at an applied bias of 5 volts, whereas at 6, 7 and 8 volt bials it follows an exponential decay behaviour. Specifically, at a bias of 5 volts the EL intensity increases and reaches its highest intensity point after 15 minutes of operation. On the other hand, at 6, 7 and 8 volts the EL intensity falls rapidly as a function of time for an increasing voltage. The higher the applied bias the greater the decay rate of the intensity. Table 7.1 summarizes the lifetime τ where the initial intensity drops to 1/e of its initial value of the OLEDs which is determined by fitting the respective data with a linear function for 5 volts :

$$y = A\tau + B \tag{7.1}$$

and with an exponential function for the rest of the applied voltages:

$$y = Ae^{-\frac{t}{\tau}} + B \tag{7.2}$$

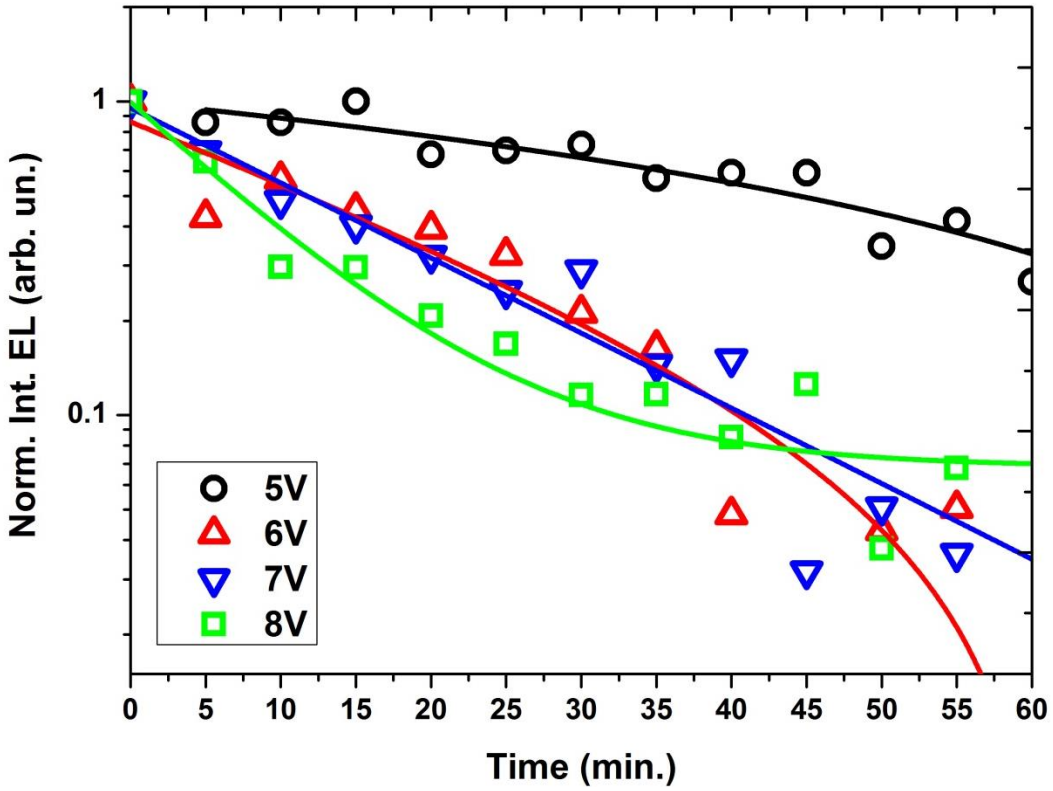

Figure 7-8 – Logarithmic plot of normalized integrated EL for the devices operating at different applied bias for a time progression of 1 hour.

Table 7.1: OLED Lifetime as a function of the applied voltage.

Voltage (V)	Lifetime τ (min.)
5 (Linear Decay)	37
6 (Exponential Decay)	24.05 ± 8.8
7 (Exponential Decay)	18.18 ± 2.6
8 (Exponential Decay)	9.55 ± 1.1

As seen from Figure 7-8 there is a good correspondence between the obtained values and their fits. The linear decrease in the intensity observed at 5 volts in comparison to the exponential decay observed at higher voltages is likely to be caused by the amount of charge carriers injected in the device that at higher bias accelerate degradation. At 5 volts the injected charges cause slow degradation of the device. As the voltage increases the lifetime of the OLEDs decreases. It is important to mention here that such systems where the EL intensity decreases rapidly with increasing bias is not likely to be used for strongly-coupled studies as the accelerated degradation observed at high voltages will lead to various loss pathways for polaritons.

7.7 Degradation in thermally-evaporated thin film based OLEDs.

OLED devices that utilise thermally evaporated thin films based on the molecular dyes DPT and MADN were investigated in order to understand if thermal evaporation is a better deposition technique compared to the solution-processed spin coating method. The evaporated organic layers had a thickness of 50 nm and 150 nm for DPT and MADN, respectively. The OLED structure was: Glass/ITO(100nm)/PEDOT:PSS(45nm)/(DPT or MADN)/Ca(5nm)/Ag(100nm).

Figure 7-9 (upper part) shows the behaviour of the DPT-based OLED under forward bias. Initially, the device is driven at 6 volts and exhibits an EL spectrum similar to the TFB:DPT EL profile as shown in figure 7.5. After one minute of operation, the OLED undergoes severe degradation in emission intensity with a 7-fold reduction recorded. In the second minute of operation the EL intensity is observed to have lost 10 times its initial overall intensity.

The applied voltage was then increased to 7 volts, which increased the emitted EL intensity. After one minute, the overall intensity decreased 5-fold. It was also observed that at the increased bias of 15 volts the two lower energy EL emission peaks are more pronounced. This resulted in irreversible quenching in OLED EL intensity.

The overall degradation of MADN to the based OLEDs differs slightly from that of DPT. The device was initially driven to 6 volts with measurements recorded over a period of 10 minutes. The voltage was then increased gradually to 9 volts. It was observed (see Figure 7-9 lower part) that the device initially emitted light under 6 volts. However, the intensity decreased slowly to 40% of its initial value within the first 30 minutes. By increasing the voltage the overall EL intensity increased but again then dropped slowly. Table 7-2 summarizes the intensity cahnges that were recorded for the DPT-based OLED over a period of two minutes and for the MADN-based OLED over a period of 10 minutes.

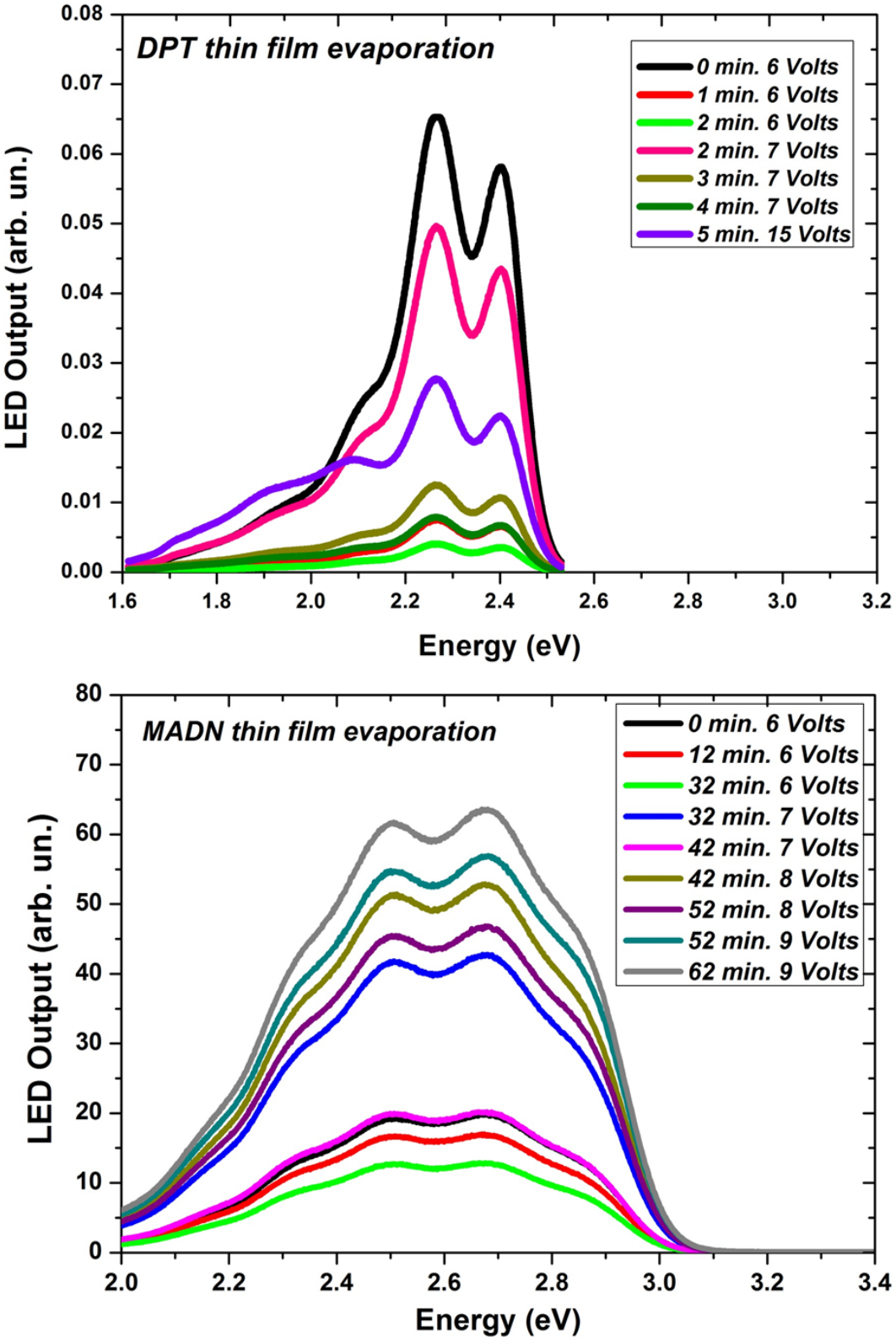

Figure 7-9 – Upper part: EL emission based on a 50-nm-thin thermally evaporated 5,12-diphenyltetracene layer. Lower part: EL emission based on a 150-nm-thin thermally evaporated MADN layer.

Table 7.2: EL intensity changes as a function of the applied voltage for MADN- and DPT-based thermally evaporated OLEDs.

	Voltage (V)	EL intensity (%)
MADN (10 minutes)		
	6	13.3 (decrease)
	7	52.5 (decrease)
	8	10.5 (decrease)
	9	10.1 (increase)
DPT (2 minutes)	6	93.5 (decrease)
	7	82.3 (decrease)

The thermally evaporated DPT OLED degraded more than 50% of its initial value within 2 minutes at both 6 and 7 volts of operation. This is in contrast difference with OLEDs previously fabricated by the spin coating process where DPT was blended with PVK. The thermally evaporated DPT layer has different electron-hole balance ratio than the OLED device where DPT is blended with PVK. This may contribute to the fast degradation observed. Moreover, lack of an electron transport/hole blocking layer might be more crucial in the thermally evaporated case that in combination with the different electron-hole balance ratio will accelerate its failure.

In the MADN OLED it is observed that the EL intensity drops in the range of 6-8 volts and slightly increases at 9 volts over a time period of 10 minutes. The small increase at this voltage can be attributed to the higher amount of electrons that are injected to the EL layer that shifts the electron-hole balance ratio. Since MADN has a high barrier for electron injection and due to its thickness, the device appears to be more stable than in the case of DPT OLED. However, both of the devices lack the ETL/HBL that can confine excitons to the emissive layer and can reduce significantly the losses due to its close proximity to the metallic cathode.

It is important here to briefly mention that formation of excimers and exciplexes might lead to increased or decreased losses during device operation, depending on the molecule and its surrounding environment [159, 160]. This may be more pronounced for the thermally evaporated DPT OLED rather than the OLEDs made from polymer:DPT blends, as the average distance between molecules increases (less dye concentration) and therefore this effect should be decreased. This effect may affect more small molecules than polymers.

7.8 Degradation in spin-coated thin film TFB: DPT -based OLEDs.

Figures 7-10 to 7-12 show the results of a set of measurements taken from OLEDs incorporating different concentrations of the materials TFB and DPT in a blend. In order to reach the strong-coupling regime the concentration of the fluorescent organic semiconductor that is related to its oscillator strength must be adequate. However, higher concentration may lead to faster degradation. In this section the effect of concentration on its stability is under

study. The thicknesses of the deposited thin films in the devices were approximately 55 nm. Each system is separately described and the most important observations are explained.

TFB:DPT 3:0.1 w/w: A high voltage is required (12 Volts) at a low DPT concentration to observe EL emission. The initial integrated intensity exhibits a small increase within the first five minutes. Thereafter, it experiences a small decrease as a function of time (see Figure 7-10 (a)). As seen from Figure 7-10 (b) the EL spectra at different times of observation differ only in intensity with their peak positions remaining unchanged.

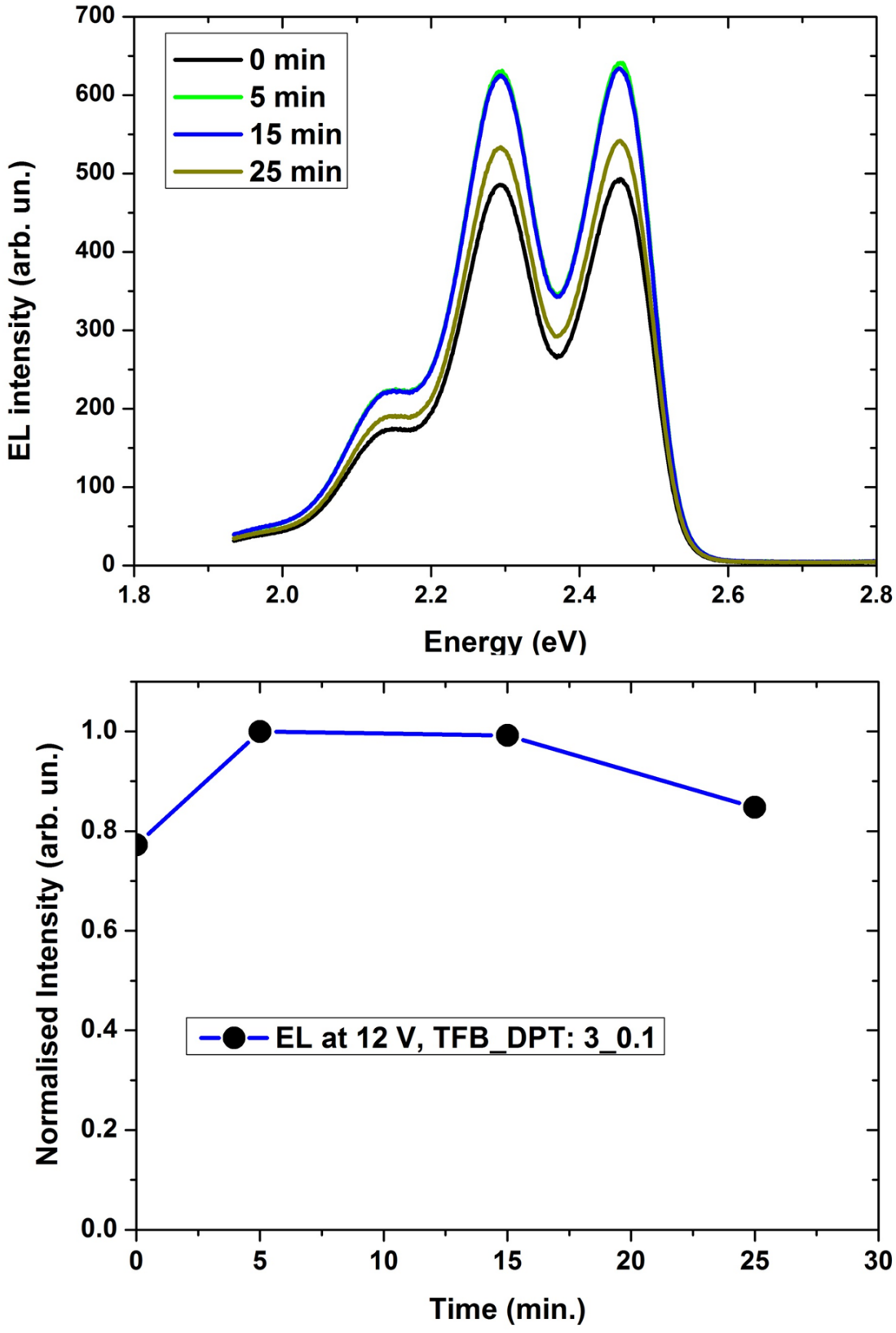

Figure 7-10 – (a) EL emission spectra at 12 volts of operation based on the TFB:DPT (3:0.1) blend at different recording times. (b) Time progression of the EL integrated intensity of DPT in TFB.

TFB:DPT 3:0.6 w/w: By increasing the DPT concentration 6-fold, from 0.1 to 0.6, the system could be driven at lower voltages (6 Volts) and is stable for a period of time of 30 minutes. The peak positions of the EL spectra recorded for 0, 5, 10 and 30 minutes of operation remain unchanged (see Figure 7-11 (a)). As seen from Figure 7-11(b) the overall intensity decreases in the first five minutes and then slowly increases reaching approximately 90% of its initial value after a period of 30 minutes.

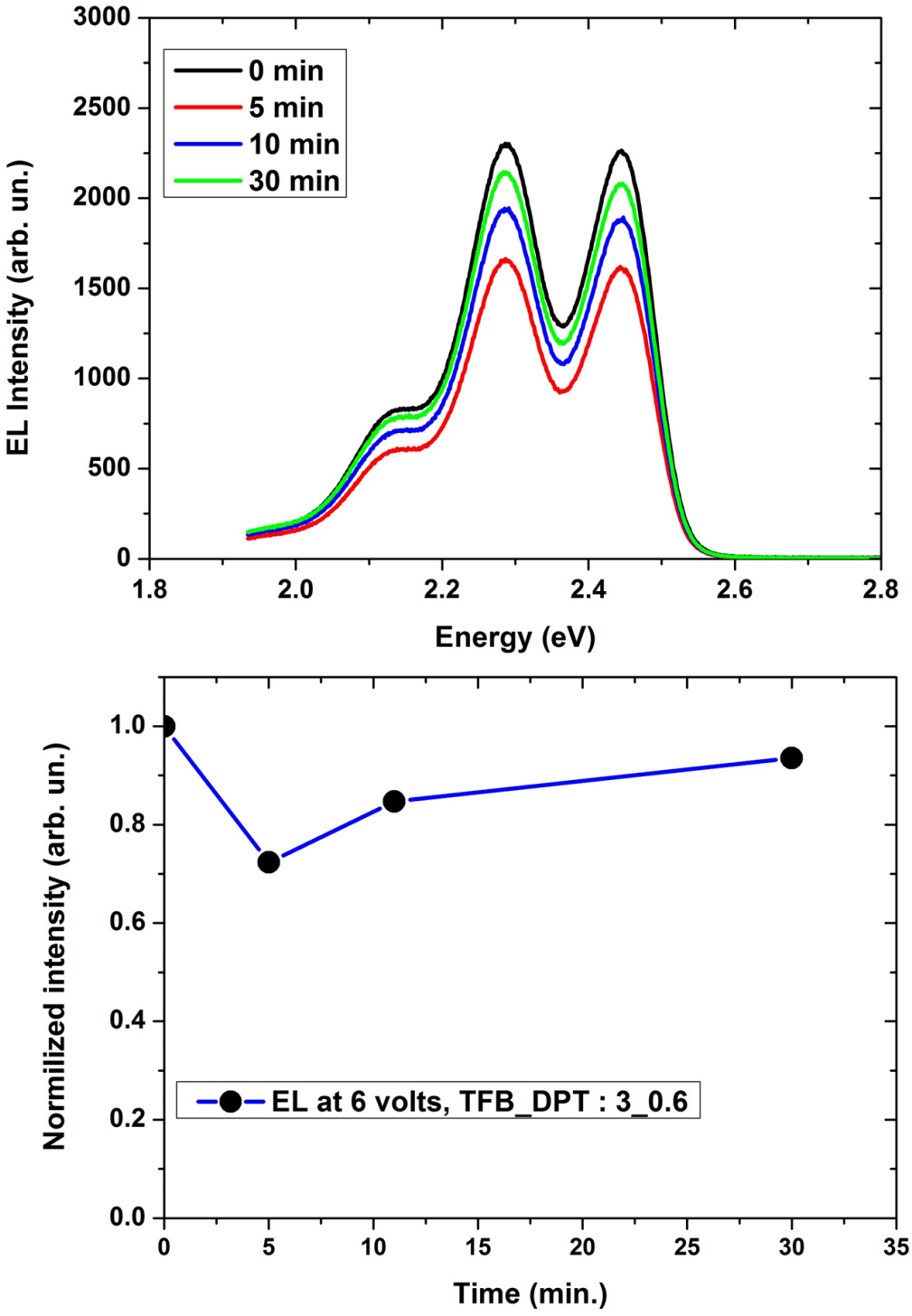

Figure 7-11 – (a) EL emission spectra at 6 volts of operation based on the TFB:DPT (3:0.6) blend at different recording times. (b) Time progression of the EL integrated intensity of DPT in TFB.

TFB:DPT 3:2.5 w/w: In this final system, the concentration of the dye is almost equal to that of the TFB host matrix. The system was extremely stable at low applied voltages and is a good candidate to generate polariton electroluminescence in OLEDs based on 5,12-diphenyltetracene. Again, there is no shift in the peak positions of the EL spectra and the relative intensity remains the same for all recordings seen in Figure 7-12 (a). Here, the OLED operates at 3 volts emitting green light. In Figure 7-12(b) the overall intensity recorded for the OLED operating at three volts, shows that in the first 5 minutes the overall EL intensity increased and then decreased very slowly over a period of 30 minutes retaining more than 90% of its initial value.

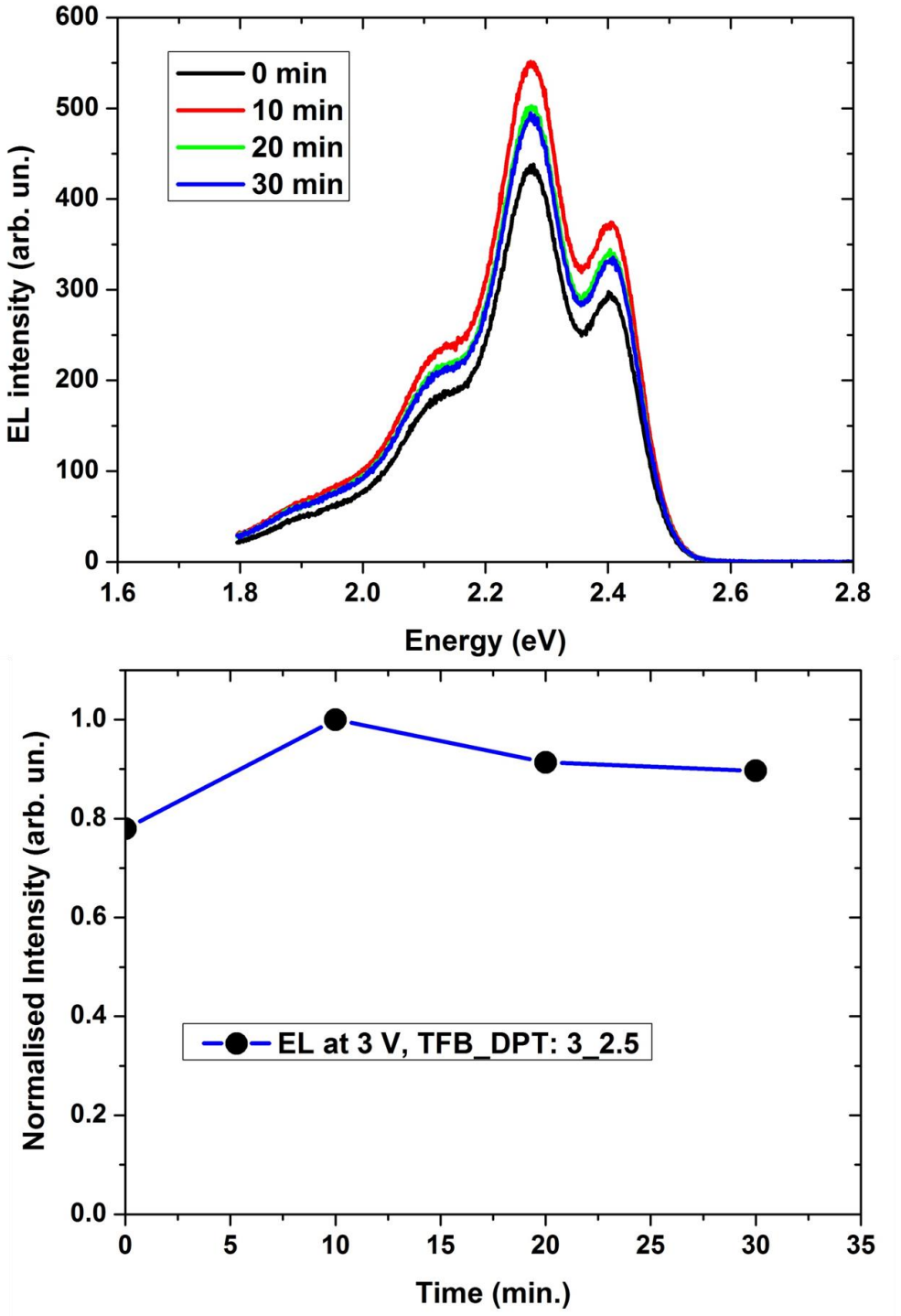

Figure 7-12 – (a) EL emission spectra at 3 volts of operation based on the TFB:DPT (3:2.5) blend at different recording times. (b) Time progression of the EL integrated intensity of DPT in TFB.

There are a number of conclusions drawn from this experiment. Firstly, as the concentration of DPT in the TFB:DPT blend increases the operating voltage decreases. The lowest operating voltage recorded in this set of experiments was at 3 volts. Secondly, all devices lost about 10% of their initial value over a period of approximately 30 minutes. This is important when studying polariton electroluminescence since fast degradation of the strongly-coupled semiconductor can lead to fast depopulation of the polariton states. Thirdly, when DPT is blended with a polymer matrix such as TFB is more stable than devices where the organic

semiconductor is in a pure form in the OLED. Such case is the thermally evaporated DPT-based OLED discussed in previous section where the OLED degrades within few minutes of operation. Fourthly, OLEDs driven at high voltages can accelerate degradation as many loss mechanisms can be activated at high bias, such as field-induced exciton dissociation [161].

7.9 Engineering issues based on the thermally-evaporated components of the device.

At the beginning of this chapter it was stated that engineering the electrical contacts of a strongly-coupled OLEDs is crucial for its electrical operation. For metal-metal strongly-coupled OLEDs it was experimentally observed that devices with higher than 30 nm of aluminium or silver anode were dominated by short circuits; however, the devices exhibited polariton dispersion characteristics despite of being or not operational.

It was found that the higher the thickness is of the deposited metal then the higher the associated probability that the unwanted metal spikes will build up extending tens of nanometres above the surface of the metal. This ultimately lead to short circuit within the device structure.

AFM measurements were employed to study the morphology: a 50 nm of thermally evaporated silver on top of an ITO layer and a 30 nm thermally evaporated MoO_3 on top of silver. An AFM image and a 3D image extracted from the AFM data are shown characteristically in Figures 7-13 (a) and (b).

In Figure 7-13 (a) it can be seen that there is an offset of approximately 16 μm between the successive thermally evaporated layers of silver and MoO_3. The cause of the offset originates most likely from the difference in the spatial position of the material sources in the evaporator. The metal sources are few centimetres apart from each other. However, the vertical distance between the source and the target is not sufficiently large to reduce this offset. Additionally, the thickness of the shadow mask used (a few mm) also contributes to the non-ideal overlap of the two layers.

Secondly, Figure 7-13 (b) shows a 3D image determined by AFM measurement. It can be seen that a spike of the order of 100 nm has grown during thermal evaporation. The spike on this occasion is located near the interface of the two deposited materials. Spikes act to enhance the electric field during device operation. This in turn results in the creation of high current densities and therefore in resistive heating in the area of the spikes that melts the organic layer and subsequently causes the formation of micro-shorts.

This has a major impact on the creation of a considered metal-metal OLED. A $\lambda/2$-cavity design will be less likely to operate in comparison to a λ-cavity design due to thickness considerations. To circumvent these obstacles a spacer layer is required to reduce the impact of these spikes. A RMS of 4.23 nm was recorded from the final MoO_3 layer indicating high roughness of the bilayer structure.

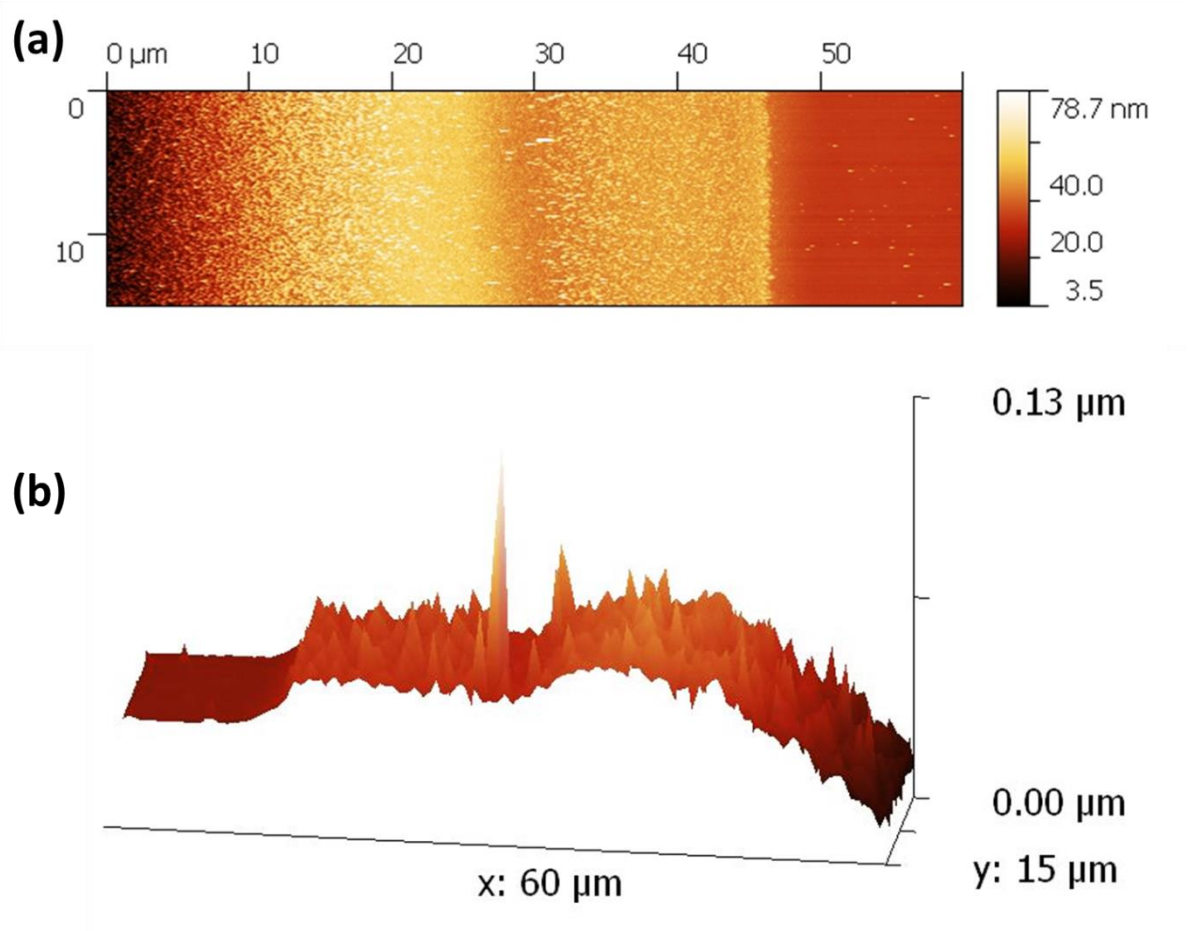

Figure 7-13 – (a) An AFM image of a thermally evaporated silver/MoO_x bilayer on top of the ITO, (b) a 3D image revealing the spike characteristics of the structure.

7.10 Conclusions

This chapter discussed some of the difficulties encountered in developing efficient polariton OLEDs.

Small-molecule DPT-based microcavity OLEDs showed current leakage (chapter 6) which was likely caused by a high electron-hole charge imbalance. In order to shift the electron-hole balance an insulating polymer matrix was used. EL emission was observed from DPA-based OLEDs, however fast degradation prevailed. This renders OLEDs with insulating polymers as unstable.

In OLEDs were the emissive layer comprised of the PVK:DPT blend it was found that there is an increase of the EL intensity as the bias increases. At higher values of voltage loss of luminance is seen that suggests accelerated degradation. Moreover, a decrease of the OLED lifetime for increased applied voltages was observed.

Thermally evaporated OLEDs were fabricated. DPT-based (50 nm) OLEDs showed very fast degradation. On the other hand MADN-based (150 nm) OLEDs showed less degradation with

time. This might have been caused by both the nature of the fluorescent material used and the thickness of the emissive layer.

OLEDs were the emissive layer comprised of the TFB:DPT blend were studied at different DPT concentrations. It was shown that by increasing the DPT concentration in the blend the operational voltage can be decreased substantially. It was also shown that the device remains stable losing about 10% of its initial value over a period of 30 minutes at low bias. Moreover, the choice of a host polymer significantly enhances the stability of the devices as is observed in TFB/DPT blends in comparison to the PVK/DPT blend-based devices.

Finally, thermal evaporation of a metallic mirror is not always beneficial in strongly-coupled OLEDs. If high roughness characterizes the metal layer then it is more likely that the device will lead to current leakage.

Chapter 8

Conclusions and Future Directions: Towards Efficient Organic Polariton LEDs.

Chapter 8 briefly summarizes the work that has been presented in this thesis. A wide coverage of experimental efforts used in the creation of organic light-emitting diodes that operate in the strong-coupling regime has been given. In this chapter special emphasis is given in the determination of some basic rules that should be considered when fabricating polariton OLEDs. Due to limitations in the engineering and material aspects of strongly-coupled OLEDs the fabrication should be directed towards alternative concepts such as the device architecture. Although the structures proposed in this chapter might in principle be complicated, they could resolve some of the OLED degradation processes. This thesis ends with some final remarks about the future of the field.

8.1 Introduction

In this research project, the physics and the engineering of organic polariton LEDs were explored with special focus given to the challenge of developing efficient microcavity OLEDs. It was shown that limitations exist in the availability of organic semiconductors that can be stable, strongly-coupled and at the same time generate luminescence under charge injection, in organic light-emitting diodes.

In this thesis the limitations that hinder the fabrication of efficient strongly-coupled OLEDs were explored. There is still a lot of theoretical and experimental work that remains to be resolved; however, all efforts in this field target in one major goal: the realization of a room temperature organic laser diode that operates in the strong-coupling regime.

Chapter 1 provided a historic review of the main experimental and theoretical steps that led to the realization of polariton condensation based on organic semiconductor materials. It also summarized the main objectives of this thesis.

Chapter 2 focused on the theory behind the optical and electrical properties of organic semiconductors.

Chapter 3 provided a description of a microcavity, its principles, and the distinction between the weak and the strong coupling regimes.

Chapter 4 discussed device engineering. Several organic semiconductors were tested and deposited in various forms and combinations. The organic materials were either thermally evaporated or solution processed. The solution process method was based on spin coating polymers or low-molecular weight organic semiconductors in pure or in blended form. All devices used an ITO layer either external to the microcavity to enhance conductivity or as an internal layer to act as a transparent electrode. Electrical and optical measurements were then performed using an automated LabVIEW software, specifically designed for measurements on optical microcavities and devices.

In Chapter 5 a J-aggregate based strongly-coupled microcavity was fabricated. The optical and electrical properties of the device were measured and compared with the values of an uncoupled OLED. It was found that the polariton device is 6 times less efficient compared to an uncoupled OLED. This experimental result was compared with theoretical simulations. Based on this analysis it was possible to determine the limiting factors that result in a reduced population of the LPB.

Chapter 6 studied the formation of polaritons in microcavities, each containing a different organic semiconductor. Firstly, the material Lumogen F Orange 240 was studied. The material was shown to be strongly-coupled in a microcavity and to form a multi-branch dispersion curve. However, the material was not able to be incorporated in OLEDs and emit electroluminescence directly from polariton states. Secondly, the small molecule 5,12-diphenyltetracene was used in organic microcavities and LEDs. This organic semiconductor was able to form an efficient device; however, limitations based on engineering issues prohibited the observation of polariton electroluminescence. Thirdly, the ladder-type polymer meLPPP

was used successfully in both microcavities and OLEDs. Although the organic semiconductor can form polariton states in a microcavity structure the emission observed from the microcavity OLED could not be assigned to polariton-based electroluminescence. The microcavity operates in the weak coupling regime due to the PAni absorption spectrum overlapping with the absorption spectrum of meLPPP.

Chapter 7 dealt mainly with material degradation issues during the operation of OLEDs based on diphenyl-substituted acene molecules (e.g. DPT) as the emissive material. These materials can be used as strongly-coupled organic materials and have been used in the past in OLEDs. In terms of material challenges, it was found that devices based on small molecules undergo degradations that depend on the concentration of the organic semiconductor, the choice of the polymer matrix in host:guest systems, or the lack of an electron transport material in the blend.

8.2 Design rules for organic polariton LEDs.

Many variables affect the performance of an organic polariton LED. For example, the organic semiconductor, the electron and hole transport materials, the electrodes and the reflective mirrors are the most fundamental. Optimising such a device is a difficult task. For example, engineering the energy minimum of the lower polariton branch (that corresponds to a specific cavity thickness), might not lead to an efficient device, as the electrical properties of the device might not be optimum at the respective cavity thickness. In this section the most important design rules for OLEDs operating in the strong coupling regime are summarized.

Rule number 1: High Q quality factor for cavities is required to increase the polariton lifetime.

The lower polariton branch of a strongly-coupled organic microcavity exhibits increased polariton lifetimes as the Q factor of the microcavity increases. Furthermore, the polariton population decreases from higher to lower k states due to: a) the decrease of the polariton scattering rate (decrease in the excitonic component) and b) the increased radiative rate (increase in the photonic component) of polaritons [162]. Therefore, a higher value of Q factor can help in the establishment of a significant macroscopic population near the bottom of the LPB. However, as it was mentioned in Chapter 4, there is a difficulty in sputtering high quality ITO or growing DBR mirrors on top of organic materials.

Figure 8-1 shows transfer matrix simulations for DBR-based mirror cavities incorporating N bi-layers. The simulations are based on a microcavity which is formed by a top and a bottom DBR mirror with an intracavity separation of 136 nm and a refractive index of n=1.9. The DBR mirrors simulated contain an equal number (N) of bilayers and are composed of SiO_2 and Ta_2O_5 $\lambda/4$ layers. In the inset of the graph, the calculated quality factor versus the number of bilayers is shown.

As seen from the figure, the increase of N causes an increase in the Q factor of the cavity. If the number N of bilayers is high then a significant amount of photons might not be able to escape through the DBR cavity mirror, as observed in the DPT-based microcavity OLED in Chapter 6.

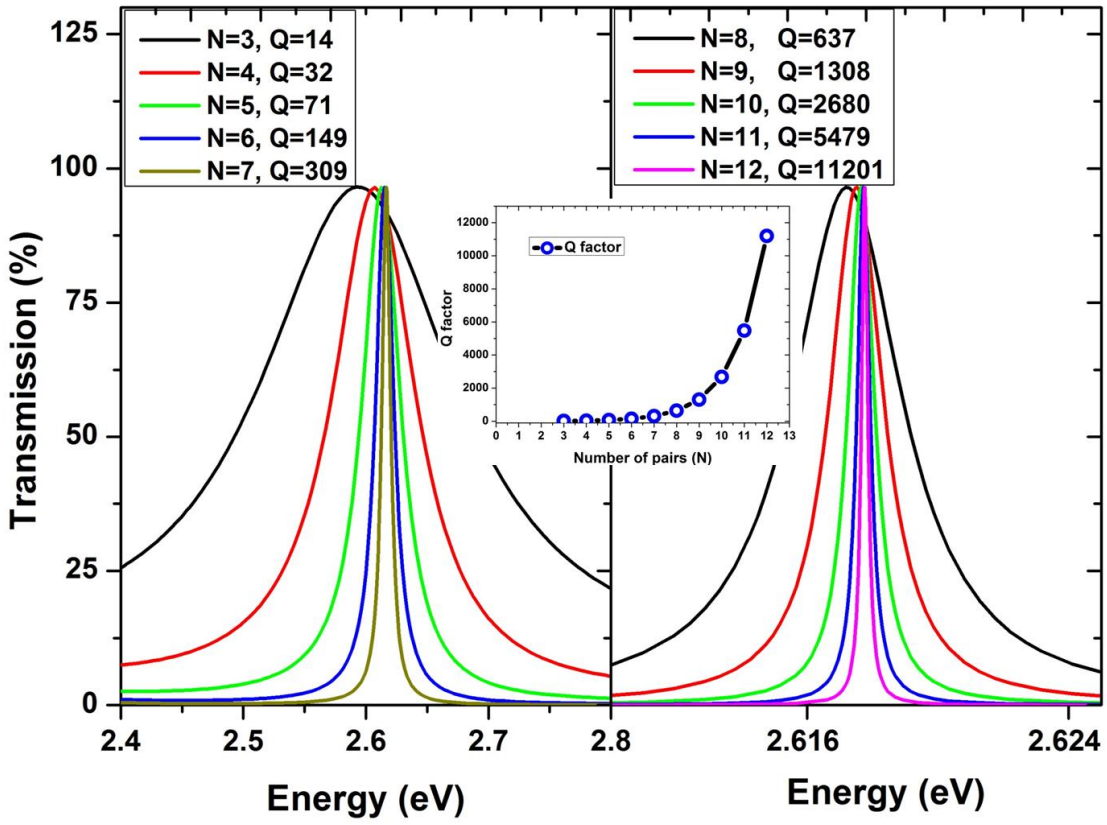

Figure 8-1 – Transfer matrix simulations for a microcavity system based on top and bottom DBR mirrors with number of bilayers N, for each mirror. In the inset of the graph the calculated Q cavity factor as a function of the number of N bilayers.

Rule number 2: The appropriate electrode material should have high transparency and very low resistivity.

A good choice for the bottom electrode on top of the DBR mirror is the indium-tin-oxide alloy. ITO is commonly used due to its high transparency (>80%) and its low sheet resistance (~15 Ω/□) [163, 164]. However, the selection of the top electrode is extremely challenging. This is due to the difficulty in depositing ITO on top of the organic semiconductor.

Metallic mirrors can alternatively be used as electrodes in microcavities. One of the drawbacks in using metallic electrodes is that they are related to losses due to internal absorption in OLEDs. Furthermore, a high thickness metal electrode will lead to a low Q cavity factor, whereas a thin metal electrode will lead to a higher Q cavity factor establishing poor electrical connection in the device. The incorporation of a thin metallic layer prior to sputtering of the DBR mirror may cause less damaging to the underlying organic material.

An alternative electrode has been recently investigated as an ITO replacement and can be used in both conventional and inverted OLED devices (in inverted OLEDs the bottom electrode is the cathode electrode). This is the so-called MAM structures [165]. MAM is an acronym that stands for the metal oxide-metal-metal oxide (e.g. MoO_x-Ag-MoO_x) trilayer structures. The

thickness of the intermediate silver layer can be reduced and still exhibit low resistivity and high optical transparency.

A range of transparent oxides have been investigated where a thin metallic Ag was sandwiched between two metal-oxide layers. These studies include the WO_3/Ag/WO_3 [166], ZnSnO/Ag/ZnSnO [167], TiO_2/Ag/TiO_2 [168], ZnO/Ag/ZnO [169], TiInZnO/Ag/TiInZnO [170], SnO_2/Ag/SnO_2 [171], and Al_2O_3/Ag/Al_2O_3 [172]. Most of the metal oxides can be deposited by RF sputtering, a technique which is not widely available to academic laboratory settings. Alternatively, thermal evaporation can be used to deposit some of the metal oxides, such as MoO_3.

Rule number 3: Selection of the electron and hole, transport and injection materials.

The hole and electron injection materials should have appropriate energy levels for charge injection from the respective electrodes. As a hole injection material PEDOT:PSS is commonly used with energy level located around 5.4 eV. Electron injection materials such as Calcium with work function of 2.9 eV can be used.

The electron transport (ETM) and hole transport (HTM) materials should be non-absorbing in the optical region of the spectrum and should have good transport properties such as high mobilities for efficient charge transfer to the emissive material. The ETM and HTM should also have similar mobilities for better electron-hole charge balance in the device. Furthermore, their energy levels should be close to the energy levels of the injection materials in order to avoid high injection barriers. The ETM and HTM should also act as efficient hole blocking and electron blocking materials, respectively.

Depending on the device architecture (conventional or inverted OLED) the hole or electron transport semiconductor should be insoluble to various organic solvents. This can be achieved either by selecting appropriately the solvent that will be used on top during the process of fabrication or to have the ability to be thermally or UV cross-linked. Finally, the charge transport materials should be stable and not degrade rapidly with time.

Rule number 4: The emissive material's concentration should be well-balanced between the onset of the strong-coupling regime and the onset of loses; especially in small-molecule OLEDs.

The emissive material whether in a pure or in a blended form will define if the OLED microcavity reaches the strong-coupling regime. One of the most important factors is the oscillator strength of the organic semiconductor. Organic microcavities containing emissive polymers or small molecules with high oscillator strength will require a reduced amount of the organic semiconductor to be used. This will increase the probability that the device will operate in the strong-coupling regime and simultaneously will reduce losses caused by high dye concentration, as observed in small-molecule OLEDs.

The placement of the organic semiconductor in the cavity will define the strength of the exciton-photon interaction. There are two important cases to consider:

The emissive material is placed close to the anti-node of the field. Here, the strength of the light-matter interaction will be strong.

The emissive material is placed close to the node of the field. Here, it is uncertain if the strength of the light and matter interaction will be sufficient to reach the strong-coupling regime.

Therefore, from a design perspective, the selection of a p-i-n architecture where the active material is located between the electron and hole transport materials and is placed at the antinode of the electric field, will give the highest light and matter interaction.

Rule number 5: Device architecture.

A high quality factor microcavity LED could be fabricated by incorporating a double DBR structure. Two possible scenarios are briefly described.

In the first scenario the concept of an inverted OLED is utilised along with the use of meLPPP as the strongly-coupled material, as shown in Figure 8-2 (a). Here, the double DBR configuration is based on 7 pairs of high (Ta_2O_5) and low (SiO_2) refractive index transparent materials. The number of bilayers in the DBR is a compromise of high reflectivity over high transmission. In this architecture the ITO is the cathode layer followed by an ultra-thin layer of PFN that will act as an electron injection layer [157, 173]. In this example the ladder polymer meLPPP is placed on top. The OLED is finalised by the thermal deposition of a MAM anode structure. This concept permits excitons to be directly generated in the meLPPP layer.

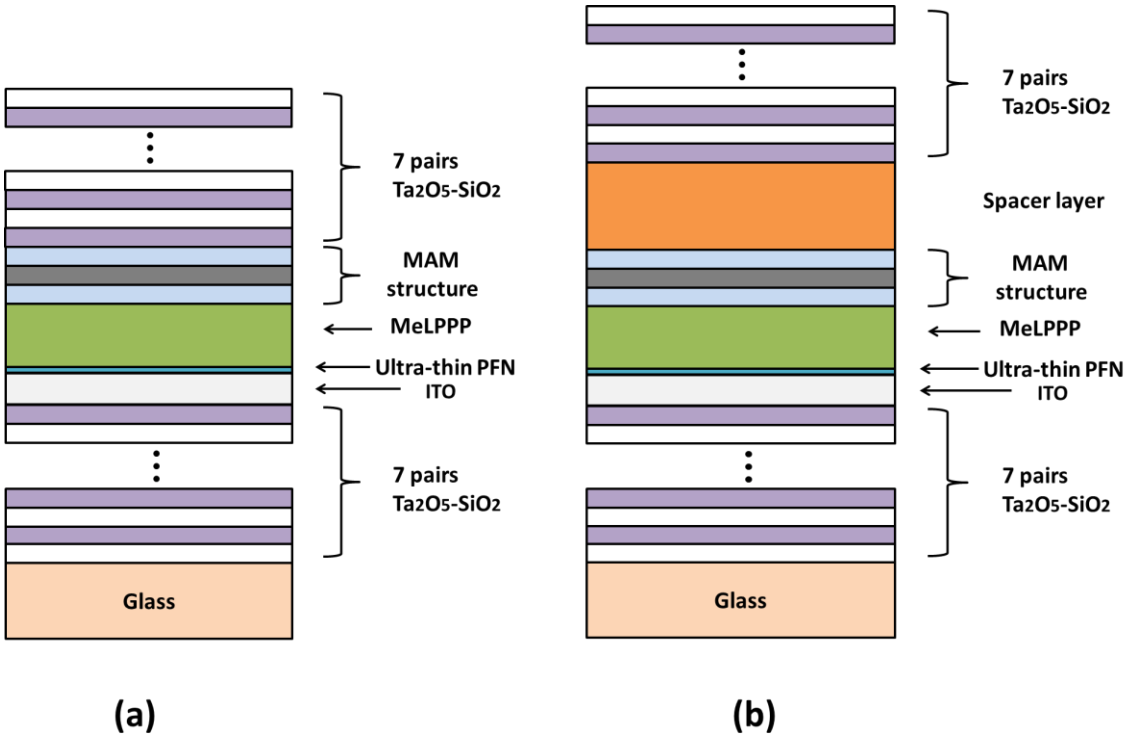

Figure 8-2 – (a) Inverted organic microcavity LED structure that utilizes the MAM concept having a highly transparent and highly conductive anode. (b) Inverted microcavity LED structure with a spacer layer.

The second scenario is shown in Figure 8-2 (b). Here meLPPP is placed outside of the electroluminescence region. This architecture separates the EL medium and the strongly-coupled medium (orange spacer layer) that is not affected by charge generation. A non-strongly coupled organic material can be used to generate light with the LPB being optically pumped. In this way the LPB could be populated efficiently circumventing losses. The main issue in this configuration is related to the limited transparency of the MAM structure.

Rule number 6: Electrical excitation operation mode: pulsed vs continuous excitation.

There are several advantages in using pulsed excitation instead of continuous excitation [174]. Firstly, the amount of current density that is delivered into the system is different in the two cases. In the pulsed excitation method higher current densities can be achieved [175]. Secondly, when using pulsed excitation, electrons and holes can be injected into the device for short time periods, reducing device degradation in the form of heat and stress [176]. Thirdly, triplet exciton losses can be reduced [177].

8.3 Alternative concepts

8.3.1 Photonic crystals:

The fabrication of high quality microcavities has proven to be so far difficult owing to the difficulty of growing a high quality DBR mirror on top of the organic material. An alternative approach could be the use of photonic crystals to confine light instead of using optical microcavities [178].

8.3.2 Microcavity OLETs

A transistor geometry [179] has the advantage of charge injection between the thin film and the contacts which allows electrical excitation in the vertical space between the source and the drain contacts. Therefore, reduction of the optical absorption in the gain region can be achieved. In this way it is possible to reach extremely high charge densities in the channel that in comparison to a vertical structure would require a destructively high voltage across the organic material.

8.3.3 Hybrid organic-inorganic polariton systems

Hybrid organic-inorganic polariton systems [180] are microcavities where Frenkel excitons and Wannier-Mott excitons simultaneously couple to the photon mode of the cavity structure. It has been suggested that these structures will have superior properties that can combine the best properties of both, e.g. the high oscillator strength of the organic semiconductor and the enhanced non-linearities found in inorganic semiconductors. Such hybrid organic-inorganic microcavities have already been realised [74, 87, 181] and are very promising for harvesting non-linearities.

8.4 Towards the fabrication of an organic laser diode through the strong coupling regime.

In simple terms the creation of an organic laser diode operating in the strong coupling regime will require low optical and electrical losses, high electrical conductivity of the electrodes, high quantum yield of the emissive material, high transparency of the electrodes and high mirror reflectivity. This simplified picture is illustrated in figure 8-3.

Figure 8-3 shows the schematic representation of the main parts in a strongly-coupled OLED; top and bottom DBRs to confine light with high Q factor, top and bottom electrodes with characteristic transparency and conductivity, hole and electron transport materials with high mobilities and oppositely charge blocking capability, and finally the strongly-coupled organic semiconductor for exciton formation and subsequently polariton generation.

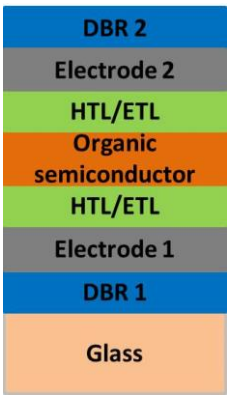

Figure 8-3 – Microcavity OLED working in the strong coupling regime with minimized losses in order to achieve organic polariton condensation.

It is very important that more research efforts must target the understanding of the mechanisms that can lead to the creation of efficient strongly-coupled OLEDs, and in the understanding of the various losses that are present in these devices.

8.5 Conclusions

To conclude, chapter 8 is the summary chapter of this thesis where the most basic rules of fabricating strongly-coupled OLEDs are given. The field of strong-coupling in organic semiconductor microcavities and LEDs is a very rich area and at the same time promising in delivering the next generation of efficient and inexpensive non-linear devices. This is reflected both by the merging areas of photonics and electronics and by the fact that the organic laser diode has as yet to be demonstrated in the field of solid state physics.

References

1. D. F. Williams and M. Schadt, "*A simple organic electroluminescent diode",* Proceedings of the IEEE, vol. 58, No. 3, pp. 476, 1970
2. C. W. Tang and S. A. VanSlyke, "*Organic electroluminescent diodes".* Appl. Phys. Lett., vol. 51, No. 12, pp. 913-915, 1987.
3. Robert W. Miles, Guillaume Zoppi, and Ian Forbes, "*Inorganic photovoltaic cells".* Materials today, vol. 10, 2007.
4. Nick Holonyak Jr., S. F. Bevacqua, "*Coherent (visible) light emission from Ga(As1−x P x) junctions".* Applied Physics Letters,Vol. 82, 1962.
5. R. S. Muller and T. I. Kamins, "*Device Electronics for Integrated Circuits"*, 3rd Edition. John Wiley & Sons, 2003.
6. Yugang Sun and John A. Rogers, "*Inorganic Semiconductors for Flexible Electronics".* Adv. Mater., Vol. 19, 2007.
7. Tayebeh Ameri, Ning Lia and Christoph J. Brabec, "*Highly efficient organic tandem solar cells: a follow up review".* Energy Environ. Sci., Vol. 6: pp. 2390–2413, 2013.
8. Henning Sirringhaus, *25th Anniversary Article: "Organic Field-Effect Transistors: The Path Beyond Amorphous Silicon".* Advanced Materials, Vol. 26, No. 9, pp. 1319-1335, 2014.
9. Dion Khodagholy et al., "*High transconductance organic electrochemical transistors".* Nature Communications, Vol. 4, 2013.
10. Anatoliy N. Sokolov, Mark E. Roberts, Zhenan Bao, "*Fabrication of low-cost electronic biosensors".* Materialstoday, Vol. 12, 2009.
11. J. Schon, C. Kloc, A. Dodabalapur, and B. Batlogg, "*An organic solid state injection laser",* Science, Vol. 289, pp. 599-601, 2000.
12. Z. Bao, B. Batlogg, S. Berg, A. Dodabalapur, R.C.Haddon, H.Hwang, C. Kloc, H. Meng and J.H.Schon, *Retraction.* Science, Vol. 298, No. 5595, pp. 961, 2002.
13. L. Elnadi, L. Alhouti, M. Omar, and M. Ragab, "*Organic thin film materials producing novel blue laser".* Chemical Physics Letters, Vol. 286, pp. 9-14, 1998.
14. Y. Tian, Z. Gan, Z. Zhou, D. W. Lynch, J. Shinar, J. hun Kang, and Q. H. Park, "*Spectrally narrowed edge emission from organic light emitting diodes".* Appl. Phys. Lett., Vol. 91, No. 14, pp. 143504, 2007.
15. Xingyuan Liu, Huibin Li, Chunyan Song, Yaqin Liao, and Miaomiao Tian, "*Microcavity organic laser device under electrical pumping".* Optics Letters, Vol. 34, No. 4, pp. 503-505, 2009.
16. Ifor D. W. Samuel, Ebinazar B. Namdas & Graham A. Turnbull, "*How to recognize lasing".* Nature Photonics, Vol. 3, pp. 546 - 549, 2009.
17. V. G. Kozlov, V. Bulovic, P. E. Burrows and S. R. Forrest, "*Laser action in organic semiconductor waveguide and double-heterostructure devices".* Nature, Vol. 389, 1997.
18. M. Berggren, A. Dodabalapur and R. E. Slusher, "*Stimulated emission and lasing in dye-doped organic thin films with Forster transfer".* Appl. Phys. Lett., Vol. 71, 1997.
19. G. Heliotis, R. Xia, D. D. C. Bradley, G. A. Turnbull, I. D. W. Samuel, P. Andrew and W. L. Barnes, "*Blue, surface-emitting, distributed feedback polyfluorene lasers".* Applied Physics Letters, Vol. 83, 2003.
20. Y. Yang, G. A. Turnbull, and I. D. Samuel, "*Hybrid optoelectronics: A polymer laser pumped by a nitride light-emitting diode".* Appl. Phys. Lett., Vol. 92, pp. 3306, 2008.
21. B.Wei, N. Kobayashi, M. Ichikawa, T. Koyama, Y. Taniguchi, and T. Fukuda, "*Organic solid laser pumped by an organic light-emitting diode".* Optics express, Vol. 14, No. 20, pp. 9436-9443, 2006.

22. Pallab Bhattacharya, Thomas Frost, Saniya Deshpande, Md Zunaid Baten, Arnab Hazari, and Ayan Das, "*Room Temperature Electrically Injected Polariton Laser".* Physical Review Letterrs, Vol. 112, pp. 236802, 2014.
23. Christian Schneider et al, "*An electrically pumped polariton laser",* Nature, Vol. 497, 2013.
24. Johannes D. Plumhof,Thilo Stöferle, Lijian Mai, Ullrich Scherf & Rainer F. Mahrt, "*Room-temperature Bose–Einstein condensation of cavity exciton–polaritons in a polymer".* Nature Materials, Vol. 13, pp. 247–252, 2014.
25. K. S. Daskalakis, S. A. Maier, R. Murray and S. Kéna-Cohen, "*Nonlinear interactions in an organic polariton condensate".* Nature Materials, Vol. 13, 2014.
26. Daniele Bajoni, Pascale Senellart, Esther Wertz, Isabelle Sagnes, Audrey Miard, Aristide Lemaître, and Jacqueline Bloch, "*Polariton Laser Using Single Micropillar GaAs–GaAlAs Semiconductor Cavities",* Phys. Rev. Lett., Vol. 100, 2008.
27. Azzini S, Gerace D, Galli M, Sagnes I, Braive R, Lemaıtre A, Bloch J and Bajoni, "*Ultra-low threshold polariton lasing in photonic crystal cavities".* Appl. Phys. Lett., Vol. 99, 2011.
28. A. Imamoglu, R. J. Ram, S. Pau and Y. Yamamoto, "*Nonequilibrium condensates and lasers without inversion: Exciton-polariton lasers".* Phys. Rev. A, Vol. 53, No. 6, 1996.
29. Wikimedia, *"Figures redrawn based on Wikimedia Commons images, edited and reused under free licence",* 2015.
30. Mathew James Stephenson, "*A study into the electronic and photophysical properteisof polycarbazoles".* Thesis, 2009.
31. Nicholas J. Turro, V. Ramamurthy, J. C. Scaiano, "*Principles of Molecular Photochemistry, An Introduction",* Sausalito, California: University Science Books, 2009.
32. T. Kobayashi, "*J-Aggregates",* World Scientific Publishing Co Pte Ltd, 1997.
33. M. Vanburgel, D. A. Wiersma, K. Duppen, J. Chem. Phys., Vol. 102, 1995.
34. Martin Grell, "*Lecture notes on Organic semiconductors",* 2010.
35. Zhenan Bao, Jason Locklin, "*Organic Field-Effect Transistors",* Taylor and Francis Group, LLC, 2007.
36. Hartmut Yersin, "*Highly Efficient OLEDs with Phosphorescent Materials",* Wiley-VCH verlag GmbH & Co, 2007.
37. G. M. Akselrod, Y. R. Tischler, E. R. Young, D. G. Nocera, and V. Bulovic, "*Exciton-exciton annihilation in organic polariton microcavities".* Phys. Rev. B, Vol. 82, pp. 113106, 2010.
38. Stefan Nowy, Benjamin C. Krummacher, Jörg Frischeisen, Nils A. Reinke, and Wolfgang Brütting, "*Light extraction and optical loss mechanisms in organic light-emitting diodes: Influence of the emitter quantum efficiency",* Appl. Phys. Lett., Vol. 104, 2008.
39. Hecht E., "*Optics, Fourth edition*," Pearson Education limited, 2014.
40. Anthony H. W. Choi, "*Handbook of Optical Microcavities*", Taylor and Francis Group, 2015.
41. M S Skolnick, T A Fisher and D M Whittaker, "*Strong coupling phenomena in quantum microcavity structures".* Semicond. Sci. Technol., Vol. 13, pp. 645–669, 1998.
42. David M. Coles, Niccolo Somaschi, Paolo Michetti, Caspar Clark, Pavlos G. Lagoudakis, Pavlos G. Savvidis & David G. Lidzey, "*Polariton-mediated energy transfer between organic dyes in a strongly coupled optical microcavity",* Nature Materials, Vol. 13, pp. 712–719, 2014.
43. P. Michetti, G. C. La Rocca, "*Photophysics of J-aggregate microcavities",* Phys. Stat. Solidi B, Vol. 245, pp. 1055-1058, 2008.
44. Paolo Michetti and Giuseppe C. La Rocca, "*Simulation of J-aggregate microcavity photoluminescence".* Phys. Rev. B, Vol. 77, pp. 195301, 2008.

45. Paolo Michetti, Giuseppe C. La Rocca, "*Exciton-phonon scattering and photoexcitation dynamics in J-aggregate microcavities",* Phys. Rev. B, Vol. 79, 2009.
46. David M. Coles , Paolo Michetti , Caspar Clark , Wing Chung Tsoi , Ali M. Adawi , Ji-Seon Kim , and David G. Lidzey, "*Vibrationally Assisted Polariton-Relaxation Processes in Strongly Coupled Organic-Semiconductor Microcavities",* Adv. Funct. Mater., Vol. 21, pp. 3691–3696, 2011.
47. Grant H. Lodden and Russell J. Holmes, "*Electrical excitation of microcavity polaritons by radiative pumping from a weakly coupled organic semiconductor",* Phys. Rev. B, Vol. 82, pp. 125317, 2010.
48. C. Weisbuch, M. Nishioka, A. Ishikawa, and Y. Arakawa, "*Observation of the coupled exciton-photon mode splitting in a semiconductor quantum microcavity",* Phys. Rev. Lett., Vol. 69, 1992.
49. D. G. Lidzey, D. D. C. Bradley, M. S. Skolnick, T. Virgili, S. Walker & D. M. Whittaker, "*Strong exciton-photon coupling in an organic semiconductor microcavity",* Nature, Vol. 395, 1998.
50. K. IGA, "*IEEE JOURNAL ON SELECTED TOPICS IN QUANTUM ELECTRONICS",* Japanese Journal of Applied Physics, Vol 6, 2000.
51. J. J. Hopfield, "*Theory of the Contribution of Excitons to the Complex Dielectric Constant of Crystals",* Phys. Rev., Vol. 112, No. 5, 1958.
52. J. J. Hopfield and D. G. Thomas, "*Polariton absorption lines",* Phys. Rev. Lett., Vol. 15, 1965.
53. K. B.Davis,M.O.Mewes, M. R. Andrews,N. J. vanDruten,D. S.Durfee,D.M. Kurn,W. Ketterle, "*Bose-Einstein condensation in a gas of sodium atoms",* Phys. Rev. Lett., Vol. 75, 1995.
54. M. H. Anderson, J. R. Ensher, M. R. Matthews, C. E. Wieman, E. A. Cornell, "*Observation of Bose-Einstein condensation in a dilute atomic vapor",* Science, Vol. 269, 1995.
55. R. Houdre, C.Weisbuch, R. P. Stanley, U. Oesterle, P. Pellandini, and M. Ilegems, "*Measurement of cavity-polariton dispersion curve from angle-resolved photoluminescence experiments",* Phys. Rev. Lett., Vol. 73, 1994.
56. Tassone F and Yamamoto Y, "*Exciton-exciton scattering dynamics in a semiconductor microcavity and stimulated scattering into polaritons",* Phys. Rev. B, Vol. 59, 1999.
57. F. Tassone, C. Piermarocchi, V. Savona, A. Quattropani, and P. Schwendimann, "*Bottleneck effects in the relaxation and photoluminescence of microcavity polaritons",* Phys. Rev. B, Vol 56, 1997.
58. A. I. Tartakovskii et al, "*Relaxation bottleneck and its sup- pression in semiconductor microcavities",* Phys. Rev. B, Vol. 62, 2000.
59. Le Si Dang, D. Heger, R. Andre, F. Boef, and R. Romestain, "*Stimulation of polariton photoluminescence in semiconductor microcavity",* Phys. Rev. Lett., Vol. 81, No. 18, pp. 3920-3923, 1998.
60. J. Kasprzak, M. Richard, S. Kundermann, A. Baas, P Jeambrun, J M J Keeling, F. M. Marchetti, M. H. Szymanska, R. Andre, J L Staehli, V Savona, P B Littlewood, B. Deveaud, and Le si Dang, "*Bose-einstein codensation of exciton polaritons",* Nature, Vol. 443, pp. 443-409. 2006.
61. S. Christopoulos, G. Baldassarri Ho¨ger von Ho¨gersthal, A. J. D. Grundy, P. G. Lagoudakis, A.V. Kavokin, and J. J. Baumberg, "*Room-Temperature Polariton Lasing in Semiconductor Microcavities",* Phys. Rev. Lett., Vol. 98, pp.126405, 2007.
62. Pallab Bhattacharya, Thomas Frost, Saniya Deshpande, Md Zunaid Baten, Arnab Hazari, and Ayan Das, "*Room Temperature Electrically Injected Polariton Laser",* Phys. Rev. Lett., Vol. 112, pp. 236802, 2014.

63. S. I. Tsintzos, N. T. Pelekanos, G. Kostantinidis, Z. Hatzopoulos and P. G. Savvidis, "*A GaAs polariton light-emitting diode operating near room temperature",* Nature, Vol. 453, 2008.
64. A. A. Khalifa, A. P. D. Love, D. N. Krizhanovskii, M. S. Skolnick, and J. S. Roberts, "Electroluminescence emission from polariton states in GaAs-based semiconductor micro- cavities", *Applied Physics Letters,* Vol 92, 2008.
65. P Tsotsis, P S Eldridge, T Gao, S I Tsintzos, Z Hatzopoulos and P G Savvidis, "*Lasing threshold doubling at the crossover from strong to weak coupling regime in GaAs microcavity",* New Jurnal of Physics, Vol. 14, 2012.
66. Hui Deng, Gregor Weihs, David Snoke, Jacqueline Bloch, and Yoshihisa Yamamoto, "*Polariton lasing vs. photon lasing in a semiconductor microcavity".* PNAS, Vol. 100, 2003.
67. Alexey Kavokin, "*Exciton-polaritons in microcavities: Recent discoveries and perspectives",* Phys. Status Solidi B, Vol. 247, No. 8, pp. 1898–1906, 2010.
68. Raphael Butte and Nicolas Grandjean, "*A novel class of coherent light emitters: polariton lasers",* Semicond. Sci. Technol., Vol. 26, No. 014030, 2011.
69. D. G. Lidzey, D. D. C. Bradley, T. Virgili, A. Armitage, S. Walker, and M. S. Skolnick, "*Room temperature polariton emission from strongly coupled organic semiconductor microcavities",* Phys. Rev. Lett., Vol. 82, 1999.
70. N. Takada, T. Kamata, D.D.C. Bradley, "*Polariton emission from polysilane-based organic microcavities",* Appl. Phys. Lett., Vol.82, 2003.
71. F Oulton, N Takada, J Koe, P N Stavrinou and D D C Bradley, "*Strong coupling in organic semiconductor microcavities",* Semicond. Sci. Technol., Vol. 18. 2003.
72. S. R. Forrest, "*Ultrathin Organic Films Grown by Organic Molecular Beam Deposition and Related Techniques",* Chem. Rev., Vol. 97, 1997.
73. R. J. Holmes and S. R. Forrest, "*Strong Exciton-Photon Coupling and Exciton Hybridization in a Thermally Evaporated Polycrystalline Film of an Organic Small Molecule",* Phys. Rev. Lett., Vol. 93, 2004.
74. Michael Slootsky, Xiaoze Liu, Vinod M. Menon, and Stephen R. Forrest, "*Room Temperature Frenkel-Wannier-Mott Hybridization of Degenerate Excitons in a Strongly Coupled Microcavity",* Phys. Rev. Lett., Vol. 112, No. 076401, 2014.
75. David G. Lidzey, Donal D. C. Bradley, Adam Armitage, Steve Walker, Maurice S. Skolnick, "*Photon-Mediated Hybridization of Frenkel Excitons in Organic Semiconductor Microcavities",* Science,Vol. 288, 2000.
76. D. G. Lidzey, A. M. Fox, M. D. Rahn, M. S. Skolnick, V. M. Agranovich and S. Walker, "*Experimental study of light emission from strongly coupled organic semiconductor microcavities following nonresonant laser excitation".* Phys. Rev. B, Vol. 65, No. 195312, 2002.
77. A. I. Tartakovskii, M. Emam-Ismail, D. G. Lidzey, M. S. Skolnick, D. D. C. Bradley, S. Walker, and V. M. Agranovich, "*Raman scattering in strongly coupled organic semiconductor microcavities".* Phys. Rev. B, Vol. 63, 2001.
78. V. M. Agranovich and Yu. N. Gartstein, "*Nature and dynamics of low-energy exciton polaritons in semiconductor microcavities",* Phys. Rev. B, Vol. 75, No. 075302, 2007.
79. M. Litinskaya, P. Reinekerb, V.M. Agranovich, "*Fast polariton relaxation in strongly coupled organic microcavities".* Journal of Luminescence, Vol. 110, pp. 364–372, 2004.
80. M. Litinskaya, P. Reinekera, V.M. Agranovich, "*Exciton–polaritons in organic microcavities",* Journal of Luminescence, Vol. 119–120, pp. 277–282, 2006.
81. V. M. Agranovich, M. Litinskaia, D. G. Lidzey, "*Cavity polaritons in microcavities containing disordered organic semiconductors",* Phys. Rev. B, Vol. 67, No. 085311, 2003.
82. Litinskaya, M., "*Propagation and localization of polaritons in disordered organic microcavities",* Phys. Lett. A, Vol. 327, pp. 3898–3903, 2008.

83. P. Michetti, G. C. La Rocca, "*Polariton states in disordered organic microcavities",* Phys. Rev. B, Vol. 71, 2005.
84. Paolo Michetti and G. C. La Rocca, "*Polariton-polariton scattering in organic microcavities at high excitation densities",* Phys. Rev. B, Vol. 82, No. 115327, 2010.
85. P. A. Hobson, W. L. Barnesa, D. G. Lidzey, G. A. Gehring, D. M. Whittaker, M. S. Skolnick and S. Walker, "*Strong exciton–photon coupling in a low-Q all-metal mirror microcavity",* Appl. Phys. Lett., Vol. 81, 2002.
86. L. G. Connolly, D. G. Lidzey, R. Butte , A. M. Adawi, D. M. Whittaker, and M. S. Skolnick, "*Strong coupling in high-finesse organic semiconductor microcavities",* Appl. Phys. Lett., Vol. 83, No. 26, 2003.
87. J. Wenus, R. Parashkov, S. Ceccarelli, A. Brehier, J.-S. Lauret, M. S. Skolnick, E. Deleporte, and D. G. Lidzey, "*Hybrid organic-inorganic exciton-polaritons in a strongly coupled microcavity".* Phys. Rev. B, Vol. 74, No. 235212, 2006.
88. S. Ke´na-Cohen and S. R. Forrest, "*Room-temperature polariton lasing in an organic single-crystal microcavity",* Nature Photonics, Vol. 4, pp. 371 - 375, 2010.
89. S Kena-Cohen, M. Davanco and S. R. Forrest, "*Strong Exciton-Photon Coupling in an Organic Single Crystal Microcavity",* Phys. Rev. Lett., Vol. 101, no. 116401, 2008.
90. Chien-Hua Yuan, Satoshi Hoshino, Seiji Toyoda, Hiroyuki Suzuki, Michiya Fujiki, and Nobuo Matsumoto, "*Room-temperature near-ultraviolet electroluminescence from a linear silicon chain",* Appl. Phys. Lett., Vol. 71, No.23, pp. 3326-3328, 1997.
91. Satish A. Patil, Ullrich Scherf, and Andrey Kadashchung, "*New conjugated ladder polymer containing carbazole moieties",* Adv. Funct. Mater., Vol. 13, 2003.
92. Scherf, U., "*Ladder-type materials",* J. Mater. Chem., Vol. 9, 1999.
93. Stéphane Kéna-Cohen ,Stefan A. Maier , and Donal D. C. Bradley, "*Ultrastrongly Coupled Exciton–Polaritons in Metal-Clad Organic Semiconductor Microcavities",* Adv. Optical Mater., Vol. 1, No. 11, 2013.
94. Jonathan R. Tischler,Jung Hoon Song, Arto Nurmikko, M. Scott Bradley, and Vladimir Bulovic, "*Strong Coupling in a Microcavity LED",* Phys. Rev. Lett., Vol. 95, No. 036401, 2005.
95. Bradley M. S., J.R.Tischler and V. Bulovic, "*Layer-by-layer J-aggregate thin films with a peak absorption constant of 10(6) cm(-1)",* Advanced Materials, Vol. 17, No. 15, pp. 1881-1884, 2005.
96. Grant H. Lodden and Russell J. Holmes, "*Thermally activated population of microcavity polariton states under optical and electrical excitation",* Phys. Rev. B, Vol. 83, No. 075301, 2011.
97. Christopher R. Gubbin, Stefan A. Maier and Stéphane Kéna-Cohen, "*Low-voltage electroluminescence from an ultrastrongly coupled polariton OLED",* Appl. Phys. Lett., Vol. 104, No. 233302, 2014.
98. Salvatore Gambino et al., "*Ultrastrong light-matter coupling in electroluminescent organic microcavities",* Applied Materials Today, Vol. 1, 2015.
99. P. Jouy, A. Vasanelli, Y. Todorov, A. Delteil, G. Biasiol, L. Sorba, and C. Sirtori, "*Transition from strong to ultra-strong coupling regime in mid-infrared metal-dielectric-metal cavities",* Appl. Phys. Lett., Vol. 98, 2011.
100. Y. Todorov, A. M. Andrews, I. Sagnes, R. Colombelli, P. Klang, G. Strasser, and C. Sirtori, "*Strong Light-Matter Coupling in Subwavelength Metal-Dielectric Microcavities at Terahertz Frequencies",* Phys. Rev. Lett., Vol. 102, 2009.
101. T. Schwartz, J. A. Hutchison, C. Genet, and T.W. Ebbesen, "*Reversible Switching of Ultrastrong Light-Molecule Coupling",* Phys. Rev. Lett., Vol. 106, 2011.
102. James A. Hutchison , Andrea Liscio , Tal Schwartz , Antoine Canaguier-Durand , Cyriaque Genet , Vincenzo Palermo , Paolo Samorì , and Thomas W. Ebbesen, "*Tuning the Work-Function Via Strong Coupling",* Adv. Mater., Vo. 25, 2013.

103. Marta Mas-Torrent, Peter Hadley, Stefan T. Bromley, Xavi Ribas, Judit Tarres, Montserrat Mas, Elies Molins, Jaume Veciana, and Concepcio Rovira, "*Correlation between Crystal Structure and Mobility in Organic Field-Effect Transistors Based on Single Crystals of Tetrathiafulvalene Derivatives",* J. Am. Chem. Soc., Vol. 126, pp. 8546-8553, 2004.
104. UQG Optics, Last time checked at 05/09/2014; Available from: http://www.uqgoptics.com/.
105. Jae-Hyung Wi, Jong-Chang Woo and Chang-Il Kim, "*Surface treatments of indium tin oxide films by using high density plasma",* Thin Solid Films, Vol. 519, pp. 6824-6828, 2011.
106. Milliron, D. J., Hill, I. G., Shen, C., Kahn, A., & Schwartz, J., "*Surface oxidation activates indium tin oxide for hole injection",*. Journal of Applied Physics, Vol. 87, 2000.
107. Stephan Kirchmeyer and Knud Reuter, "*Scientific importance, properties and growing applications of poly(3,4-ethylenedioxythiophene)",* Journal of Materials Chemistry, Vol. 15, No. 21, pp. 2077-2088, 2005.
108. Thomas Stocker, Anna Kohler, and Ralf Moos, "*Why Does the Electrical Conductivity in PEDOT:PSS Decrease with PSS Content? A Study Combining Thermoelectric Measurements with Impedance Spectroscopy",* Journal of polymer science part B, Polymer Physics, Vol. 50, pp. 976–983, 2012.
109. Paolo Vacca, Mario Petrosino, Riccardo Miscioscia, Giuseppe Nenna, Carla Minarini, Dario Della Sala, Alfredo Rubino, *Poly(3,4-ethylenedioxythiophene):poly(4-styrenesulfonate) ratio: Structural, physical and hole injection properties in organic light emitting diodes.* Thin Solid Films, Vol. 516, No. 12, pp. 4232-4237, 2008.
110. J. C. Scott, J. H. Kaufman, P. J. Brock, R. DiPietro, J. Salem, and J. A. Goitia, "*Degradation and failure of MEH-PPV light-emitting diodes",* J. Appl. Phys, Vol. 79, No. 5, pp. 2745-2751, 1995.
111. Javan H. Cook, Hameed A. Al-Attar, Andy P. Monkman, "*Effect of PEDOT–PSS resistivity and work function on PLED performance",* Organic Electronics, Vol. 15, No. 1, pp. 254-250, 2014.
112. Sam-Shajing Sun, Larry R. Dalton, *Introduction to Organic Electronic and Optoelectronic Materials and Devices*, New York: CRC Press, Taylor & Francis Group, 2008.
113. R.S. Kumar, Mark Auch, Eric Ou, Guenther Ewald, Chua Soo Jin, "*Low moisture permeation measurement through polymer substrates for organic light emitting devices",* Thin Solid Films, Vol. 417, pp. 120–126, 2002.
114. Rakhi Grover, Ritu Srivastava, Omwati Rana, D. S. Mehta, M. N. Kamalasanan, "*New Organic Thin-Film Encapsulation for Organic Light Emitting Diodes* Journal of Encapsulation and Adsorption Sciences", Vol. 1, No. 2, pp. 23-28, 2011.
115. Kröger, M., Hamwi, S., Meyer, J., Riedl, T., Kowalsky, W., & Kahn, A. , "*Role of the deep-lying electronic states of MoO3 in the enhancement of holeinjection in organic thin films",* Appl. Phys. Lett., Vol. 95, 2009.
116. L. Chai, R. T. White, M. T. Greiner, and Z. H. Lu, "*Experimental demonstration of the universal energy level alignment rule at oxide/organic semiconductor interfaces",* Phys. Rev. B, Vol. 89, No. 035202, 2014.
117. Griffin, J., "*Transition Metal Oxides and Their Use as Hole Extraction Materials in Organic Photovoltaic Devices"*, Thesis in *Physics and Astronomy*. University of Sheffield, 2014.
118. F Werfeli and E Minni , "*Photoemission study of the electronic structure of Mo and Mo oxides",* J. Phys. C: Solid State Phys, Vol. 16, pp. 6091-6100, 1983.
119. Yanming Sun , Christopher J. Takacs , Sarah R. Cowan , Jung Hwa Seo , Xiong Gong , Anshuman Roy , and Alan J. Heeger, "*Efficient, Air-Stable Bulk Heterojunction Polymer Solar Cells Using MoOx as the Anode Interfacial Layer",* Advanced Materials, Vol. 23, pp. 2226-2230, 2011.

120. Bhupendra K Sharma and Neeraj Khare, "*Effect of UV exposure on rectifying behavior of polyaniline/ZnO heterojunction",* Semicond. Sci. Technol., Vol. 28, pp. 125022, 2013.
121. Roberts D. A.*,"Radiometry and Photometry: lab notes on units",* Photonics Spectra, Vol. 4, pp. 59-63, 1987.
122. Keith A. Knauer, *HIGH-PERFORMANCE SINGLE-UNIT AND STACKED INVERTED TOP-EMITTING ELECTROPHOSPHORESCENT ORGANIC LIGHT-EMITTING DIODES*, Thesis in *Georgia Institute of Technology*, Georgia, 2015.
123. Alexander Eisfeld, John S. Briggs, "*The J-band of organic dyes: lineshape and coherence length",* Chemical Physics Letters, Vol. 281, pp. 61-70, 2002.
124. Jonathan R. Tischler, M. Scott Bradley, and Vladimir Bulovic, "*Strong-coupling in a Microcavity LED",* Phys. Rev. Lett., Vol. 95, No. 036401, 2005.
125. David M. Coles, Paolo Michetti, Caspar Clark, Ali M. Adawi and David G. Lidzey, "*Temperature dependence of the upper-branch polariton population in an organic semiconductor microcavity",* Phys. Rev. B., Vol. 84, 2011.
126. T. Virgili, D. Coles, A. M. Adawi, C. Clark, P. Michetti, S. K. Rajendran, D. Brida, D. Polli, G. Cerullo, and D. G. Lidzey, "*Ultrafast polariton relaxation dynamics in an organic semiconductor microcavity", Phys. Rev. B*, Vol. 83, 2011.
127. David M. Coles, Anthony J. H. M. Meijer, Wing C. Tsoi, Martin D. B. Charlton, Ji-Seon Kim, and David G. Lidzey, "*A Characterization of the Raman Modes in a J-Aggregate-Forming Dye: A Comparison between Theory and Experiment",* Physical Chemistry A, Vol. 114, pp. 11920–11927, 2010.
128. J. Moll, S. Daegne, J. R. Durrant, and D. A. Wiersma, J. Chem. Phys., Vol. 102, pp. 6362, 1995.
129. Hui Wang, Kevin P. Klubek, and C. W. Tang, "*Current efficiency in organic light-emitting diodes with a hole-injection layer",* Appl. Phys. Lett., Vol. 93, 2008.
130. D. Kasemann, R. Bruckner, H. Frob, and K. Leo, "*Organic light-emitting diodes under high currents explored by transient electroluminescence on the nanosecond scale",* Phys. Rev. B, Vol. 84, 2011.
131. Grant H. Lodden and Russell J. Holmes, "*Polarization splitting in polariton electroluminescence from an organic semiconductor microcavity with metallic reflectors",* Appl. Phys. Lett., Vol. 98, No. 233301, 2011.
132. Brenda C. Rowan, Lindsay R. Wilson, and Bryce S. Richards, Member, IEEE, "*Advanced Material Concepts for Luminescent Solar Concentrators",* IEEE Journal of Selected Topics In Quantum Electronics, Vol. 14, No. 5, pp. 1312-1322, 2008.
133. S. K. Rajendran et al., "*Direct evidence of Rabi oscillations and antiresonance in a strongly coupled organic microcavity",* Phys. Rev. B, Vol. 91, 2015.
134. Ajay K. Pandey and Jean-Michel Nunzi, "*Upconversion injection in rubrene/perylene-diimide-heterostructure electroluminescent diodes",* Appl. Phys. Lett., Vol. 90, 2007.
135. Huang, C., "*PERYLENE DIIMIDE-BASED MATERIALS FOR ORGANIC ELECTRONICS AND OPTICAL LIMITING APPLICATIONS*", Thesis in *Chemistry and Biochemistry*. Georgia Institute of Technology, 2010,
136. Min-Ki Kang and Dae-Gyu Moon, "*Highly Efficient Phosphorescent White Organic Light-Emitting Devices with a Poly(N-vinylcarbazole) Host Layer",* TRANSACTIONS ON ELECTRICAL AND ELECTRONIC MATERIALS, Vol. 12, 2011.
137. Shuyu Zhang, Graham A. Turnbull, Ifor D.W. Samuel, "*Highly efficient solution-processable europium-complex based organic light-emitting diodes",* Organic Electronics, Vol. 13, pp. 3091–3096, 2012.
138. Tengling Ye, Jiangshan Chen and Dongge Ma, "*Electroluminescence of poly(N-vinylcarbazole) films: fluorescence, phosphorescence and electromers",* Physical Chemistry Chemical Physics, Vol. 12, 2010.

139. Y. Sato, T. Ogata, S. Ichinosawa, Y. Murata, "*Characteristics of organic electroluminescent devices with new dopants",* Synthetic Metals, Vol. 91, pp. 103-107, 1997.
140. C. BURGDORFF, T. KIRCHER and H. G. LOHMANNSROBEN, "*Photophysical properties of tetracene derivatives in solutio",* Spectrochimica Acta, Vol. 44A, No. 11, pp. 1137-1141, 1988.
141. Sean T. Roberts, R. Eric McAnally, Joseph N. Mastron, David H. Webber, Matthew T. Whited, Richard L. Brutchey, Mark E. Thompson, and Stephen E. Bradforth, "*Efficient Singlet Fission Discovered in a Disordered Acene", Film.* J. Am. Chem. Soc., Vol. 134, pp. 6388−6400, 2012.
142. C. W. Tang, S. A. VanSlyke, and C. H. Chen, "*Electroluminescence of doped organic thin films",* Journal of applied physics, Vol. 65, 1989.
143. Chizu Sekine, Yoshiaki Tsubata, Takeshi Yamada, Makoto Kitano and Shuji Doi, "*Recent progress of high performance polymer OLED and OPV materials for organic printed electronics",* Sci. Technol. Adv. Mater., Vol. 15, 2014.
144. Bernard Geffroy, Philippe le Roy and Christophe Prat, "*Organic light-emitting diode (OLED) technology: materials, devices and display technologies",* Polymer International, Vol. 55, 2006.
145. Xiaolong Yang, Guijiang Zhou and Wai-Yeung Wong, "*Recent design tactics for high performance white polymer light-emitting diodes",* Materials Chemistry C, Vol. 2, 2014.
146. Stefan Tasch, Wilhelm Graupner, and Gunther Leising, "*Organic light-emitting devices", A Survey*,Edited by J. Shinar, Iowa: Springer-Verlag New York, 2004.
147. Hideyuki Murata, Charles D. Merritt, Hiroshi Inada, Yasuhiko Shirota, and Zakya H. Kafafi, "*Molecular organic light-emitting diodes with temperature-independent quantum efficiency and improved thermal durabilit",* Appl. Phys. Lett, Vol. 75, No. 21, pp. 3252-3254, 1999.
148. Eun-Mi Han, Lee-Mi Do, Noritaka Yamamoto, Masamichi Fujihira, "*Crystallization of organic thin films for electroluminescent devices",* Thin Solid Films, , 273, 1996.
149. Vi-En Choong, Song Shi, Jay Curless, Chan-Long Shieh, H.-C. Lee, Franky So, Jun Shen, and Jie Yang, "*Organic light-emitting diodes with a bipolar transport layer",* Appl. Phys. Lett, Vol. 75, No. 2, pp. 172-174, 1999.
150. D. Y. Kondakov, J. R. Sandifer, C. W. Tang, and R. H. Young, "*Nonradiative recombination centers and electrical aging of organic light-emitting diodes: Direct connection between accumulation of trapped charge and luminance loss",* JOURNAL OF APPLIED PHYSICS, Vol. 93, No. 2, pp. 1108-1119, 2003.
151. P. E. Burrows, V. Bulovic, S. R. Forrest, L. S. Sapochak, D. M. McCarty, and M. E. Thompson, "*Reliability and degradation of organic light emitting devices",* Appl. Phys. Lett., Vol. 65, No. 23, pp. 2922-2924, 1994.
152. A Ra Cho, Eun Hye Kim, Soo Young Park, Lee Soon Park, "*Flexible OLED encapsulated with gas barrier film and adhesive gasket.* Synthetic metals", Vol. 193, 2014.
153. S. Tasch, A. Niko, G. Leising, and U. Scherf, "*Highly efficient electroluminescence of new wide band gap ladder-type poly(para-phenylenes)",* Appl. Phys. Lett., 68, 1995.
154. M. G. Harrison, S. Moller, G. Weiser, G. Urbasch, R. F. Mahrt, H. Bassler, "*Electro-optical studies of a soluble conjugated polymer with particularly low intrachain disorder",* Phys. Rev. B, Vol. 60, 1999.
155. Kazuki Bando, Hikaru Nagai, Masamitsu Amano, Keigo Kanezashi, Shohei Kumeta, and Hisao Kondo, "*Cavity Polaritons in a Single-Crystalline Organic Microcavity Prepared at Room Temperature Using a Simple Solution Technique",* Applied Physics Express, Vol. 6, No. 111601, 2013.
156. Jeong Keun Park, Kum Hee Lee, Sunwoo Kang, Jin Yong Lee, Jung Sun Park, Ji Hoon Seo, Young Kwan Kim, and Seung Soo Yoon, "*Highly efficient blue-emitting materials based*

on 10-naphthylanthracene derivatives for OLEDs. Organic Electronics", Vol. 11, pp. 905-915, 2010.

157. Kai Zhang et al., "*High efficiency solution processed inverted white organic light emitting diodes with a cross-linkable amino-functionalized polyfluorene as a cathode interlayer",* Journal of Materials Chemistry C, Vol. 2, 2014.
158. Olga L. Griffith and Stephen R. Forrest, "*Exciton Management in Organic Photovoltaic Multidonor Energy Cascade",* Nano Letters, Vol. 14, 2014.
159. Brian W. D' Andrade and Stephen R. Forrest, "*White organic light Emitting Devices for Solid-State Lightning",* Advanced Materials, Vol. 16, 2004.
160. Samson A. Jenekhe and John A. Osahemi, "*Excimers and exciplexes of conjugated polymers",* Science, 265, 1994.
161. Sahika Inal, Marcel Schubert, Alan Sellinger, and Dieter Neher, "*The Relationship between the Electric Field-Induced Dissociation of Charge Transfer Excitons and the Photocurrent in Small Molecular/Polymeric Solar Cells",* Physical Chemistry Letters, Vol. 1, 2010,
162. David M. Coles, et. al, "*Imaging the polariton relaxation bottleneck in strongly coupled organic semiconductor microcavities",* Phys. Rev. B, Vol. 88, 2013.
163. Akshay Kumar and Chongwu Zhou, "*The Race To Replace Tin-Doped Indium Oxide: Which Material Will Win?"* ACS NANO, Vol. 4, 2010.
164. P. P. Edwards, A. Porch, M. O. Jones, D. V. Morgan and R. M. Perks, "*Basic materials physics of transparent conducting oxides",* Dalton Transactions, 2004.
165. Baolin Tian, Graeme Williams, Dayan Ban and Hany Aziz, "*Transparent organic light-emitting devices using a MoO3/Ag/MoO3 cathode",* Appl. Phys. Lett., Vol. 110, 2011.
166. Kangmin Jeon, Hongseok Youn, Seongbeom Kim, Seongbeom Shin and Minyang Yang, "*Fabrication and characterization of WO3/Ag/WO3 multilayer transparent anode with solution processed WO3 for polymer light-emitting diodes",* Nanoscale Research Letters, Vol. 7, 2012.
167. Jong-Wook Lim, Se-In Oh, Kyoungtae Eun, Sung-Hoon Choa, Hyun-Woo Koo, Tae-Woong Kim, and Han-Ki Kim, "*Mechanical Flexibility of ZnSnO/Ag/ZnSnO Films Grown by Roll-to-Roll Sputtering for Flexible Organic Photovoltaics",* Japanese Journal of Applied Physics, Vol. 51, 2012.
168. John C. C. Fan and Frank J. Bachner, "*Transparent heat mirrors for solar-energy applications",* Applied Optics, Vol. 15, 1976.
169. D.R. Sahu, Shin-Yuan Lin, Jow-Lay Huang, "*ZnO/Ag/ZnO multilayer films for the application of a very low resistance transparent electrode",* Applied Surface Science, Vol. 252, 2005.
170. Ho-Hyeong Kim et al., "*TiInZnO/Ag/TiInZnO multilayer films for transparent conducting electrodes of dye-sensitized solar cells",* Japanese Journal of Applied Physics, Vol. 53, 2014.
171. S.H. Yu, C.H. Jia, H.W. Zheng, L.H. Ding, W.F. Zhang, "*High quality transparent conductive SnO2/Ag/SnO2 tri-layer films deposited at room temperature by magnetron sputtering",* Materials Letters, Vol. 85, 2012.
172. Jin-A Jeong, Han-Ki Kim, "*Al2O3/Ag/Al2O3 multilayer thin film passivation prepared by plasma damage-free linear facing target sputtering for organic light emitting diodes",* Thin Solid Films, Vol. 547, 2013.
173. Jung-Hung Chang et al., "*Solution-processed transparent blue organic light-emitting diodes with graphene as the top cathode",* Nature Scientific Reports, Vol. 5, 2015.
174. Sarah Schols; Andrey Kadashchuk; Paul Heremans ; Anke Helfer ; Ullrich Scherf, "*Triplet excitation scavenging as method to control the triplet concentration",* SPIE Proceedings, Vol. 7415, 2009.
175. Nir Tessler, Nick T. Harrison, and Richard H. Friend, "*High Peak Brightness Polymer Light-Emitting Diodes",* Advanced Materials, Vol. 10, 1998.

176. N. Tessler, N. T. Harrison, D. S. Thomas, and R. H. Friend, "*Current heating in polymer light emitting diodes",* Appl. Phys. Lett., Vol. 73, 1998.
177. Stijn Verlaak, David Cheyns, Maarten Debucquoy, Vladimir Arkhipov, and Paul Heremans, "*Numerical simulation of tetracene light-emitting transistors: A detailed balance of exciton processes",* Appl. Phys. Lett., 2004.
178. Azzini S, Gerace D, Galli M, Sagnes I, Braive R, Lemaıtre A, Bloch J and Bajoni, "*Ultra-low threshold polariton lasing in photonic crystal cavities",* App. Phys. Lett., Vol. 99, 2011.
179. Raffaella Capelli, et al., "*Organic light-emitting transistors with an efficiency that outperforms the equivalent light-emitting diodes",* Nature Materials, Vol. 9, 2010.
180. V. M. Agranovich, Yu. N. Gartstein, and M. Litinskaya, "*Hybrid Resonant OrganicInorganic Nanostructures for Optoelectronic Applications",* Chemical Reviews, Vol. 111, pp. 5179–5214, 2011.
181. R. J. Holmes, S. Kéna-Cohen, V. M. Menon, and S. R. Forrest, "*Strong coupling and hybridization of Frenkel and Wannier-Mott excitons in an organic-inorganic optical microcavity",* Phys. Rev. B, Vol. 74, No. 235211, 2006.

Publications and presentations

Journal Publications

Nikolaos Christogiannis, Niccolo Somaschi, Paolo Michetti, David M. Coles, Pavlos G. Savvidis, Pavlos G. Lagoudakis, and David G. Lidzey., Characterising the electroluminescence emission from a strongly-coupled organic semiconductor microcavity LED, Advanced Optical Materials, 1, 2013.

Antonis Dragoneas, Nikolaos Christogiannis, Lee Hague and Martin Grell, Visible-light-induced charge carrier detrapping effects in organic thin-film transistors, in preparation..

Conferences and meeting presentations

Marie Curie Researchers Symposium, 25-27th September 2011.

European Optical Society (EOSAM), "Polariton electroluminescence in OLEDs", 25-28 September 2012, Aberdeen, Scotland, UK.

Munich-Germany meeting, "Towards to high density polariton population in organic electrically-driven devices", January 2013.

Materials Research Society (MRS) Conference, "Characterising the electroluminescence emission from a strongly coupled organic semiconductor LED", April 1-5, 2013, San Francisco, California, USA.

14th Conference on Physics of light-Matter Coupling in Nanostructures, "Strong-polariton electroluminescence from an organic polariton LED", Hersonissos, Crete, 31 May 2013.

10th international conference on Nanosciences & Nanotechnologies, "Optical and electrical characterization of strongly-coupled organic light emitting diodes", 9-12 July, Thessaloniki, Greece.

Summer schools

Orea 2011, Erasmus intensive programme, Organic Electronics and Applications, 4th July-15th July 2011, in Chania, Crete.

Orea 2012, Erasmus intensive programme, Organic Electronics and Applications, 9th July-20th July 2012, in Chania, Crete.

Appendices

Appendix A

n,k(E) calculated values of the J-aggregates of the TDBC dye.

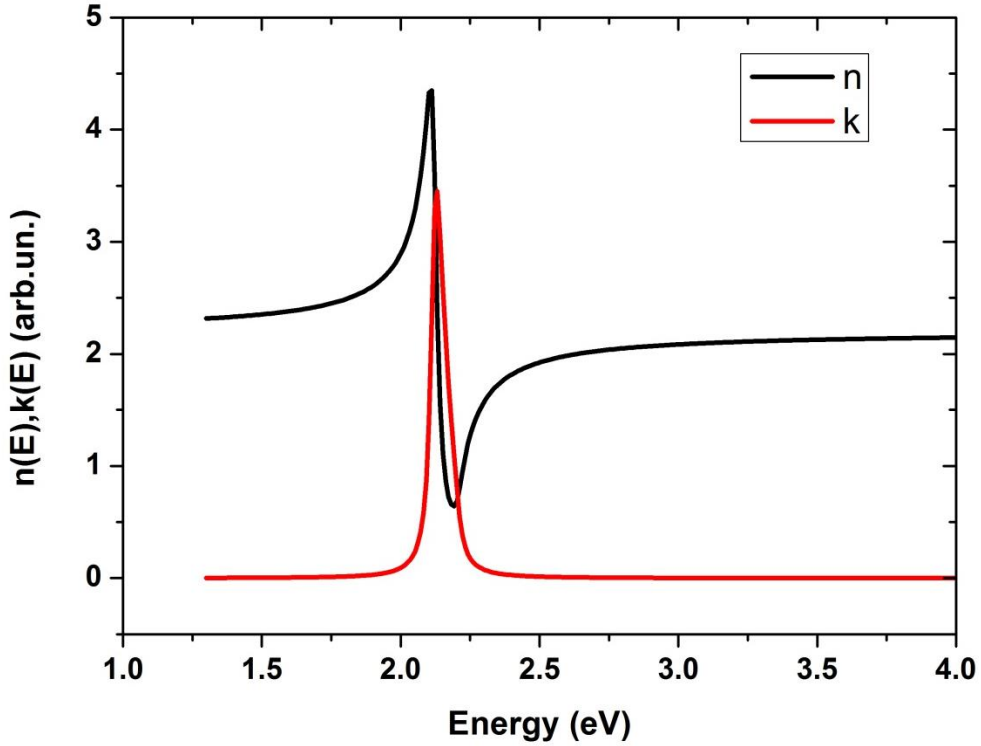

Appendix B

Photonic and excitonic fractions as a function of angle for a 2-level model:

$$\begin{bmatrix} E_{Ph} - i\gamma_{ph} & V \\ V & E_{ex} - i\gamma_{ph} \end{bmatrix} \begin{bmatrix} \alpha \\ \beta \end{bmatrix} = E(\theta) \begin{bmatrix} \alpha \\ \beta \end{bmatrix}$$

$$(E_{Ph} - i\gamma_{ph})\alpha + \beta V = E(\theta)\alpha$$

$$\alpha V + (E_{ex} - i\gamma_{ph})\beta = E(\theta)\beta$$

$$\beta = \frac{(E(\theta) - E_{Ph} + i\gamma_{ph})}{V} a =>$$

$$\beta^2 = \frac{(E(\theta) - E_{Ph} + i\gamma_{ph})^2}{V^2} a^2$$

$$\alpha^2 + \beta^2 = 1$$

$$a^2 = 1 - \beta^2 = 1 - \frac{\left(E(\theta) - E_{Ph} + i\gamma_{ph}\right)^2}{V^2} a^2 =>$$

$$a^2 = \frac{V^2}{V^2 + \left(E(\theta) - E_{Ph} + i\gamma_{ph}\right)^2}$$

$$\beta^2 = \frac{\left(E(\theta) - E_{Ph} + i\gamma_{ph}\right)^2}{V^2 + \left(E(\theta) - E_{Ph} + i\gamma_{ph}\right)^2}$$

Photonic and excitonic fractions as a function of angle for a 3-level model:

$$\begin{bmatrix} E_0 - i\gamma_{ph} & V_1 & V_2 \\ V_1 & E_{ex1} - i\gamma_{ex1} & 0 \\ V_2 & 0 & E_{ex2} - i\gamma_{ex2} \end{bmatrix} \begin{bmatrix} \alpha \\ \beta \\ \gamma \end{bmatrix} = E(\theta) \begin{bmatrix} \alpha \\ \beta \\ \gamma \end{bmatrix}$$

$$(E_0 - i\gamma_{ph})\alpha + \beta V_1 + \gamma V_2 = E(\theta)\alpha$$

$$V_1 a + (E_{ex1} - i\gamma_{ex1})\beta = E(\theta)\beta$$

$$V_2 a + (E_{ex2} - i\gamma_{ex2})\gamma = E(\theta)\gamma$$

$$\beta = \frac{V_1}{(E(\theta) - E_{ex1} + i\gamma_{ex1})} a$$

$$\gamma = \frac{V_2}{(E(\theta) - E_{ex2} + i\gamma_{ex2})} a$$

$$\alpha^2 + \beta^2 + \gamma^2 = 1$$

$$\alpha^2 + \beta^2 + \gamma^2$$
$$= \alpha^2 + \frac{{V_1}^2}{(E(\theta) - E_{ex1} + i\gamma_{ex1})^2} a^2 + \frac{{V_2}^2}{(E(\theta) - E_{ex2} + i\gamma_{ex2})^2} a^2$$
$$= \alpha^2 \left[1 + \frac{{V_1}^2}{(E(\theta) - E_{ex1} + i\gamma_{ex1})^2} + \frac{{V_2}^2}{(E(\theta) - E_{ex2} + i\gamma_{ex2})^2} \right]$$
$$= \alpha^2 \left[\frac{\begin{matrix} (E(\theta) - E_{ex1} + i\gamma_{ex1})^2 (E(\theta) - E_{ex2} + i\gamma_{ex2})^2 + \\ {V_1}^2((\theta) - E_{ex2} + i\gamma_{ex2})^2 + {V_2}^2 (E(\theta) - E_{ex1} + i\gamma_{ex1})^2 \end{matrix}}{(E(\theta) - E_{ex1} + i\gamma_{ex1})^2 (E(\theta) - E_{ex2} + i\gamma_{ex2})^2} \right] = 1 \Rightarrow$$

$$\alpha^2 = \frac{(E(\theta) - E_{ex1} + i\gamma_{ex1})^2 (E(\theta) - E_{ex2} + i\gamma_{ex2})^2}{\begin{matrix} (E(\theta) - E_{ex1} + i\gamma_{ex1})^2 (E(\theta) - E_{ex2} + i\gamma_{ex2})^2 + \\ {V_1}^2((\theta) - E_{ex2} + i\gamma_{ex2})^2 + {V_2}^2 (E(\theta) - E_{ex1} + i\gamma_{ex1})^2 \end{matrix}}$$

$$\beta^2 = \frac{{V_1}^2}{(E(\theta) - E_{ex1} + i\gamma_{ex1})^2} a^2$$
$$= \frac{{V_1}^2}{(E(\theta) - E_{ex1} + i\gamma_{ex1})^2}$$
$$* \frac{(E(\theta) - E_{ex1} + i\gamma_{ex1})^2 (E(\theta) - E_{ex2} + i\gamma_{ex2})^2}{(E(\theta) - E_{ex1} + i\gamma_{ex1})^2 (E(\theta) - E_{ex2} + i\gamma_{ex2})^2 + {V_1}^2 (E(\theta) - E_{ex2} + i\gamma_{ex2})^2 + {V_2}^2 (E(\theta) - E_{ex1} + i\gamma_{ex1})^2}$$
$$= \frac{{V_1}^2 (E - E_{ex2})^2}{(E(\theta) - E_{ex1} + i\gamma_{ex1})^2 (E(\theta) - E_{ex2} + i\gamma_{ex2})^2 + {V_1}^2 (E(\theta) - E_{ex2} + i\gamma_{ex2})^2 + {V_2}^2 (E(\theta) - E_{ex1} + i\gamma_{ex1})^2}$$

$$\gamma^2 = \frac{{V_2}^2}{(E(\theta) - E_{ex2} + i\gamma_{ex2})^2} a^2$$
$$= \frac{{V_2}^2}{(E(\theta) - E_{ex2} + i\gamma_{ex2})^2}$$
$$* \frac{(E(\theta) - E_{ex1} + i\gamma_{ex1})^2 (E(\theta) - E_{ex2} + i\gamma_{ex2})^2}{(E(\theta) - E_{ex1} + i\gamma_{ex1})^2 (E(\theta) - E_{ex2} + i\gamma_{ex2})^2 + {V_1}^2 (E(\theta) - E_{ex2} + i\gamma_{ex2})^2 + {V_2}^2 (E(\theta) - E_{ex1} + i\gamma_{ex1})^2}$$
$$= \frac{{V_2}^2 (E - E_{ex1} + i\gamma_{ex1})^2}{(E(\theta) - E_{ex1} + i\gamma_{ex1})^2 (E(\theta) - E_{ex2} + i\gamma_{ex2})^2 + {V_1}^2 (E(\theta) - E_{ex2} + i\gamma_{ex2})^2 + {V_2}^2 (E(\theta) - E_{ex1} + i\gamma_{ex1})^2}$$

Abbreviations, acronyms and symbols

Abbreviations, acronyms and symbols	
GaN	Gallium nitride
GaAlAs	Gallium aluminium arsenide
AlAs	Aluminium arsenide
TiO_2	Titanium dioxide
MoO_3	Molybdenum trioxide
ITO	Indium-tin-oxide
Al_2O_3	Aluminium oxide
SiO_2	Silicon dioxide
ZnO	Zinc oxide
Ta_2O_5	Tantalum pentoxide
LiF	Lithium fluoride
GaAs	Gallium arsenide
TDAF	2,7-bis[9,9-di(4-methylphenyl)-fluoren-2-yl]-9,9-di(4-methylphenyl)fluorene
TDBC	1,1'-diethyl-3,3'-bis(4-sulfobutyl)-5,5',6,6'-tetrachlorobenzimidazolocarbocyanine
TPP	Tetraphenyl porphyrin
Alq_3	Tris-(8-hydroxyquinoline)aluminum
DCM	4-dicyanomethylene)-2-methyl-6-(p-dimethylaminostyryl)-4H
Sq	Squarrylium
PEDOT:PSS	Poly(3,4-ethylenedioxythiophene)-poly(styrenesulfonate)
PAni	Polyaniline
PVK	Poly(9-vinylcarbazole)
TFB	Poly[(9,9-dioctylfluorenyl-2,7-diyl)-co-(4,4'-(N-(4-sec-butylphenyl)diphenylamine)]
PBD	2-(4-Biphenylyl)-5-phenyl-1,3,4-oxadiazole
BCP	Bathocuproine
MADN	2-Methyl-9,10-bis(naphthalen-2-yl)anthracene, 2-Methyl-9,10-di(2-naphthyl)anthracene, 2-Methyl-9,10-di(7-naphthalenyl)anthracene, 2-methyl-9,10-di-2-naphthalenylanthracene, 2-Methyl-9,10-di(2'-naphthyl)anthracene
DPA	9,10-Diphenylanthracene
DPT	5,12-Diphenyltetracene
LumF,LF	Lumogen F Orange 240
F8BT	Poly(9,9-dioctylfluorene-*alt*-benzothiadiazole), Poly[(9,9-di-*n*-octylfluorenyl-2,7-diyl)-*alt*-(benzo[2,1,3]thiadiazol-4,8-diyl)]
PFO	Poly[2,7-(9,9-dioctylfluorene)-*alt*-4,7-bis(thiophen-2-yl)benzo-2,1,3-thiadiazole]

NP	Poly[(9,9-dioctyl-2,7-divinylenefluorenylene)-alt-co-(1,4-phenylene)]
PVA	Poly(vinulalcohol)
PBPS	Polysilane
NTCDA	1,4,5,8-Naphthalenetetracarboxylic dianhydride
ZnTPP	Zinc tetraphenylporphyrin
meLPPP	ladder-type conjugated poly(phenylene)
Ag	Silver
Al	Aluminium
Ca	Calcium
H_2O	Water
MeOH	Methanol
IPA	Isopropanol
HCl	Hydrochloric acid
DI	De-ionised
OLED	Organic light-emitting diode
MCOLED	Microcavity organic light-emitting diode
LED	Light-emitting diode
OPV	Organic photovoltaic cell
OFET	Organic field-effect transistor
OLET	Organic light-emitting transistor
HOMO	Highest occupied molecular orbital
LUMO	Lowest occupied molecular orbital
ε_0	Electric permittivity of free space
ε_r	Relative permittivity of the material
IC	Internal conversion
ST,ISC	Inter-system crossing
IP	Ionization potential
X	Electron affinity
ϕ	Work function
$\vec{\mu}$	Dipole moment
ϕ_d	Energy shift due to dipole at interface
ϕ_{hole}	Hole injection barrier
$\phi_{electron}$	Electron injection barrier
ϕ_{anode}	Anode work function
$\phi_{cathode}$	Cathode work function
ϕ_{bi}	Built-in energy
V_{bi}	Built-in potential
A	Effective Richardson constant
K_B	Boltzmann's constant
E	Electric field
q	Charge
$V_m(E)$	Injection barrier lowering energy
J_{RS}	Richardson-Schottky current density
J_{FN}	Fowler-Nordheim current density
$\hbar$	Planck's constant
m*	Reduced mass

T	Temperature
$E_{F,m}$	Fermi energy of metal
$E_{F,org}$	Fermi energy of organic semiconductor
VL	Vacuum level
N	Number of monomers
μ	mobility
E_{act}	Activation energy
K_{mn}	Donor-acceptor transfer rate
V_{mn}	Interaction potential matrix element
$\delta(E_n-E_m)$	δ-function
τ	Lifetime
n	Refractive index
$g_A(E)$	Normalised donor absorption spectrum
$g_D(E)$	Normalised emission absorption spectrum
R_0	Förster radius
K_{DA}	Donor-acceptor energy exchange rate
K_{Dex}	Dexter transfer rate
HTL	Hole transport layer
ETL	Electron transport layer
EML	Emissive layer
HBL	Hole blocking layer
EBL	Electron blocking layer
η_{ext}	External quantum efficiency
γ	Charge balance ratio
$\eta_{S/T}$	Singlet-triplet ratio
q	Quantum efficiency
η_{out}	Outcoupling factor
PL	Photoluminescence
EL	Electroluminescence
QW	Quantum well
BEC	Bose-Einstein condensation
VCSEL	Vertical cavity surface emitting laser
DBR	Distributed bragg reflector
Q	Quality factor
δ	detuning
J_{th}	Current density lasing threshold
LPB	Lower polariton branch
MPB	Middle polariton branch
UPB	Upper polariton branch
PECVD	Plasma enhanced chemical vapour deposition
θ	angle
THz	Terahertz
t_L	Thickness of low refractive index material
t_H	Thickness of high refractive index material
λ	Wavelength
E	Energy
n_0	Refractive index of air
n_S	Refractive index of surrounding medium

T	Transmittance
R	Reflectance
A	Absorption
TE	Transverse electric mode
TM	Transverse magnetic mode
L_{DBR}	Penetration depth
λ_B	Central wavelength of DBR
ncav	Average cavity refractive index
L_C	Cavity length
E_γ	Photon energy
θ_{int}	Internal angle
θ_{ext}	External angle
ω	Angular frequency
QED	Quantum electrodynamics
k	Dephasing rate
γ	Damping rate
Ω	Light-matter interaction rate
P	Purcell factor
V	Cavity volume
FWHM	Full-width at half maximum
$\vec{H}$	Magnetic field strength
$\vec{D}$	Electric displacement
$\vec{J}$	Current density
$\vec{E}$	Electric field strength
$\vec{B}$	Magnetic induction
E_{exc}	Exciton energy
V	Interaction potential
α	Photon mixing coefficient
β	Exciton mixing coefficient
γ	Vibronic mixing coefficient
1-D	1 dimentional
E_v	Vibrational energy
η(c)	Viscocity
ZIF	Zero insertion force
PMT	Photomultiplier tube
P(λ)	Photopic response
Φ	Responsivity
Cd	Candela
NA	Numerical aperture
LBL	Layer-by-layer technique
I(θ)	Intensity
P	Population
η_{eff}	Effective refractive index
Γ	Radiative decay
CW	Continuous wave
T_g	Glass transition temperature
Φ	Relative efficiency

Acknowledgements

This project was very challenging from various viewpoints. I will be concise by thanking the people who helped me in the process.

I would like to thank my advisor D. G. Lidzey for trusting me with this very challenging topic as well as for his assistance, the discussions we had and for helping me improving my presentation skills.

I would like to thank my good friends Antonis and Delia in Sheffield, especially for their support and friendship throughout all the difficult stages I had to go through, for the uncountable good times we had together and for being there for me when I need them the most. And all the rest of the people I met in Sheffield for all the good times we had together.

From my colleagues, I would like to thank D. Coles for his help at the initial stage of my PhD as well as the entire EPMM group for all the good times, the discussions, and the interaction we had. Also, a great thanks to Pavlos Lagoudakis and Niccolo Somaschi from the University of Southampton, Pavlos Savvidis from University of Crete, and Paolo Michetti from the University of Wurzburg.

I would like to thank my sister and my parents for their constant support and for believing in me.

Last but not least, I would like to express my gratitude to my love that made me realize the meaning of the term unconditional love.